Development of high-performance catalysts for EtOH synthesis via CO_2 hydrogenation and syngas conversion

（CO_2 水素化と合成ガス変換による EtOH 合成触媒の開発）

Du Pengfei

Graduate School of Chemical Sciences and Engineering
Hokkaido University

2025

Table of contents

Chapter 1

General Introduction

1.1 The importance of ethanol to human societies

As the global population continues to grow and economies expand, the demand for natural resources, especially fossil fuels, has surged to unprecedented levels.[1–4] What followed is the scarcity of natural resources, the high consumption of fossil fuel energy, and the rise in total greenhouse gas emissions are pressing concerns that demand urgent action.[5–7] As a result, to solve the energy and resources issues and climate changes, the development of clean and renewable energy, which is inexhaustible and environmentally friendly, has become critically urgent in the 21st century.[2,6,7]

Among all the renewable chemicals, ethanol, also known as ethyl alcohol, is an important chemical compound with a wide range of applications in various industries.[8,9] It is also used for different purposes in our daily lives (**Figure 1. 1**). For example, ethanol is used in medical wipes and the most common antibacterial hand sanitizing gels and is effective against most bacteria and fungi and many viruses;[2,10] And, ethanol is the alcohol found in alcoholic drinks such as beer or whiskey; beside that, ethanol can be considered as an additive to the gasoline,[2,10] 10-20% ethanol enable provide enhanced power and performance of gasoline, due to higher-octane number than gasoline. Furthermore, ethanol is the ideal solvent for many various products in our daily life and industrial items, because it is safer.[11] It is reported that (**Figure 1. 2**),[12] in 2023, the Global Ethanol Market Size was valued at USD 91.76 Billion, and the Global Ethanol Market Size is expected to reach USD 158.13 Billion by 2033, with a growing rate of 5.59%.

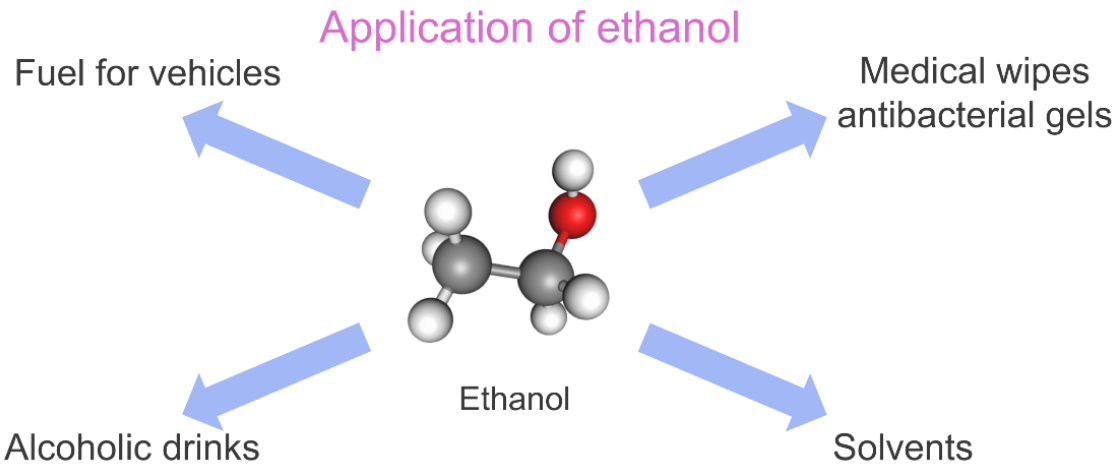

Figure 1.1. the application of ethanol in different fields.

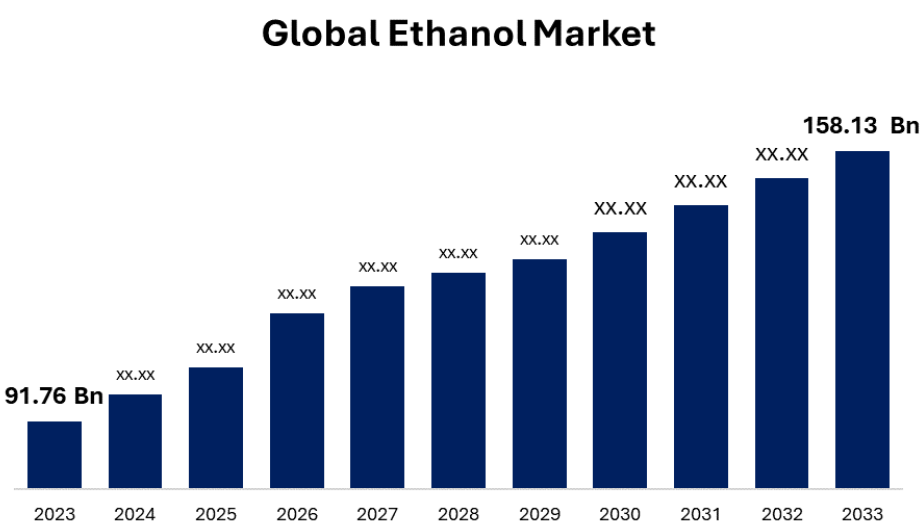

Figure 1. 2. Global ethanol market size forecasts (to 2023).[12]

1.2 The production of ethanol

Currently, bioethanol is the primary source of renewable biofuel, primarily derived from agricultural products such as potato, lignocellulosic biomass, corn starch and sugarcane.[13–16] Among them,[17] the United States and Brazil lead the world in production, generating about 15 billion and 7.5 billion gallons, respectively, in 2021. These two countries account for around 82% of global ethanol production.[17]

Due to rising alcohol demand, alternative technologies for higher alcohol synthesis (HAS) have been investigated, with some achieving industrial application.[18] For example, the Institute of Coal Chemistry at the Chinese Academy of Sciences has developed innovative CuFe-based catalysts for C_{2+} alcohols from syngas, reaching a space-time yield of alcohol exceeding 0.23 kg kg_{cat}^{-1} h^{-1}.[19] Additionally, the Dalian Institute of Chemical Physics has constructed the first ethanol production facility using an indirect coal-based process, involving coal-to-syngas conversion, syngas-to-methanol/DME, methanol/DME carbonylation, and subsequent hydrogenation.[20]

Despite considerable industrial and academic advancements in recent years, developing new reaction methodologies (direct routes, such as CO_2 hydrogenation and syngas conversion) with more efficient catalysts remains a promising area for further exploration.[21,22]

1.3 CO_2 hydrogenation to ethanol

Massive CO_2 emission has resulted in a series of ecological problems such as global warming, ocean acidification, and a marked decline in biodiversity.[23–25] According to recent climate reports, the global average temperature is forecast to increase by more than 4 °C by 2100, and the concentration of CO_2 in the atmosphere is increasing at a rate of 2 ppm/year.[26,27] Catalytic hydrogenation of CO_2 to ethanol, a process that not only contributes to CO_2 reduction but also yields a valuable chemical feedstock and renewable fuel. Compared to the methanol synthesis process from CO_2 hydrogenation, ethanol production offers a higher equilibrium conversion and operates over a wider temperature range, allowing for more complete utilization and consumption of CO_2 (**Figure 1. 3).** Moreover, the efficient use of hydrogen (H_2) aligns with Japan's vision of a "Hydrogen Society," as promoted by the Japanese government.[28,29]

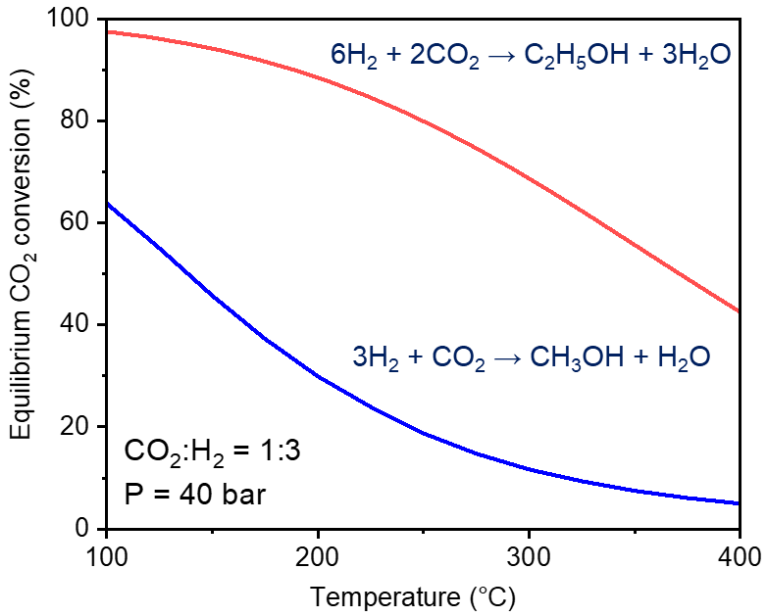

Figure 1. 3. In comparison of equilibrium CO_2 conversion to ethanol and methanol

The heterogeneous catalytic hydrogenation of CO_2 to ethanol represents a promising yet challenging route, hindered not only by the thermodynamic stability of CO_2 but also by the complexity of various reaction pathways and the difficulty in controlling C–C coupling.[18,30–33] It necessitates highly efficient catalysts to achieve high conversion rates and product selectivity. Although recent advancements in catalyst design have demonstrated considerable potential in enhancing the efficiency of this process, the development of novel catalyst systems with high selectivity and stability is still crucial for making CO_2 hydrogenation to ethanol practical.[21,22] At present, in heterogeneous catalysis, the main catalysts facilitating

CO_2 hydrogenation to ethanol are noble metal-based and transition metal catalysts, as below in details.

Noble metal-based catalysts have been extensively investigated for CO_2 hydrogenation to ethanol, owing to their exceptional activity and selectivity.[18,34–38] Among them, Rh-based catalysts are known to be suitable catalysts for the selective hydrogenation of CO into ethanol, prompting researchers to explore the use of Rh catalysts for CO_2 hydrogenation to produce higher alcohols.[34,35] A recent study by Ji et al. investigated Fe and Na co-modified Rh/CeO_2 catalysts, revealing that Fe and Na were the most effective promoters for enhancing CO_2 hydrogenation to ethanol.[30] The modified Rh/CeO_2 catalyst achieved a high ethanol selectivity of 29.8% with a CO_2 conversion rate of 13.0%, outperformed the previously Rh-based catalysts under comparable conditions. In addition, Huang et al. performed the hydrogenation of CO_2 into ethanol using ordered Pd–Cu nanoparticles in a batch reactor.[39] The studied Pd_2Cu NPs/P25 catalyst exhibited the excellent selectivity and yield of ethanol of up to 92.0%, along with good durability. Other noble metals, including Au,[40] Pd,[36,38] Ir[41] and Pt,[42] have been investigated for CO_2 hydrogenation to ethanol. However, the reported noble metal catalysts measured in fixed-bed reactors were all facing the similar problem of poor ethanol selectivity, even when different reaction conditions were employed.

Transition metal-based catalysts play a pivotal role in the hydrogenation of CO_2 to ethanol, owing to their capacity to facilitate various reaction pathways, including CO_2 activation, intermediate formation, and C–C coupling. Cu-based catalysts are effective for non-dissociative CO adsorption and are known for their low affinity to form *CH_x intermediates from CO.[43,44] However, the addition of other sites or promoters to Cu catalysts can promote the formation of CH_x species and improve their C-C coupling activity.[43,44] Cobalt is well known as good catalyst for Fischer–Tropsch synthesis (FTS) to form hydrocarbons.[45] However, it is reported that some oxygenates are also formed when Co is highly dispersed.[31,46] Various promoters and supports are commonly used to modify Co-based catalysts for improving their activity toward C_{2+} oxygenate synthesis.[46] For Fe based catalyst, the FeC_x species enable promote dissociative adsorption of CO and carbon-chain growth.[47–51] Thus, once Fe has been utilized to combine with other metals, such as Rh, Cu and Zn,[48,52,53] the performance for the catalysts will be improved effectively. For example, CuNaFe catalyst exhibited the pronounced performance with the space-time yields (STY) for ethanol and olefins reaching 153 and 680 mg g^{-1} h^{-1}, respectively, under optimized conditions (310 °C, 3.0 MPa, and 28800 mL g^{-1} h^{-1}).[54]

1.4 CO hydrogenation to ethanol

In addition to CO_2 hydrogenation to ethanol, syngas conversion is another promising approach to produce ethanol, because ethanol is initially produced as a byproduct in the direct route in Fischer–Tropsch Synthesis (FTS).[55–58] However, with the growing demand for ethanol and the continued study of syngas conversion, the transformation of syngas into higher alcohols (HAs) has become a subject of intensive research in recent decades.[59–67] Similar to FTS, the direct conversion of syngas to ethanol involves complex C–C coupling process, thus the reaction mechanism remains unclear.[55,68,69] Nevertheless, it is widely reported that a CO(H) insertion mechanism is involved, requiring bifunctional catalytic sites.[70–72] One site facilitates the formation of a CH_x intermediate,[73] while another site enables the coupling of CO or CHO with CH_x to form C_{2+} oxygenates.[70,71] These C_{2+} oxygenates can then undergo further hydrogenation to produce ethanol or other higher alcohols. Catalysts that can enhance CH_x production and improve the insertion of CO or CHO into CH_x, rather than directly forming hydrocarbons via the coupling of CH_x itself, are considered advantageous for increasing ethanol yield.[69]

Significant efforts have been devoted to developing various heterogeneous catalysts for the direct conversion of syngas into higher alcohols (HAs).[62–65,70,74] Among these, Rh-based catalysts were first reported in the 1980s,[33,67,75,76] supported on SiO_2, for the direct conversion of syngas to C_{2+} oxygenates. Subsequent research has shown that Rh-based catalysts, when used with promoters and appropriate supports, can exhibit enhanced performance.[77–81] For example, Wang et al. developed a RhMn@S-1 catalyst using Silicalite-1 as the matrix.[77] This catalyst achieved a C_2-oxygenate selectivity of 88.3% among the total oxygenates, with a 42.4% CO conversion. Additionally, Mo-based[74,82] and modified Fischer-Tropsch synthesis (FTS) catalysts, including Fe-[83,84] and Co-based[64,85,86] systems, have been optimized to balance chain growth and hydrogenation for efficient higher alcohols synthesis. Alkali promoters and metal oxides have been used to suppress over-hydrogenation,[78,79] while in some cases, metal functions are incorporated into the support material to further promote the formation of higher alcohols.[87,88] Despite many efforts have been made to discover the efficient catalysts for ethanol synthesis via CO_2 hydrogenation or syngas conversion, it is still lack of excellent catalysts that fulfill the requirements of researchers.[9,22,60]

1.5 Thesis outline

In this thesis, the attention will be focused on the development of high-performance catalysts for various ethanol synthesis reactions (CO_2 hydrogenation and syngas conversion). This thesis will be divided into the following chapters:

Chapter 2: Ethanol Synthesis via Catalytic CO_2 Hydrogenation over Multi-Elemental KFeCuZn/ZrO_2 Catalysts

We developed an efficient catalyst, K–Fe–Cu–Zn/ZrO_2 (KFeCuZn/ZrO_2), which enhances the EtOH space time yield (STY_{EtOH}) to 5.4 mmol g_{cat}^{-1} h^{-1}, under optimized conditions (360 °C, 4 MPa, and 12 L g_{cat}^{-1} h^{-1}). Furthermore, we investigated the roles of each constituent element using *in situ/operando* spectroscopy, and these results demonstrate that all components are necessary for efficient ethanol synthesis.

Chapter 3: Machine learning-assisted development of high-performance ethanol synthesis catalysts via CO_2 hydrogenation

An extrapolated machine learning (ML) method was employed to develop highly efficient catalysts for ethanol synthesis via CO_2 hydrogenation. Starting with an initial dataset of 58 catalysts (274 data points), we conducted 24 iterations of a closed loop discovery system (ML predictions + experimental validation), testing a total of 555 catalysts (2477 data points). The multi-element Pd(0.8)–Au(0.3)/K(2.5)–Sr(1)–Fe(20)–Zn(4)–Cd(2)–Yb(1)–Re(1)/CeO_2(25%)-ZrO_2 catalyst, where the numbers in parentheses represent the content amount (wt%), was identified as the most effective catalyst (STY_{EtOH}: 8.2 mmol g_{cat}^{-1} h^{-1}) for EtOH synthesis. Additionally, more than 70 catalysts with superior activity were discovered through this data-driven approach. Operando spectroscopic studies on redox mechanism for CO2 hydrogenation to CO on In2O3 catalysts

Chapter 4: Direct Syngas-to-Ethanol Conversion over Lithium-Promoted Rh/MgO Catalysts.

Direct conversion of syngas to ethanol using Li-promoted RhO_x/MgO catalysts (RhO_x/Li_2O/MgO), displaying the superior performance (ethanol selectivity and space time yield (STY_{EtOH}) reached 20% and 12.2 mmol g_{cat}^{-1} h^{-1}, respectively) than those of the Rh/MgO catalysts promoted with other alkali metals and Rh/Li_2O catalysts on other support materials. *In situ/operando* spectroscopic techniques, combined with other characterisations and

theoretical calculations, have elucidated the interactions between Li_2O and Rh on the MgO surface.

1.6 Reference

(1) Wang, J.; Azam, W. Natural Resource Scarcity, Fossil Fuel Energy Consumption, and Total Greenhouse Gas Emissions in Top Emitting Countries. *Geoscience Frontiers* **2024**, *15*, 101757.

(2) Cséfalvay, E.; Akien, G. R.; Qi, L.; Horváth, I. T. Definition and Application of Ethanol Equivalent: Sustainability Performance Metrics for Biomass Conversion to Carbon-Based Fuels and Chemicals. *Catal. Today* **2015**, *239*, 50–55.

(3) Bergougui, B. Moving toward Environmental Mitigation in Algeria: Asymmetric Impact of Fossil Fuel Energy, Renewable Energy and Technological Innovation on CO_2 Emissions. *Energy Strategy Rev.* **2024**, *51*, 101281.

(4) Yi, S.; Raza Abbasi, K.; Hussain, K.; Albaker, A.; Alvarado, R. Environmental Concerns in the United States: Can Renewable Energy, Fossil Fuel Energy, and Natural Resources Depletion Help? *Gondwana Res.* **2023**, *117*, 41–55.

(5) Moriarty, P.; Honnery, D. What Is the Global Potential for Renewable Energy? *Renew. Sust. Energ. Rev.*, 2012, *16*, 244–252.

(6) Deshmukh, M. K. G.; Sameeroddin, M.; Abdul, D.; Abdul Sattar, M. Renewable Energy in the 21st Century: A Review. *Mater. Today Proc.* **2023**, *80*, 1756–1759.

(7) Hassan, Q.; Viktor, P.; J. Al-Musawi, T.; Mahmood Ali, B.; Algburi, S.; Alzoubi, H. M.; Khudhair Al-Jiboory, A.; Zuhair Sameen, A.; Salman, H. M.; Jaszczur, M. The Renewable Energy Role in the Global Energy Transformations. *Renew. Energy Focus* **2024**, *48*, 100545.

(8) Torres-Jimenez, E.; Jerman, M. S.; Gregorc, A.; Lisec, I.; Dorado, M. P.; Kegl, B. Physical and Chemical Properties of Ethanol-Diesel Fuel Blends. *Fuel* **2011**, *90*, 795–802.

(9) Nie, X.; Li, W.; Jiang, X.; Guo, X.; Song, C. Recent Advances in Catalytic CO_2 Hydrogenation to Alcohols and Hydrocarbons. *Adv. in Catal.*, **2019**, 65, 121–233.

(10) Cséfalvay, E.; Akien, G. R.; Qi, L.; Horváth, I. T. Definition and Application of Ethanol Equivalent: Sustainability Performance Metrics for Biomass Conversion to Carbon-Based Fuels and Chemicals. *Catal. Today* **2015**, *239*, 50–55.

(11) Li, J.; Zhao, R.; Xu, Y.; Wu, X.; Bean, S. R.; Wang, D. Fuel Ethanol Production from Starchy Grain and Other Crops: An Overview on Feedstocks, Affecting Factors, and Technical Advances. *Renew. Energy*. **2022**, *188*, 223–239.

(12) *Global Ethanol Market*. https://www.sphericalinsights.com/reports/ethanol-market (accessed 2024-09-20).

(13) Chu, D.; Xin, Y.; Zhao, C. Production of Bio-Ethanol by Consecutive Hydrogenolysis of Corn-Stalk Cellulose. *Chin. J. Catal.* **2021**, *42*, 844–854.

(14) Lan, E. I.; Liao, J. C. Microbial Synthesis of N-Butanol, Isobutanol, and Other Higher Alcohols from Diverse Resources. *Bioresour. Technol.* **2013**, *135*, 339–349.

(15) Jansen, M. L. A.; Bracher, J. M.; Papapetridis, I.; Verhoeven, M. D.; de Bruijn, H.; de Waal, P. P.; van Maris, A. J. A.; Klaassen, P.; Pronk, J. T. Saccharomyces Cerevisiae Strains for Second-Generation

Ethanol Production: From Academic Exploration to Industrial Implementation. *FEMS Yeast Res*., 2017, 10.1093/femsyr/fox044.

(16) Bai, F. W.; Anderson, W. A.; Moo-Young, M. Ethanol Fermentation Technologies from Sugar and Starch Feedstocks. *Biotechnol. Adv*., **2008**, 26, 89–105.

(17) Da Silva Fernandes, F.; De Souza, É. S.; Carneiro, L. M.; Alves Silva, J. P.; De Souza, J. V. B.; Da Silva Batista, J. Current Ethanol Production Requirements for the Yeast Saccharomyces Cerevisiae. *Int. J. Microbiol*. Hindawi Limited 2022.

(18) Xu, D.; Wang, Y.; Ding, M.; Hong, X.; Liu, G.; Tsang, S. C. E. Advances in Higher Alcohol Synthesis from CO_2 Hydrogenation. *Chem* **2021**, *7*, 849–881.

(19) Kegong, F. (2012). *Novel catalyst and its matching process technology for mixed alcohol synthesis via syngas.* http://english.sxicc.cas.cn/st/rdp/201212/t20121225_97491.html (accessed 2024-09-20).

(20) Xinyi, L. (2017). *The world's first plant for ethanol production from coal successfully put into operation*. http://english.dicp.cas.cn/ns_17179/icn/201703/t20170321_175116. html. http://english.dicp.cas.cn/ ns_17179/icn/201703/t20170321_175116. html. (accessed 2024-09-20).

(21) Xu, D.; Yang, H.; Hong, X.; Liu, G.; Edman Tsang, S. C. Tandem Catalysis of Direct CO_2 Hydrogenation to Higher Alcohols. *ACS Catal.* **2021**, *11*, 8978–8984.

(22) Ye, R. P.; Ding, J.; Gong, W.; Argyle, M. D.; Zhong, Q.; Wang, Y.; Russell, C. K.; Xu, Z.; Russell, A. G.; Li, Q.; Fan, M.; Yao, Y. G. CO_2 Hydrogenation to High-Value Products via Heterogeneous Catalysis. *Nat. Commun*., **2019**, 10, 5698.

(23) He, Y.; Müller, F. H.; Palkovits, R.; Zeng, F.; Mebrahtu, C. Tandem Catalysis for CO_2 Conversion to Higher Alcohols: A Review. *Appl. Catal. B-Environ.*, 345, 123663.

(24) Han, Y.; Fang, C.; Ji, X.; Wei, J.; Ge, Q.; Sun, J. Interfacing with Carbonaceous Potassium Promoters Boosts Catalytic CO2 Hydrogenation of Iron. *ACS Catal.* **2020**, *10*, 12098–12108.

(25) Sun, X.; Yu, J.; Zada, H.; Han, Y.; Zhang, L.; Chen, H.; Yin, W.; Sun, J. Reaction-Induced Unsaturated Mo Oxycarbides Afford Highly Active CO_2 Conversion Catalysts. *Nat. Chem.* **2024**, 10.1038/s41557-024-01628–4.

(26) Valone, T. F. Linear Global Temperature Correlation to Carbon Dioxide Level, Sea Level, and Innovative Solutions to a Projected 6&Deg;C Warming by 2100. *Journal of Geoscience and Environment Protection* **2021**, *09*, 84–135.

(27) Valone, T. F. Predictive Connection for 2100 between Atmospheric Carbon, Global Warming and Ocean Height Based on Climate History. *Int. J. Environ. Clim. Chang.* **2019**, 562–594.

(28) Matsuda, S.; Kubota, H. The Feasibility of a "Hydrogen Society." **2016**.

(29) Behling, N.; Williams, M. C.; Managi, S. Fuel Cells and the Hydrogen Revolution: Analysis of a Strategic Plan in Japan. *Econ. Anal. Policy* **2015**, *48*, 204–221.

(30) Ji, S.; Hong, F.; Mao, D.; Guo, Q.; Yu, J. Enhanced Ethanol Synthesis from CO_2 Hydrogenation over Fe and Na Co-Modified Rh/CeO_2 Catalysts. *Chem. Eng. J.* **2024**, *495*, 153633.

(31) Zhang, S.; Wu, Z.; Liu, X.; Shao, Z.; Xia, L.; Zhong, L.; Wang, H.; Sun, Y. Tuning the Interaction between Na and Co_2C to Promote Selective CO_2 Hydrogenation to Ethanol. *Appl. Catal., B* **2021**, *293*, 120207.

(32) Tatsumi, T.; Muramatsu, A.; Tominaga, H.-O. Alcohol synthesis from CO_2/H_2 on Silica-supported molybdenum catalysts. *Chem. Lett.* **1985**, 593–594.

(33) Inoue, T.; Iizuka, T.; Tanabe, K. Hydrogenation of Carbon Dioxide and Carbon Monoxide over Supported Rhodium Catalysts under 10 Bar Pressure. *Appl. Catal.* **1989**, *46*, 1–9.

(34) Zhang, F.; Zhou, W.; Xiong, X.; Wang, Y.; Cheng, K.; Kang, J.; Zhang, Q.; Wang, Y. Selective Hydrogenation of CO_2 to Ethanol over Sodium-Modified Rhodium Nanoparticles Embedded in Zeolite Silicalite-1. *J. Phys. Chem. C* **2021**, *125*, 24429–24439.

(35) Kusama, H.; Okabe, K.; Sayama, K.; Arakawa, H. CO_2 Hydrogenation to Ethanol over Promoted Rh/SiO_2 Catalysts. *Catal. Today* **1996**, *28*, 261–266.

(36) Lou, Y.; jiang, F.; Zhu, W.; Wang, L.; Yao, T.; Wang, S.; Yang, B.; Yang, B.; Zhu, Y.; Liu, X. CeO_2 Supported Pd Dimers Boosting CO_2 Hydrogenation to Ethanol. *Appl. Catal., B* **2021**, *291*, 120122.

(37) Wang, G.; Luo, R.; Yang, C.; Song, J.; Xiong, C.; Tian, H.; Zhao, Z. J.; Mu, R.; Gong, J. Active Sites in CO_2 Hydrogenation over Confined VO_x-Rh Catalysts. *Sci. China: Chem.* **2019**, *62*, 1710–1719.

(38) Wang, Y.; Zhou, Y.; Zhang, X.; Wang, M.; Liu, T.; Wei, J.; Zhang, G.; Hong, X.; Liu, G. PdFe Alloy-Fe_5C_2 Interfaces for Efficient CO_2 Hydrogenation to Higher Alcohols. *Appl. Catal., B* **2024**, *345*, 123691.

(39) Bai, S.; Shao, Q.; Wang, P.; Dai, Q.; Wang, X.; Huang, X. Highly Active and Selective Hydrogenation of CO_2 to Ethanol by Ordered Pd-Cu Nanoparticles. *J. Am. Chem. Soc.* **2017**, *139*, 6827–6830.

(40) Wang, D.; Bi, Q.; Yin, G.; Zhao, W.; Huang, F.; Xie, X.; Jiang, M. Direct Synthesis of Ethanol via CO_2 Hydrogenation Using Supported Gold Catalysts. *Chem. Commun.* **2016**, *52*, 14226–14229.

(41) Kishida1994.

(42) He, Z.; Qian, Q.; Ma, J.; Meng, Q.; Zhou, H.; Song, J.; Liu, Z.; Han, B. Water-Enhanced Synthesis of Higher Alcohols from CO_2 Hydrogenation over a Pt/Co_3O_4 Catalyst under Milder Conditions. *Angew. Chem., Int. Ed.* **2016**, *128*, 747–751.

(43) Spivey, J. J.; Egbebi, A. Heterogeneous Catalytic Synthesis of Ethanol from Biomass-Derived Syngas. *Chem. Soc. Rev.* **2007**, *36*, 1514–1528.

(44) Luk, H. T.; Mondelli, C.; Ferré, D. C.; Stewart, J. A.; Pérez-Ramírez, J. Status and Prospects in Higher Alcohols Synthesis from Syngas. *Chem. Soc. Rev.* **2017**, *46*, 1358–1426.

(45) Gnanamani, M. K.; Jacobs, G.; Keogh, R. A.; Shafer, W. D.; Sparks, D. E.; Hopps, S. D.; Thomas, G. A.; Davis, B. H. Fischer-Tropsch Synthesis: Effect of Pretreatment Conditions of Cobalt on Activity and Selectivity for Hydrogenation of Carbon Dioxide. *Appl. Catal. A Gen.* **2015**, *499*, 39–46.

(46) Liu, G.; Yang, G.; Peng, X.; Wu, J.; Tsubaki, N. Recent Advances in the Routes and Catalysts for Ethanol Synthesis from Syngas. *Chem. Soc. Rev.* **2022**, *51*, 5606–5659.

(47) Zhou, Y.; Wang, Y.; Lu, H.; Liu, T.; Hong, X.; Liu, G. Highly Dispersed K- and Pd-Comodified Fe Catalyst for CO_2 Hydrogenation to Higher Alcohols. *ACS Sustain. Chem. Eng.* **2024**, *12*, 3322–3330.

(48) Xu, D.; Ding, M.; Hong, X.; Liu, G. Mechanistic Aspects of the Role of K Promotion on Cu–Fe-Based Catalysts for Higher Alcohol Synthesis from CO_2 Hydrogenation. *ACS Catal.* **2020**, *10*, 14516–14526.

(49) Yao, R.; Wei, J.; Ge, Q.; Xu, J.; Han, Y.; Ma, Q.; Xu, H.; Sun, J. Monometallic Iron Catalysts with Synergistic Na and S for Higher Alcohols Synthesis via CO_2 Hydrogenation. *Appl. Catal. B* **2021**, *298*, 120556.

(50) Li, S.; Guo, H.; Luo, C.; Zhang, H.; Xiong, L.; Chen, X.; Ma, L. Effect of Iron Promoter on Structure and Performance of K/Cu–Zn Catalyst for Higher Alcohols Synthesis from CO_2 Hydrogenation. *Catal. Letters* **2013**, *143*, 345–355.

(51) Li, S.; Yang, J.; Song, C.; Zhu, Q.; Xiao, D.; Ma, D. Iron Carbides: Control Synthesis and Catalytic Applications in CO_x Hydrogenation and Electrochemical HER. *Adv. Mater.* **2019**, *31*, 10.1002/adma.201901796.

(52) Caparrós, F. J.; Soler, L.; Rossell, M. D.; Angurell, I.; Piccolo, L.; Rossell, O.; Llorca, J. Remarkable Carbon Dioxide Hydrogenation to Ethanol on a Palladium/Iron Oxide Single-Atom Catalyst. *ChemCatChem* **2018**, *10*, 2365–2369.

(53) Kusama, H.; Okabe, K.; Sayama, K.; Arakawa, H. Ethanol Synthesis by Catalytic Hydrogenation of CO_2 over Rh/$FeSiO_2$ Catalysts. *Energy* **1997**, *22* (2–3), 343–348.

(54) Si, Z.; Wang, L.; Han, Y.; Yu, J.; Ge, Q.; Zeng, C.; Sun, J. Synthesis of Alkene and Ethanol in CO_2 Hydrogenation on a Highly Active Sputtering CuNaFe Catalyst. *ACS Sustain. Chem. Eng.* **2022**, *10*, 14972–14979.

(55) De Smit, E.; Weckhuysen, B. M. The Renaissance of Iron-Based Fischer-Tropsch Synthesis: On the Multifaceted Catalyst Deactivation Behaviour. *Chem. Soc. Rev.* **2008**, *37* (12), 2758–2781.

(56) Lohitharn, N.; Goodwin, J. G.; Lotero, E. Fe-Based Fischer-Tropsch Synthesis Catalysts Containing Carbide-Forming Transition Metal Promoters. *J. Catal.* **2008**, *255*, 104–113.

(57) Ishida, T.; Yanagihara, T.; Liu, X.; Ohashi, H.; Hamasaki, A.; Honma, T.; Oji, H.; Yokoyama, T.; Tokunaga, M. Synthesis of Higher Alcohols by Fischer-Tropsch Synthesis over Alkali Metal-Modified Cobalt Catalysts. *Appl. Catal., A* **2013**, *458*, 145–154.

(58) Wang, C.; Fang, W.; Liu, Z.; Wang, L.; Liao, Z.; Yang, Y.; Li, H.; Liu, L.; Zhou, H.; Qin, X.; Xu, S.; Chu, X.; Wang, Y.; Zheng, A.; Xiao, F. S. Fischer–Tropsch Synthesis to Olefins Boosted by MFI Zeolite Nanosheets. *Nat. Nanotechnol.* **2022**, *17*, 714–720.

(59) Ao, M.; Pham, G. H.; Sunarso, J.; Tade, M. O.; Liu, S. Active Centers of Catalysts for Higher Alcohol Synthesis from Syngas: A Review. *ACS Catal.,* **2018**, *8*, 7025–7050.

(60) Liu, G.; Yang, G.; Peng, X.; Wu, J.; Tsubaki, N. Recent Advances in the Routes and Catalysts for Ethanol Synthesis from Syngas. *Chem. Soc. Rev*. **2022**, *51*, 5606–5659.

(61) Luk, H. T.; Mondelli, C.; Ferré, D. C.; Stewart, J. A.; Pérez-Ramírez, J. Status and Prospects in Higher Alcohols Synthesis from Syngas. *Chem. Soc. Rev*. **2022**, *51*, 5606–5659.

(62) Qin, T.; Lin, T.; Qi, X.; Wang, C.; Li, L.; Tang, Z.; Zhong, L.; Sun, Y. Tuning Chemical Environment and Synergistic Relay Reaction to Promote Higher Alcohols Synthesis via Syngas Conversion. *Appl. Catal. B* **2021**, *285*, 119840.

(63) Luk, H. T.; Mondelli, C.; Mitchell, S.; Siol, S.; Stewart, J. A.; Curulla Ferré, D.; Pérez-Ramírez, J. Role of Carbonaceous Supports and Potassium Promoter on Higher Alcohols Synthesis over Copper-Iron Catalysts. *ACS Catal.* **2018**, *8*, 9604–9618.

(64) Zeng, Z.; Li, Z.; Guan, T.; Guo, S.; Hu, Z.; Wang, J.; Rykov, A.; Lv, J.; Huang, S.; Wang, Y.; Ma, X. CoFe Alloy Carbide Catalysts for Higher Alcohols Synthesis from Syngas: Evolution of Active Sites and Na Promoting Effect. *J. Catal.* **2022**, *405*, 430–444.

(65) Gong, J.; Liu, J.; Wang, S.; Guo, G.; Fan, J.; Huang, W. Effects of Mn, Zr and Ni Promoters on the Performance of CuZnO Catalyst for Ethanol Synthesis via CO Hydrogenation. *ChemistrySelect* **2022**, *7*, e202200311.

(66) Van Den Berg, F. G. A.; Glezer, J. H. E.; Sachtler', W. M. H. The Role of Promoters in CO/H_2 Reactions: Effects of MnO and MoO_2 in Silica-Supported Rhodium Catalysts. *J. Catal.* **1985**, *93*, 340–352.

(67) Kip, B. J.; Hermans, E. G. F.; Van Wolput, J. H. M. C.; Hermans, N. M. A.; Grondelle, J. Van; Prins, R. Hydrogenation of Carbon Monoxide over Rhodium/Silica Catalysts Promoted with Molybdenum Oxide and Thorium Oxide. *Appl. Catal.* **1987**, *35*, 109–139.

(68) Mäki-Arvela, P.; Aho, A.; Simakova, I.; Yu. Murzin, D. Sustainable Aviation Fuel from Syngas through Higher Alcohols. *ChemCatChem*., 2022, *14*, e202201005

(69) Gupta, M.; Smith, M. L.; Spivey, J. J. Heterogeneous Catalytic Conversion of Dry Syngas to Ethanol and Higher Alcohols on Cu-Based Catalysts. *ACS Catal*., **2011**, *1*, 641–656.

(70) Choi, Y. M.; Liu, P. Mechanism of Ethanol Synthesis from Syngas on Rh(111). *J. Am. Chem. Soc.* **2009**, *131*, 13054–13061.

(71) Zhang, K.-X.; Liu, Z.-P. *In Situ* Surfaced Mn–Mn Dimeric Sites Dictate CO Hydrogenation Activity and C_2 Selectivity over MnRh Binary Catalysts. *J. Am. Chem. Soc.* **2024**,146, 27138–27151.

(72) Inderwildi, O. R.; Jenkins, S. J.; King, D. A. Fischer-Tropsch Mechanism Revisited: Alternative Pathways for the Production of Higher Hydrocarbons from Synthesis Gas. *J. Phys. Chem. C* **2008**, *112*, 1305–1307.

(73) Zhong, L.; Yu, F.; An, Y.; Zhao, Y.; Sun, Y.; Li, Z.; Lin, T.; Lin, Y.; Qi, X.; Dai, Y.; Gu, L.; Hu, J.; Jin, S.; Shen, Q.; Wang, H. Cobalt Carbide Nanoprisms for Direct Production of Lower Olefins from Syngas. *Nature* **2016**, *538*, 84–87.

(74) Hu, J.; Wei, Z.; Zhang, Y.; Huang, R.; Zhang, M.; Cheng, K.; Zhang, Q.; Qi, Y.; Li, Y.; Mao, J.; Zhu, J.; Wu, L.; Wen, W.; Yu, S.; Pan, Y.; Yang, J.; Wei, X.; Jiang, L.; Si, R.; Yu, L.; Wang, Y.; Deng, D. Edge-Rich Molybdenum Disulfide Tailors Carbon-Chain Growth for Selective Hydrogenation of Carbon Monoxide to Higher Alcohols. *Nat. Commun.* **2023**, *14*, 6808.

(75) Van Der Lee, G.; Schuller, B.; Post, H.; Favre, T. L. F.; Ponec', V. *On the Selectivity of Rh Catalysts in the Formation of Oxygenates*. *J. Catal.* **1986**, *98*, 522-529.

(76) Masaru Ichikawa, B. Catalytic synthesis of ethanol from CO and H_2 under atmospheric pressure over pyrolysed rhodium carbonyl clusters on TiO_2, ZrO_2, and La_2O_3, *J. Chem. Soc., Chem. Commun.*, **1978**, 566-567.

(77) Wang, C.; Zhang, J.; Qin, G.; Wang, L.; Zuidema, E.; Yang, Q.; Dang, S.; Yang, C.; Xiao, J.; Meng, X.; Mesters, C.; Xiao, F. S. Direct Conversion of Syngas to Ethanol within Zeolite Crystals. *Chem* **2020**, *6*, 646–657.

(78) Feng, Y.; Zhang, Y.; Wang, J.; Ling, L.; Zhang, R.; Fan, M.; Hou, B.; Li, D.; Wang, B. Promotion of Anatase/Rutile Junction to Direct Conversion of Syngas to Ethanol on the Rh/TiO_2 Catalysts. *ACS Catal.* **2024**, *14*, 1874–1881.

(79) Tran, C. C.; Kaliaguine, S. Rhodium-Doped Iron Oxides Promoted by Sodium for Highly Selective Hydrogenation of CO_2 to Ethanol and C_{2+} Hydrocarbons. *Chem. Engin. J.* **2024**, *496*, 153636.

(80) Zhou, W.; Docherty, S. R.; Ehinger, C.; Zhou, X.; Copéret, C. The Promotional Role of Mn in CO_2 Hydrogenation over Rh-Based Catalysts from a Surface Organometallic Chemistry Approach. *Chem. Sci.* **2023**, *14*, 5379–5385.

(81) Yu, J.; Mao, D.; Ding, D.; Guo, X.; Lu, G. New Insights into the Effects of Mn and Li on the Mechanistic Pathway for CO Hydrogenation on $Rh\text{-}Mn\text{-}Li/SiO_2$ Catalysts. *J. Mol. Catal. A Chem.* **2016**, *423*, 151–159.

(82) ten Have, I. C.; Valle, E.; Gallo, A.; Snider, J. L.; Duyar, M. S.; Jaramillo, T. F. Development of Molybdenum Phosphide Catalysts for Higher Alcohol Synthesis from Syngas by Exploiting Support and Promoter Effects. *Energy Technol.* **2019**, *7*, 1801102.

(83) Lu, Y.; Cao, B.; Yu, F.; Liu, J.; Bao, Z.; Gao, J. High Selectivity Higher Alcohols Synthesis from Syngas over Three-Dimensionally Ordered Macroporous Cu-Fe Catalysts. *ChemCatChem* **2014**, *6*, 473–478.

(84) Xiao, K.; Bao, Z.; Qi, X.; Wang, X.; Zhong, L.; Fang, K.; Lin, M.; Sun, Y. Advances in Bifunctional Catalysis for Higher Alcohol Synthesis from Syngas. *Chin. J. Catal*. 2013, *34*, 116–129.

(85) Tien-Thao, N.; Alamdari, H.; Zahedi-Niaki, M. H.; Kaliaguine, S. $LaCo_{1-X}Cu_xO_{3-\delta}$ Perovskite Catalysts for Higher Alcohol Synthesis. *Appl. Catal. A Gen.* **2006**, *311*, 204–212.

(86) Subramanian, N. D.; Balaji, G.; Kumar, C. S. S. R.; Spivey, J. J. Development of Cobalt-Copper Nanoparticles as Catalysts for Higher Alcohol Synthesis from Syngas. *Catal. Today* **2009**, *147*, 100–106.

(87) Gupta, S.; Fernandes, R.; Patel, R.; Spreitzer, M.; Patel, N. A Review of Cobalt-Based Catalysts for Sustainable Energy and Environmental Applications. *Appl. Catal. A Gen.* **2006**, *661*, 119254.

(88) Lopez, L.; Velasco, J.; Cabrera, S.; Boutonnet, M.; Järås, S. Effect of Syngas Conversion and Catalyst Reduction Temperature in the Synthesis of Ethanol: Concentration of Water Vapor in Mesoporous Rh/MCM-41 Catalyst. *Catal. Commun.* **2015**, *69*, 183–187.

Chapter 2

Ethanol Synthesis via Catalytic CO_2 Hydrogenation over Multi-Elemental KFeCuZn/ZrO_2 Catalyst

2.1 Introduction

CO_2 hydrogenation into chemicals and fuels is recognized as a pivotal process for achieving a sustainable carbon cycle.[1–4] The CO_2 hydrogenation into C_{2+} alcohols has great industrial significance but is scientifically challenging, primarily because of the intricate reaction mechanisms involved and necessity of forming carbon-carbon (C–C) bonds, resulting in the low selectivity of C_{2+} alcohols.[5–8] Among the various C_{2+} alcohol products,[6,7] ethanol (EtOH) has received widespread attention in recent years as an alternative fuel,[9–11] promising hydrogen carrier,[9,12] and versatile building block chemical for producing high-value products.[9,13–15] EtOH generation not only involves competition from several parallel reactions, including the formation of C_{2+} hydrocarbons and methanol, but also requires precise control of the dissociative and non-dissociative activation of C–O bonds to obtain surface alkyl and CO (H) species, respectively.[5,6,12,16] Therefore, achieving high selectivity and yield toward EtOH is challenging but urgently desired for future CO_2 utilization.[5,9,13,14]

Various catalytic systems have been reported for the hydrogenation of CO_2 into EtOH. Among these catalytic materials, noble-metal-based catalysts (Pd[17–20] and Rh[21–25]) are usually applied to promote C−O activation and the subsequent C−C coupling for EtOH synthesis.[7,13] The high price of noble metal catalysts limits their further application; thus, researchers have shifted their attention to 3d transition metal catalysts, such as Cu-,[19,26–29] Fe-,[30–34] and Co[4,35–38]-based catalysts, coupled with promoter elements such as alkali metal oxides. Among the 3d transition metal catalysts, Fe–Cu catalysts stand out as a cost-effective option with exceptional catalytic activity to produce C_{2+} alcohols from CO_2.[30,32,39] However, they also generate a substantial amount of hydrocarbons as byproducts.[32,39,40] Although some recent work has suggested that the introduction of Zn into Cs-promoted Fe–Cu based catalysts would be more efficient in producing EtOH,[30] the catalytic performance does not meet industrial requirements. In addition, little is known about the role of each element. Further improvements in the catalyst systems are essential for developing industrially valuable reaction processes.

Herein, we present a highly efficient catalytic system, namely K-promoted FeCuZn/ZrO_2 (KFeCuZn/ZrO_2), which significantly enhances the rate of EtOH production through CO_2 hydrogenation. Under optimized conditions (360 °C, 4 MPa, and 12 L g_{cat}^{-1} h^{-1}), our catalyst (KFeCuZn/ZrO_2) exhibits high activity (STY_{EtOH}: 5.4 mmol g_{cat}^{-1} h^{-1}) in the EtOH synthesis, compared to different supports. We thoroughly investigated the role of each constituent element using *in situ/operando* spectroscopic techniques and various characterizations.

2.2 Experimental details

2.2.1 Chemicals and catalyst preparation

Chemicals and materials were purchased from commercial suppliers and used without further purification. ZrO_2 (RC-100), equivalent to JRC-ZRO-3, was supplied by Daiichi Kigenso Kagaku Kogyo. TiO_2 (P25) was obtained from Evonik. γ-Al_2O_3 (Puralox) was obtained from Sasol. SiO_2 (CariACT Q-10) was purchased from Fuji Silysia Chemical Company, Ltd.

KFeCuZn/support catalysts were prepared using a simple impregnation method. In this process, the support material was impregnated with an aqueous solution of KNO_3 (>98%; Wako Pure Chemical Industries), $Fe(NO_3)_3 \cdot 9H_2O$ (>98%; Wako Pure Chemical Industries), $Zn(NO_3)_2 \cdot 6H_2O$ (>98%; Kanto Chemical), and $Cu(NO_3)_2 \cdot 3H_2O$ (>99%; Aldrich). For example, KFeCuZn/ZrO_2 (3, 15, 10, and 5 %wt of K, Fe, Zn, and Cu, respectively) was prepared by adding a certain amount of K, Fe, Cu, and Zn precursors and ZrO_2 to a glass vessel (100 mL) containing 20 mL of deionized water. The mixture was stirred at 200 rpm for 60 min at room temperature. Subsequently, water was removed from the mixture by evaporation *in vacuum*, followed by drying at 120 °C under ambient pressure, for ~12 h. The resulting material was calcined for 3 h at 500 °C in air.

2.2.2 Characterization

X-ray diffraction (XRD) analysis was conducted on a Miniflex (Rigaku) diffractometer using Cu Kα radiation. High-angle annular dark-field scanning transmission electron microscopy (HAADF-STEM) and energy-dispersive X-ray spectroscopy (EDS) were performed using an FEI Titan G2 microscope. The samples were prepared by dropping an ethanolic solution containing a catalyst onto carbon-supported Mo grids. N_2 adsorption measurements were conducted using an AUTOSORB 6AG (Yuasa Ionics) instrument at 77 K. Before the measurements, the calcined pieces of samples were grinded and outgassed under vacuum at 200 °C for 3 h. The specific surface areas and pore size distribution of our samples were acquired by the Brunauer− Emmett− Teller (BET) method.

H_2 temperature-programmed reduction (H_2-TPR) was performed on a BELCat II instrument with a TCD detector. Briefly, ~100 mg of the catalyst was placed into a quartz tube and purged with Ar at 200 °C (2 h) to remove physically adsorbed water and surface

carbonates. Then, the sample was cooled to 50 °C, followed by subsequent heating to 800 °C in 10 vol% H_2 balanced with Ar, at a ramping rate of 10 °C/min.

CO_2 temperature programmed surface reaction (CO_2-TPSR) was conducted on a BELCat II instrument with a mass spectrometer (BELMass; MicrotracBEL Corp.). ~100 mg of catalyst was placed in a quartz tube and reduced by 10% H_2/Ar at 400 °C for 0.5 hour. The carrier gas was then changed to He and the sample cooled to 50 °C. Subsequently, 10% CO_2/He was introduced to allow CO_2 adsorption on the catalyst surface for 1 hour. The sample was then heated to 700 °C in a mixture of 10% H_2/Ar at a ramp rate of 10 °C/min. Ion fragmentation was monitored by BELMass at m/z=40 for Ar, m/z=15 for CH_4, m/z=28 for CO and m/z=44 for CO_2.

Pulse hydrogenation measurements were performed in a fixed-bed reactor. In detail, 100 mg of the used KFeCuZn/ZrO_2 catalyst was reactivated under the reaction gas (40 mL/min) at 320 °C for 1 h. After that, a pulse of CH_3CHO (500 μL for every injection) was introduced every 10 min for four cycles under a carrier gas (H_2/CO_2/Ar in a ratio of 74.4/24.8/0.8 and the total flow rate is 40 mL/min). The signals of CH_3CHO and CH_3CH_2OH were monitored using an online mass spectrometer.

Operando diffuse reflectance infrared Fourier transform (DRIFT) spectra were recorded on a JASCO FT/IR-4600 instrument equipped with a mercury-cadmium-telluride (MCT) detector. The sample was pressed into a DRIFT cell (DR-650 Ci) using a CaF_2 window. The spectra were measured by accumulating 20 scans at a resolution of 8 cm^{-1}, 0.5 MPa and temperature range of 200–320 °C. The reference spectrum in He flow (20 scans), taken at the measurement temperature, was subtracted from each spectrum. A high-sampling-rate GC-TCD (490 Micro GC; Agilent Technologies Inc.) was installed at the outlet for the analysis of methanol and ethanol.

Fe *K*-edge, Cu *K*-edge, and Zn *K*-edge X-ray absorption spectroscopy (XAS) were performed in transmission mode at BL01B1 of SPring-8 at the Japan Synchrotron Radiation Research Institute (JASRI) (Proposal no: 2023A1931). A Si (111) double crystal monochromator was used. Boron nitride (BN) was used to make a pellet sample when the required amount was less than 20 mg. The spectra of reference compounds were recorded at room temperature, in air. The obtained XAS spectra were analyzed using the Athena and Artemis software ver. 0.9.26, included in the Demeter package.[41]

For *in situ* XAS measurements, samples in pellet forms (φ: 7 mm) were introduced into a cell equipped with Kapton film windows and gas lines connected to the micro-gas chromatograph. Pretreatment of the samples involved heating under a flow of H_2 (300 mL/min) at 300 °C for 30 min. Subsequently, 25% CO_2/He (400 mL/min), 75% H_2/He (400 mL/min), and CO_2 (100 mL/min) + H_2 (300 mL/min) were introduced into the cell with He purge intervals between gas introductions.

2.2.3 Catalytic reaction

CO_2 hydrogenation reactions were conducted in a fixed-bed continuous-flow reactor operating at a total pressure of 4 MPa (40 bar). We used 1% Ar/99% H_2 (purity; H_2: 99.99999%, Ar: 99.9999%) and CO_2 (purity; 99.995%) gas cylinders to supply the reaction gases. The reactor was supplied with a gas mixture of H_2/CO_2/Ar in a ratio of 74.4/24.8/0.8, with Ar serving as an internal standard gas. Prior to the catalytic measurements, 200 mg of the catalyst was placed between quartz wool inside a 1/4 inch fixed-bed reactor (inside diameter: 3.79 mm). The catalyst was pretreated under ambient pressure at a H_2/Ar (99%) flow rate of 20 mL/min and temperature of 400 °C for 0.5 h. Following the pretreatment, a H_2/CO_2/Ar (74.4/24.8/0.8) flow at a total flow rate of 40 mL/min was passed through the catalyst bed at 4 MPa. The weight hourly space velocity (WHSV) was 12 L g_{cat}^{-1} h^{-1}. We conducted an aging treatment for 10 h at 400 °C under the reaction gas atmosphere as an accelerated aging test before recording the results of the catalytic reaction (**Figure 2. 1**). The products were analyzed using an online gas chromatograph (Shimadzu GC-2014) equipped with TCD (Shincarbon-ST column) and FID (Porapak Q column) detectors, within a reaction temperature range of 240–400 °C.

The CO_2 conversion (X_{CO2}) was calculated as follows.

$$X_{CO2} = \frac{\frac{c_{CO2}^{in}}{c_{Ar}^{in}} - \frac{c_{CO2}^{out}}{c_{Ar}^{out}}}{\frac{c_{CO2}^{in}}{c_{Ar}^{in}}} \times 100\%$$

The selectivity (S_i) for individual products was calculated by the following equation:

$$S_i = \frac{c_i \times n_i}{\sum(c_i \times n_i)} \times 100\%$$

Here, c_i is the molar fraction of product *i* (CO_2, CO, hydrocarbons, or oxygenates), and n_i is the carbon number of product *i* in the reaction.

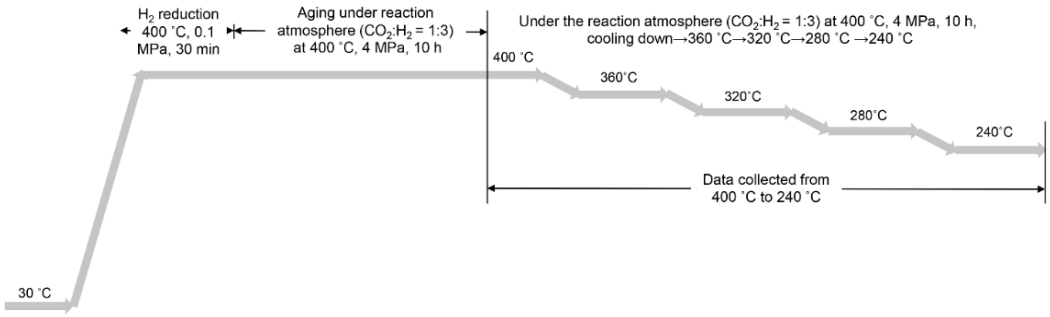

Figure 2. 1. Typical experimental procedure for catalytic tests. After conducting H_2 reduction pre-treatment at 400 °C, accelerated aging treatment was performed at 400 °C in the reaction gas atmosphere. The catalytic performance at temperatures ranging from 400 °C to 240 °C was then recorded.

The EtOH decomposition experiments were conducted in a batch reactor using the spent catalyst. The spent catalyst (50 mg) was placed in a quartz tube and reduced using H_2 at 300 °C for 30 min. Subsequently, ethanol (0.3 mL) and octane (0.7 mL) were introduced into the quartz tube and fixed in a batch reactor. The above mixture was magnetically stirred at 260 °C under N_2 (0.5 MPa) for 3 h. Gas-phase products were collected and analyzed using a GC-FID (Shimadzu GC-2014; Porapak Q column) with a methanizer (Shimadzu MTN-1), whereas the liquid-phase products were analyzed using a gas chromatograph with a GC-FID (Shimadzu GC-14B; Ultra ALLOY capillary column UA+-1; Frontier Laboratories, Ltd.).

CO hydrogenation and additional CO_2 hydrogenation over the KFeCuZn/ZrO_2 catalyst reactions were conducted in the same fixed-bed continuous-flow reactor with the same WHSV (18.45 L g_{cat}^{-1} h^{-1}) and operated at the same pressure of 3 MPa for comparison. The reactor was supplied with a gas mixture of H_2/CO (CO_2)/Ar in a ratio of 74.4/24.8/0.8 (CO or CO_2: H_2 = 1:3), with Ar serving as an internal standard gas. We conducted an aging treatment for 10 h at 400 °C under the reaction gas atmosphere as an accelerated aging test before recording the results of the catalytic reaction (as described in Fig. S1). The products were analyzed using an online gas chromatograph (Shimadzu GC-2014) equipped with TCD (Shincarbon-ST column) and FID (Porapak Q column) detectors, within a reaction temperature range of 240–400 °C.

2.3 Results and discussion

3.3.1 Catalytic CO_2 hydrogenation to EtOH

CO_2 hydrogenation reactions were conducted under specific operating conditions of P = 4 MPa, T = 280–400 °C, and WHSV = 12 L g_{cat}^{-1} h^{-1}. As shown in **Figure 2. 2a**, the KFeCuZn/ZrO_2 catalyst exhibits the highest selectivity towards C_{2+} alcohol products, with ~40 and 16.5% selectivity towards C_{2+} alcohols and EtOH, respectively, while achieving a CO_2 conversion of 52.4%. In particular, the KFeCuZn/ZrO_2 catalyst also displays an excellent space time yield (STY) of EtOH, with a STY_{EtOH} of 5.4 mmol g_{cat}^{-1} h^{-1}. In comparison, the CO_2 conversion fell within a comparable range of 49.6–56.7% for the other studied catalysts (KFe/ZrO_2, KFeCu/ZrO_2 and KFeZn/ZrO_2). Additionally, for the Cu-added catalyst (KFeCu/ZrO_2), the EtOH selectivity was approximately 14%, accompanied by a high ethanol space-time yield (STY_{EtOH}) reaching up to 4.0 mmol g_{cat}^{-1} h^{-1}, which surpasses those of catalysts without Cu (KFe/ZrO_2 and KFeZn/ZrO_2). This suggests that Cu plays a significant role in facilitating the activation and coupling of CO_2 molecules for ethanol production.[40] Although the addition of Zn (KFeZn/ZrO_2) did not directly result in an obvious enhancement in EtOH production, the catalyst incorporating both Cu and Zn (KFeCuZn/ZrO_2) demonstrated the highest selectivity and STY_{EtOH}. Literature data on EtOH synthesis from CO_2/H_2 (**Table 2. 1**) are compared with our best catalytic system. Our catalyst displayed the best STY_{EtOH} for EtOH synthesis even after the accelerated aging test at 400 °C for 10 h.

To emphasize the pivotal roles of potassium and iron, we intentionally omitted these elements from the compared catalysts, as illustrated in **Figure 2. 2a**. Notably, the FeCuZn/ZrO_2 catalyst, while maintaining a CO_2 conversion of 47% comparable to that of the KFeZnCu/ZrO_2 catalyst, exhibited a significant increase in CH_4 selectivity, reaching 37%. Simultaneously, the selectivity for total alcohols and EtOH decreased sharply to 9 and 3.4%, respectively. Furthermore, the STY_{EtOH} for the FeCuZn/ZrO_2 catalyst was measured at 0.6 mmol g_{cat}^{-1} h^{-1}. This significantly reduced alcohol activity in the absence of K underscores the essential role of K in C_{2+} alcohol synthesis and the inhibition of over-hydrogenation.[34,39,40] The EtOH production significantly decreased over the KCuZn/ZrO_2 catalyst under the same conditions because of the absence of Fe, which resulted in the loss of the ability of the catalyst for C–C coupling.[42,43] Furthermore, **Figure 2. 3a** displayed a volcano-shaped curve for STY_{EtOH} with increasing Fe loading, and the most suitable loading is 15%$_{wt}$. **Figure 2. 2b** illustrates CO_2 hydrogenation experiments using different supports, such as Al_2O_3, TiO_2, and SiO_2. All three catalysts showed an obvious decrease in the EtOH selectivity to less than 2%.

In terms of STY_{EtOH}, the KFeZnCu/ZrO_2 catalyst significantly outperformed the others, indicating that ZrO_2 is an excellent carrier for EtOH synthesis.

In addition, the effects of the reaction conditions, including reaction temperature, pressure, and WHSV, on EtOH synthesis were investigated in detail. On varying the reaction temperature within the range of 280–400 °C (**Figure 2. 3b**), the STY of EtOH and C_{2+} alcohol distribution exhibited a characteristic volcano-shaped curve. The appropriate temperature for acquiring EtOH is 360 °C. Additionally, the reaction pressure was varied from 3 to 5 MPa (**Figure 2. 3c**), and the highest STY_{EtOH} (5.4 mmol g_{cat}^{-1} h^{-1}) were achieved at 4 MPa, making it a more favorable pressure regime for C_{2+} alcohol synthesis. Furthermore, we explored the influence of the WHSV (**Figure 2. 3d**) by varying it between 9–15 L g_{cat}^{-1} h^{-1} and observed the most suitable WHSV was 12 L g_{cat}^{-1} h^{-1}. Moreover, the stability test was performed for the KFe-based catalysts (**Figure 2. 1c** and **Figure 2. 4**). Among them, KFeCu/ZrO_2, KFeZn/ZrO_2 and KFeCuZn/ZrO_2 showed robust stability, maintaining their performance for at least 60 h at 360 °C. Only KFe/ZrO_2 displayed slight decrease in STY_{EtOH} after 35 h.

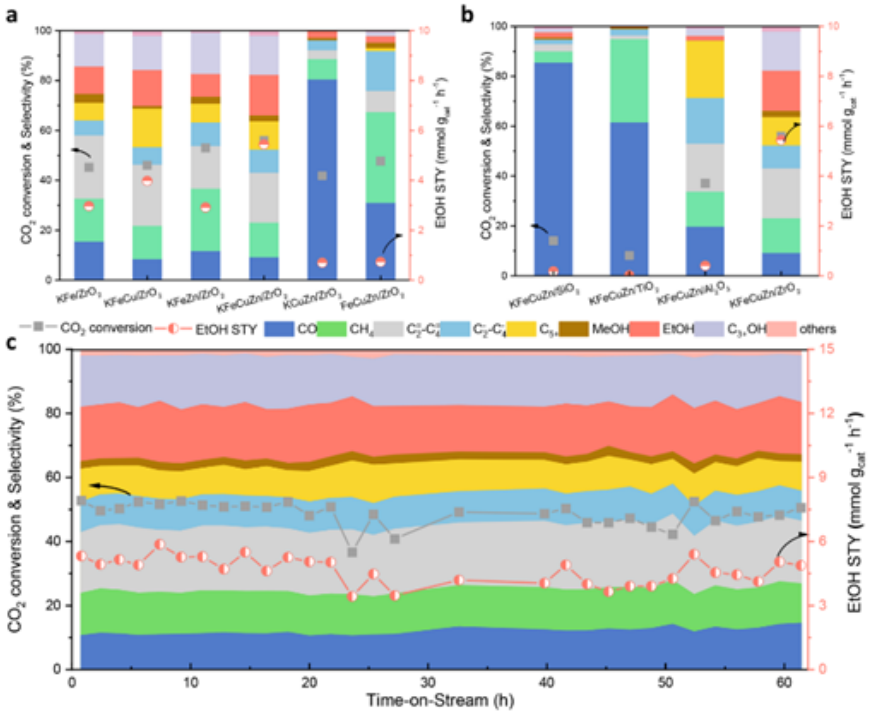

Figure 2. 2. Catalytic performance. (a) CO_2 conversion and product selectivity at 360 °C and STY_{EtOH} over KFe/ZrO_2 based catalysts; (b) CO_2 conversion, product selectivity, and STY_{EtOH} over different supporting; and (c) stability test for KFeCuZn/ZrO_2 at 360 °C. Pretreatment condition: 400 °C, 0.1 MPa, H_2 (99%), and 0.5 h. Reaction condition: 12 L g_{cat}^{-1} h^{-1}, 4.0 MPa, and H_2/CO_2/Ar (74.4/24.8/0.8%). Ar was used as an internal standard gas. The data was collected after 3 h, when the temperature and rection were stable. Accelerated aging treatment was performed before reaction at 400°C for 10 h under the reaction environment. Others include acetaldehyde and ethyl formate. In Figure 2a and b, the gray dot is CO_2 conversion; red dot is STY_{EtOH}.

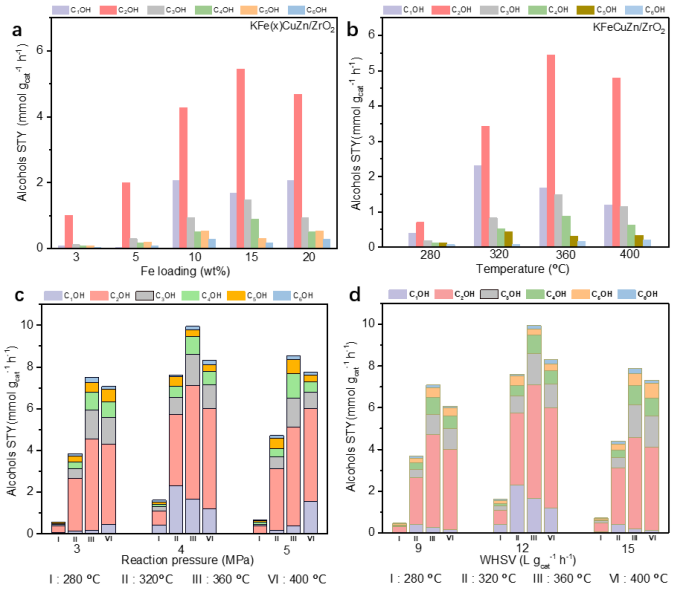

Figure 2. 3. (a) Alcohols STY distribution over the catalysts with different Fe loading at 360 °C; (b) Alcohols STY distribution at 280–400°C. Conditions: 0.2 g catalyst, H_2: CO_2= 3:1, and internal standard gas: Ar (0.8 vol%$_I$), 4 MPa, and 12 L g_{cat}^{-1} h^{-1}. Influence of pressure (c) and weight hourly space velocity (WHSV, d) on alcohols STY at 280-400 °C. Conditions: 0.2 g catalyst, H_2: CO_2 = 1:3, and internal standard gas: Ar (1 %$_{vol}$), 3-5 MPa, and 9-15 L g_{cat}^{-1} h^{-1}.

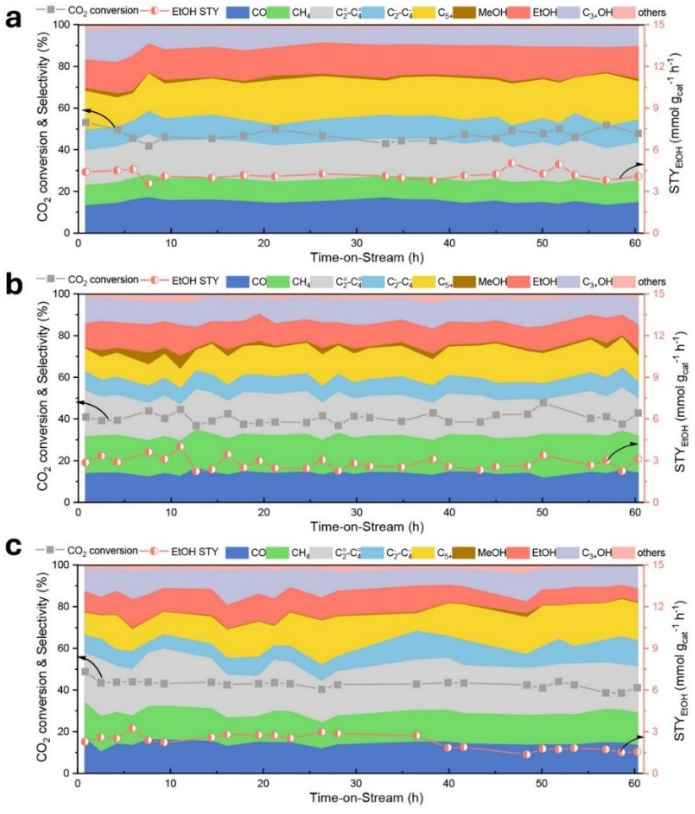

Figure 2. 4. Stability test for $KFeCu/ZrO_2$ $KFeZn/ZrO_2$ and KFe/ZrO_2 at 360 °C. Pretreatment condition: 400 °C, 0.1 MPa, H_2/Ar (99/1%), and 0.5 h. Reaction condition: 12 L g_{cat}^{-1} h^{-1}, 4.0 MPa, and H_2/CO_2/Ar (74.4/24.8/0.8%). Ar was used as an internal standard gas. Accelerated aging treatment was performed before reaction at 400°C for 10 h under the reaction environment. Others include acetaldehyde and ethyl formate. In Figure 4, the gray dots are CO_2 conversion; red dot is STY_{EtOH}.

Table 2. 1. Catalytic performances for CO_2 hydrogenation to form ethanol in this work and literature.

Catalyst	T (°C)	P (MPa)	WHSV (L g_{cat}^{-1} h^{-1})	CO_2 Conversion (%)	CO selectivity (%)	EtOH selectivity (%)	STY_{EtOH} (mmol g_{cat}^{-1} h^{-1})	References
KFeCuZn/ZrO_2*	320	4	12	39.1	17.8	14.6	3.5	This work
KFeCuZn/ZrO_2*	360	4	12	52.5	9.6	16.5	5.4	This work
Na-Co/SiO_2	250	5	6	21	27	6	0.5	[44]
Cs-$Cu_{0.8}$ $Fe_{1.0}$ $Zn_{1.0}$	330	5	4.5	35	20	12	1.1	[30]
Na-ZnFe@C	320	5	9	38.4	7.6	20.3	3.4	[31]
K/Cu-Zn-Fe	300	7	5	44.2	5.9	19.5	2.3	[45]
K−In/Ce−ZrO_2	300	10	4.5	19	57	5 (C_{2+})	0.4 (C_{2+})	[34]
2K20Fe5Rh/SiO_2	250	7.5	7	18	5	16	0.4	[23]
4.6K/CuMnZnFe	320	5	6	30.4	30.6	~7	1.7	[39]
RhFeLi/TiO_2	250	3	6000 h^{-1}	15.7	12.5	35.8	~1.3 (mmol · L_{cat}^{-1} · h^{-1})	[46]
Co/$La_4Ga_2O_9$	280	3	3	9.6	10.8	23.3	0.2	[36]
Pd/Fe_3O_4	300	0.1	60	0.3	0	97.5	0.4	[18]
Pd/CeO_2	240	3	3	9.2		99.2	1.2	[17]
Na-Rh@S-1	250	5	6	10	32	16	0.6	[21]
2%Na-Fe@C/5%KCuZnAl	320	5	4.5	39.2	9.4	35	3.6	[47]
Li-Rh/SiO_2	240	5	6	7	15.7	18.4	0.4	[48]
$Mo_1Co_1K_{0.6}$	320	5	3	23.5	77.2	8.9	0.1	[49]
K-CuMgZnFe/CZA	320	5	6	42.3	13.8	~17.4 (C_{2+})	~2.4 (C_{2+})	[50]
FeNaS-0.6	320	3	8	32.0	20.7	15.9 (C_{2+})	1.7 (C_{2+})	[51]
Cu/CeO_2	190	0.1	9	~0.1	~3	84	0.02	[29]
Pd_2Ce@Si	240	3	3	6	~2	94	0.8	[52]
Co_2C−CuZnAl	250	5	12	21	12.5	~18.9	~2.2	[53]
PdFe-6.9(37nm)	320	5	6	35.6	20.7	18.2 (C_{2+})	~1.9 (C_{2+})	[20]
$CuZnFe_{0.5}K_{0.15}$	300	6	5000 h^{-1}	42.3	49.2	36.7 (C_{2+})	3.4 (C_{2+})	[28]
Cu/Co_3O_4-2h	250	3	36	13.9	6.5	15.2	1.9	[54]
Rh-VO_x /MCM-4	250	3	6000 h^{-1}	12.1	20.1	24.1	1.1	[55]
Cu@Na-Beta	300	1.3	12	7.9	30.5	69.5	3.4	[27]
90Fe10Co (1.0)K	240	1.2	1.5	14.5	45.5	10.8	0.07	[56]
$Cu_{25}Fe_{22}Co_3K_3$-$CuZn_{1.0}K_{0.15}$	350	6	5000 h^{-1}	32.4	45.3	< 12	< 0.6 (mmol · L_{cat}^{-1} · h^{-1})	[57]
CoMoS	340	10.4	0.43	32	57.5	12.9	0.07	[58]
Na–CuCo-9	330	4	5	20.1	26.5	18.0	~2.3	[4]
K-CuZnAl/$Zr_{(0.03)}$-CuFe	320	4	24	28.8	~13.4	19.7 (C_{2+})	3.8 (C_{2+})	[59]
Rh-Fe/TiO_2	270	2	8	9.2	28.4	6.4	0.6	[60]
Rh-Fe/SiO_2	260	5	6	16.7	19.7	16	1.4	[25]
IrMo-SiO_2	200	4.9	2000 h^{-1}	7	41.7	4.3	0.04	[61]
Rh/CeO_2-SiO_2	240	5	3	8.3	33.5	6.1 (C_{2+})	0.2 (C_{2+})	[62]
RhLi/Y	250	3	6	13.1	86.6	2.7(C_{2+})	0.8 (C_{2+})	[63]
α-$CoMoO_4$/K	250	3	1.2	7.2	27.8	4.8 (C_{2+})	0.2 (C_{2+})	[64]
β-MoC_y	200	2	9	6	39	3 (C_{2+})	0.1 (C_{2+})	[65]
Pt/Co_3O_4	200	2	3	27	0	4.2 (C_{2+})	0.3 (C_{2+})	[66]
In_2O_3−Fe_2O_3−K−Al_2O_3	300	2	4	36	~40	42 (C_{2+})	3.02 (C_{2+})	[67]
3KCuFeZn/CuZnAlZr	300	5	3	27	28	24.6 (C_{2+})	0.9 (C_{2+})	[68]

3.3.2 Structural characterization

Multiple characterization methods were used to reveal the physical characterizations and structural evolution. The BET specific surface areas and pore volumes (**Table 2. 2**), obtained from the N_2 adsorption measurements at 77 K, decreased upon increase in loading amount of the supported species. Pore size distributions were not significantly different among samples measured (**Figure 2. 5**). XRD patterns (**Figure 2. 6**) show that the ZrO_2 support is composed of monoclinic and minor tetragonal phases based on the diffraction angles and intensities. Phase transformations of the loading elements were also observed at different reaction stages. For example, for the $KFeCuZn/ZrO_2$ catalyst, metallic Fe was obtained after H_2 reduction pretreatment (**Figure 2. 6**); subsequently, metallic Fe was oxidized to Fe_3O_4 and carburized to Fe_5C_2 after the reaction.[42,69] Iron carbide (Fe_5C_2) is an essential phase for C–C coupling in the Fischer–Tropsch (F–T) process over Fe-based catalysts.[42] Cu-derived peaks were not observed by XRD after calcination and reduction, probably due to the highly dispersed nature of Cu. Metallic copper was observed after the reaction owing to the sintering of Cu under a reductive atmosphere for a longer time. For the Zn species, only ZnO diffraction peaks were observed, indicating that no phase changes occurred during the entire reaction process. In comparison with the other control catalysts (**Figure 2. 6**), the same evolution processes (reduction and carburization of Fe, reduction and aggregation of Cu, and stability of ZnO on Zn) were observed for the catalysts containing the relative elements.

Table 2. 2. the specific surface area and pore volume of studied KFe-based catalysts.

Samples	BET specific surface area (m^2/g)	Pore volume (cm^3/g)
KFe/ZrO_2	60.4	0.059
$KFeCu/ZrO_2$	54.8	0.051
$KFeZn/ZrO_2$	41.4	0.039
$KFeCuZn/ZrO_2$	40.6	0.036

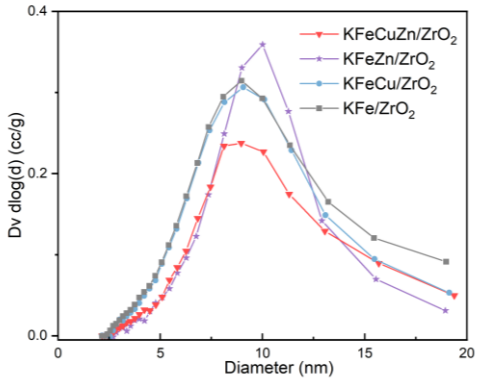

Figure 2. 5. Pore size distribution curve of the studied samples calculated from desorption branch of the isotherm by the BJH method.

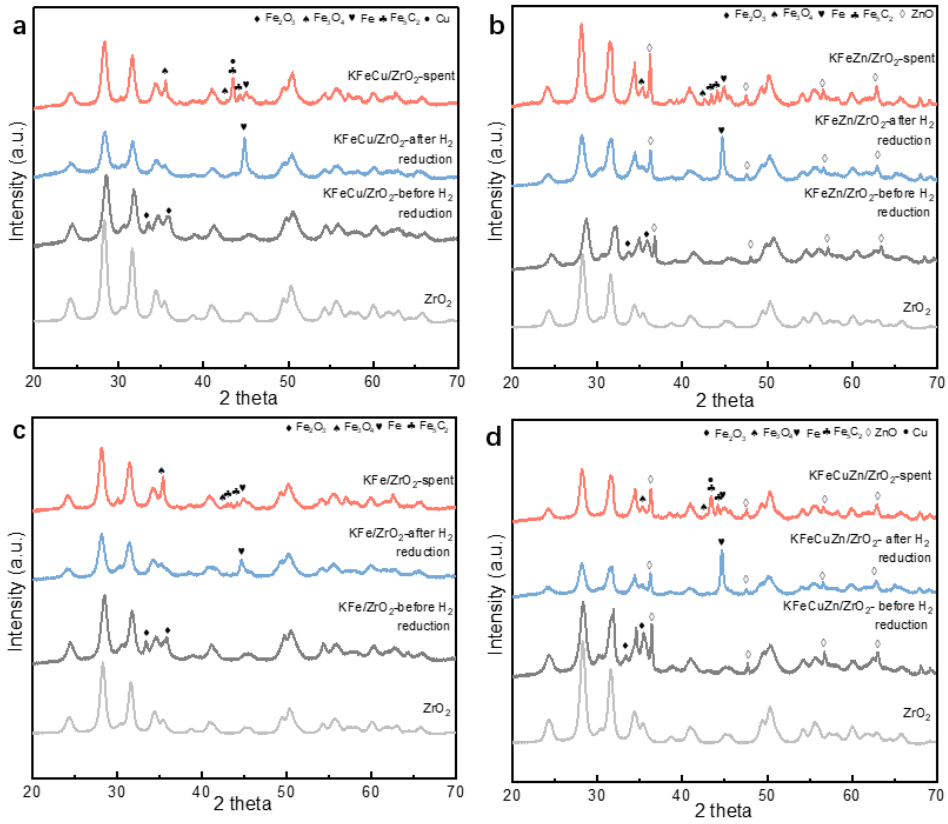

Figure 2. 6. XRD patterns for (a) KFeCu/ZrO_2; (b) KFeZn/ZrO_2; (c) KFe/ZrO_2; and (d) KFeCuZn/ZrO_2before and after H_2 reduction, as well as after reaction. “Spent catalyst" refers to a sample that has undergone a 20-hour accelerated aging treatment at 400 °C under the reaction condition.

To further clarify the phase transformations of Fe, Cu, and Zn species, X-ray adsorption spectroscopy (XAS) was performed on KFeCuZn/ZrO_2. The *ex situ* X-ray absorption near edge structure (XANES) spectra of the Fe *K*-edge (**Figure 2. 7a**) show that after H_2 reduction as the pretreatment, the absorption edge shifted to almost the same energy as that of the Fe foil, suggesting that the Fe species in KFeZnCu/ZrO_2 were completely reduced. Similarly, after the reaction, the absorption edge moved to a higher energy compared to that of the Fe foil, suggesting the partial oxidation of Fe, in line with the XRD results. Extended X-ray absorption fine structure (EXAFS) results further helped to understand the local environmental changes (**Figure 2. 7b** and **Table 2. 3**). After the H_2 reduction pretreatment, the Fe–Fe bonds at 2.45 and 2.83 Å appeared, whereas the Fe–O bond at 1.99 Å disappeared.[47,70] After the reaction, Fe–C and Fe–O appeared, and the Fe–Fe bond weakened, indicating the generation of FeO_x and FeC_x, consistent with the XRD results. In the case of Cu (**Figure 2. 7c**), as exhibited in *ex situ* XANES spectra, CuO was reduced to metallic Cu after reduction, which was maintained until the end of the reaction, as supported by the curve fitting of the EXAFS spectra (**Figure 2. 7d** and **Table 2. 4**). Additionally, as

indicated by the Zn *K*-edge XANES (**Figure 2. 7e**), after reduction, a weak shift to a lower energy was observed, implying the presence of a minor amount of metallic Zn, as confirmed by the EXAFS curve fitting results (**Figure 2. 7f** and **Table 2. 5**). In contrast, after the reaction, the energy increased to that of the closed ZnO reference and only one component of ZnO was captured (**Table 2. 5**), indicating that the zinc species prefers oxygen over hydrogen.[71]

H_2-TPR experiments were carried out to clarify the reduction ability of different additive elements and H_2 activation capacity over different catalysts. As depicted in **Figure 2. 8**, considering mono-component supported catalysts such as Fe/ZrO_2, Cu/ZrO_2, and Zn/ZrO_2, Cu displayed the lowest reduction temperature and was the most readily reduced element, followed by Fe. In agreement with the XRD and XAS results, no reduction was observed in the ZnO content. In contrast, the introduction of K could promoted the generation of reduction peak at 600 °C, unlike with pure ZrO_2.[40] Contrastingly, after loading the promoter, the reduction temperatures of Fe and Cu increased for KFe/ZrO_2 and KCu/ZrO_2, inhibiting the reduction of the active elements.[39,40] Furthermore, in comparison with KFe/ZrO_2 and KFeCu/ZrO_2, the temperature for the reduction of Fe_2O_3 to Fe_3O_4 on the KFeCu/ZrO_2 catalyst decreased to 390 °C.[72] In contrast, the reduction temperature of FeO_x remained virtually unchanged over the KFeZn/ZrO_2 catalyst, suggesting that the introduction of Zn was ineffective in promoting the reduction of the Fe species. However, after loading Zn into KFeCu/ZrO_2, the reduction temperature increased slightly, indicating that the introduction of Zn led to a decrease in the reduction ability.[71,73]

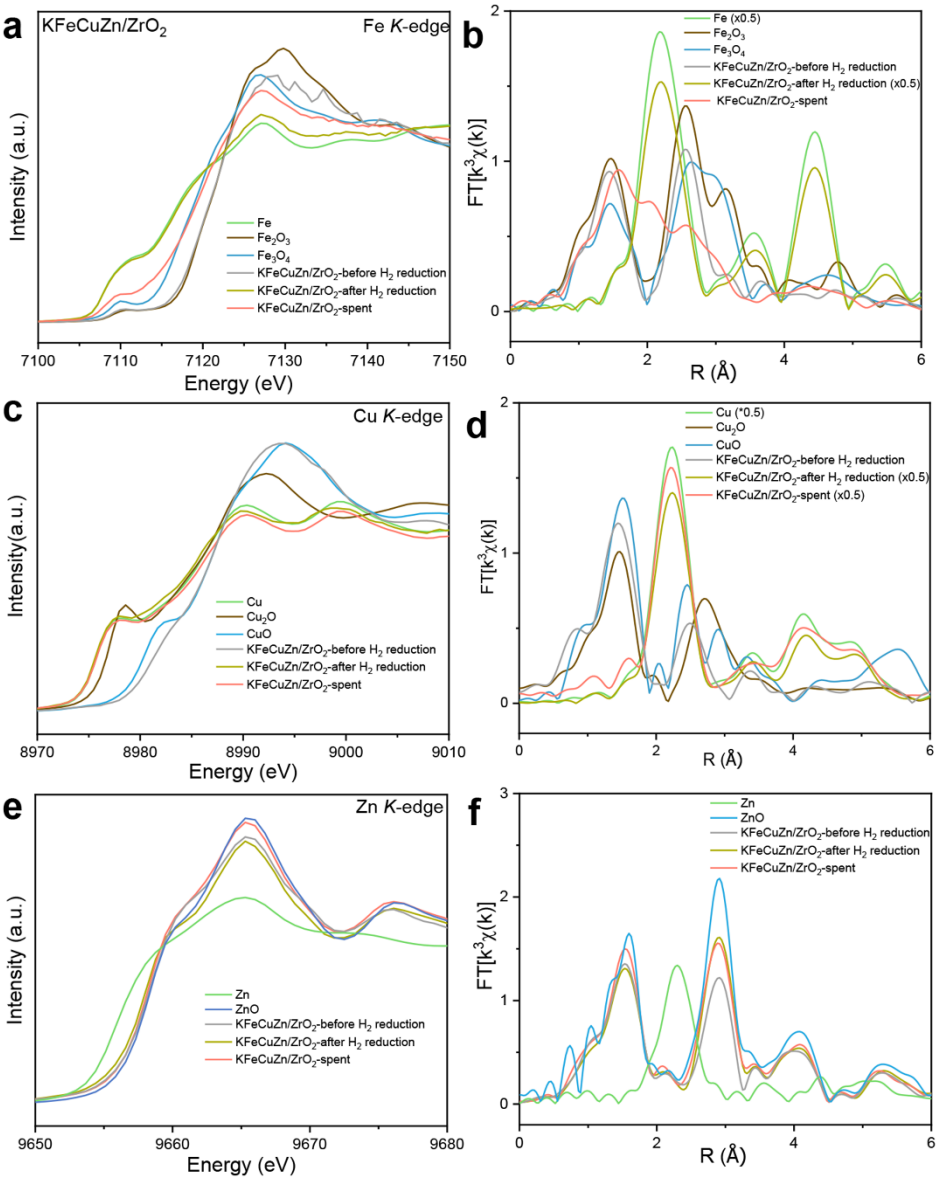

Figure 2. 7. *Ex situ* XAS spectra over KFeCuZn/ZrO$_2$ before and after H$_2$ reduction at 400 °C as a pretreatment and after reaction (spent). (a) Normalized Fe *K*-edge XANES spectra; (b) FT-EXAFS spectra for Fe; (c) normalized Cu *K*-edge XANES spectra; (d) FT-EXAFS spectra for Cu; (e) normalized Zn *K*-edge XANES spectra; and (f) FT-EXAFS spectra for Zn. “Spent catalyst" refers to a sample that has undergone a 20-hour accelerated aging treatment at 400 °C under the reaction condition.

Table 2. 3. Curve-fitting results of the *ex situ* Fe *K*-edge FT-EXAFS spectra of the KFeCuZn/ZrO_2 catalyst.

Sample	shell	CN	R (Å)	σ^2 (Å^2)	ΔE	R factor
KFeCuZn/ZrO_2-before H_2 reduction	Fe–O	4.4±0.7	1.99±0.01	0.007	2.43	0.014
	Fe–O–Fe	4.6±0.9	2.98±0.01	0.008		
KFeCuZn/ZrO_2-after H_2 reduction	Fe–Fe	5.8±2.1	2.45±0.02	0.005	0.85	0.008
	Fe–Fe	4.8±2.2	2.83±0.01	0.005		
KFeCuZn/ZrO_2-spent	Fe–O(C)	3	1.99±0.02	0.003	8	0.017
	Fe–C(O)	2.7±1.1	1.87±0.01	0.003		
	Fe–C–Fe	3.9±0.3	2.58±0.01	0.01		
	Fe–C–Fe	1.1±0.6	2.40±0.02	0.008		
	Fe–O–Fe	5.6±1.2	3.42±0.01	0.01		

CN: coordination numbers; R: bond distance; σ^2: Debye-Waller factors; R factor: goodness of fit. S_0^2 was set to 0.8, according to the EXAFS fit of Fe foil.

Table 2. 4. Curve-fitting results of the *ex situ* Cu *K*-edge FT-EXAFS spectra of the KFeCuZn/ZrO_2 catalyst.

Sample	shell	CN	R (Å)	σ^2 (Å^2)	ΔE	R factor
KFeCuZn/ZrO_2- before H_2 reduction	Cu–O	3.9±0.5	1.93±0.005	0.005	5.2	0.019
	Cu–O–Cu	2.0±0.4	2.91±0.013	0.008		
KFeCuZn/ZrO_2- after H_2 reduction	Cu–Cu	8.9±1.2	2.54±0.004	0.009	4.42	0.014
KFeCuZn/ZrO_2-spent	Cu–Cu	10.4±1.1	2.54±0.007	0.009	4.57	0.014

CN: coordination numbers; R: bond distance; σ^2: Debye-Waller factors; R factor: goodness of fit. S_0^2 was set to 0.87, according to the EXAFS fit of Cu foil.

Table 2. 5. Curve-fitting results of the *ex situ* Zn *K*-edge FT-EXAFS spectra of the KFeCuZn/ZrO_2 catalyst.

Sample	shell	CN	R (Å)	σ^2 (Å^2)	ΔE	R factor
KFeCuZn/ZrO_2- before H_2 reduction	Zn–O	3.2±0.01	1.95±0.005	0.005	1.6	0.018
	Zn–O–Zn	8.3±0.01	3.22±0.013	0.010		
KFeCuZn/ZrO_2- after H_2 reduction	Zn–O	2.8±0.8	3.22±0.02	0.004	1.2	0.04
	Zn–Zn	1.2±0.8	2.58±0.05	0.01		
KFeCuZn/ZrO_2-spent	Zn–O–Zn	11±1.5	3.22±0.02	0.01		
	Zn–O	3.1±0.6	3.22±0.01	0.004	1.6	0.03
	Zn–O–Zn	10.8±1.1	3.22±0.01	0.01		

CN: coordination numbers; R: bond distance; σ^2: Debye-Waller factors; R factor: goodness of fit. S_0^2 was set to 0.96, according to the EXAFS fit of Zn foil.

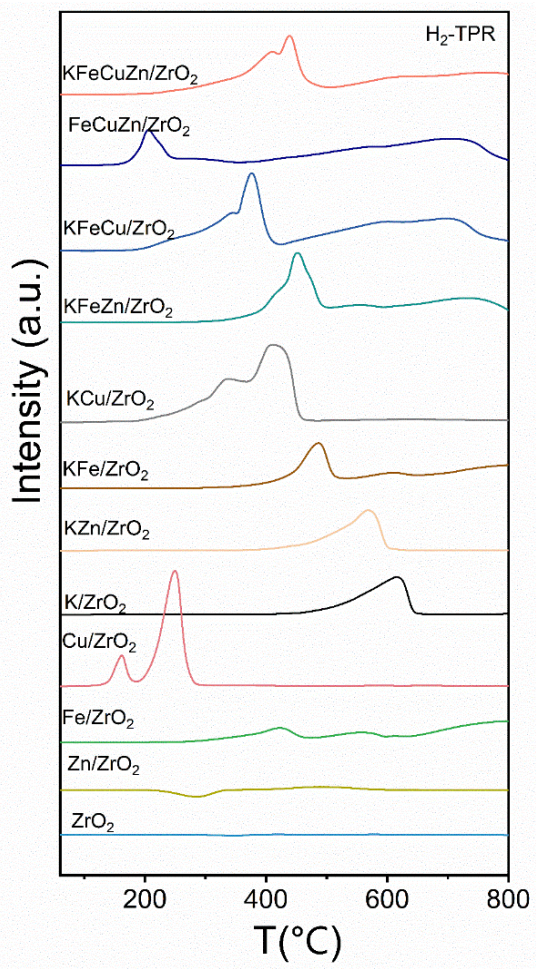

Figure 2. 8. H_2-TPR results over different control catalysts. Condition: Ar pretreatment at 200 °C for 1hr, heating in 10% H_2/Ar from 50 to 800 °C.

HAADF-STEM and EDS were performed for fresh and spent KFeCuZn/ZrO_2, as shown in **Figures 2. 9-12**. Because of the weak Z-contrast, identifying the crystal phase and interplanar spacing of the Fe, Cu, and Zn species was challenging. Therefore, we only observed the elemental distributions. The HAADF-STEM and EDS elemental mapping images revealed that K, Fe, Cu, and Zn over the KFeCuZn/ZrO_2 catalyst were homogeneously distributed on ZrO_2 for fresh KFeCuZn/ZrO_2 (**Figure 2. 9**). After the reaction, K, Fe, and Zn remained highly dispersed in ZrO_2 (**Figures 2. 10-12**). The particle size of Cu increased a little, indicating the aggregation of Cu over KFeCuZn/ZrO_2. In comparison, larger Cu nanoparticles were observed over the spent KFeCu/ZrO_2, elucidating that the introduction of Zn limited Cu sintering (**Figures 2. 13 and 14**). Inhibition of sintering of Cu nanoparticles was also reported for Cs-CuZnFe[30] and CuZnO-Al_2O_3[74] systems.

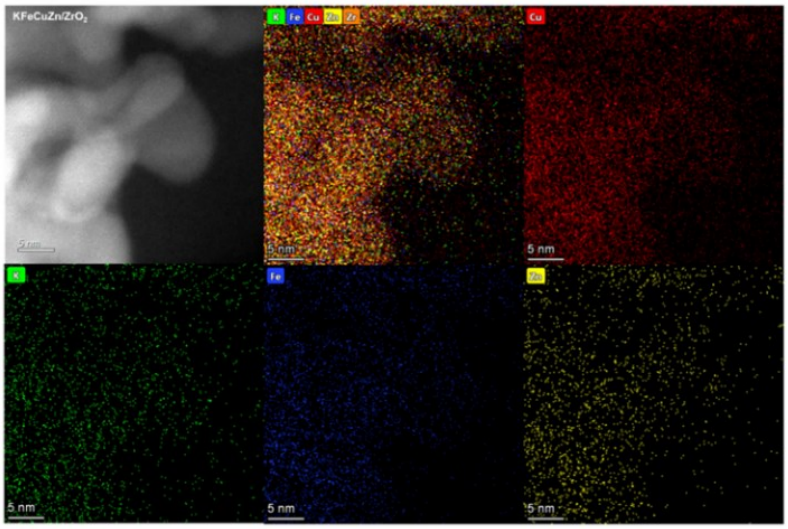

Figure 2. 9. HAADF-STEM image and corresponding EDS mapping images of the fresh KFeCuZn/ZrO_2 that has undergone calcination at 500 °C under air.

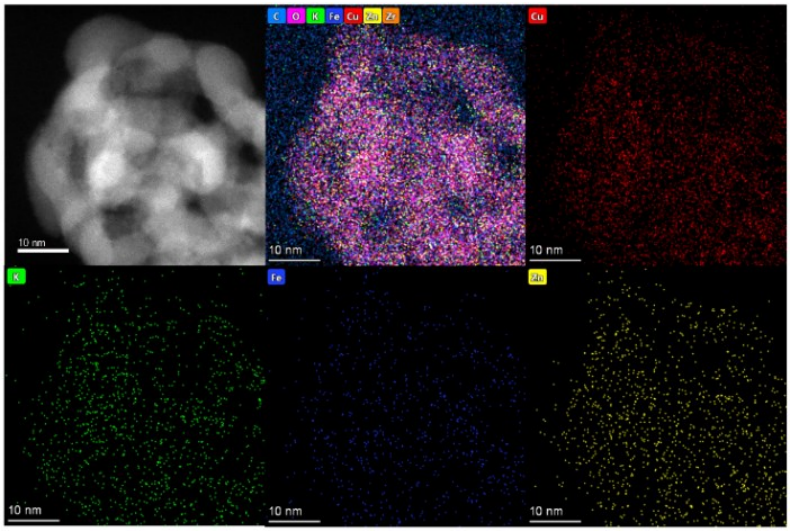

Figure 2. 10. HAADF-STEM image and EDS mapping images of the fresh KFeCuZn/ZrO_2 that has undergone H_2 pretreatment at 400 °C.

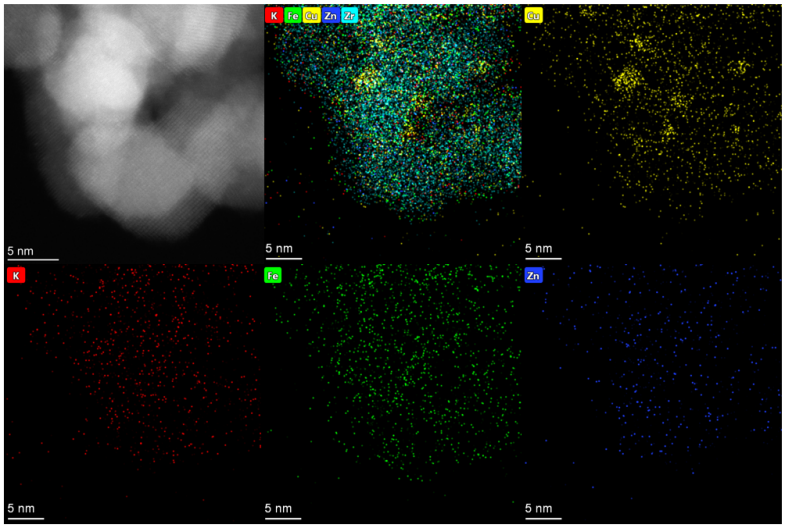

Figure 2. 11. HAADF-STEM image and corresponding EDS mapping images of the spent KFeCuZn/ZrO_2 that has undergone a 20-hour accelerated aging treatment at 400 °C under the reaction condition.

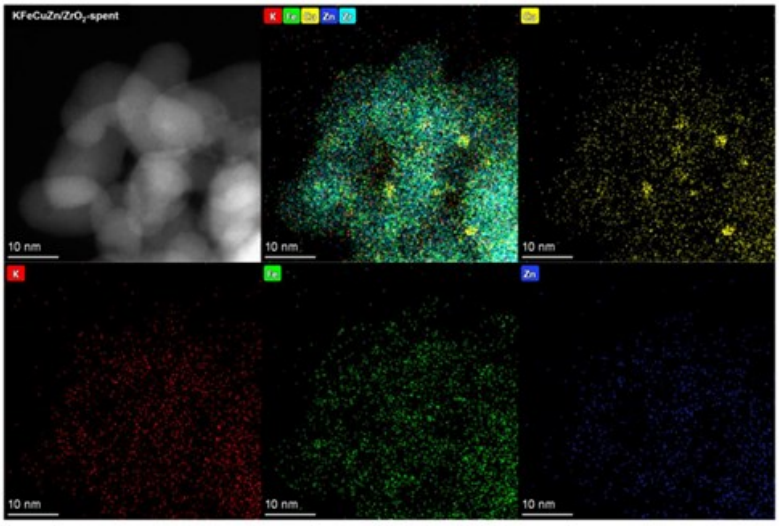

Figure 2. 12. HAADF-STEM image and EDS mapping images of the spent KFeCuZn/ZrO_2 that has undergone a 20-hour accelerated aging treatment at 400 °C under the reaction condition.

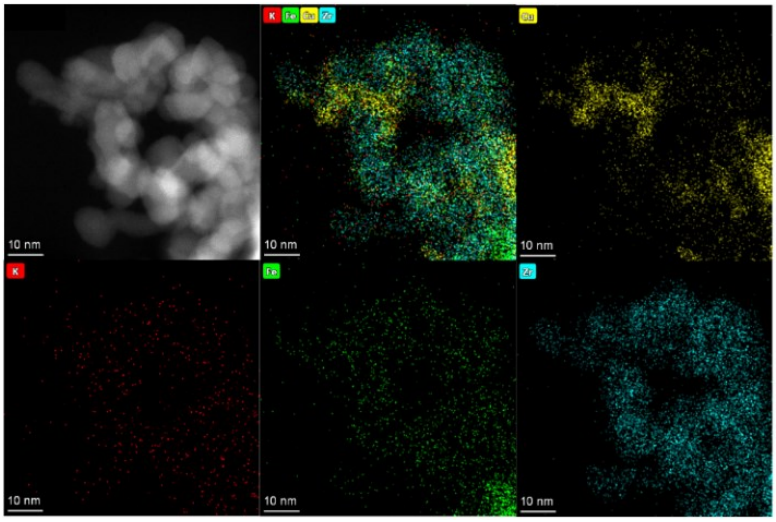

Figure 2. 13. HAADF-STEM image and corresponding EDS mapping images of the spent KFeCu/ZrO_2 that has undergone a 20-hour accelerated aging treatment at 400 °C under the reaction condition.

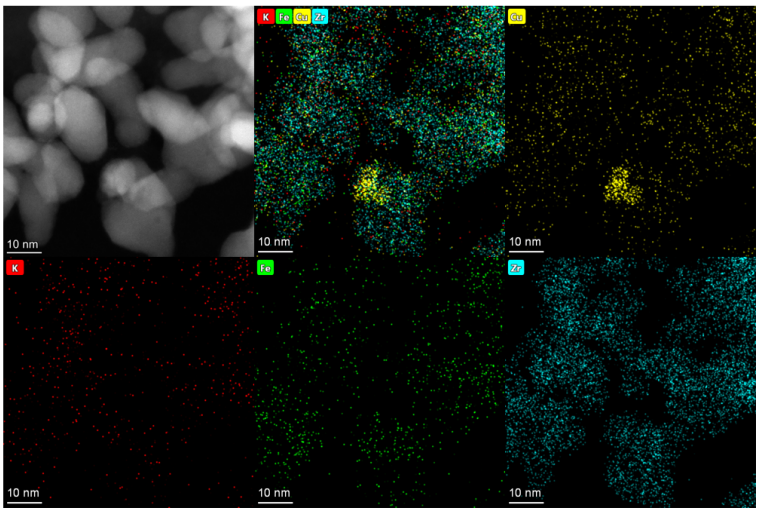

Figure 2. 14. HAADF-STEM image and EDS mapping images of the spent KFeCu/ZrO_2 that has undergone a 20-hour accelerated aging treatment at 400 °C under the reaction condition.

3.3.3 Mechanistic studies

In situ XAS was employed to clarify the chemical states under He, CO_2, and CO_2 + H_2 atmospheres at 400 °C and ambient pressure after H_2 pretreatment. The Fe *K*-edge XANES spectra (**Figure 2. 15a**) of KFeCuZn/ZrO_2 clearly showed that the absorption edge shifted to higher energies after the introduction of CO_2 (**Figure 2. 15b**), indicating that the Fe species were oxidized by CO_2. These results clearly proved that CO_2 functioned as an oxidizing agent, facilitating the oxidation of Fe species.[75]

For the Cu *K*-edge and Zn *K*-edge, although there were minor shifts upon the introduction of CO_2, the edge positions remained almost unchanged upon the introduction of CO_2+H_2. These results suggested that the redox reactions of Cu and Zn were not involved in the CO_2 hydrogenation reaction.

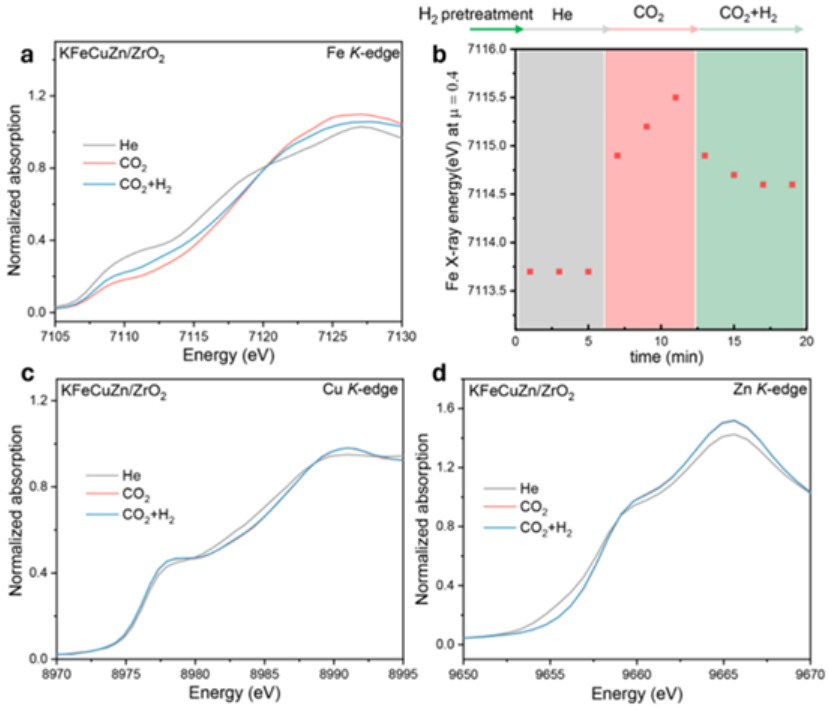

Figure 2. 15. *In situ* XAFS spectra over KFeCuZn/ZrO_2. (a) Normalized Fe *K*-edge XANES spectra; (b) X-ray energy at normalized absorption (μ = 0.4) under different atmospheres; (c) Cu *K*-edge XANES spectra; and (d) Zn *K*-edge XANES spectra. Conditions: 400 °C and 1 bar.

The *operando* DRIFTS was performed to elucidate the mechanism underlying the hydrogenation of CO_2 to EtOH and role of each element. These *operando* DRIFTS experiments were conducted under specific conditions, including a pressure of 0.5 MPa, temperature of 320 °C (with an exception for KFeCuZn/ZrO_2, where the temperature range was 200–320 °C), and H_2: CO_2 ratio of 3:1. The critical assignments of the surface species

and adsorbed methanol and ethanol species are provided in **Table 2. 6** and **Figure 2. 16**. Observations at 200 °C for KFeCuZn/ZrO_2 indicate the presence of adsorbed CO_2 at 1269 and 1514 cm^{-1},[30,76] which can be attributed to the carbonate species (bicarbonate species at 1620 cm^{-1})[77] and surface formate located at 2775/1593/1393 cm^{-1}.[22,40,78] No CH_3O* or CH_3CH_2O* were detected (**Figure 2. 18a**). After the reaction temperature increased to 240°C, a weak peak, which can be attributed to an important intermediate of CH_3CHO* in EtOH synthesis, was observed at 1410 cm^{-1}.[40] When the temperature reached 280°C (**Figure 2. 17a**), with an increase in the exposure time, the intensity of the CH_3CHO* assignment gradually increased at 1410 cm^{-1}. After ~25 min, it was consumed, and subsequently, peaks assignable to ethoxy (2852/2922/2956 cm^{-1}) were observed.[27,30,39] In addition, EtOH in gas phase was tracked and quantified using online gas chromatography (**Figure 17b**). A CH_3CHO pulse experiment was also performed in a CO_2+H_2 environment using the spent KFeZnCu/ZrO_2 catalyst (**Figure 2. 19**). The introduction of CH_3CHO into the reaction environment resulted in a rapid increase in the intensity of the CH_3CH_2OH signal. This clearly indicates that the hydrogenation of CH_3CHO to CH_3CH_2OH is highly facile under the given conditions. Furthermore, the DRIFTS spectra also showed a minor peak at 2820 cm^{-1}, which can be assigned to CH_3O*,[30,78] along with a decrease in the intensity of the peak at 2770 cm^{-1}, assignable to formate. Upon reaching a temperature of 320 °C, the intensity of CH_3CH_2O* became more pronounced (**Figure 2. 18b**). In addition, another assignment appeared, with CH_3CH_2O* characterized by δ(CH_2) vibrations at 1462 cm^{-1}.[40] The methane appeared at 3011 cm^{-1},[39,40] which was not seen at lower temperatures. Notably, some papers reported that the peaks for CH_3CH_2O* and CH_3O* overlapped in the 2940–2980 cm^{-1} region.[27,30] According to the quantification of the micro-GC results the formation rate of EtOH was much higher than that of methanol (**Figure 2. 18c**). Thus, we assigned the peaks at 2852, 2922, and 2956 cm^{-1} to CH_3CH_2O*, which is regarded as an important intermediate for EtOH formation.[27,30]

Table 2. 6. DRIFTS peak assignments of the surface species for CO_2 hydrogenation.

Surface species	Wavenumber (cm^{-1})	References
*CO_3	1227–1281	30
*HCO_3	1620-1640	77
*CH_3O	2826, 1070, 2940, 2841-2866	78
*HCOO	2676–2774, 1593–1610, 1337–1397	30,79
*CH_3CH_2O	2856, 2928, 2963, 1458,1095	27,40

*CH_3CHO	1415, 1340, 1720	30,40
CH_4	3016	30
CO (gas)	2110, 2179	40
Linear–CO	2060–2098	40
Bridging–CO	1900–1940	40

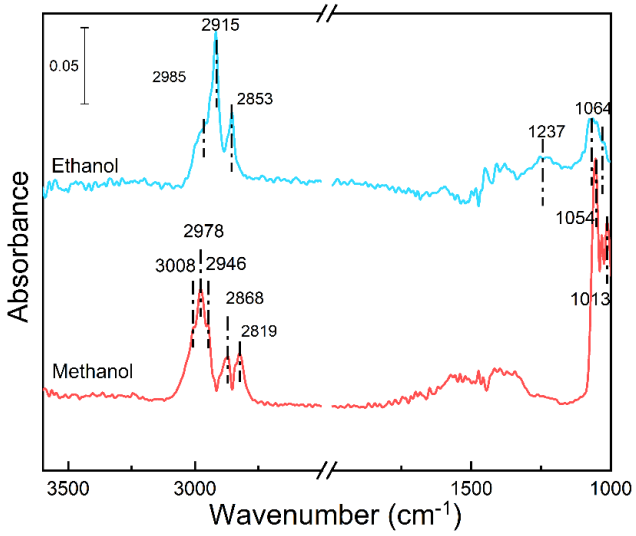

Figure 2. 16. *In situ* DRIFTS spectra of methanol and ethanol adsorption on spent $KFeCuZn/ZrO_2$.

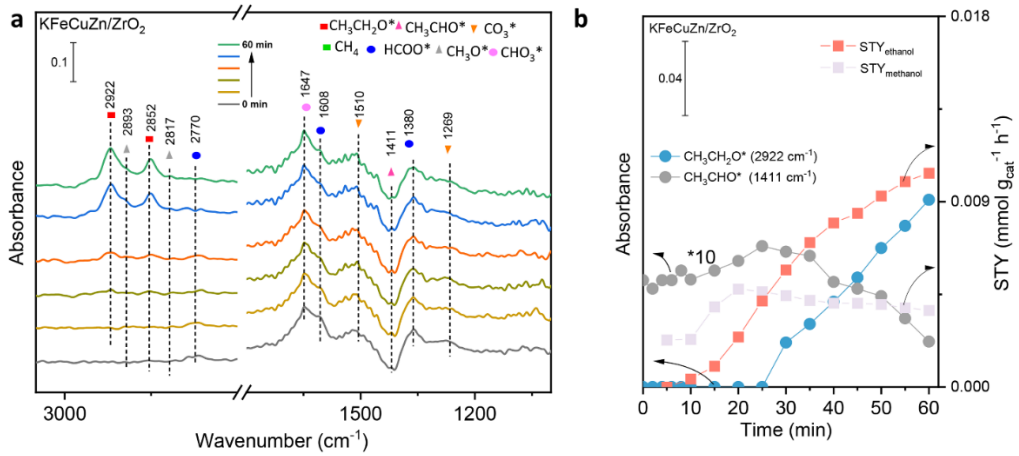

Figure 2. 17. *Operando* DRIFTS spectra. (a) The time resolution spectra of the CO_2 + H_2 reaction over the $KFeCuZn/ZrO_2$ at 280 °C; (b) Dynamic IR peak intensities of CH_3CHO* (1411 cm^{-1}) and CH_3CH_2O* (2922 cm^{-1}) and some of products (ethanol and methanol) amount from micro-GC at 280 °C.

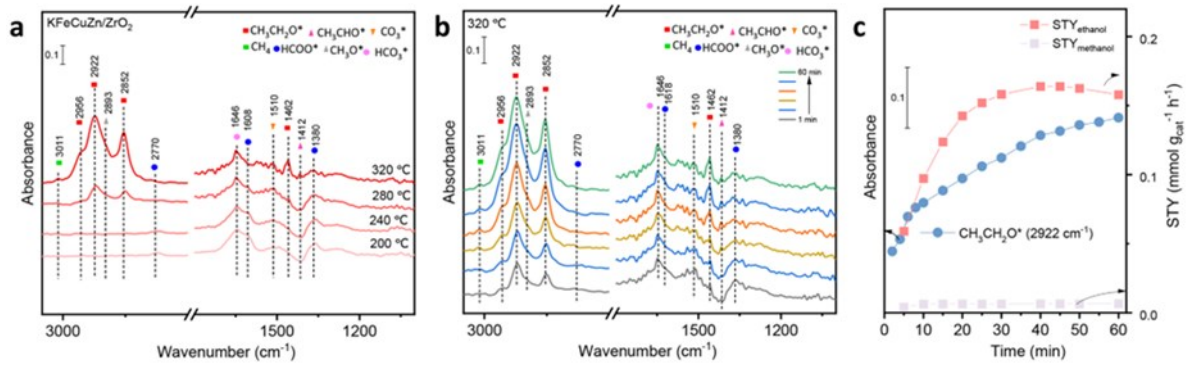

Figure 2. 18. *Operando* DRIFTS spectra. (a) DRIFTS spectra of the CO_2 + H_2 reaction over KFeCuZn/ZrO_2 after 60 min at 0.5 MPa and different temperatures; (b) time resolution spectra of the CO_2 + H_2 reaction over KFeCuZn/ZrO_2 at 0.5 MPa and 320 °C; (c) dynamic IR peak intensities of CH_3CH_2O* (2922 cm^{-1}) and STY of ethanol and methanol, quantified by micro-GC at 320 °C.

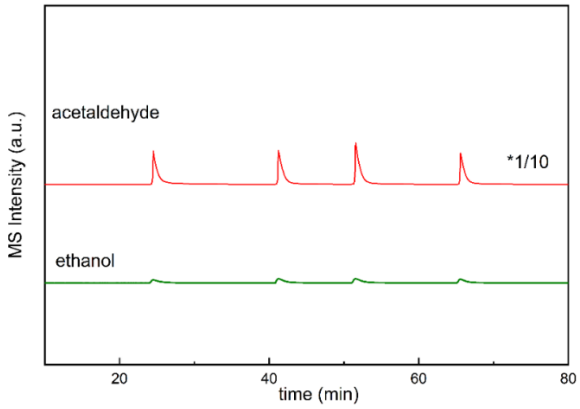

Figure 2. 19. Pulse experiment over the spent KFeCuZn/ZrO_2 catalyst taken under 0.1 MPa CO_2/H_2 flow at 320 °C.

DRIFTS experiments were also conducted on various catalysts to identify the roles of the different elements. KFeCuZn/ZrO_2 catalyst displayed the highest CH_3CH_2O* intensity after 60 min (**Figure 2. 20a**). In comparison, the FeCuZn/ZrO_2 catalyst exhibited strong CH_4 peaks at 1302 and 3011 cm^{-1} during DRIFTS analysis (**Figure 2. 20a**),[80] which indicated K enabled suppression of CH_4 formation.[40,81] Simultaneously, there was a significant decrease in produced EtOH, the amount of adsorbed carbonate[30,76] at 1268 and 1510 cm^{-1} and formate species[22,40,78] at 1388 and 1594 cm^{-1}. These results indicate that the addition of potassium has a positive impact on enhancing CO_2 adsorption/activation and facilitates alcohol synthesis. In contrast, KFe/ZrO_2, KFeZn/ZrO_2, and KFeCu/ZrO_2 showed similar surface species but with variations in intensity compared to the KFeCuZn/ZrO_2 catalyst, indicating the same mechanism with different efficiencies. The evolution of CH_3CH_2O* is shown in **Figure 2. 20b**. The peak intensities of CH_3CH_2O* over KFeCuZn/ZrO_2 and KFeCu/ZrO_2 are similar and higher than those of the catalysts without Cu. This indicates that the addition of

Cu is helpful for the evolution of $CH_3CH_2O^*$, leading to EtOH formation. Concretely, introduction of Cu significantly promotes the formation of CO (CO_2-TPSR, **Figure 2. 21**). It was reported[30,39,40,47] that increased CO provides a great chance of coupling with CH_x on iron carbide surface to form CH_3CHO, which in turn is hydrogenated to $CH_3CH_2O^*$ and subsequently CH_3CH_2OH, over Fe-Cu based catalysts. Because of the similar catalyst components, it is thought that EtOH was produced via the same pathway over our catalyst. Simultaneously, as previously reported, Cu helps non-dissociative activation of CO and its coupling with alkyl (CH_x) species to form ethanol.[30,39,40,47] Therefore, for KFe/ZrO_2 and $KFeZn/ZrO_2$ catalysts, the lack of Cu would result in the slight increase of CO and CH_4 selectivity. Although the Zn-assisted $KFeCu/ZrO_2$ catalyst showed a higher selectivity for EtOH and STY_{EtOH}, the difference between $KFeCuZn/ZrO_2$ and $KFeCu/ZrO_2$ remains unclear, according to DRIFT results.

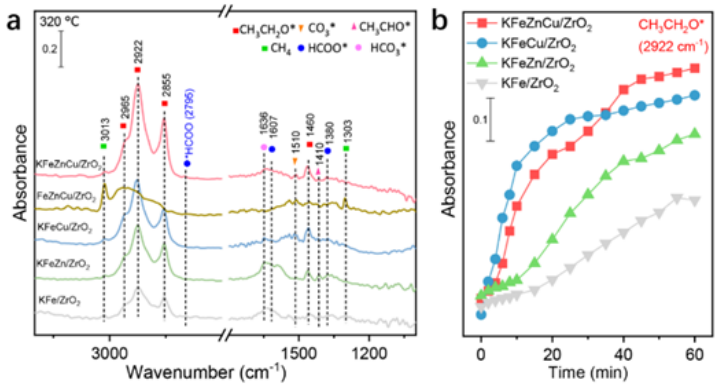

Figure 2. 20. *In situ* DRIFTS spectra. (a) Different catalysts under the CO_2 + H_2 reaction after 60 min at 320 °C and 0.5 MPa; (b) dynamic IR peak intensities of $CH_3CH_2O^*$ (2922 cm^{-1}) at 320 °C for different catalysts.

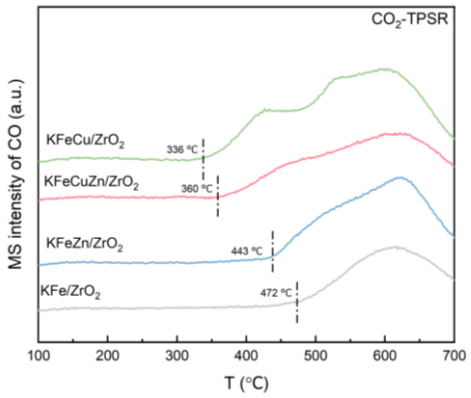

Figure 2. 21. MS signals of m/z=28 in CO_2-TPSR after CO_2 pre-adsorbed catalysts under 5%H_2/Ar flow, over $KFeZnCu/ZrO_2$, $KFeZn/ZrO_2$, $KFeCu/ZrO_2$, and KFe/ZrO_2.

CO_2 adsorption and EtOH decomposition experiments were conducted to elucidate the role and impact of Zn in EtOH synthesis. The DRIFTS results for CO_2 adsorption (**Figure 2.**

22) revealed that the addition of Zn to the KFeZn/ZrO_2 and KFeCuZn/ZrO_2 catalysts enhanced CO_2 adsorption, leading to more formate and carbonates. The results of the ethanol decomposition experiments over KFeCu/ZrO_2 and KFeCuZn/ZrO_2 using a batch reactor are shown in **Figure 2. 23**. The carbonaceous products by the ethanol decomposition are CO_x, CH_4 and acetaldehyde over KFeCuZn/ZrO_2 and KFeCu/ZrO_2 catalysts, with the CH_3CH_2OH decomposition rate of 0.13 and 0.28 mg g_{cat}^{-1} h^{-1}, respectively. This result indicates that the presence of Zn restricts EtOH decomposition (backward reaction), leading to higher selectivity toward EtOH.

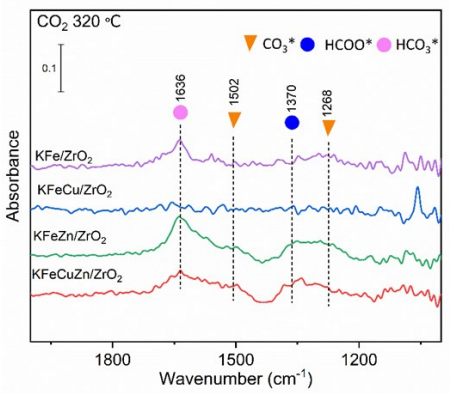

Figure 2. 22. *In situ* DRIFTS spectra of the CO_2 adsorption over the different catalysts, taken under 0.5 MPa at 320 °C.

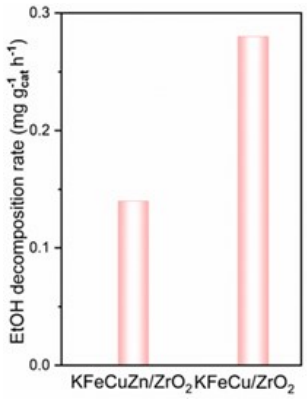

Figure 2. 23. EtOH decomposition over the KFeCuZn/ZrO_2 and KFeCu/ZrO_2 catalysts (conditions: batch reactor, spent catalysts: 50 mg, N_2: 0.5 MPa, at 260˚C, 3 h, ethanol (0.3 mL) + octane (0.7 mL)).

3.3.4 CO hydrogenation over KFeCuZn/ZrO_2

Although the one-step conversion of CO_2 to value-added chemicals such as EtOH is attractive, the kinetically unreactive and thermodynamically stable nature of CO_2 pose significant challenges.[8,28,67,82] CO hydrogenation to EtOH is another promising method for producing EtOH;[83–87] thus, we briefly explored the application of our catalysts in CO hydrogenation.[88–93] CO_2 and CO hydrogenation experiments were conducted on the

KFeCuZn/ZrO_2 catalyst under the same experimental conditions of 280 °C, 3 MPa, and CO or CO_2: H_2 = 1:3. The performance results revealed a higher STY of EtOH (1.8 mmol g_{cat}^{-1} h^{-1}) in CO hydrogenation (**Figure 2. 25a**). Furthermore, in a comparison of the CO_2 + H_2 DRIFTS experiments, a higher amount of CH_3CH_2O* (2852, 2922, 2956 cm^{-1})[27,30] was observed in the CO_2 (20% CO) + H_2 DRIFTS experiments on KFeCuZn/ZrO_2 (**Figure 2. 24**). These two experiments imply that CO hydrogenation to EtOH is more facile than CO_2 hydrogenation. In addition, CO+H_2 *in situ* DRIFTS was performed to clarify the potential roles of each element. According to the acquired IR spectra (**Figure 2. 25b**), the intermediates were similar to those observed in the CO_2+H_2 DRIFTS results. The intensity of the peak at 1712 cm^{-1}, attributed to CH_3CHO* over KFeCuZn/ZrO_2, was found to be higher compared to the other catalysts.[30,94] Additionally, KFeCuZn/ZrO_2 displayed stronger peaks at 2852, 2922, and 2956 cm^{-1}, corresponding to CH_3CH_2O* (**Figure 2. 25b and c**), in comparison to the other catalysts.[27,30,39,40] The CH_3CH_2O* intensities of KFe/ZrO_2 and KFeZn/ZrO_2 were similar and much weaker than those of KFeCuZn/ZrO_2 (**Figure 2. 25c**).

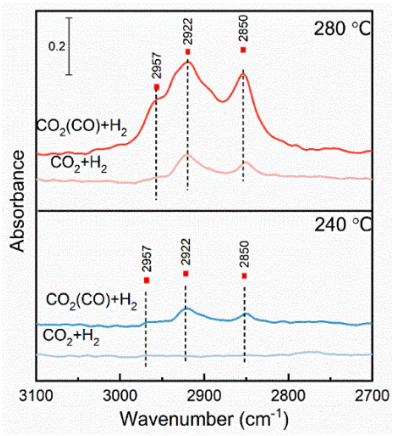

Figure 24. *In situ* DRIFTS spectra of the CO_2 + H_2 and CO co-feeding (20%CO in CO_x) reactions over the KFeCuZn/ZrO2 catalyst taken under 0.5 MPa at 240 and 280 °C.

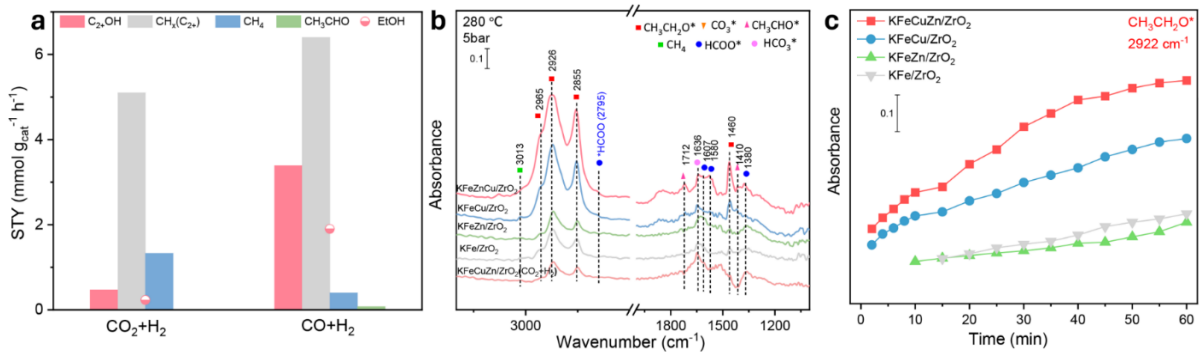

Figure 25. CO hydrogenation to EtOH. (a) Catalytic performance over the KFeCuZn/ZrO_2 catalyst under a CO/H_2 or CO_2/H_2 flow at 280 °C and 3 MPa; (b) in situ DRIFTS spectra of the CO + H_2 reaction over the different catalysts under a CO/H_2 flow at 280°C and 0.5 MPa; and (c) dynamic IR peak intensities of CH_3CH_2O* (2922 cm^{-1}) at 280°C.

2.4 Conclusion

In summary, we reported an efficient catalyst for ethanol synthesis, namely $KFeCuZn/ZrO_2$, which achieves the STY_{EtOH} of 5.4 mmol g_{cat}^{-1} h^{-1} under the optimized conditions (360 °C, 4 MPa, and 12 L g_{cat}^{-1} h^{-1}) and elucidated the essential roles of K, Fe, Cu, and Zn in EtOH synthesis. *In situ/operando* spectroscopic techniques and various characterizations revealed the essential roles of K and Fe in EtOH synthesis. The introduction of Cu accelerated the generation of CH_3CH_2O*, which is an important intermediate in EtOH production. The addition of Zn inhibited EtOH decomposition, thereby improving the efficiency of EtOH synthesis. The importance of all the components was proven and emphasized in CO_2 hydrogenation to EtOH. Finally, this catalyst demonstrated high performance in EtOH synthesis from syngas ($CO + H_2$).

2.5 References

(1) Ali, S. S.; Ali, S. S.; Tabassum, N. A Review on CO_2 Hydrogenation to Ethanol: Reaction Mechanism and Experimental Studies. *J. Environ. Chem. Eng.* **2022**, *10*, 106962.

(2) Gao, P.; Li, S.; Bu, X.; Dang, S.; Liu, Z.; Wang, H.; Zhong, L.; Qiu, M.; Yang, C.; Cai, J.; Wei, W.; Sun, Y. Direct Conversion of CO_2 into Liquid Fuels with High Selectivity over a Bifunctional Catalyst. *Nat. Chem.* **2017**, *9*, 1019–1024.

(3) Tatsumi, T.; Muramatsu, A.; Tominaga, H.-O. Alcohol synthesis from CO_2/H_2 on silica-supported molybdenum catalysts. *Chem. Lett.* **1985**, 593–594.

(4) Irshad, M.; Chun, H. J.; Khan, M. K.; Jo, H.; Kim, S. K.; Kim, J. Synthesis of N-Butanol-Rich C_{3+} Alcohols by Direct CO_2 Hydrogenation over a Stable Cu–Co Tandem Catalyst. *Appl. Catal., B* **2024**, *340*, 123201.

(5) Xu, D.; Wang, Y.; Ding, M.; Hong, X.; Liu, G.; Tsang, S. C. E. Advances in Higher Alcohol Synthesis from CO_2 Hydrogenation. *Chem* **2021**, *7*, 849–881.

(6) Latsiou, A. I.; Charisiou, N. D.; Frontistis, Z.; Bansode, A.; Goula, M. A. CO_2 Hydrogenation to Produce Higher Alcohols: Trends in Catalyst Developments, Challenges and Opportunities. *Catal. Today* **2023**, *420*, 114179.

(7) Hafeez, S.; Harkou, E.; Al-Salem, S. M.; Goula, M. A.; Dimitratos, N.; Charisiou, N. D.; Villa, A.; Bansode, A.; Leeke, G.; Manos, G.; Constantinou, A. Hydrogenation of Carbon Dioxide (CO_2) to Fuels in Microreactors: A Review of Set-Ups and Value-Added Chemicals Production. *React. Chem. Eng.* **2022**, *7*, 795–812.

(8) Wang, Y.; Xu, D.; Zhang, X.; Hong, X.; Liu, G. Selective C_{2+} Alcohol Synthesis by CO_2 Hydrogenation via a Reaction-Coupling Strategy . *Catal. Sci. Technol.* **2022**, *12*, 1539–1550.

(9) Iodice, P.; Cardone, M. Ethanol/Gasoline Blends as Alternative Fuel in Last Generation Spark-Ignition Engines: A Review on Co and Hc Engine out Emissions. *Energies (Basel)* **2021**, *14*, 4034.

(10) Al-Baghdadi, M. A. S. Hydrogen-Ethanol Blending as an Alternative Fuel of Spark Ignition Engines. *Renew. Energ.* **2003**, *28*, 1471–1478.

(11) Xu, D.; Yang, H.; Hong, X.; Liu, G.; Edman Tsang, S. C. Tandem Catalysis of Direct CO_2 Hydrogenation to Higher Alcohols. *ACS Catal.* **2021**, *11*, 8978–8984.

(12) Zhang, S.; Wu, Z.; Liu, X.; Hua, K.; Shao, Z.; Wei, B.; Huang, C.; Wang, H.; Sun, Y. A Short Review of Recent Advances in Direct CO_2 Hydrogenation to Alcohols. *Top Catal.* **2021**, *64*, 371–394.

(13) Li, X.; Ke, J.; Li, R.; Li, P.; Ma, Q.; Zhao, T. S. Research Progress of Hydrogenation of Carbon Dioxide to Ethanol. *Chem. Eng. Sci.* **2023**, *282*, 119226.

(14) Mendiburu, A. Z.; Lauermann, C. H.; Hayashi, T. C.; Mariños, D. J.; Rodrigues da Costa, R. B.; Coronado, C. J. R.; Roberts, J. J.; de Carvalho, J. A. Ethanol as a Renewable Biofuel: Combustion Characteristics and Application in Engines. *Energy* **2022**, *257*, 124688.

(15) Al-Faliti, M.; Dvorak, B.; Aly Hassan, A. Removal of a Mixture of Formaldehyde and Methanol Vapors in Biotrickling Filters under Mesophilic and Thermophilic Conditions: Potential Application in Ethanol Production. *J. Air Waste Manage. Assoc.* **2022**, *72*, 602–616.

(16) Inui, T.; Yamamoto, T.; Inoue, M.; Hara, H.; Takeguchi, T.; Kim, J.-B. Highly Effective Synthesis of Ethanol by CO_2-Hydrogenation on Well Balanced Multi-Functional FT-Type Composite Catalysts. *Appl. Catal., A* **1999**, *186*, 395–406.

(17) Lou, Y.; jiang, F.; Zhu, W.; Wang, L.; Yao, T.; Wang, S.; Yang, B.; Yang, B.; Zhu, Y.; Liu, X. CeO_2 Supported Pd Dimers Boosting CO_2 Hydrogenation to Ethanol. *Appl. Catal., B* **2021**, *291*, 120122.

(18) Caparrós, F. J.; Soler, L.; Rossell, M. D.; Angurell, I.; Piccolo, L.; Rossell, O.; Llorca, J. Remarkable Carbon Dioxide Hydrogenation to Ethanol on a Palladium/Iron Oxide Single-Atom Catalyst. *ChemCatChem* **2018**, *10*, 2365–2369.

(19) Bai, S.; Shao, Q.; Wang, P.; Dai, Q.; Wang, X.; Huang, X. Highly Active and Selective Hydrogenation of CO_2 to Ethanol by Ordered Pd-Cu Nanoparticles. *J. Am. Chem. Soc.* **2017**, *139*, 6827–6830.

(20) Wang, Y.; Zhou, Y.; Zhang, X.; Wang, M.; Liu, T.; Wei, J.; Zhang, G.; Hong, X.; Liu, G. PdFe Alloy-Fe_5C_2 Interfaces for Efficient CO_2 Hydrogenation to Higher Alcohols. *Appl. Catal., B* **2024**, *345*, 123691.

(21) Zhang, F.; Zhou, W.; Xiong, X.; Wang, Y.; Cheng, K.; Kang, J.; Zhang, Q.; Wang, Y. Selective Hydrogenation of CO_2 to Ethanol over Sodium-Modified Rhodium Nanoparticles Embedded in Zeolite Silicalite-1. *J. Phys. Chem. C* **2021**, *125*, 24429–24439.

(22) Zheng, K.; Li, Y.; Liu, B.; Jiang, F.; Xu, Y.; Liu, X. Ti-Doped CeO_2 Stabilized Single-Atom Rhodium Catalyst for Selective and Stable CO_2 Hydrogenation to Ethanol. *Angew. Chem., Int. Ed.* **2022**, *61*, e2022109.

(23) Goryachev, A.; Pustovarenko, A.; Shterk, G.; Alhajri, N. S.; Jamal, A.; Albuali, M.; van Koppen, L.; Khan, I. S.; Russkikh, A.; Ramirez, A.; Shoinkhorova, T.; Hensen, E. J. M.; Gascon, J. A Multi-Parametric Catalyst Screening for CO_2 Hydrogenation to Ethanol. *ChemCatChem* **2021**, *13*, 3324–3332.

(24) Ye, X.; Ma, J.; Yu, W.; Pan, X.; Yang, C.; Wang, C.; Liu, Q.; Huang, Y. Construction of Bifunctional Single-Atom Catalysts on the Optimized β-Mo_2C Surface for Highly Selective Hydrogenation of CO_2 into Ethanol. *J. Energy Chem.* **2022**, *67*, 184–192.

(25) Kusama, H.; Okabe, K.; Sayama, K.; Arakawa, H. Ethanol synthesis by catalytic hydrogenation of CO_2 over Rh-Fe/SiO_2 catalysts. *energy* **1997**, *22*, 343–348.

(26) Liu, S.; Yang, C.; Zha, S.; Sharapa, D.; Studt, F.; Zhao, Z. J.; Gong, J. Moderate Surface Segregation Promotes Selective Ethanol Production in CO_2 Hydrogenation Reaction over CoCu Catalysts. *Angew. Chem., Int. Ed.* **2022**, *61*, e202109027.

(27) Ding, L.; Shi, T.; Gu, J.; Cui, Y.; Zhang, Z.; Yang, C.; Chen, T.; Lin, M.; Wang, P.; Xue, N.; Peng, L.; Guo, X.; Zhu, Y.; Chen, Z.; Ding, W. CO_2 Hydrogenation to Ethanol over Cu@Na-Beta. *Chem* **2020**, *6*, 2673–2689.

(28) Li, S.; Guo, H.; Luo, C.; Zhang, H.; Xiong, L.; Chen, X.; Ma, L. Effect of Iron Promoter on Structure and Performance of K/Cu-Zn Catalyst for Higher Alcohols Synthesis from CO_2 Hydrogenation. *Catal. Lett.* **2013**, *143*, 345–355.

(29) da Silva, A. H. M.; Vieira, L. H.; Santanta, C. S.; Koper, M. T. M.; Assaf, E. M.; Assaf, J. M.; Gomes, J. F. Ethanol Formation from CO_2 Hydrogenation at Atmospheric Pressure Using Cu Catalysts: Water as a Key Component. *Appl. Catal., B* **2023**, *324*, 122221.

(30) Xu, D.; Ding, M.; Hong, X.; Liu, G.; Tsang, S. C. E. Selective C_{2+} Alcohol Synthesis from Direct CO_2 Hydrogenation over a Cs-Promoted Cu-Fe-Zn Catalyst. *ACS Catal.* **2020**, *10*, 5250–5260.

(31) Wang, Y.; Wang, W.; He, R.; Li, M.; Zhang, J.; Cao, F.; Liu, J.; Lin, S.; Gao, X.; Yang, G.; Wang, M.; Xing, T.; Liu, T.; Liu, Q.; Hu, H.; Tsubaki, N.; Wu, M. Carbon-Based Electron Buffer Layer on ZnO_x-Fe_5C_2-Fe_3O_4 Boosts Ethanol Synthesis from CO_2 Hydrogenation. *Angew. Chem., Int. Ed.* **2023**, *62*, e20231178.

(32) Guo, W.; Gao, W. G.; Wang, H.; Tian, J. J. Higher Alcohols Synthesis from CO_2 Hydrogenation over K_2O-Modified $CuZnFeZrO_2$ Catalysts. *Adv. Mat. Res.* **2014**, *827*, 20–24.

(33) Si, Z.; Wang, L.; Han, Y.; Yu, J.; Ge, Q.; Zeng, C.; Sun, J. Synthesis of Alkene and Ethanol in CO_2 Hydrogenation on a Highly Active Sputtering CuNaFe Catalyst. *ACS Sustain. Chem. Eng.* **2022**, *10*, 14972–14979.

(34) Xi, X.; Zeng, F.; Zhang, H.; Wu, X.; Ren, J.; Bisswanger, T.; Stampfer, C.; Hofmann, J. P.; Palkovits, R.; Heeres, H. J. CO_2 Hydrogenation to Higher Alcohols over K-Promoted Bimetallic Fe−in Catalysts on a Ce−ZrO_2 Support. *ACS Sustain. Chem. Eng.* **2021**, *9*, 6235–6249.

(35) Zhang, H.; Han, H.; Xiao, L.; Wu, W. Highly Selective Synthesis of Ethanol via CO_2 Hydrogenation over $CoMoC_x$ Catalysts. *ChemCatChem* **2021**, *13*, 3333–3339.

(36) An, K.; Zhang, S.; Wang, J.; Liu, Q.; Zhang, Z.; Liu, Y. A Highly Selective Catalyst of Co/$La_4Ga_2O_9$ for CO_2 Hydrogenation to Ethanol. *J. Energy Chem.* **2021**, *56*, 486–495.

(37) Riani, P.; Garbarino, G.; Cavattoni, T.; Busca, G. CO_2 Hydrogenation and Ethanol Steam Reforming over Co/SiO_2 Catalysts: Deactivation and Selectivity Switches. *Catal. Today* **2021**, *365*, 122–131.

(38) Zhang, S.; Wu, Z.; Liu, X.; Shao, Z.; Xia, L.; Zhong, L.; Wang, H.; Sun, Y. Tuning the Interaction between Na and Co_2C to Promote Selective CO_2 Hydrogenation to Ethanol. *Appl. Catal., B* **2021**, *293*, 120207.

(39) Xu, D.; Ding, M.; Hong, X.; Liu, G. Mechanistic Aspects of the Role of K Promotion on Cu−Fe-Based Catalysts for Higher Alcohol Synthesis from CO_2 Hydrogenation. *ACS Catal.* **2020**, *10*, 14516–14526.

(40) Liu, T.; Xu, D.; Song, M.; Hong, X.; Liu, G. K-ZrO_2 Interfaces Boost CO_2 Hydrogenation to Higher Alcohols. *ACS Catal.* **2023**, *13*, 4667–4674.

(41) Ravel, B.; Newville, M. ATHENA, ARTEMIS, HEPHAESTUS: Data Analysis for X-Ray Absorption Spectroscopy Using IFEFFIT. *J. Synchrotron Radiat.* **2005**, *12*, 537–541.

(42) Wang, C.; Fang, W.; Liu, Z.; Wang, L.; Liao, Z.; Yang, Y.; Li, H.; Liu, L.; Zhou, H.; Qin, X.; Xu, S.; Chu, X.; Wang, Y.; Zheng, A.; Xiao, F. S. Fischer–Tropsch Synthesis to Olefins Boosted by MFI Zeolite Nanosheets. *Nat. Nanotechnol.* **2022**, *17*, 714–720.

(43) Lohitharn, N.; Goodwin, J. G.; Lotero, E. Fe-Based Fischer-Tropsch Synthesis Catalysts Containing Carbide-Forming Transition Metal Promoters. *J. Catal.* **2008**, *255*, 104–113.

(44) Zhang, S.; Wu, Z.; Liu, X.; Shao, Z.; Xia, L.; Zhong, L.; Wang, H.; Sun, Y. Tuning the Interaction between Na and Co_2C to Promote Selective CO_2 Hydrogenation to Ethanol. *Appl. Catal., B* **2021**, *293*, 120207.

(45) Takagawa, M.; Okamoto, A.; Fujimura, H.; Izawa, Y.; Arakawa, H. Ethanol Synthesis from Carbon Dioxide and Hydrogen. *Stud. Surf. Sci. Catal.* **1998**, *114*, 525–528.

(46) Yang, C.; Mu, R.; Wang, G.; Song, J.; Tian, H.; Zhao, Z. J.; Gong, J. Hydroxyl-Mediated Ethanol Selectivity of CO_2 Hydrogenation. *Chem. Sci.,* **2019**, *10*, 3161–3167.

(47) Wang, Y.; Wang, K.; Zhang, B.; Peng, X.; Gao, X.; Yang, G.; Hu, H.; Wu, M.; Tsubaki, N. Direct Conversion of CO_2 to Ethanol Boosted by Intimacy-Sensitive Multifunctional Catalysts. *ACS Catal.* **2021**, *11*, 11742–11753.

(48) Kusama, H.; Okabe, K.; Sayama, K.; Arakawa, H. CO_2 Hydrogenation to Ethanol over Promoted Rh/SiO2 Catalysts. *Catal. Today* **1996**, *28*, 261–266.

(49) Liu, S.; Zhou, H.; Zhang, L.; Ma, Z.; Wang, Y. Activated Carbon-Supported Mo-Co-K Sulfide Catalysts for Synthesizing Higher Alcohols from CO_2. *Chem. Eng. Technol. 2* **2019**, *42*, 962–970.

(50) Xu, D.; Yang, H.; Hong, X.; Liu, G.; Edman Tsang, S. C. Tandem Catalysis of Direct CO_2 Hydrogenation to Higher Alcohols. *ACS Catal.* **2021**, *11*, 8978–8984.

(51) Yao, R.; Wei, J.; Ge, Q.; Xu, J.; Han, Y.; Ma, Q.; Xu, H.; Sun, J. Monometallic Iron Catalysts with Synergistic Na and S for Higher Alcohols Synthesis via CO_2 Hydrogenation. *Appl. Catal., B* **2021**, *298*, 120556.

(52) Chen, J.; Zha, Y.; Liu, B.; Li, Y.; Xu, Y.; Liu, X. Rationally Designed Water Enriched Nano Reactor for Stable CO_2 Hydrogenation with Near 100% Ethanol Selectivity over Diatomic Palladium Active Sites. *ACS Catal.* **2023**, *13*, 7110–7121.

(53) Zhang, S.; Huang, C.; Shao, Z.; Zhou, H.; Chen, J.; Li, L.; Lu, J.; Liu, X.; Luo, H.; Xia, L.; Wang, H.; Sun, Y. Revealing and Regulating the Complex Reaction Mechanism of CO_2 Hydrogenation to Higher Alcohols on Multifunctional Tandem Catalysts. *ACS Catal.* **2023**, *13*, 3055–3065.

(54) Yang, C.; Liu, S.; Wang, Y.; Song, J.; Wang, G.; Wang, S.; Zhao, Z.; Mu, R.; Gong, J. The Interplay between Structure and Product Selectivity of CO_2 Hydrogenation. *Angew. Chem., Int. Ed.* **2019**, *131* (33), 11364–11369.

(55) Wang, G.; Luo, R.; Yang, C.; Song, J.; Xiong, C.; Tian, H.; Zhao, Z. J.; Mu, R.; Gong, J. Active Sites in CO_2 Hydrogenation over Confined VO_x-Rh Catalysts. *Sci. China: Chem.* **2019**, *62*, 1710–1719.

(56) Gnanamani, M. K.; Hamdeh, H. H.; Jacobs, G.; Shafer, W. D.; Hopps, S. D.; Thomas, G. A.; Davis, B. H. Hydrogenation of Carbon Dioxide over K-Promoted FeCo Bimetallic Catalysts Prepared from Mixed Metal Oxalates. *ChemCatChem* **2017**, *9*, 1303–1312.

(57) Guo, H.; Li, S.; Peng, F.; Zhang, H.; Xiong, L.; Huang, C.; Wang, C.; Chen, X. Roles Investigation of Promoters in K/Cu-Zn Catalyst and Higher Alcohols Synthesis from CO_2 Hydrogenation over a Novel Two-Stage Bed Catalyst Combination System. *Chem. Lett.* **2015**, *145*, 620–630.

(58) Nieskens, D. L. S.; Ferrari, D.; Liu, Y.; Kolonko, R. The Conversion of Carbon Dioxide and Hydrogen into Methanol and Higher Alcohols. *Catal. Commun.* **2011**, *14*, 111–113.

(59) Zhang, Q.; Wang, S.; Shi, X.; Dong, M.; Chen, J.; Zhang, J.; Wang, J.; Fan, W. Conversion of CO_2 to Higher Alcohols on K-CuZnAl/Zr-CuFe Composite. *Appl. Catal., B* **2024**, *346*, 123748.

(60) Gogate, M. R.; Davis, R. J. Comparative Study of CO and CO_2 Hydrogenation over Supported Rh-Fe Catalysts. *Catal. Commun.* **2010**, *11*, 901–906.

(61) Kishida, M.; Yamada, K.; Nagata, H.; Wakabayashi, K. CO2 Hydrogenation for C_{2+} Alcohols Synthesis over Silica-Supported Ir-Mo Catalysts. *Chem. Lett.* **1994**, 555–556.

(62) Kusama, H.; Okabe, K.; Sayama, K.; Arakawa, H. Rhodium Catalysts Promoted by Cerium Oxide in the CO_2 Hydrogenation to Ethanol. *J. Jpn. Pet. Inst.* **1999**, *42*, 178–179.

(63) Kitamura Bando, K.; Soga, K.; Kunimori, K.; Arakawa, H. Effect of Li Additive on CO_2 Hydrogenation Reactivity of Zeolite Supported Rh Catalysts. *Appl. Catal., A* **1998**, *175*, 67–81.

(64) Calafat, A.; Âtima Vivas, F.; Ân, J.; Brito, L.; San, C.; Âbal, E. T.; Âchira, V. Effects of Phase Composition and of Potassium Promotion on Cobalt Molybdate Catalysts for the Synthesis of Alcohols from CO_2 and H_2. *Appl. Catal., A* **1998**, *172*, 217–224.

(65) Xu, W.; Ramirez, P. J.; Stacchiola, D.; Rodriguez, J. A. Synthesis of α-MoC_{1-x} and β-MoC_y Catalysts for CO_2 Hydrogenation by Thermal Carburization of Mo-Oxide in Hydrocarbon and Hydrogen Mixtures. *Chem. Lett.* **2014**, *144*, 1418–1424.

(66) Ouyang, B.; Xiong, S.; Zhang, Y.; Liu, B.; Li, J. The Study of Morphology Effect of Pt/Co_3O_4 Catalysts for Higher Alcohol Synthesis from CO_2 Hydrogenation. *Appl. Catal., A* **2017**, *543*, 189–195.

(67) Goud, D.; Churipard, S. R.; Bagchi, D.; Singh, A. K.; Riyaz, M.; Vinod, C. P.; Peter, S. C. Strain-Enhanced Phase Transformation of Iron Oxide for Higher Alcohol Production from CO_2. *ACS Catal.* **2022**, *12*, 11118–11128.

(68) Wang, Y.; Xu, D.; Zhang, X.; Hong, X.; Liu, G. Selective C_{2+} Alcohol Synthesis by CO_2 Hydrogenation via a Reaction-Coupling Strategy. *Catal. Sci. Technol.* **2022**, *12*, 1539–1550.

(69) Boreriboon, N.; Jiang, X.; Song, C.; Prasassarakich, P. Higher Hydrocarbons Synthesis from CO_2 Hydrogenation Over K- and La-Promoted Fe–Cu/TiO_2 Catalysts. *Top. Catal.* **2018**, *61* (15–17), 1551–1562.

(70) ASAKURA, K.; NOMURA, M.; KURODA, H. Fe K-Edge XANES and EXAFS of the X-Ray Absorption Spectra of $FeCl_3$ Aqueous Solutions. *Bull. Chem. Soc. Jpn.* **1985**, *58*, 1543–1550.

(71) Merte, L. R.; Peng, G.; Bechstein, R.; Rieboldt, F.; Farberow, C. A.; Grabow, L. C.; Kudernatsch, W.; Wendt, S.; Lægsgaard, E.; Mavrikakis, M.; Besenbacher, F. The Active Site of Methanol over Cu/ZnO/Al_2O_3 Catalysts. *Science (1979)* **2012**, *336*, 889–893.

(72) Peña, D.; Jensen, L.; Cognigni, A.; Myrstad, R.; Neumayer, T.; van Beek, W.; Rønning, M.; Peña, D.; Jensen, L.; Neumayer, T.; Cognigni, A.; Rønning, M.; van Beek, W. The Effect of Copper Loading on Iron Carbide Formation and Surface Species in Iron-Based Fischer-Tropsch Synthesis Catalysts. *ChemCatChem* **2018**, *10*, 1300–1312.

(73) Amet, F.; Ke, C. T.; Borzenets, I. V.; Wang, J.; Watanabe, K.; Taniguchi, T.; Deacon, R. S.; Yamamoto, M.; Bomze, Y.; Tarucha, S.; Finkelstein, G. Quantifying the promotion of Cu Catalysts by ZnO for methanol Synthesis. *Science (1979)* **2016**, *352*, 966–969.

(74) Hajduk, Š.; Dasireddy, V. D. B. C.; Likozar, B.; Dražić, G.; Orel, Z. C. CO_x-Free Hydrogen Production via Decomposition of Ammonia over Cu–Zn-Based Heterogeneous Catalysts and Their Activity/Stability. *Appl. Catal., B* **2017**, *211*, 57–67.

(75) Du, P.; Qi, R.; Zhang, Y.; Gu, Q.; Xu, X.; Tan, Y.; Liu, X.; Wang, A.; Zhu, B.; Yang, B.; Zhang, T. Single-Atom-Driven Dynamic Carburization over Pd1–FeO_x Catalyst Boosting CO_2 Conversion. *Chem* **2022**, *8*, 3252–3262.

(76) Mohtar, M.; Omar, R. The effect of K_2CO_3 treatment on self-adhesive carbon grain prepared from oil palm empty fruit bunch. *Solid State Sci. Technol.* **2005**, *13*, 24–31.

(77) Dostagir, N. H. M.; Rattanawan, R.; Gao, M.; Ota, J.; Hasegawa, J. Y.; Asakura, K.; Fukouka, A.; Shrotri, A. Co Single Atoms in ZrO_2 with Inherent Oxygen Vacancies for Selective Hydrogenation of CO_2 to CO. *ACS Catal.* **2021**, *11*, 9450–9461.

(78) Chang, X.; Han, X.; Pan, Y.; Hao, Z.; Chen, J.; Li, M.; Lv, J.; Ma, X. Insight into the Role of Cu-ZrO2 Interaction in Methanol Synthesis from CO_2 Hydrogenation. *Ind. Eng. Chem. Res.* **2022**, *61*, 6872–6883.

(79) Ro, I.; Liu, Y.; Ball, M. R.; Jackson, D. H. K.; Chada, J. P.; Sener, C.; Kuech, T. F.; Madon, R. J.; Huber, G. W.; Dumesic, J. A. Role of the Cu-ZrO_2 Interfacial Sites for Conversion of Ethanol to Ethyl Acetate and Synthesis of Methanol from CO_2 and H_2. *ACS Catal.* **2016**, *6*, 7040–7050.

(80) Wu, J.; Li, S.; Li, G.; Li Bv, C.; Xin, Q. FT-IR Investigation of Methane Adsorption on Silica. *Appl. Surf. Sci.* **1994**, *81*, 37–41.

(81) Wang, M.; Wang, P.; Zhang, G.; Cheng, Z.; Zhang, M.; Liu, Y.; Li, R.; Zhu, J.; Wang, J.; Bian, K.; Liu, Y.; Ding, F.; Senftle, T. P.; Nie, X.; Fu, Q.; Song, C.; Guo, X. Stabilizing Co_2C with H_2O and K Promoter for CO_2 Hydrogenation to C_{2+} Hydrocarbons. *Sci. Adv.* **2023**, *9*, eadg0167.

(82) Inoue, T.; Iizuka, T.; Tanabe, K. Hydrogenation of Carbon Dioxide and Carbon Monoxide over Supported Rhodium Catalysts under 10 Bar Pressure. *Appl. Catal.* **1989**, *46*, 1–9.

(83) Ge, Y.; Zou, T.; Martín, A. J.; Pérez-Ramírez, J. ZrO_2-Promoted Cu-Co, Cu-Fe and Co-Fe Catalysts for Higher Alcohol Synthesis. *ACS Catal.* **2023**, *13*, 9946–9959.

(84) Preikschas, P.; Plodinec, M.; Bauer, J.; Kraehnert, R.; Naumann D'Alnoncourt, R.; Schlögl, R.; Driess, M.; Rosowski, F. Tuning the Rh-FeO_x Interface in Ethanol Synthesis through Formation Phase Studies at High Pressures of Synthesis Gas. *ACS Catal.* **2021**, *11*, 4047–4060.

(85) Wang, X.; Ramírez, P. J.; Liao, W.; Rodriguez, J. A.; Liu, P. Cesium-Induced Active Sites for C-C Coupling and Ethanol Synthesis from CO_2 Hydrogenation on Cu/ZnO ($000\bar{1}$) Surfaces. *J. Am. Chem. Soc.* **2021**, *143*, 13103–13112.

(86) Hu, J.; Wei, Z.; Zhang, Y.; Huang, R.; Zhang, M.; Cheng, K.; Zhang, Q.; Qi, Y.; Li, Y.; Mao, J.; Zhu, J.; Wu, L.; Wen, W.; Yu, S.; Pan, Y.; Yang, J.; Wei, X.; Jiang, L.; Si, R.; Yu, L.; Wang, Y.; Deng, D. Edge-Rich Molybdenum Disulfide Tailors Carbon-Chain Growth for Selective Hydrogenation of Carbon Monoxide to Higher Alcohols. *Nat. Commun.* **2023**, *14*, 6808.

(87) Lu, Y.; Yu, F.; Hu, J.; Liu, J. Catalytic Conversion of Syngas to Mixed Alcohols over Zn-Mn Promoted Cu-Fe Based Catalyst. *Appl. Catal., A* **2012**, *429–430*, 48–58.

(88) Schumann, M.; Nielsen, M. R.; Smitshuysen, T. E. L.; Hansen, T. W.; Damsgaard, C. D.; Yang, A. C. A.; Cargnello, M.; Grunwaldt, J. D.; Jensen, A. D.; Christensen, J. M. Rationalizing an Unexpected Structure Sensitivity in Heterogeneous Catalysis-CO Hydrogenation over Rh as a Case Study. *ACS Catal.* **2021**, *11*, 5189–5201.

(89) Kip, B. J.; Hermans, E. G. F.; Van Wolput, J. H. M. C.; Hermans, N. M. A.; Grondelle, J. Van; Prins, R. Hydrogenation of Carbon Monoxide over Rhodium/Silica Catalysts Promoted with Molybdenum Oxide and Thorium Oxide. *Appl. Catal.* **1987**, *35*, 109–139.

(90) Gupta, M.; Smith, M. L.; Spivey, J. J. Heterogeneous Catalytic Conversion of Dry Syngas to Ethanol and Higher Alcohols on Cu-Based Catalysts. *ACS Catal.* **2011**, *1*, 641–656.

(91) Liu, Y.; Murata, K.; Inaba, M.; Takahara, I.; Okabe, K. Synthesis of Ethanol from Syngas over $Rh/Ce_{1-x}Zr_xO_2$ Catalysts. *Catal. Today* **2011**, *164*, 308–314.

(92) Ishida, T.; Yanagihara, T.; Liu, X.; Ohashi, H.; Hamasaki, A.; Honma, T.; Oji, H.; Yokoyama, T.; Tokunaga, M. Synthesis of Higher Alcohols by Fischer-Tropsch Synthesis over Alkali Metal-Modified Cobalt Catalysts. *Appl. Catal., A* **2013**, *458*, 145–154.

(93) Van Den Berg, F. G. A.; Glezer, J. H. E.; Sachtler', W. M. H. The Role of Promoters in CO/H_2 Reactions: Effects of MnO and MoO_2 in Silica-Supported Rhodium Catalysts. *J. Catal.* **1985**, *93*, 340–352.

(94) Mann, A. K. P.; Wu, Z.; Calaza, F. C.; Overbury, S. H. Adsorption and Reaction of Acetaldehyde on Shape-Controlled CeO_2 Nanocrystals: Elucidation of Structure-Function Relationships. *ACS Catal.* **2014**, *4*, 2437–2448.

Chapter 3

Machine learning-assisted development of high-performance ethanol synthesis catalysts via CO_2 hydrogenation

3.1 Introduction

Ethanol synthesis via CO_2 hydrogenation is a promising approach to reducing dependence on fossil fuels for the production of valuable chemicals and fuel additives, while promoting a circular economy and addressing climate change concerns.[1–5] Despite many years of study development, these efforts have not yet resulted in an industry process.[1,2,5] Effective ethanol synthesis requires catalytic surfaces with multiple functionalities in proximity, typically involving multifunctional or tandem catalysts, to facilitate C–O dissociation, C–C coupling, and CO_x(H) insertion steps at specific active sites.[2,6–8] Due to the mechanistic complexity and the presence of other side reactions, such as C1 product (CO and methane),[5,9] hydrocarbon,[10] and other oxygenates[6] enhancing the efficiency of ethanol production from CO_2 hydrogenation presents a significant challenge.[3,5,11–13] Efforts involving tailored synthesis,[2] advanced characterization tools like electronic microscopy[14] and *operando* spectroscopy,[15] and theoretical modulation[16,17] have been pursued to identify performance descriptors and in turn improve activity. However, these efforts failed to deliver the expected benefits, highlighting a need for alternative approaches with high efficiency in screening the high-performance catalysts.[5,18,19]

In recent years, artificial intelligence (AI) and machine learning (ML) has opened up new opportunities to achieve groundbreaking advancements in chemistry/materials fields and significantly accelerate the design and discovery of novel catalysts materials.[20–23] Traditionally, catalyst development has been a time-consuming and labor-intensive process, often reliant on empirical trial-and-error methods.[18] However, ML has emerged as a driving force in catalysis research, offering unprecedented opportunities to streamline rapidly the development of next-generation catalysts.[18,20] The application of ML approaches to catalysis has attracted considerable attention from researchers worldwide.[20,21,23–25] Proof-of-concept examples have demonstrated the potential of ML to reduce both the time and cost associated with catalyst development.[26] However, despite these early successes,[27,28] the journey towards shedding light into the truly novel compounds and materials remains a formidable challenge. In ML, the challenge of discovering novel element that achieve high efficiency beyond those currently studied remains a significant obstacle.[27,29,30]

To address this challenge, our research group has developed a new ML approach that each catalyst is represented as a set of elemental descriptors,[31,32] such as electronegativities, melting points… which are scaled by the element content. These elemental features are then aggregated into a single feature vector using a permutation-invariant readout operation,

known as sorted weighted elemental descriptor (SWED).[27,31,32] Recently, by combing this ML approach with real-world experimental catalysis data, we have developed the high-performance catalyst ($Pt/Add_i/TiO_2$, where the number of maximum additives (i) is 5) for reverse water-gas shift (RWGS).[27] However, a grant challenge remains for ML models capable to explore diverse chemical spaces and discovering the totally novel (from loading elements to support), highly effective catalysts.[33,34] Additionally, for ethanol synthesis, which involves complex reaction pathways, it is still unclear whether ML methods can partially unlock the underlying connections, accelerating the discovery of high-performance ethanol synthesis catalysts.

In this study, we have applied an exploratory ML approach to develop the new multi-elemental catalysts for CO_2 hydrogenation to ethanol. 555 catalysts were experimentally tested in total (ML prediction + experimental validation) with 58 catalysts as initial data points. More than 70 catalysts with superior activity compared to the originally identified best catalyst were identified and Pd(0.8)–Au(0.3)/K(2.5)–Sr(1)–Fe(20)–Zn(4)–Cd(2)–Yb(1)–Re(1)/CeO_2 (25%)-ZrO_2 (PdAuKSrFeZnCdYbRe/CeO_2(25%)-ZrO_2) catalyst, where the numbers in parentheses represent the content amount (wt%), was found as the best catalyst (STY_{EtOH}: 8.2 mmol g_{cat}^{-1} h^{-1}) for EtOH synthesis. The effect of each element was further investigated through various spectroscopic methods combining with kinetic study.

3.2 Experimental details

3.2.1 Chemicals and catalyst preparation

$PGM_1(X_{P1})$–$PGM_2(X_{P2})$/$PR_1(X_{Pr1})$–$PR_2(X_{Pr2})$/$Add_1(X_{A1})$–$Add_2(X_{A2})$–$Add_3(X_{A3})$–Add_4 (X_{A4})–$Add_5(X_{A5})$/Support (PGM = Pt, Pd, Ir, Ru, Rh and Au, PR (Promoter) = K, Li, Cs, Sr, Na, Mg, Ba, Ca and Rb, Add_X = Additive element; X_{PX} is the loading amount of PGM_X, X_{PrX} is the loading amount of PR_X, X_{AX} is the loading amount of Add_X) was prepared by using the sequential impregnation method. Note that the Add element having the atomic number (AN) from 13 (Al) to 83 (Bi) except for Cl, Ar, Se, As, Br, Kr, Xe, Tc, Pm, Hg, Tl, noble gasses, and platinum group metals (PGMs) were used as catalyst components in this work. For the specific process, a related amount of support and corresponding precursors of the additives and promoters were added in a 100 mL glass vessel containing appropriate amount of deionized water and stirred for 60 min with 200 rpm agitation at room temperature. The mixture was evaporated to dryness

at 50 °C, dried at 110 °C overnight and calcined in air for 3 h to obtain $PR_1(X_{Pr1})$–$PR_2(X_{Pr2})$/$Add_1(X_{A1})$–$Add_2(X_{A2})$–$Add_3(X_{A3})$–$Add_4(X_{A4})$–$Add_5(X_{A5})$/Support. The formed $PR_1(X_{Pr1})$–$PR_2(X_{Pr2})$/$Add_1(X_{A1})$–$Add_2(X_{A2})$–$Add_3(X_{A3})$–$Add_4(X_{A4})$–$Add_5(X_{A5})$/Support was then impregnated in an aqueous solution containing the PGM elements under magnetic stirring. The mixture was evaporated to dryness at 50 °C, dried in air at 110 °C overnight to obtain $PGM_1(X_{P1})$–$PGM_2(X_{P2})$/$PR_1(X_{Pr1})$–$PR_2(X_{Pr2})$/$Add_1(X_{A1})$–$Add_2(X_{A2})$–$Add_3(X_{A3})$–$Add_4(X_{A4})$–$Add_5(X_{A5})$/Support.

3.2.2 Characterization

X-ray diffraction (XRD) analysis was conducted on a Miniflex (Rigaku) diffractometer using Cu Kα radiation. High-angle annular dark-field scanning transmission electron microscopy (HAADF-STEM) and energy-dispersive X-ray spectroscopy (EDS) were performed using an FEI Titan G2 microscope. The samples were prepared by dropping an ethanolic solution containing a catalyst onto carbon-supported Cu grids.

Operando diffuse reflectance infrared Fourier transform (DRIFT) spectra were conducted on a JASCO FT/IR-4600 instrument equipped with a mercury-cadmium-telluride (MCT) detector. The sample was pressed into a DRIFT cell (DR-650 Ci) using a CaF_2 window. The spectra were recorded by accumulating 20 scans at a resolution of 8 cm^{-1}, under CO_2 (5 mL/min) +H_2 (15 mL/min) atmosphere, at a pressure of 0.5 MPa, within a temperature range of 280-320 °C. The reference spectrum was acquired in He environment (flow rate: 20 mL/min; 20 scans), at the measurement temperature, which was subtracted from each spectrum. A high-sampling-rate GC-TCD (490 Micro GC; Agilent Technologies Inc.) was installed at the outlet for the analysis of methanol and ethanol.

Ambient-pressure X-ray photoelectron spectroscopy (AP-XPS) measurements was performed at beamline 13B of the Photon Factory (PF) of the High Energy Accelerator Research Organization (KEK). The powder catalysts were coated onto a Si substrate using a drop-and-dry method with deionized water as the dispersant. The incident X-ray energy was set to 1250 eV. The sample temperature was measured using a thermocouple attached directly to the sample holder in the analysis chamber. Before the measurement, the catalyst was reduced at 400 °C for 30 min with H_2. During the *in situ* measurement, the catalyst was exposed to H_2 at 0.1 Torr and subsequently to CO_2 at 0.1 Torr at 320 °C.

X-ray absorption spectroscopy (XAS) was conducted in transmission/fluorescence mode at BL01B1 of SPring-8 at the Japan Synchrotron Radiation Research Institute (JASRI)

(Proposal no: 2023B2096). The Si (111) and (311) double crystal monochromator was used for X-ray energies below and above 16 KeV (Sr *K*-edge), respectively. Boron nitride (BN) was used to make a pellet sample when the calculated catalyst amount by XAFS sample software was less than 20 mg. The spectra of reference compounds were recorded at room temperature, in air. The obtained XAS spectra were analyzed using the Athena and Artemis software ver. 0.9.26, included in the Demeter package.[35]

For *in situ* XAS measurements, samples in pellet forms (φ: 7/13 mm, based on the computed catalyst amount) were introduced into a cell equipped with Kapton film windows and gas lines connected to the micro-gas chromatograph (Agilent Technologies Inc.). Pretreatment of the samples involved heating under a flow of H_2 (300 mL/min) at 400 °C for 30 min. Subsequently, He (300 mL/min), CO_2 (300 mL/min), H_2 (300 mL/min), and CO_2 (100 mL/min) + H_2 (300 mL/min) were in turn introduced into the cell.

3.2.3 Catalytic reaction

CO_2 hydrogenation reactions were conducted in a fixed-bed continuous-flow reactor operating at a total pressure of 4 MPa (40 bar). We used 1% Ar/99% H_2 (purity; H_2: 99.99999%, Ar: 99.9999%) and CO_2 (purity; 99.995%) gas cylinders to supply the reaction gases. The reactor was supplied with a gas mixture of H_2/CO_2/Ar in a ratio of 74.4/24.8/0.8, with Ar serving as an internal standard gas. Prior to the catalytic measurements, 200 mg of the catalyst was placed between quartz wool inside a 1/4 inch fixed-bed reactor (inside diameter: 3.79 mm). The catalyst was pretreated under ambient pressure at a H_2/Ar (99%) flow rate of 20 mL/min and temperature of 400 °C for 0.5 h. Following the pretreatment, a H_2/CO_2/Ar (74.4/24.8/0.8) flow at a total flow rate of 40 mL/min was passed through the catalyst bed at 4 MPa. The weight hourly space velocity (WHSV) was 12 L g_{cat}^{-1} h^{-1}. We conducted an aging treatment for 10 h at 400 °C under the reaction gas atmosphere as an accelerated aging test before recording the results of the catalytic reaction (**Figure 3. 1**). The products were analyzed using an online gas chromatograph (Shimadzu GC-2014) equipped with TCD (Shincarbon-ST column) and FID (Porapak Q column) detectors, within a reaction temperature range of 240–400 °C.

The CO_2 conversion (X_{CO2}) was calculated as follows.

$$X_{CO2} = \frac{\frac{c_{CO2}^{in}}{c_{Ar}^{in}} - \frac{c_{CO2}^{out}}{c_{Ar}^{out}}}{\frac{c_{CO2}^{in}}{c_{Ar}^{in}}} \times 100\%$$

The selectivity (S_i) for individual products was calculated by the following equation:

$$S_i = \frac{c_i \times n_i}{\sum(c_i \times n_i)} \times 100\%$$

Here, c_i is the molar fraction of product *i* (CO_2, CO, hydrocarbons, or oxygenates), and n_i is the carbon number of product *i* in the reaction.

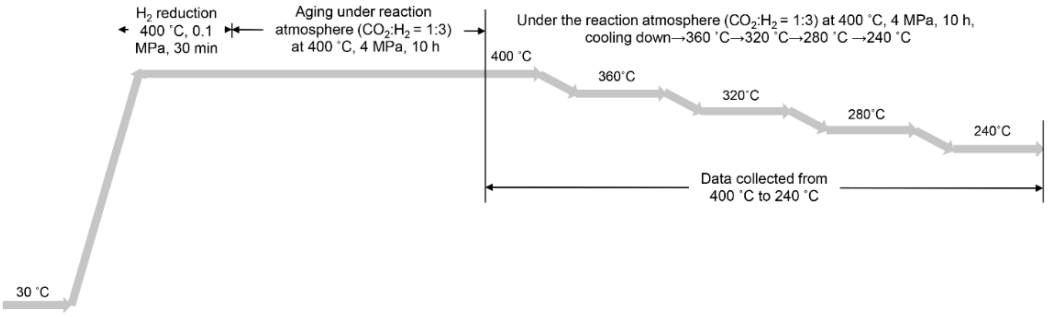

Figure 3. 1. Typical experimental procedure for catalytic tests. After conducting H_2 reduction pre-treatment at 400 °C, accelerated aging treatment was performed at 400 °C in the reaction gas atmosphere. The catalytic performance at temperatures ranging from 400 °C to 240 °C was then recorded.

3.2.4 ML methods

In this study, a machine learning (ML) method assisted for the discovery of high-performance (ML target: STY_{EtOH}; unit: mmol g_{cat}^{-1} h^{-1}) ethanol synthesis catalysts. The specific ML approach as follows:

The elemental descriptors were selected to characterize both the catalysts and the chemical reactions of interest. These descriptors include the following parameters: As elemental descriptors for PGMs: atomic radius (AR), surface energy (SE), and adsorption energy (Ead) of CO_2 on the metallic surface; for promoters: the group and the period of the periodic table, density, 'Ion rad', electronegativity (EN) according to Pauling, melting point (m.p.), Thermal conductivity (TC), SE; for additives: the group of the periodic table, density, EN according to Pauling, melting point (m.p.), delta fusion enthalpy (d_fus_H), density, thermal expansion (TE), SE, formation energy of metal (E_form_M). As support descriptors, we selected nine parameters: EN_bulk, density, band gap (BG), ionization potential. Those

selected descriptors have relatively low correlation with each other and showed the highest prediction accuracy in the 10-fold cross-validation method.

For ML model, the Extra Trees Regressor (ETR)[36] was selected, because, in cases with small and underspecified samples, the ETR regression enable yield more informative predictions through trying to isolate the noise from the data, and ETR enable to reduce the risk of data over-fitting[27] Widely used implementations of scikit-learn (version 0.23.2)[37] were employed for all ML models (ETR and other compared ML models).

For hyperparameter tunings, we tested a reasonable range of candidate values in an exhaustive way (grid search) shown in **Table 3. 1**, chose the best hyperparameter by 5-fold cross validation on the training set, and used it for calculating the predicted values for the test set (the hyperparameters not explicitly indicated in the table were set to the scikit-learn). Namely, to avoid the data leakage, we strictly followed a standard practice of "nested" cross validation, also known as double cross validation, to estimate the prediction accuracies;[38,39] we used 5-fold CV for the internal CV, and used Monte Carlo CV (also known as repeated random subsampling CV) with 100-times of random leave-20%-out trials for the external CV to increase the statistical reliability for validating the test prediction accuracies with fixing the number of training data.

Table 3. 1. Ranges used in the hyperparameter searches for the ML methods (if not specified, the default values of scikit-learn were used).

Type		Method	Hyperparameters [Tested range]
Linear		Lasso	alpha ∈ [10^{-2},10^{-1},1.0,10^{1},10^{2}]
		Ridge	alpha ∈ [10^{-2},10^{-1},1.0,10^{1},10^{2}]
Nonlinear	Kernel methods	GPR	kernel=Matern 5/2, alpha = 0.01, n_restarts_optimizer = 10, normalize_y = True
		SVR	kernel='rbf', C ∈ [1.0,10,10^{2},…, 10^{5}], gamma ∈ [1.0,10^{-1},10^{-2},…,10^{-9},10^{-10}], epsilon ∈ [10^{-2},10^{-1},1.0,10^{1},10^{2}]
	Tree ensemble methods	RFR	n_estimators ∈ [100, 250, 500, 1000, 1500], max_depth ∈ [3, 4, 5,…, 9]
		ETR	n_estimators ∈ [100, 250, 500, 1000, 1500], max_depth ∈ [3, 4, 5,…, 9]

We have used three types of the input representations of catalysts; (i) a naive representation, which uses only elemental compositions or support name; (ii) an exploitative representation, which uses both elemental compositions/support name and elements/support properties; and (iii) an explorative representation, which uses only elemental/support properties. For the input representations of elemental compositions, each catalyst was

represented as a vector of compositional fractions of each element and support for 62 elements (PGM: 6; PR: 9; Add: 47) and 22 supports under consideration. For the input representation of elemental properties, each catalyst is represented as the sum of vectors of each elemental descriptor scaled by its compositional fraction, i.e., for a catalyst $PGM_1(X_{P1})$–$PGM_2(X_{P2})$/$PR_1(X_{Pr1})$–$PR_2(X_{Pr2})$/$Add_1(X_{A1})$–$Add_2(X_{A2})$–$Add_3(X_{A3})$–$Add_4(X_{A4})$–$Add_5(X_{A5})$/Support,

$$X_{P1}\, vec(PGM_1) + X_{P2}\, vec(PGM_2) + X_{P3}\, vec(PR_1) + X_{P3}\, vec(PR_2) + X_{A1}\, vec(Add_1) + X_{A2}\, vec(Add_2) + X_{A3}\, vec(Add_3) + X_{A4}\, vec(Add_4) + X_{A5}\, vec(Add_5) + vec(support)$$

where $vec(PGM_x)$, $vec(PR_x)$, $vec(Add_y)$ $vec(support)$ are the elemental descriptor vector for PGM, promoters, additive elements and support, respectively, which is also referred to as the composition-based feature vector (CBFV) in other work.[40,41] The naive representation generates 84-dimensional features according to the numbers of loading elements and supports. Therefore, this representation tends to be very sparse and statistically uninformative when the training dataset is not large but contains many elements and supports. Moreover, it is incapable of handling elements that are absent or statistically infrequent in the training data. On the other hand, explorative representation has the same dimension as the user-specified elemental descriptor that often produces statistically much more stable results for small-data problems and is not explicitly constrained by the elements covered in the training dataset. Moreover, technically speaking, in the latter representation, each catalyst is represented as a set of elemental descriptors and scaled by its composition fraction and aggregated into a single feature vector for the given fraction of the catalyst (PGM, Promoter, Add, and Support) by sum pooling, a permutation-invariant operation.

Notably, the exploratory model that characterizes catalysts solely based on their physic-chemical properties using specific descriptors, without explicitly delineating the individual contributions of distinct elements, enables a more extrapolative and ambitious exploration beyond the training data, potentially identifying previously unseen elements. In this study, we adopted a 'grid search' approach to propose new catalyst candidates by manually specifying the loading amount of each metal (M) element to achieve global optimization. This method eliminates the need for a recovery procedure and instead computes the Expected Improvement (EI) score using the following equation for the given compositions.[42,43]

$$EI(\boldsymbol{x}) = \mathbb{E}\{\max(\mu(\boldsymbol{x}) - y^*, 0)\} = (\mu(\boldsymbol{x}) - y^*) \cdot \Phi\left(\frac{\mu(\boldsymbol{x}) - y^*}{\sigma(\boldsymbol{x})}\right) + \sigma(\boldsymbol{x}) \cdot \phi\left(\frac{\mu(\boldsymbol{x}) - y^*}{\sigma(\boldsymbol{x})}\right)$$

where $\mu(\boldsymbol{x})$ and $\sigma(\boldsymbol{x})$ are the predicted value and the standard deviation of an ML surrogate for an input $\boldsymbol{x}$, while the expectation $\mathbb{E}$ assumes a Gaussian distribution with a PDF of ϕ and CDF of Φ. EI scores can be intuitively considered as a quantity that indicates how much improvement over the current best y^* can be expected for an input $\boldsymbol{x}$. The EI is schematically shown in **Figure 3. 2**.

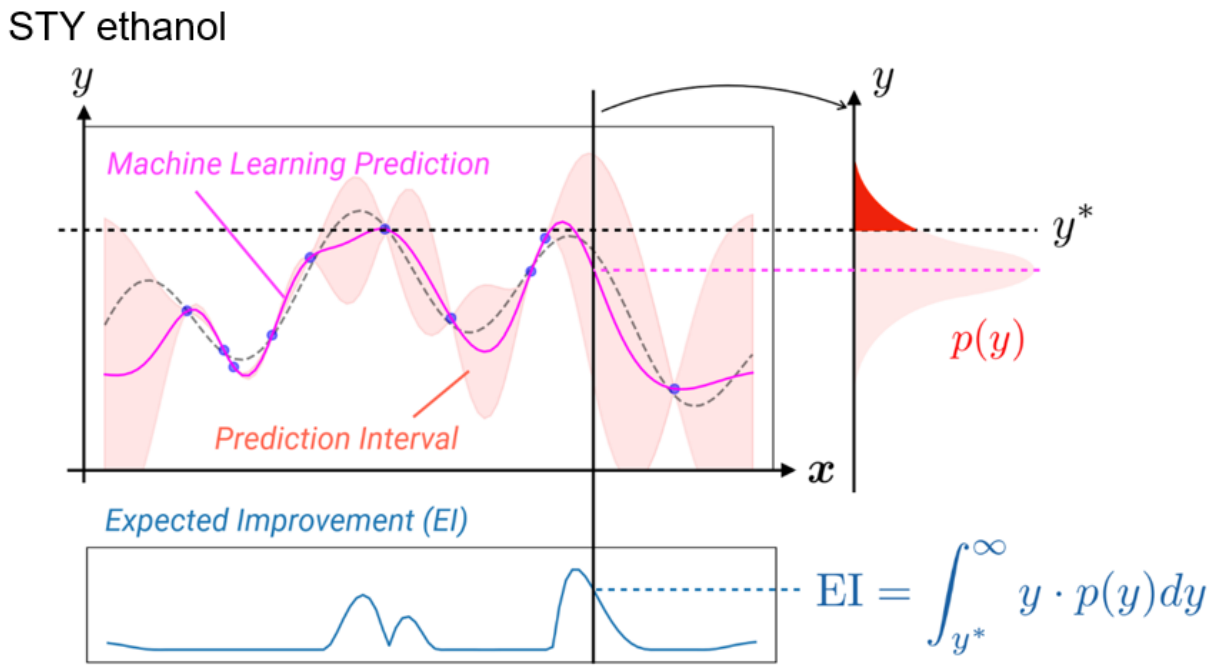

Figure 3. 2. Description of the expected improvement (EI). The EI score $\mathbb{E}\{\max(\mu(\boldsymbol{x}) - y^*, 0)\}$ corresponds to the average of the improvement in y (STY ethanol) weighted by the probability of the red-colored region, thus considering not only the predicted values but also their predicted *variances*. Because the ML prediction (pink curve) usually cannot exceed the best (maximum) value of the training data, it is inadequate to directly use the predicted values to attempt to find data points with higher STY ethanol values.

Clustering was typically performed to group very similar candidates into K clusters. In cases where clustering was not used, we simply selected the catalysts based on the top proposed catalyst compositions. We normally used K = 100 because the elbow and silhouette analyses suggested that 100 was the optimal number of clusters. The elbow method was employed to find the point of inflection (elbow) in the plot of the explained variation as a function of the number of clusters, serving as a criterion for determining the optimal number of clusters. The silhouette analysis was applied to quantify the similarity among the observations within a cluster, thus providing additional support for identifying the optimal number of clusters. A representative analysis result using the 300 data points with explorative

ML methods based on ETR revealed that K = 50–100 is optimal. In addition, no clusters had silhouette scores below the average when K = 100 (with N = 10 perturbations).

3.2.5 Procedure of ML-assisted CO_2-to-EtOH catalysts discovery

The initial dataset of 58 catalysts (274 data points), created from previous reported work and some similar components, is labeled as iteration 0. Using an exploitative ML model based on ETR, we suggested new catalyst candidates, synthesized some based on their EI ranking, conducted the CO_2 to EtOH reaction, and updated the performance to finish the predicting and testing loop (**Figure 3. 3a**). We repeated this cycle, updating the dataset each time, for 24 iterations, testing a total of 555 catalysts (2477 data points). At each iteration, due to the above clustering with K = 100, thus the ML approach provided a list of 100 top-ranking catalysts, from which we manually selected diverse catalysts (~20) for testing.

3.3 Results and discussion

3.3.1 ML-Driven Discovery of CO_2 Hydrogenation to Ethanol Catalysts

For a catalyst ($PGM_1(X_{P1})$–$PGM_2(X_{P2})$/$PR_1(X_{Pr1})$–$PR_2(X_{Pr2})$/$Add_1(X_{A1})$–$Add_2(X_{A2})$–$Add_3(X_{A3})$–$Add_4(X_{A4})$–$Add_5(X_{A5})$/Support) prediction, starting with an initial dataset of 58 catalysts (comprising 274 data points), we trained an exploratory machine learning model using Extra-Trees Regression (ETR).[36] We then calculated the expected improvement (EI)[42,43] for all test points in the catalyst composition grid, next, based on the EI scores and variety of catalyst, we manually selected several promising catalyst candidates (see more details in experimental section). These candidates were synthesized and executed in the performance testing, and we conducted 24 cycles of a closed-loop discovery system (ML prediction + experimental validation; **Figure 3. 3a**). We experimentally tested a total of 555 catalysts, each at multiple (four or five) different temperatures (**Figure 3. 3b**), identifying more than 70 catalysts with superior activity compared to the previously reported high-performance catalyst KFeCuZn/ZrO_2.[44] As shown in **Figure 3. 3b**, the initial iterations (fewer than 5) presented challenges in improving catalytic activity and identifying effective catalysts. This was primarily due to the limited dataset and the exploration of previously untested elements, which resulted in low prediction accuracy. However, as the dataset expanded and prediction accuracy improved, by the 12th iteration, we had successfully pinpointed the best performance catalyst. Although no superior catalysts were discovered in the later iterations (greater than 12), it is necessary to highlight that more efficient catalysts were identified during this phase, demonstrating the success of the ML prediction + performance testing process. This process exemplifies the exploration–exploitation trade-off in ML, where balancing between "exploration" to gather more data on uncertain areas and "exploitation" to utilize existing data is crucial. When the elemental pool is almost filled, the ML model prefers to optimize the corresponding components and the metal loading to acquire the high-performance catalysts.

As discussed above, the increasing volume of catalyst activity data and the number of cycles accelerated the discovery of high-performance catalysts, which also agreed the model's prediction accuracy significantly improved. Furthermore, the R^2 value[45,46] and the test errors (RMSE, MSE, MAE)[45,46] of the predicted ethanol formation rate, validated using a standard cross-validation (CV) procedure,[39] were evaluated and presented separately in the **Figure 3. 3e**. The sorted weighted elemental descriptor (SWED),[31,32] considering both elemental content and features, displayed higher accuracy and lower test errors than either

elements/supporting component only or elemental/ supporting properties only. After 24 cycles, the prediction accuracy of the SWED model reached an R^2 value of 0.81, surpassing the other two prediction models that only consider the compositional or elemental features.[39] And we have to point out that the prediction accuracy obtained (R^2 = 0.81) is higher than those reported in most ML studies involving experimental data on heterogeneous catalysis and related material science topics.[20,31] This result not only demonstrates the reliability of the SWED model but also highlights the capability of the machine learning model to statistically guide promising directions for future research.

We further compared prediction performance of the different ML regressions on SWED model, as shown in **Figure 3. 4**, and all the relative hyperparameters were listed in **Table 3. 1.** Among them, the tree ensemble regression displayed the highest prediction accuracy. The tree ensemble regression functions as a form of pseudo-piecewise-linear interpolation.[27] In addition, for the tree ensemble regression, when data points are limited, interpolating the noisy training data can yield more informative predictions compared to trying to distinguish noise from data in these underspecified situations with small sample sizes. In contrast to Random Forests Regression (RFR), ETR is less sensitive to hyperparameters than RFR and requires less tuning in training data, thus, it displayed higher accuracy than RFR in training data (**Figure 3. 4**). Based on the aforementioned reasons, we primarily used the ETR as our ML algorithm. And our approach is based on highly safe/conservative predictions, because the tree ensemble models make conservative predictions in the out-of-training regions (it is a histogram approximation, and any predicted values are the local averages of the training samples, even in the out-of-training regions).[47,48] Nevertheless, it successfully found some catalysts containing elements not in the training data, which is worth emphasizing. The core function of ML prediction is based on the interpolation of provided data points; therefore, no ML model architecture can solely perform extrapolative predictions without incorporating additional information or data-independent assumptions.[19,20,27]

To further validate the ML prediction accuracy, we also conducted control reaction to address all components that are necessary to achieve the highest ethanol formation rate. As shown in **Figure 3. 3c** and **Table 3. 2**, the composition of the best catalyst discovered through this data-driven approach was PdAuKSrFeZnCdYbRe/CeO_2(25%)-ZrO_2, which exhibited the highest ethanol formation rate of 8.2 mmol g_{cat}^{-1} h^{-1} and a selectivity of 23 % than other compared catalysts, simultaneously, the highest reported in the literature to date (**Table 3. 3**). Among these control catalysts, the catalyst without Fe resulted in a significant decrease in

ethanol production, indicating a loss in the catalyst's ability for C–C coupling.[49,50] Similarly, after dropping K, a notable reduction in alcohol activity highlighted the crucial role of K in C_{2+} alcohol synthesis and its function in inhibiting over-hydrogenation.[51,52] Overall, this machine learning model not only develops catalysts with known high-performance components but also explores new elements (i.e., Yb, Cd) that have not yet been utilized in this field.[18,20,23,31] The catalytic stability of PdAuKSrFeZnCdYbRe/CeO_2(25%)-ZrO_2 was evaluated over a 600-hour reaction period, revealing no significant changes in CO_2 conversion, product selectivity, and ethanol formation rate, which indicates grant potential for industrial application (**Figure 3. 3d**). Additionally, the influences of the reaction conditions, including reaction temperature, WHSV, calculation temperature and pressure on CO_2 hydrogenation to EtOH, were studied, and the conditions of 12 L g_{cat}^{-1} h^{-1}, 360 °C and 4 MPa displayed more pronounced activity (**Figure 3. 5**).

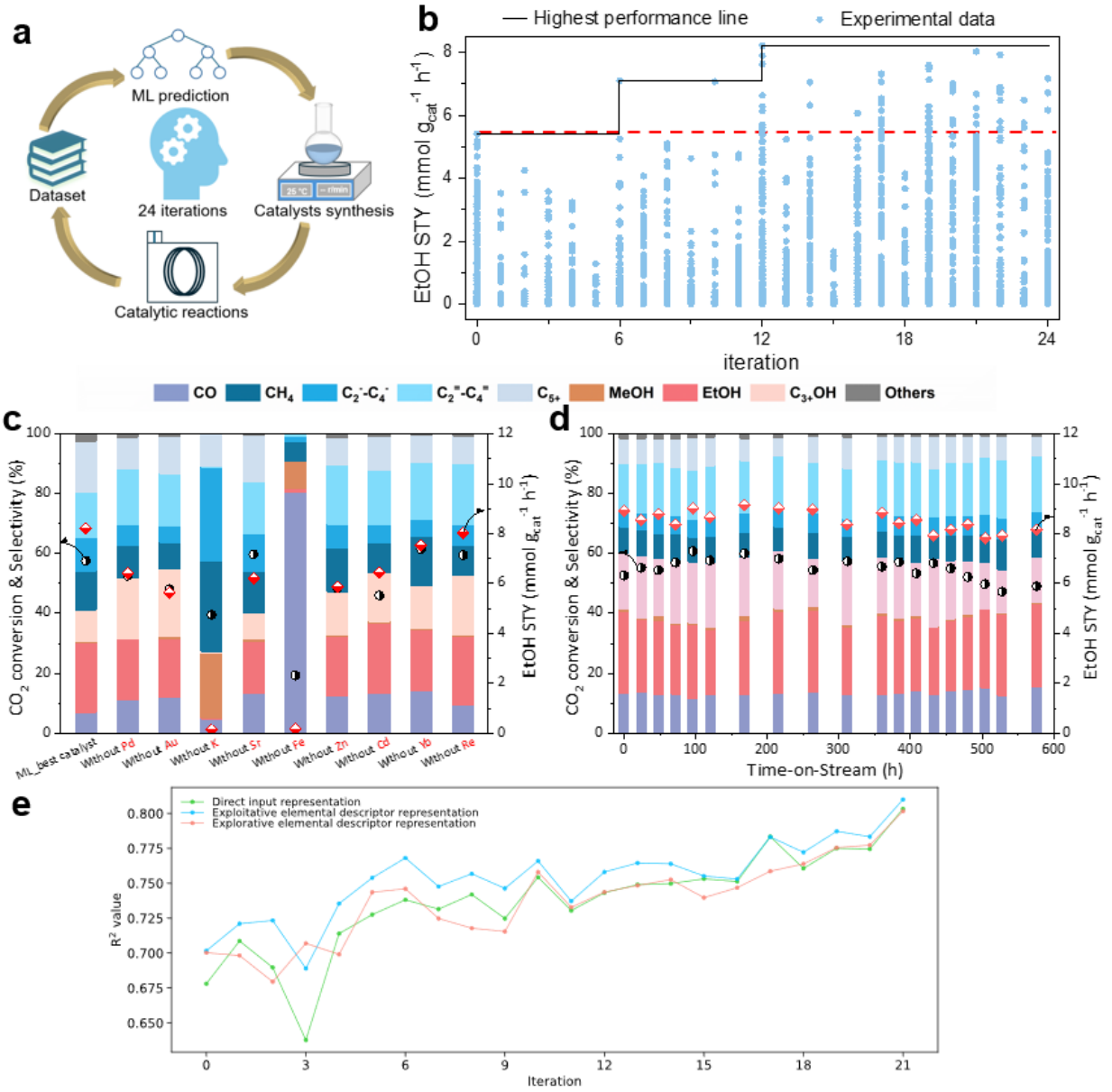

Figure 3. 3. ML-assisted discovery of high-performance CO_2 hydrogenation to ethanol catalysts. (a): the procedure of ML-assisted ethanol synthesis catalysts discovery; (b): the performance results of ethanol formation rate at different iterations (total: 24) under the concrete conditions (CO_2:H_2=1:3, 12 L g_{cat}^{-1} h^{-1}, 240-400 °C and 4 MPa). The solid gray line shows the best ethanol formation rate at each iteration, and for comparison, the dashed red line shows the ethanol formation rate for KFeCuZn/ZrO_2, the best one at the first iteration. (c): The R^2 values were calculated by the cross validation (CV) method in the three different ML methods mentioned in experimental section at each iteration prior to experimental validation; (d): CO_2 conversion and product selectivity at 360 °C and STY_{EtOH} over the best catalyst (PdAuKSrFeZnCdYbRe/CeO_2(25%)-ZrO_2) and the relative control catalysts; (e) stability test for best catalyst (PdAuKSrFeZnCdYbRe/CeO_2(25%)-ZrO_2) at 360 °C. Pretreatment condition: 400 °C, 0.1 MPa, H_2 (99%), and 0.5 h. Reaction condition: 12 L·g_{cat}^{-1} h^{-1}, 4.0 MPa, and H_2/CO_2/Ar (74.4/24.8/0.8%). Ar was used as an internal standard gas. The data was collected after 3 h, when the temperature and rection were stable. Accelerated aging treatment was performed before reaction at 400 °C for 10 h under the reaction environment. Others include acetaldehyde and ethyl formate. The black dot is CO_2 conversion; red dot is EtOH STY.

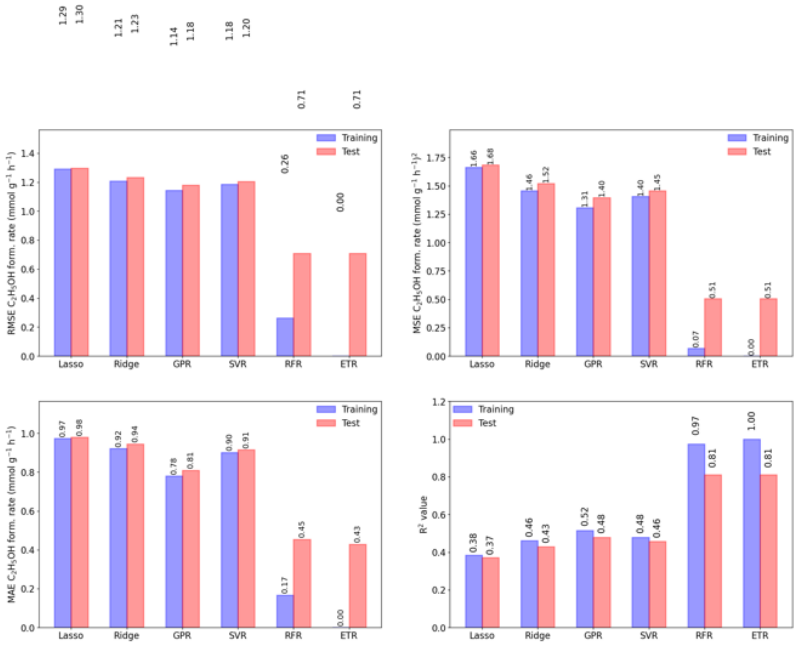

Figure 3. 4. Comparison of the prediction accuracy for the ethanol formation rate of the 555 catalysts using different ML regressions. The prediction accuracy was quantified based on four criteria (R^2, MAE, RMSE, and MSE) by 10-fold cross validation. Among the six tested ML algorithms, ETR gave the highest predictive accuracy for all the criteria.

Table 3. 2. The ethanol synthesis performances of studied catalysts in this work.

Catalysts[a]	CO_2 conversion (%)	selectivity (%)									STY_{EtOH} (mmol g_{cat}^{-1} h^{-1})
		MeOH	EtOH	$C_{3+}OH$	CH_4	$C^{2=}$–$C^{4=}$	C^{2-}–C^{4-}	C_{5+}	CO	others	
Best catalyst	57.6	0.3	23.2	10.7	13.0	15.1	11.2	17.1	7.0	2.4	8.2
Without Pd	52.6	0.2	20.3	20.3	10.9	18.9	6.8	10.5	11.1	1.0	6.4
Without Au	48.2	0.8	19.4	22.7	8.9	17.4	5.5	12.3	12.0	0.9	5.6
Without K	39.5	21.4	0.5	0.6	30.1	0.1	31.5	11.0	4.7	0	0.1
Without Sr	59.8	0.9	17.3	8.8	13.8	17.6	12.4	15.6	13.3	0.3	6.2
Without Fe	19.3	9.0	1.4	0	6.7	0.9	1.5	0	80.4	0	0.2
Without Zn	48.5	0.4	20.2	14.4	14.6	19.8	7.9	9.0	12.3	1.4	5.9
Without Cd	46.0	0.7	23.3	16.4	10.0	18.2	5.9	11.3	13.3	0.9	6.4
Without Yb	61.6	0.1	20.4	14.4	16.7	19.1	5.3	9.0	14.4	0.9	7.5
Without Re	59.5	0.3	23.0	19.8	10.3	20.4	6.8	9.2	9.5	1.0	8.0

[a]For the efficient evaluation of catalyst durability, accelerated aging treatment at 400 °C for 10 h was performed before the reaction.

Table 3. 3. Catalytic performances for CO_2 hydrogenation to form ethanol in this work and literature.

Catalyst	T (°C)	P (MPa)	WHSV (L g_{cat}^{-1} h^{-1})	CO_2 Conversion (%)	CO selectivity (%)	EtOH selectivity (%)	STY_{EtOH} (mmol g_{cat}^{-1} h^{-1})	References
Best catalyst[a]	360	4	12	58.9	4.5	23.2	8.2	This work
$KFeCuZn/ZrO_2$[a]	360	4	12	52.5	9.6	16.5	5.4	[44]
$Na\text{-}Co/SiO_2$	250	5	6	21	27	6	0.5	[53]
$Cs\text{-}Cu_{0.8}\ Fe_{1.0}\ Zn_{1.0}$	330	5	4.5	35	20	12	1.1	[54]
Na-ZnFe@C	320	5	9	38.4	7.6	20.3	3.4	[55]
K/Cu-Zn-Fe	300	7	5	44.2	5.9	19.5	2.3	[56]
$K-In/Ce-ZrO_2$	300	10	4.5	19	57	5 (C_{2+})	0.4 (C_{2+})	[52]
$2K20Fe5Rh/SiO_2$	250	7.5	7	18	5	16	0.4	[57]
4.6K/CuMnZnFe	320	5	6	30.4	30.6	~7	1.7	[51]
$RhFeLi/TiO_2$	250	3	6000 h^{-1}	15.7	12.5	35.8	~1.3 (mmol · L_{cat}^{-1} · h^{-1})	[58]
$Co/La_4Ga_2O_9$	280	3	3	9.6	10.8	23.3	0.2	[59]
Pd/Fe_3O_4	300	0.1	60	0.3	0	97.5	0.4	[60]
Pd/CeO_2	240	3	3	9.2		99.2	1.2	[61]
Na-Rh@S-1	250	5	6	10	32	16	0.6	[62]
2%Na-Fe@C/5%KCuZnAl	320	5	4.5	39.2	9.4	35	3.6	[63]
$Li\text{-}Rh/SiO_2$	240	5	6	7	15.7	18.4	0.4	[64]
$Mo_1Co_1K_{0.6}$	320	5	3	23.5	77.2	8.9	0.1	[65]
K-CuMgZnFe/CZA	320	5	6	42.3	13.8	~17.4 (C_{2+})	~2.4 (C_{2+})	[11]
FeNaS-0.6	320	3	8	32.0	20.7	15.9 (C_{2+})	1.7 (C_{2+})	[66]
Cu/CeO_2	190	0.1	9	~0.1	~3	84	0.02	[67]
$Pd_2Ce@Si$	240	3	3	6	~2	94	0.8	[68]
$Co_2C-CuZnAl$	250	5	12	21	12.5	~18.9	~2.2	[69]
PdFe-6.9(37nm)	320	5	6	35.6	20.7	18.2 (C_{2+})	~1.9 (C_{2+})	[70]
$CuZnFe_{0.5}K_{0.15}$	300	6	5000 h^{-1}	42.3	49.2	36.7 (C_{2+})	3.4 (C_{2+})	[71]
Cu/Co_3O_4-2h	250	3	36	13.9	6.5	15.2	1.9	[72]
Rh-VO_x /MCM-4	250	3	6000 h^{-1}	12.1	20.1	24.1	1.1	[73]
Cu@Na-Beta	300	1.3	12	7.9	30.5	69.5	3.4	[74]
90Fe10Co (1.0)K	240	1.2	1.5	14.5	45.5	10.8	0.07	[75]
$Cu_{25}Fe_{22}Co_3K_3$-$CuZn_{1.0}K_{0.15}$	350	6	5000 h^{-1}	32.4	45.3	< 12	< 0.6 (mmol · L_{cat}^{-1} · h^{-1})	[76]
CoMoS	340	10.4	0.43	32	57.5	12.9	0.07	[77]
Na–CuCo-9	330	4	5	20.1	26.5	18.0	~2.3	[7]
K-CuZnAl/$Zr_{(0.03)}$-CuFe	320	4	24	28.8	~13.4	19.7 (C_{2+})	3.8 (C_{2+})	[78]
$Rh\text{-}Fe/TiO_2$	270	2	8	9.2	28.4	6.4	0.6	[79]
$Rh\text{-}Fe/SiO_2$	260	5	6	16.7	19.7	16	1.4	[80]
$IrMo\text{-}SiO_2$	200	4.9	2000 h^{-1}	7	41.7	4.3	0.04	[81]
$Rh/CeO_2\text{-}SiO_2$	240	5	3	8.3	33.5	6.1 (C_{2+})	0.2 (C_{2+})	[82]
RhLi/Y	250	3	6	13.1	86.6	2.7(C_{2+})	0.8 (C_{2+})	[83]
α-$CoMoO_4$/K	250	3	1.2	7.2	27.8	4.8 (C_{2+})	0.2 (C_{2+})	[84]
β-MoC_y	200	2	9	6	39	3 (C_{2+})	0.1 (C_{2+})	[85]
Pt/Co_3O_4	200	2	3	27	0	4.2 (C_{2+})	0.3 (C_{2+})	[86]
$In_2O_3-Fe_2O_3-K-Al_2O_3$	300	2	4	36	~40	42 (C_{2+})	3.02 (C_{2+})	[87]
3KCuFeZn/CuZnAlZr	300	5	3	27	28	24.6 (C_{2+})	0.9 (C_{2+})	[88]

[a]For the efficient evaluation of catalyst durability, accelerated aging treatment at 400 °C for 10 h was performed before the reaction.

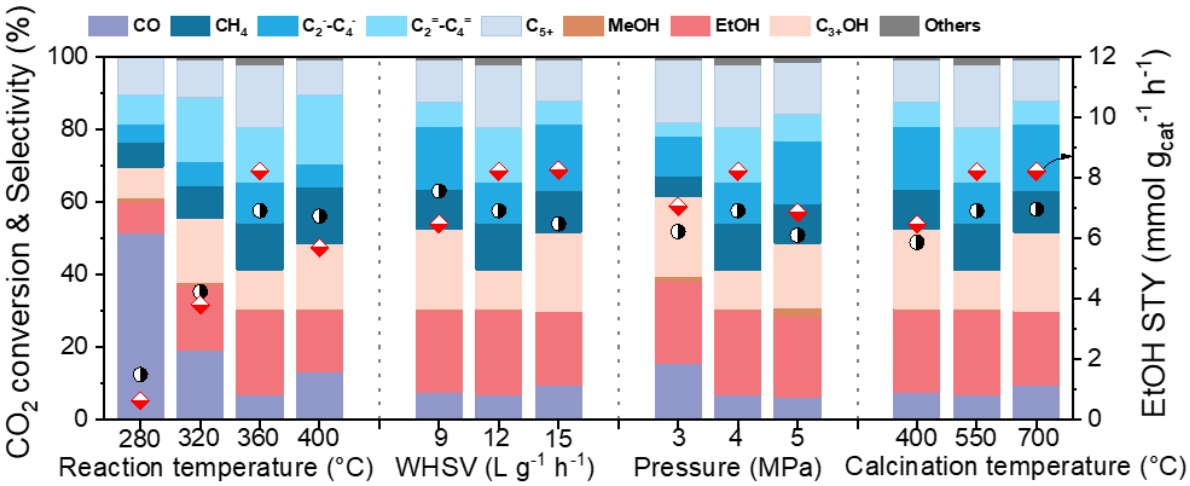

Figure 3. 5. Influence of experimental conditions (including: reaction temperature, gas hourly space velocity (WHSV), reaction pressure and the calcination temperature) for performance over the best catalyst (PdAuKSrFeZnCdYbRe/CeO_2(25%)-ZrO_2) at 280-400 °C. Conditions: 0.2 g catalyst, H_2: CO_2 = 1:3, and internal standard gas: Ar (0.8 vol%), 3-5 MPa, and 9–15 L g_{cat}^{-1} h^{-1}.

3.3.2 Visualization of database and ML-based statistical analysis

To clearly identify and understand the database, **Figure 3. 6** shows histograms of the component elements for our dataset which is composed of 2477 experimental data with unique catalyst compositions and elements. Elements K, Fe, Cu, Zn, Cd and Co appeared most frequently. The influence of the loading metal (PGM, PR and Add) on the frequently appearing elements is displayed in **Figures 3. 7-9**. In the cases of PGM and PR, the catalysts with low loading presented the high STY of ethanol. Most of the additive elements, i.e. Er, Al, Nb, Ta, Yb, Re, Y, tended to show the high ethanol STY at low loading, except for Fe which preferred high loading to give good performance. Additionally, the Periodic tables show the number of each element that appeared in the original dataset and current dataset to clearly indicate which elements appeared during the ML-aided catalyst exploration. Obviously, many kinds of elements which were not included in the original dataset were evaluated by ML, for example, most of the compositions in the best catalyst, such as Pd, Au, Sr, Cd, Yb, and Re, were not present in the original dataset. Cd and Yb, in particular, had never been reported in this field, making the identified catalyst composition highly unpredictable even for human experts.

While machine learning (ML) is often applied as a black box,[42,89] lacking direct insights into its learned representations, supervised ML models can effectively pinpoint crucial chemical components influencing predictions, even in the absence of explicit understanding

of its underlying mechanisms. Extrapolative ML can reveal not only the effective catalyst compositions but also the required elemental features and electronic properties for the precise designing of ideal catalysts.[31,32] Feature importance scores and SHapley Additive exPlanations (SHAP) analyses were employed to assess the significance of descriptors in ML predictions,[89–91] which directly considers the elemental composition/features, enhancing the understanding of each element's contribution to the data. In this work, as depicted in **Figure 3. 10**, the reaction temperature displayed a higher importance score than other factors. Fe, K and Yb were considered as important descriptors for the catalyst composition, whereas CeO_2(25%)-ZrO_2, ZrO_2_JRC5_NND and ZrO_2_JRC3-100 were identified as important descriptors for the support. According to the optimized descriptors, Esurf and Density for additives, EN_bulk for support and Atom rad for PGM were important features of elements and support. Furthermore, SHAP enables visualization of how the model output (EtOH formation rate) depends on each descriptor's value (**Figure 3. 6e**). For instance, lower values highlighted in red for reaction temperature correlate with higher EtOH formation rates (SHAP value). Descriptors such as Fe and K in catalyst composition, and support descriptors like CeO_2 (25%)-ZrO_2, were identified as pivotal factors.

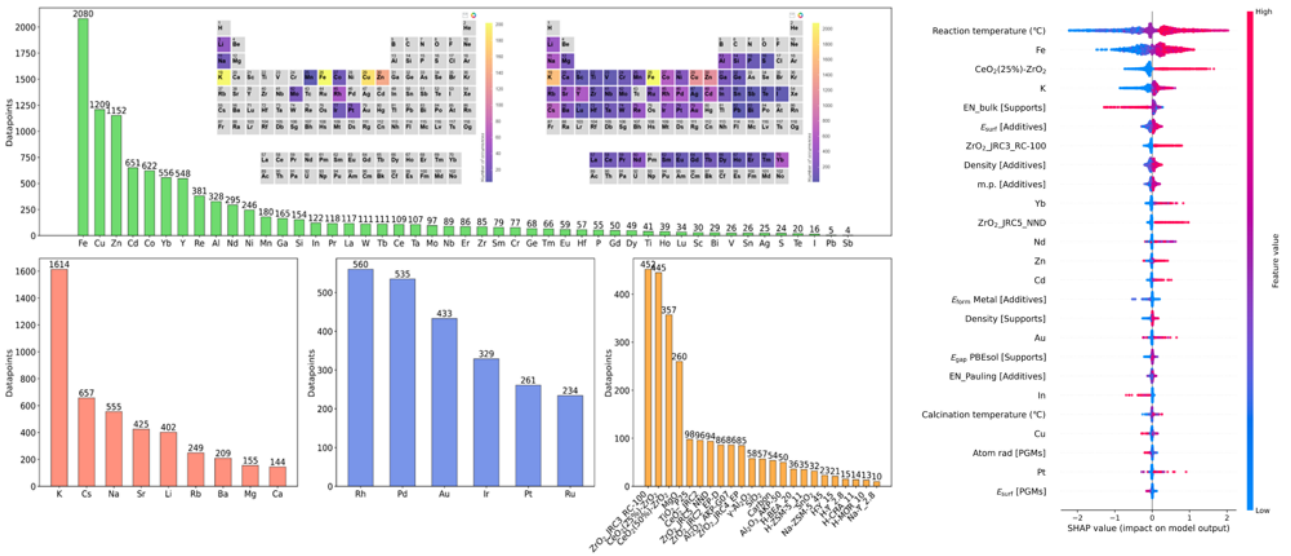

Figure 3. 6. Visualization of ethanol synthesis catalyst datasets and SHAP (SHapley Additive exPlanations) analysis**.** Frequency for each additive oxide component (a), electronic promoter (b), PGM group elements (c) and support (d); the elements in the original (left) and final (right) datasets are shown in the periodic tables. (e) SHAP values of the descriptors (summary plot) used to predict ethanol formation rate of all the catalysts in our dataset (red and blue for SHAP analysis correspond to high and low features, respectively). Here, features appear in descending order according to the sum of their absolute SHAP values. Dots are displaced vertically to visualize the density of data points at a given SHAP value.

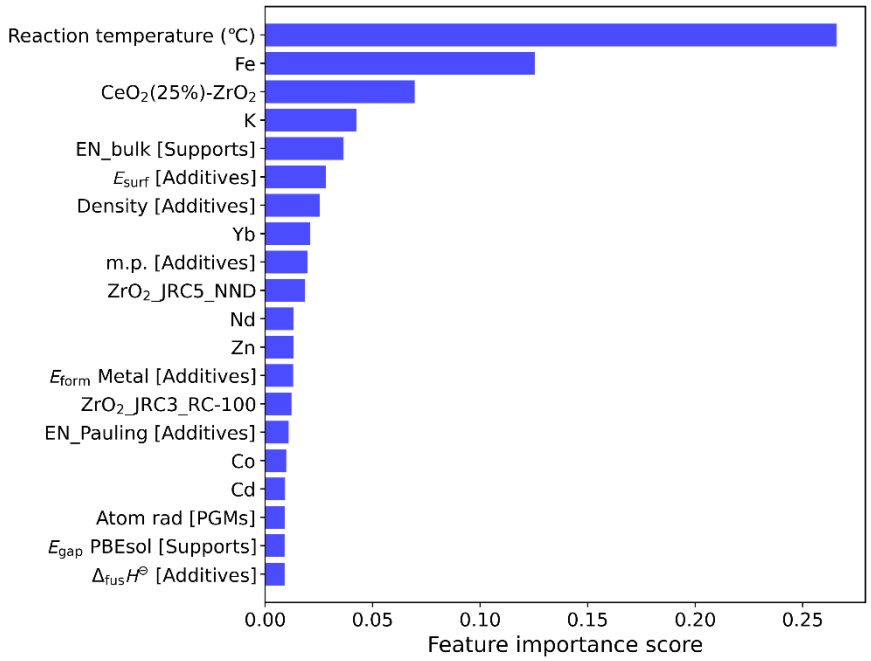

Figure 3. 10. Feature importance.

3.3.3 Catalyst characterization

Following the ML-statistical analysis, we aimed to investigate the geometric and electronic properties of our top-performing catalyst, as well as the reaction mechanism for ethanol synthesis. The X-ray diffraction (XRD) patterns (**Figure 3. 11**) confirmed that the CeO_2(25%)-ZrO_2 support predominantly exhibits a tetragonal phase of ZrO_2 doped with Ce.[92] Following the H_2 reduction, Fe_2O_3 is fully converted to metallic Fe, which subsequently transforms into Fe_5C_2 and Fe_3O_4 after reaction,[44,57–59] reflecting the dynamic behavior of Fe species under catalytic conditions, consistent with previous studies.[44,54,63,93] The XRD analysis also reveals that the Zn species remains exclusively in the ZnO phase, signifying the absence of phase transitions during the entire reaction sequence. Moreover, the metallic Cd is detectable following H_2 reduction and the subsequent catalytic reaction. The other elements (Pd, Au, K, Sr, Yb, Re) were not detected by XRD, primarily due to their low loading and high dispersion on the catalyst. The HAADF-STEM and EDS elemental mapping images further revealed the sintering of Pd, Cd, and Au and the formation of a trimetallic alloy structure, after H_2 reduction and reaction (**Figures 3. 12-13**). The size distribution analysis (**Figure 3. 12 inset** and **Figure 3. 13 inset**) indicates a marked increase in the trimetallic alloy size, expanding from 2.6 nm after H_2 reduction to 4.6 nm after catalytic reaction. In

contrast, other components exhibited a consistent homogeneous distribution demonstrating stability in their spatial arrangement after the H_2 reduction and reaction (spent).

The trimetallic structure was further confirmed by X-ray absorption spectroscopy (XAS). As depicted in **Figure 3. 14a, b** and **c**, the *ex situ* X-ray absorption near edge structure (XANES) spectra for the Pd *K*-edge, Cd *K*-edge, and Au *L2*-edge demonstrate the presence of metallic states following H_2 reduction and after catalytic reaction. The EXAFS spectra of Pd provide additional evidence of formation of alloy, as the Pd–Pd (Au, Cd) coordinating path exhibits a shift to a higher distance of 2.79 Å (**Figure 3. 14d** and **Table 3. 4**) aligning with the results obtained from STEM results. Moreover, the extended X-ray absorption fine structure (EXAFS) analysis of Cd demonstrates a significant shift in the Cd metallic path to a lower value compared to the standard value of 2.96 Å. Curve fitting result further elucidate the formation of Cd–Pd (Au, Cd) bonds, with distances of 2.76 Å for the H_2 reduced catalyst and 2.77 Å for the spent catalyst (**Figure 3. 14e** and **Table 3. 5**). Furthermore, extended EXAFS analysis at Au *L2*-edge (**Figure 3. 14f** and **Table 3. 6**) reveals that the first coordination shell exhibits is located at 2.84 Å for the H_2 reduced catalyst and 2.85 Å for the spent catalyst, both of which are elongated relative to the Au foil (2.79 Å). This bond expansion is likely due to lattice compression induced by the incorporation of Cd or Pd atoms. These results provide compelling evidence for the formation of a trimetallic Pd, Au and Cd structure, corroborated by STEM results.

Beyond the Pd, Au, and Cd alloys, further investigations into the other supported metals were conducted. XANES analysis at the Fe *K*-edge demonstrated that Fe_2O_3 was reduced to metallic Fe under H_2 reduction conditions, followed by partial oxidation of the Fe species under CO_2 + H_2 atmosphere, as indicated by the energy shift (**Figure 3. 15a**). Local structure analysis via EXAFS (**Figure 3. 15b** and **Table 3. 7**) revealed that, following H_2 pretreatment, Fe–Fe bonds at 2.43 and 2.82 Å replaced the Fe–O bond at 1.99 Å.[63] However, post reaction, the emergence of Fe–C and Fe–O bonds, coupled with the disappearance of the Fe–Fe bond, suggests the formation of FeO_x and FeC_x. Additionally, XANES analysis at the Ce *L3*-edge (**Figure 3. 16a**) showed a distinct shift to lower energy indicating the reduction of Ce^{4+} to Ce^{3+} in both H_2 reduced and spent catalysts.[94] This shift is due to cerium's reducibility and its ability to exhibit multiple oxidation states. By contrast, the remaining elements, including Zn (**Figure 3. 16b**), Zr (**Figure 3. 17a, c** and **Table 3. 8**) and Sr (**Figure 3. 17b, d** and **Table 3. 9**), did not change their chemical states and remained in the oxidative states of ZnO, ZrO_2 and SrO, respectively, after H_2 pretreatment and reaction.

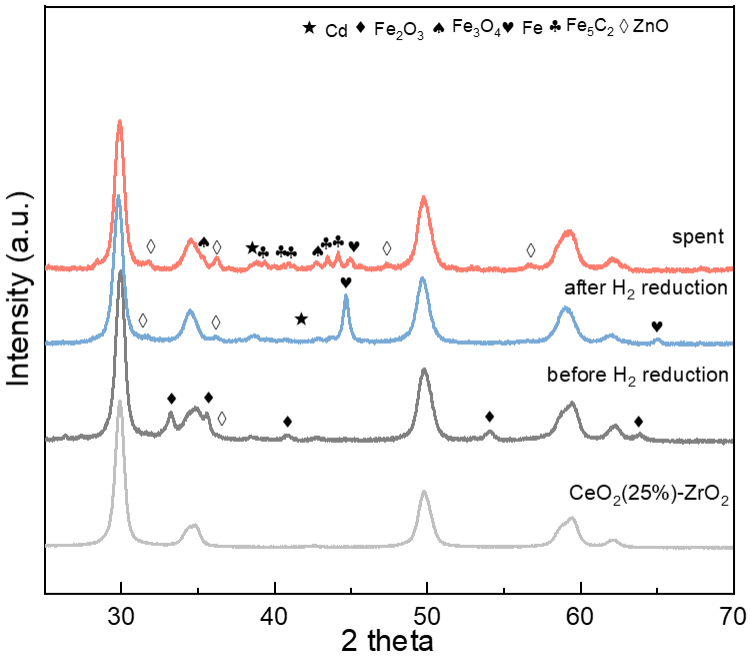

Figure 3. 11. XRD patterns of best catalyst (PdAuKSrFeZnCdYbRe/CeO_2(25%)-ZrO_2) before and after H_2 reduction at 400 °C as a pretreatment and after reaction. “Spent catalyst" refers to a sample that has undergone a 20-hour accelerated aging treatment at 400 °C under the reaction conditions.

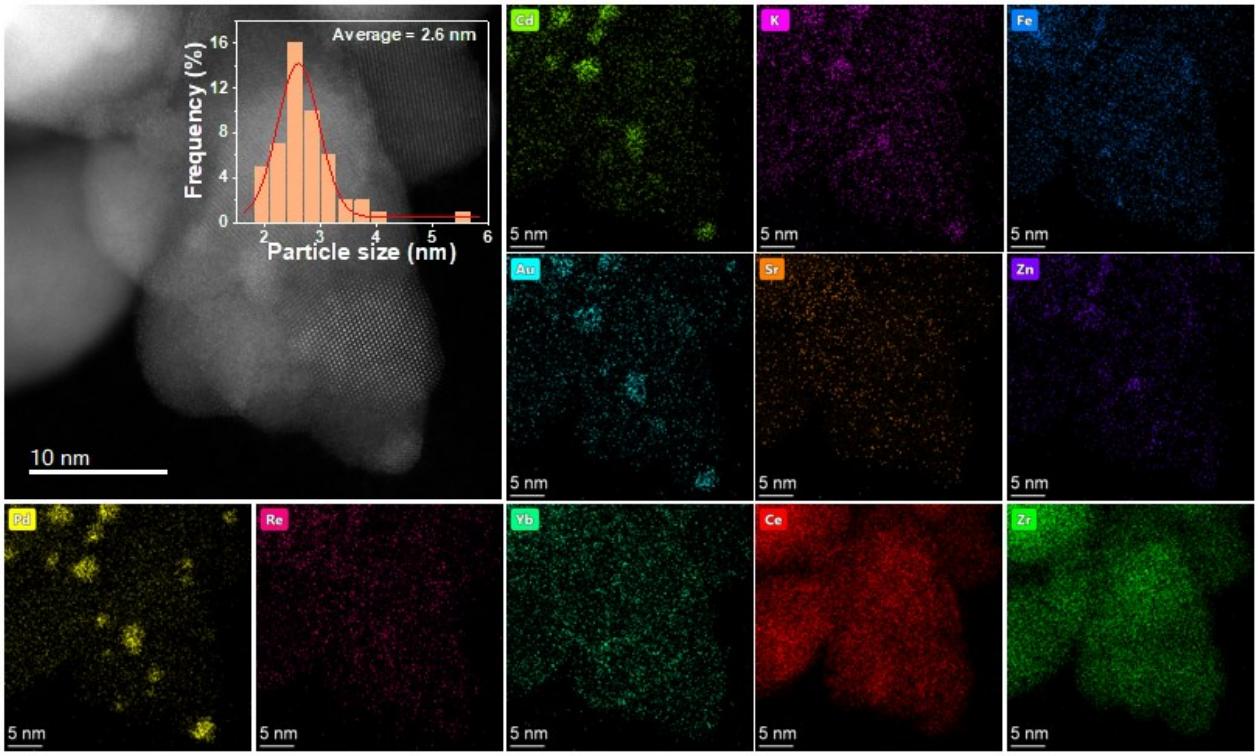

Figure 3. 12. HAADF-STEM image and corresponding EDS mapping images of the best catalyst (particle size distribution insertion) that has undergone H_2 reduction pretreatment at 400 °C

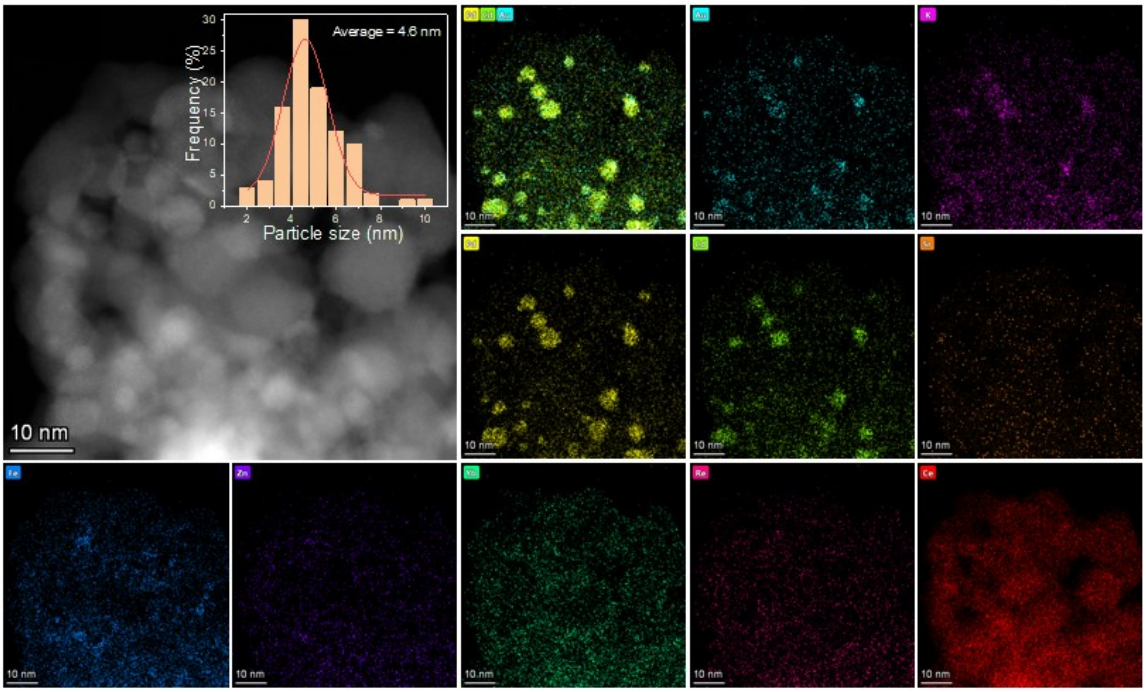

Figure 3. 13. HAADF-STEM image and corresponding EDS mapping images of the spent best catalyst (PdAuKSr FeZnCdYbRe/CeO_2(25%)-ZrO_2) that has undergone a 20-hour accelerated aging treatment at 400 °C under the reaction condition.

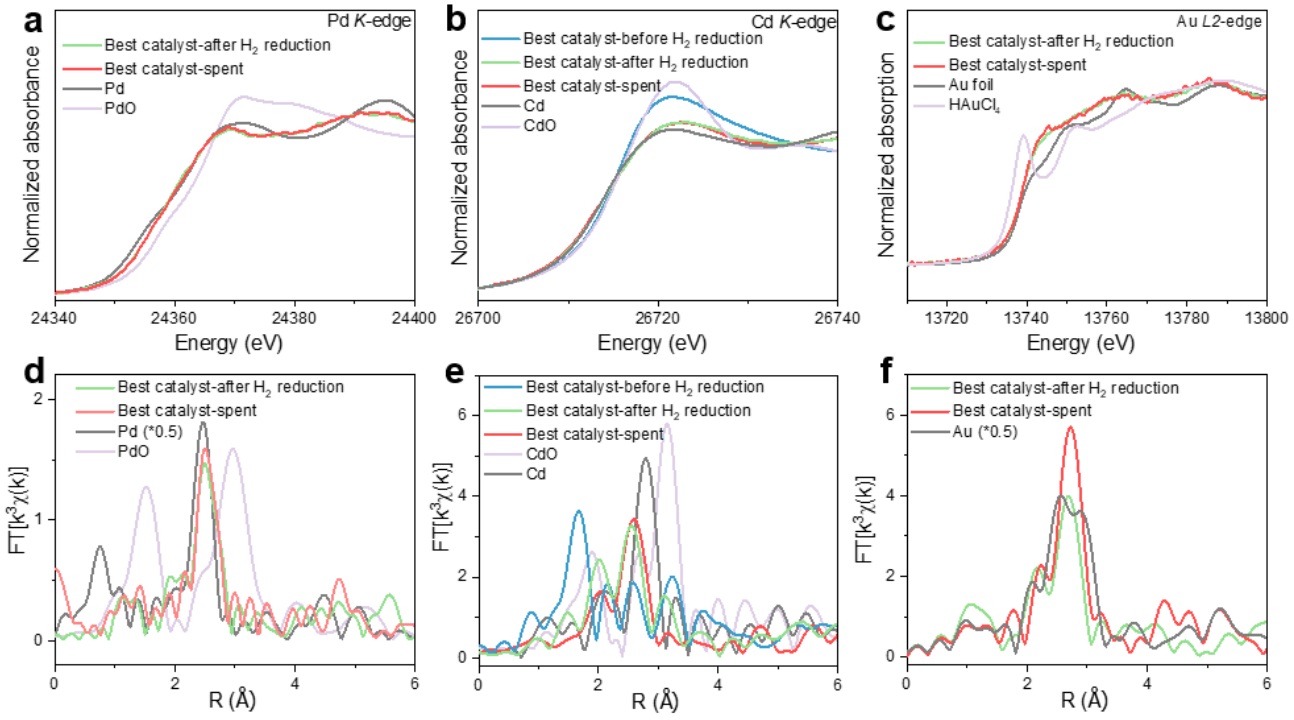

Figure 3. 14. *Ex situ* XAS spectra over best catalyst (PdAuKSrFeZnCdYbRe/CeO_2(25%)-ZrO_2) before and after H_2 reduction at 400 °C as a pretreatment and after reaction (spent). (a) Normalized Pd *K*-edge XANES spectra; (b) FT-EXAFS spectra for Pd; (c) normalized Cd *K*-edge XANES spectra; (d) FT-EXAFS spectra for Cd; (e) normalized Au *L*2-edge XANES spectra; and (f) FT-EXAFS spectra for Au. “Spent catalyst" refers to a sample that has undergone a 20-hour accelerated aging treatment at 400 °C under the reaction condition.

Table 3. 4. Curve-fitting results of the *ex situ* Pd *K*-edge FT-EXAFS spectra of the ML_best catalyst.

Sample	Shell	CN	R (Å)	σ^2 (Å^2)	ΔE	R factor
Pd foil	Pd–Pd	12	2.74±0.02	0.005	6.5	0.01
Best catalyst-after H_2 reduction	Pd–Pd (Au, Cd)	7.9±0.6	2.79±0.03	0.008	1.5	0.03
Best catalyst-spent	Pd–Pd (Au, Cd)	7.1±0.7	2.79±0.01	0.007	0.7	0.03

CN: coordination numbers; R: bond distance; σ^2: Debye-Waller factors; R factor: goodness of fit. S_0^2 was set to 0.81, according to the EXAFS fit of Pd foil.

Table 3. 5. Curve-fitting results of the *ex situ* Cd *K*-edge FT-EXAFS spectra of the ML_best catalyst.

Sample	shell	CN	R (Å)	σ^2 (Å^2)	ΔE	R factor
Cd foil	Cd–Cd	6	2.95±0.07	0.01	2.61	0.02
Best catalyst-after H_2 reduction	Cd–Pd (Au, Cd)	3.5±0.8	2.76±0.06	0.01	0.28	0.02
Best catalyst-spent	Cd–Pd (Au, Cd)	3.1±0.3	2.77±0.06	0.009	1.9	0.03

CN: coordination numbers; R: bond distance; σ^2: Debye-Waller factors; R factor: goodness of fit. S_0^2 was set to 0.95, according to the EXAFS fit of Cd.

Table 3. 6. Curve-fitting results of the *ex situ* Au *L2*-edge FT-EXAFS spectra of the ML_best catalyst.

Sample	shell	CN	R (Å)	σ^2 (Å^2)	ΔE	R factor
Au foil	Au–Au	12	2.86±0.08	0.008	3.4	0.01
Best catalyst-after H_2 reduction	Au–Cd (Au, Pd)	4.1±0.4	2.84±0.01	0.01	2.1	0.03
Best catalyst-spent	Au–Cd (Au, Pd)	4.9±0.8	2.85±0.05	0.009	2.8	0.02

CN: coordination numbers; R: bond distance; σ^2: Debye-Waller factors; R factor: goodness of fit. S_0^2 was set to 0.98, according to the EXAFS fit of Au foil.

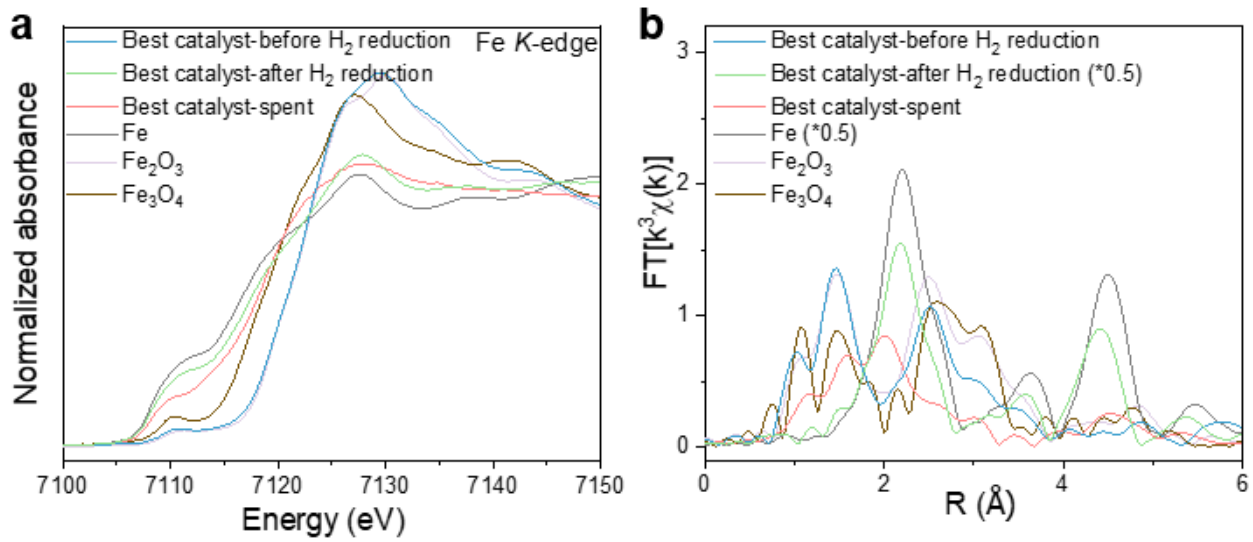

Figure 3. 15. *Ex situ* XAS spectra of ML_best catalyst (PdAuKSrFeZnCdYbRe/CeO_2(25%)-ZrO_2) before and after H_2 reduction at 400 °C as a pretreatment and after reaction (spent). (a) Normalized Fe *K*-edge XANES spectra; (b) FT-EXAFS spectra for Fe. “Spent catalyst" refers to a sample that has undergone a 20-hour accelerated aging treatment at 400 °C under the reaction condition.

Table 3. 7. Curve-fitting results of the *ex situ* Fe *K*-edge FT-EXAFS spectra of the ML_best catalyst.

Sample	shell	CN	R (Å)	σ^2 (Å^2)	ΔE	R factor
Fe_2O_3	Fe–O	3	1.97			
	Fe–O	3	2.2			
Fe	Fe–Fe	8	2.47			
	Fe–Fe	6	2.85			
Fe_5C_2	Fe–C	2	1.95			
	Fe–C	4	2.03			
	Fe–C–Fe	2	2.47			
	Fe–C–Fe	3	2.59			
ML_best catalyst-before H_2 reduction	Fe–O	4.3±0.4	2.00±0.03	0.006	0.29	0.02
	Fe–O–Fe	4.9±0.6	2.98±0.01	0.007		
ML_best catalyst- after H_2 reduction	Fe–Fe	4.2±1.1	2.43±0.04	0.004	10	0.01
	Fe–Fe	5.5±1.3	2.82±0.04	0.005		
ML_best catalyst-spent	Fe–O(C)	2	1.98±0.02	0.006	4.2	0.03
	Fe–C–Fe	1.8±0.3	2.51±0.04	0.003		
	Fe–C–Fe	1.7±0.3	2065±0.05	0.003		

CN: coordination numbers; R: bond distance; σ^2: Debye-Waller factors; R factor: goodness of fit. S_0^2 was set to 0.8, according to the EXAFS fit of Fe foil.

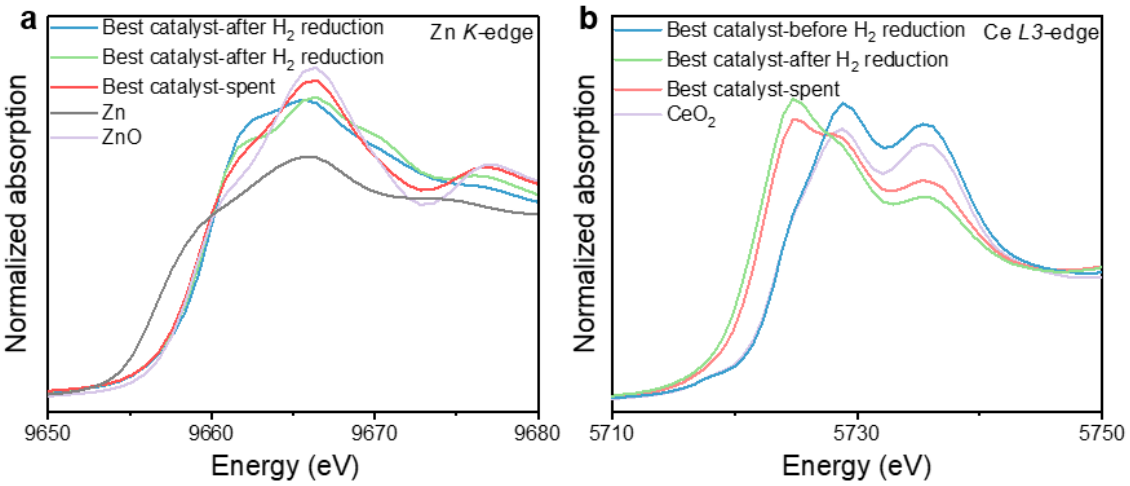

Figure 3. 16. *Ex situ* XAS spectra of ML_best catalyst (PdAuKSrFeZnCdYbRe/CeO_2(25%)-ZrO_2) before and after H_2 reduction at 400 °C as a pretreatment and after reaction (spent). (a) Normalized Ce *L3*-edge XANES spectra; (b) Normalized Zn *K*-edge XANES spectra. “Spent catalyst" refers to a sample that has undergone a 20-hour accelerated aging treatment at 400 °C under the reaction condition.

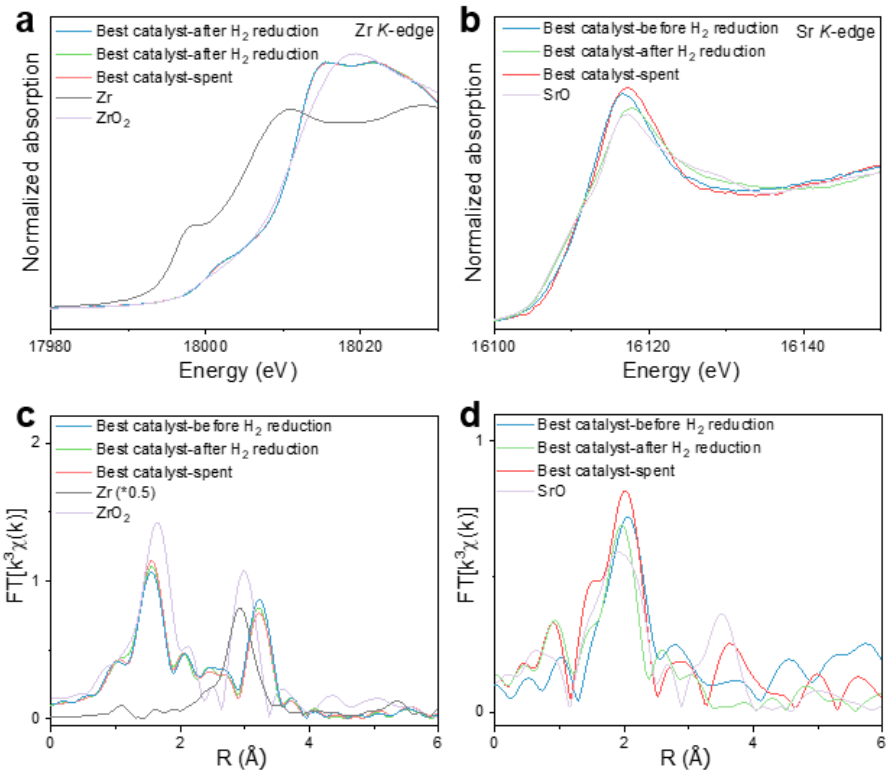

Figure 3. 17. *Ex situ* XAS spectra of ML_best catalyst (PdAuKSrFeZnCdYbRe/CeO_2(25%)-ZrO_2) before and after H_2 reduction at 400 °C as a pretreatment and after reaction (spent). Normalized Fe *K*-edge (a) and Sr *K*-edge (b) XANES spectra; (b) FT-EXAFS spectra for Zr (c) and Sr (d). “Spent catalyst" refers to a sample that has undergone a 20-hour accelerated aging treatment at 400 °C under the reaction condition.

Table 3. 8. Curve-fitting results of the *ex situ* Zr *K*-edge FT-EXAFS spectra of the ML_best catalyst.

Sample	shell	CN	R (Å)	σ^2 (Å^2)	ΔE	R factor
ZrO_2	Zr–O	2	2.01			
	Zr–O	3	2.16			
	Zr–O	2	2.26			
Best catalyst-before H_2 reduction	Zr–O	5.9±1.1	2.11±0.05	0.007	6.9	0.02
Best catalyst-after H_2 reduction	Zr–O	6.5±0.7	2.12±0.04	0.008	5.7	0.03
Best catalyst-spent	Zr–O	6.8±0.7	2.11±0.05	0.008	8	0.03

CN: coordination numbers; R: bond distance; σ^2: Debye-Waller factors; R factor: goodness of fit. S_0^2 was set to 0.8, according to the EXAFS fit of Zr foil.

Table 3. 9. Curve-fitting results of the *ex situ* Sr *K*-edge FT-EXAFS spectra of the ML_best catalyst.

Sample	shell	CN	R (Å)	σ^2 (Å^2)	ΔE	R factor
SrO	Sr–O	6	2.58			
Best catalyst-before H_2 reduction	Sr–O	5.2±0.5	2.59±0.01	0.007	1.7	0.03
Best catalyst-after H_2 reduction	Sr–O	4.9±0.5	2.54±0.03	0.006	5.7	0.02
Best catalyst-spent	Sr–O	5.8±0.5	2.59±0.01	0.006	6.2	0.03

CN: coordination numbers; R: bond distance; σ^2: Debye-Waller factors; R factor: goodness of fit. S_0^2 was set to 0.89, according to the EXAFS fit of Sr foil.

3.3.4 Mechanistic studies

In situ XAS was conducted to elucidate the chemical states under H_2, CO_2, and CO_2 + H_2 atmospheres at 400 °C and ambient pressure, as the procedures shown in **Figure 3. 18a**. The Fe *K*-edge and Ce *L3*-edge XANES spectra (**Figure 3. 18b** and **c**) of PdAuKSrFeZnCdReYb clearly showed that the absorption edge shifted to higher energies after the introduction of CO_2 and subsequently moved to lower energy after the introduction of the H_2 atmosphere, indicating that the Fe and Ce species exhibited notable redox behaviors. Additionally, the Zn *K*-edge (**Figure 3. 18d**), Zr *K*-edge (**Figure 3. 19b**), Cd *K*-edge (**Figure 3. 19c**) and Sr *K*-edge (**Figure 3. 19d**) presented a minor energy shift following the introduction of CO_2, which differed slightly from the *ex situ* results. We suggested that this difference is due to the race of active Zn, Zr, Cd and Sr species on the surface being reduced and oxidized, these species are easily oxidized upon exposed to air. However, the *K*-edge XANES spectra of Pd did not change under different atmosphere (**Figure 3. 19e**).

AP-XPS experiments were performed on the best catalyst under the various conditions (See details in experimental section) and the changes of chemical valence of elements on the catalyst surface were clearly revealed. To clearly track the evolution of chemical states due to the pressure gap, we first conducted the reduction pretreatment over the studied catalyst at 400 °C for 30 minutes. The following AP-XPS measurement processes were shown in **Figure 3. 18e**. Under the H_2 atmosphere, for Fe $2p_{3/2}$ spectrum (**Figure 3. 18f**), the peaks located at 707, and 709.2 eV[9,95] are attributed to Fe^0 and Fe^{2+}. The two higher binding energy at 710.9 eV and 713.4 eV are assigned to Fe^{3+} octahedral species and Fe^{3+} tetrahedral species[95] suggesting the presence of magnetite. Following CO_2 introduction, the peak of Fe^0 disappeared because the metallic Fe was oxidized by CO_2. And the binding energy of Fe^{2+} and Fe^{3+} became more pronounced, elucidating that the chemical states of Fe are strongly dependent on the working environments (**Table 3. 10**).[62] For the Re *4f* XPS results (**Figure 3. 17g**), after H_2 reduction, multi-oxidation states of Re, including: Re^0 at 40.5 eV,[96,97] $Re^{\delta+-1+}$ at 41.08 eV,[97] Re^{2+} at 41.5 eV,[97] Re^{2+} at 41.5 eV,[96] Re^{4+} at 43.0 eV,[96] were seen from the Re $4f_{7/2}$ result. Furthermore, the quantity of surface cationic Re species, as summarized in **Table 3. 11**, enhanced with an introduction of CO_2, simultaneously, the variety of oxidized Re species also increased with the emergence of Re^{6+} at 45.2[96] and Re^{7+} at 46.5 eV.[96,97] The aforementioned changes of Re species uncovered Re was significantly sensitive to the reaction atmosphere, changeable chemical valences and high oxophilicity.[96,98] In the case of Zn (**Figure 3. 18h**), the Zn^0 species located at 1020.6 eV[99] was oxidized by CO_2

following the switch from H_2 to CO_2 (**Table 3. 12**). For the Zr *3d* XPS results (**Figure 3. 20**), the peak area at 182.8 eV corresponding to Zr^{4+} increased, while the intensity of the Zr^{3+} species at 182 eV slightly decreased when the measurement environment changed from H_2 to CO_2.[100] In addition, the binding energy intensity at 183.7 eV,[101,102] assigned to Yb^{2+} in the Yb *4d* XPS spectrum, decreased after CO_2 treatment, while the peak area associated with Yb^{3+} species at 184.7 eV[101,102] enhanced (**Figure 3. 20** and **Table 3. 13**).

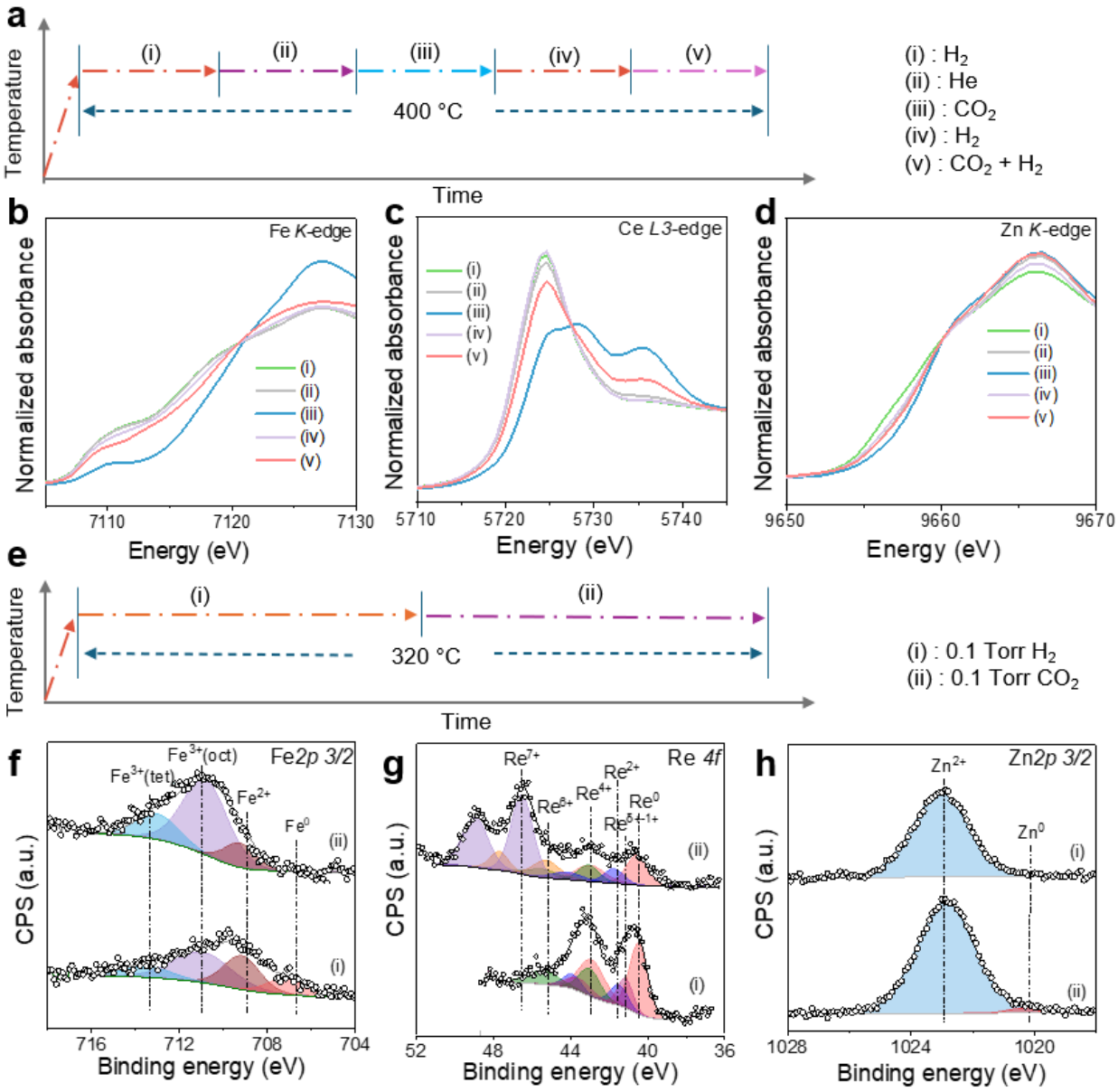

Figure 3. 18. *In situ* spectroscopy characterization of the best catalyst (PdAuKSrFeZnCdYbRe-/CeO_2(25%)-ZrO_2). (a) Typical experimental procedure for *in situ* XAS characterization, at 400 °C and under ambient pressure; (b) Normalized Fe *K*-edge XANES spectra; (c) Ce *L3*-edge XANES spectra; (d) Zn *K*-edge XANES spectra; (e): Typical experimental procedure for AP-XPS, at 320 °C and under 0.1 Torr and different atmosphere (H_2 to CO_2); AP-XPS of Fe *2p* (f), Re*4f* (g) and Zn*2p* (h) of the best catalyst.

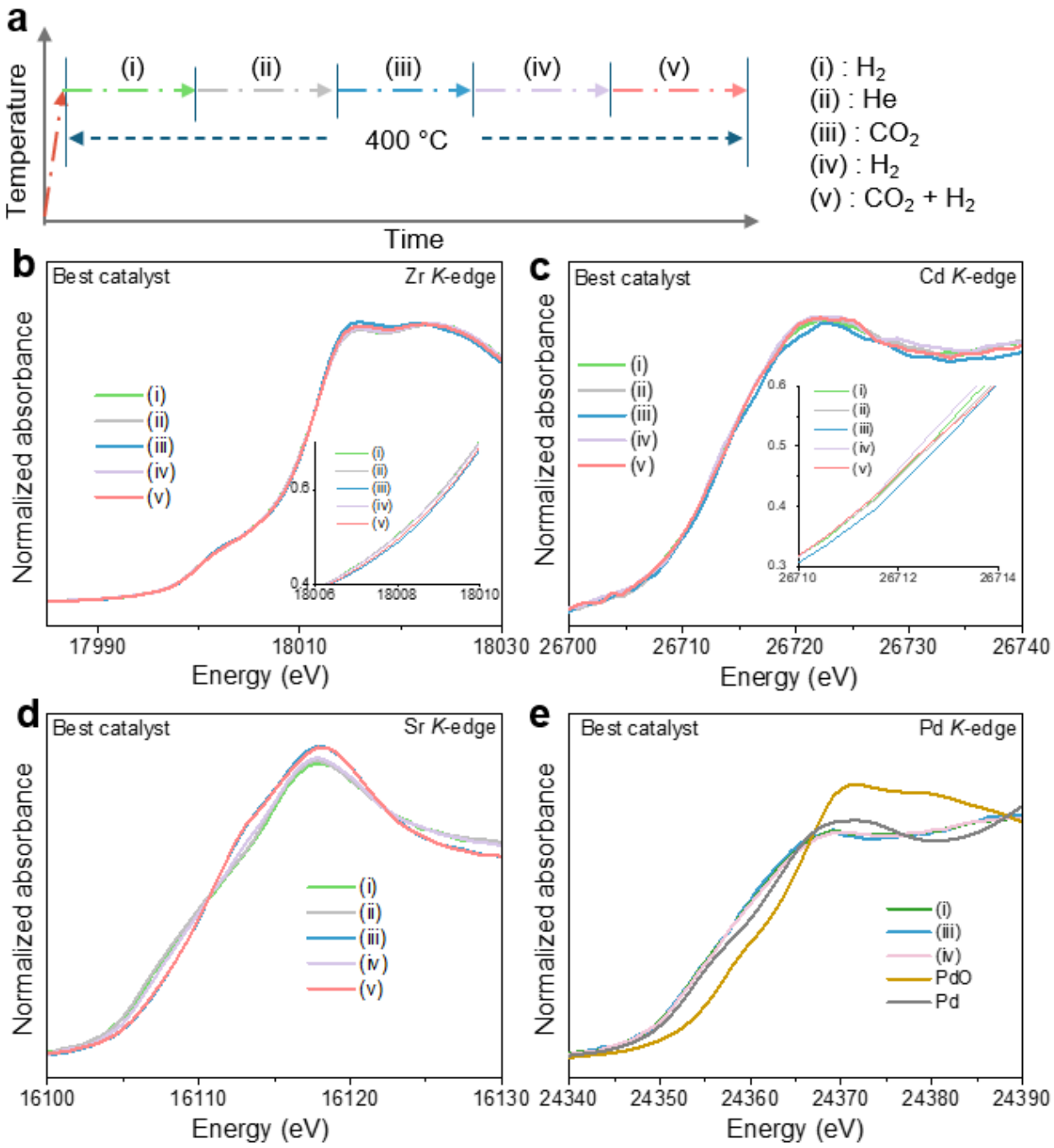

Figure 3. 19. *In situ* XAFS spectra of best catalyst (PdAuKSrFeZnCdYbRe/CeO_2(25%)-ZrO_2). (a) Typical experimental procedure for *in situ* XAS characterization, at 400 °C and under ambient pressure; (b) Normalized Zr *K*-edge XANES spectra; (c) Cd *K*-edge XANES spectra; (d) Sr *K*-edge XANES spectra; and (e) Pd *K*-edge XANES spectra. Conditions: 400 °C and 1 bar.

Table 3. 10. Peak Concentrations in the Fe *2p* spectra of best catalyst at above measurement conditions.

Gas condition	Peak concentration (%)		
	Fe^{3+}	Fe^{2+}	Fe^{0}
(i) 0.1 Torr H_2	55.54	29.74	14.72
(ii) 0.1 Torr CO_2	85.56	14.44	

Table 3. 11. Peak Concentrations in the Re *4f* spectra of best catalyst at above measurement conditions.

Gas condition	Peak concentration (%)					
	Re^{0}	$Re^{\delta+-1+}$	Re^{2+}	Re^{4+}	Re^{6+}	Re^{7+}
(i) 0.1 Torr H_2	48.15	16.51	13.35	21.99		
(ii) 0.1 Torr CO_2	18.23		8.02	9.66	13.45	50.63

Table 3. 12. Peak Concentrations in the Zn *2p* spectra of best catalyst at above measurement conditions.

Gas condition	Peak concentration (%)	
	Zn^{2+}	Zn^{0}
(i) 0.1 Torr H_2	98.05	1.95
(ii) 0.1 Torr CO_2	100	0

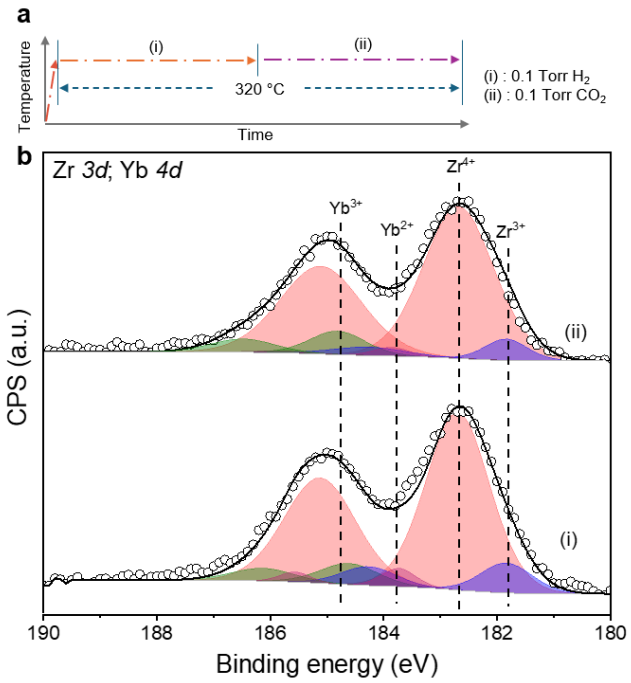

Figure 3. 20. NAP-XPS of Zr *3d* spectra of the best catalyst under different atmosphere (H_2 at 0.1 Torr and subsequently to CO_2 at 0.1 Torr) at 320 ºC.

Table 3. 13. Peak Concentrations in Zr *3d* and Yb *4d* spectra of best catalyst at above measurement conditions.

Gas condition	Peak concentration (%)			
	Zr^{4+}	Zr^{3+}	Yb^{3+}	Yb^{2+}
(i) 0.1 Torr H_2	77.24	10.58	8.34	3.84
(ii) 0.1 Torr CO_2	81.58	6.82	9.71	1.89

The *operando* DRIFTS was carried out to investigate the mechanism of CO_2 hydrogenation to EtOH and to understand the role of loaded element. All *operando* DRIFTS experiments were employed under 5 bar, at 320 °C (with an exception for our best catalyst, where the temperature range was 280–320 °C), with a H_2: CO_2 ratio of 3:1. The critical assignments of the surface intermediate species are displayed in **Table 3. 14**. Initially, as shown in **Figure 3. 21a**, observations at 280 °C for the best catalyst indicate the presence of adsorbed CO_2 at 1283 and 1325 cm^{-1},[54,103] which can be attributed to the carbonate species (bicarbonate species[104] at 1625 cm^{-1}) and surface formate located at 1593/1385 cm^{-1}.[44,105] Further reaction to 20 min, the adsorbed CO_2 was consumed, with the intensities of formates and carbonates species became weaker, simultaneously, the CO gas peaks emerged, agreeing the occurrence of reverse water gas shift (RWGS) reaction[27] With a continuous increase in the exposure time, peaks assignable to CH_3CH_2O* (1462/2852/2922/2956 cm^{-1})[44,51,54,74] appeared and the ethanol was also confirmed via micro-GC (**Figure 3. 21b**). In addition to the C_2 oxygenates, the minor CH_3O*(2810/2893 cm^{-1})[44,54,105] and CH_3OH were seen by DRIFT spectra and micro-GC, also indicating our catalyst preferred C_{2+} oxygenates rather than C1 oxygenate. When the temperature reached 320 °C (**Figure 3. 22a** and **Figure 3. 21c**), obviously, all observed peaks of CH_3CH_2O* at 280 °C became more pronounced. Simultaneously, the intensity of the peak at 1460 cm^{-1} attributable to $\delta(CH_2)$ vibrations of CH_3CH_2O* emerged and increased.[93] The gas methane, which was not observed at lower temperature, rose at 3011 cm^{-1}.[93] Furthermore, the formation rate of methanol reached to 0.18 mmol g_{cat}^{-1} h^{-1}, which was significantly higher than that of methanol based on the quantification of the micro-GC results, shedding light on the advantages of ethanol synthesis on the studied catalyst (**Figure 3. 21d**).

To shed light on the roles of the relative elements in EtOH synthesis, we further carried on the DRIFTS experiments on distinct catalysts, within specific reaction conditions at 320 °C and 0.5 MPa (**Figure 3. 22b**, and **Figure 3. 23**). By contrast, the catalysts without Fe and K displayed the minor intensity of CH_3CH_2O* than others, suggesting the essential roles of these two elements. In the case of role of Fe, it is widely accepted that FeO_x could be reduced and carburized to form the FeC_x species for C–C coupling[50,106,107] and our XRD and XAS curve fitting already confirmed the presence of highly active species of Fe_5C_2.[50] Then, once the K was dropped, there was a significant decrease in the amount of adsorbed carbonate and formate species (**Figure 3. 22b**), indicating that addition of K enhanced CO_2 adsorption,[54,75] providing more activated CO_2 for subsequent reaction processes. Besides

that, it was reported that, in CO_2 hydrogenation process on Fe-based catalysts, introduction of K enable not only acceleration of Fe carburization,[50,107,108] but also enhancement of ethanol selectivity,[51] which also confirmed by performance results. Next in cases of Yb and Re, we observed more pronounced CH_x at 2912 cm^{-1} and CH_3O* at 2893 cm^{-1},[54,93] although the intensity of CH_3CH_2O* was comparable with the best catalyst (**Figure 3. 22b** and **c**), after dropping one of those two elements. Based on the experimental observations, we claimed that Yb and Re slightly limited the production of methanol and other hydrocarbon products, improving the selectivity of ethanol. However, we observed changes only in the intensities of intermediate species and ethanol formation rate quantified by micro-GC, after removing Sr, Pd, Au, Cd, or Zn, without any alteration in their variety of intermediates, comparing to the best catalyst (**Figure 3. 22b** and **c**). The *operando* DRIFT experiments clearly unravel the superiority of the PdAuKSrFeZnCdYbRe/CeO_2(25%)-ZrO_2 catalyst in ethanol synthesis compared to all other evaluated catalysts. This highlights the critical contribution of each component and reaffirms the potential of data science in accelerating the development of high-performance catalysts.

Table 3. 14. DRIFTS peak assignments of the surface species for CO_2 hydrogenation.

Surface species	Wavenumber (cm^{-1})	References
*CO_3	1227–1281	54
*HCO_3	1620-1640	104
*CH_3O	2826, 1070, 2940, 2841-2866	105
*HCOO	2676–2774, 1593–1610, 1337–1397	54,109
*CH_3CH_2O	2856, 2928, 2963, 1458,1095	74,93
*CH_3CHO	1415, 1340, 1720	54,93
CH_4	3016	54
CO (gas)	2110, 2179	93
Linear–CO	2060–2098	93
Bridging–CO	1900–1940	93

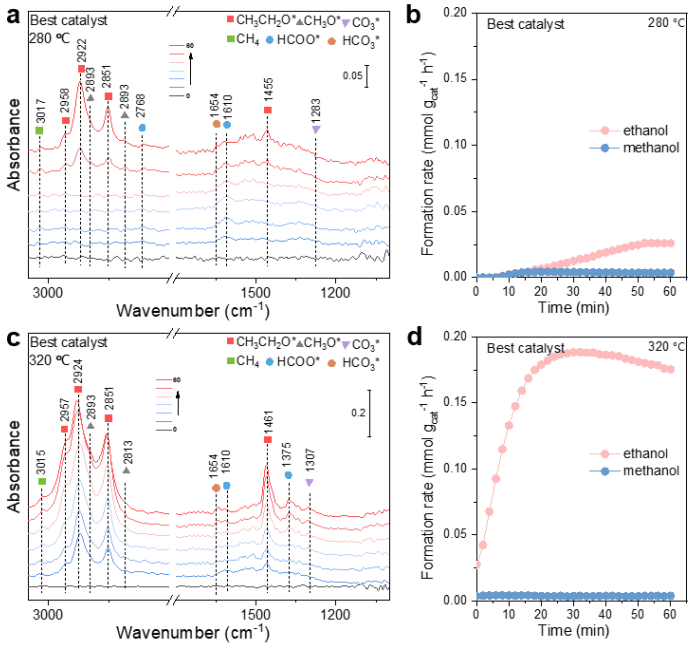

Figure 3. 21. *Operando* DRIFTS spectra. (a) time resolution spectra of the CO_2 + H_2 reaction over best catalyst at 0.5 MPa and 280 °C; (b) formation rate of ethanol and methanol, quantified by micro-GC at 280 °C; (c) time resolution spectra of the CO_2 + H_2 reaction over best catalyst at 0.5 MPa and 320 °C; (d) formation rate of ethanol and methanol, quantified by micro-GC at 320 °C.

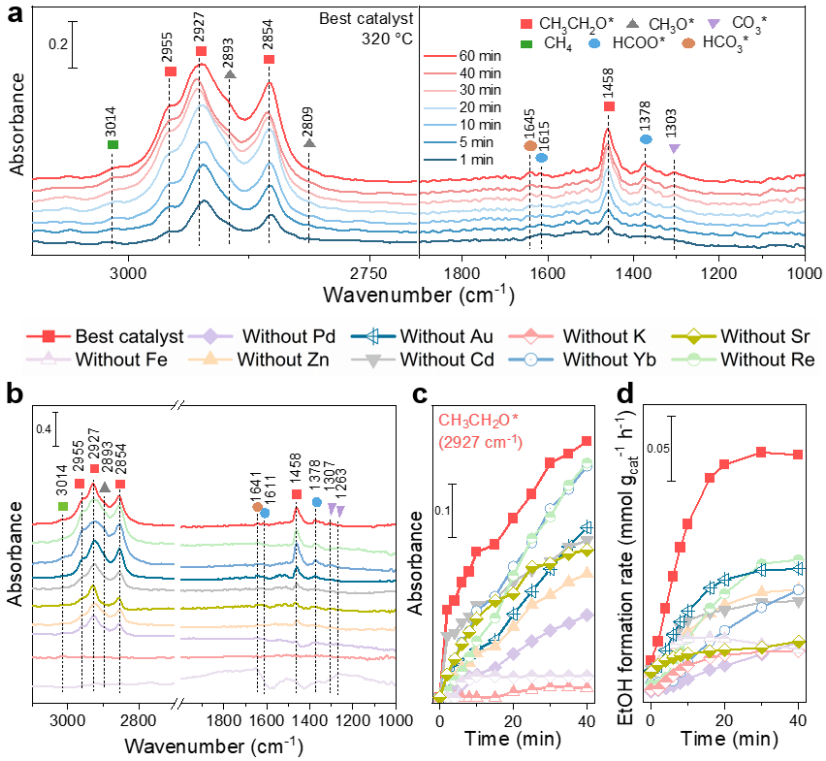

Figure 3. 22. *Operando* DRIFTS spectra. (a) the time resolution DRIFTS spectra of the CO_2 + H_2 reaction over the best catalyst (PdAuKSrFeZnCdYbRe/CeO_2(25%)-ZrO_2) at 0.5 MPa and 320 °C; (b) comparison of different catalysts under the CO_2 + H_2 reaction after 60 min at 320 °C and 0.5 MPa; (c) dynamic IR peak intensities of CH_3CH_2O* (2922 cm^{-1}) at 320 °C for different catalysts; (d) ethanol formation rate for different catalysts quantified by micro-GC at 320 °C.

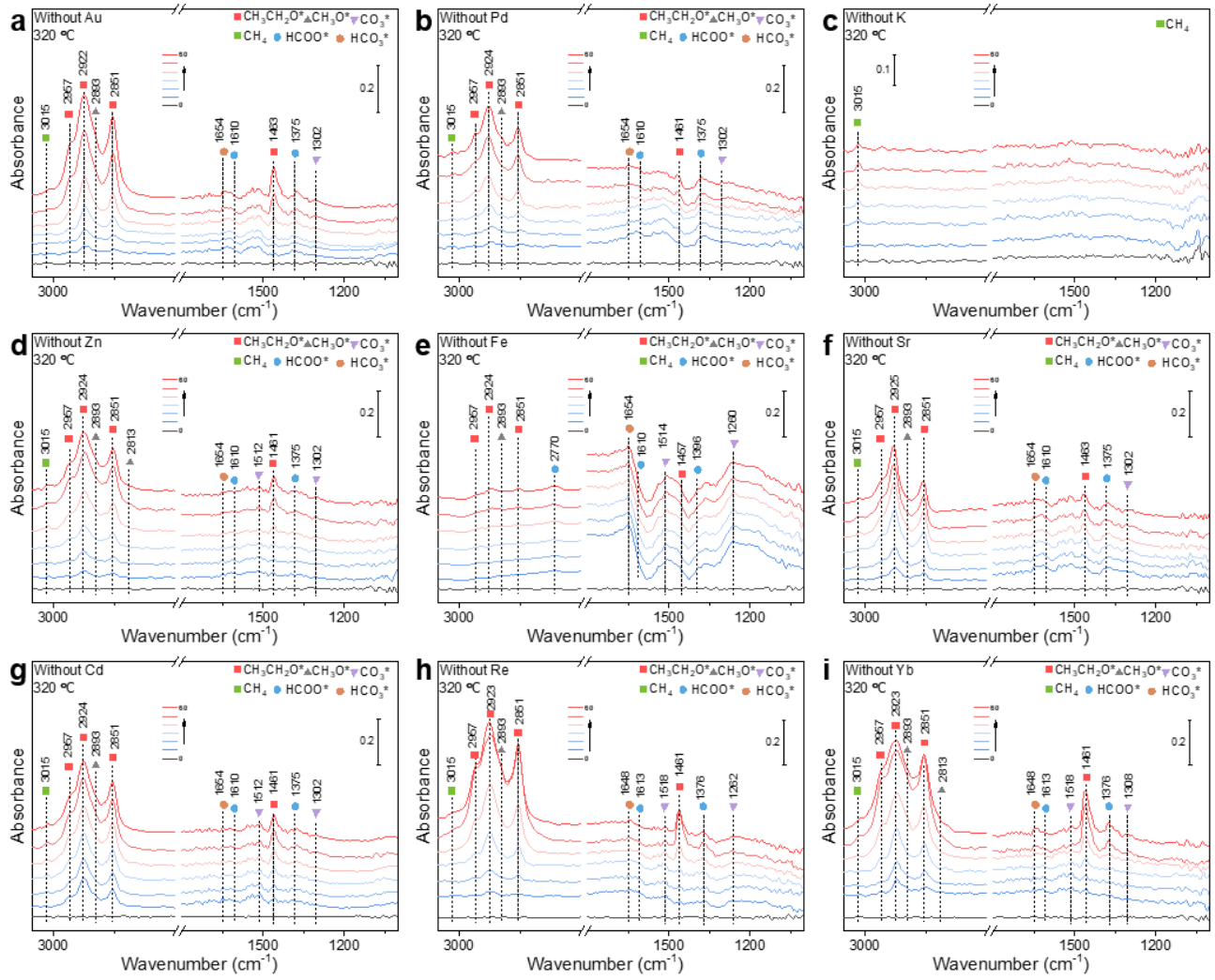

Figure 3. 23. *Operando* DRIFTS spectra. (a) DRIFTS spectra of the CO_2 + H_2 reaction over KFeCuZn/ZrO_2 after 60 min at 0.5 MPa and different temperatures; (b) time resolution spectra of the CO_2 + H_2 reaction over KFeCuZn/ZrO_2 at 0.5 MPa and 320 °C; (c) dynamic IR peak intensities of CH_3CH_2O* (2922 cm^{-1}) and STY of ethanol and methanol, quantified by micro-GC at 320 °C. *Operando* DRIFTS spectra. (a) time resolution spectra of the CO_2 + H_2 reaction on different control catalysts (a: without Au; b: without Pd; c: without K; d: without Zn; e; without Fe; f: without Sr; g: without Cd; h: without Re; i: without Yb) at 0.5 MPa and 320 °C.

3.4 Conclusion

In this study, we advance research on multi-elemental catalysts for ethanol synthesis, by using the extrapolative machine learning approach identified over 70 catalysts that exhibited superior STY_{EtOH} activity compared to the previously established best catalyst. This strategy identified PdAuKSrFeZnCdYbRe/CeO_2(25%)-ZrO_2 as the optimal catalyst composition, achieving a remarkable STY_{EtOH} of 8.2 mmol g_{cat}^{-1} h^{-1} under specified conditions (12 L g_{cat}^{-1} h^{-1}, 360 °C and 4 MPa). This data-driven method unveiled unprecedented catalyst compositions with exceptional performance, highlighting the model's ability to discover new elements like Yb and Cd that were previously overlooked, highlighting the transformative potential of extrapolative ML in catalyst design. The extensive characterization and *in situ/operando* spectroscopic techniques were employed to examine catalyst structure and the role of each element. Notably, Fe and K emerged as critical components; Fe is essential for C–C coupling, while K plays a vital role in ethanol synthesis and inhibits over-hydrogenation. The synergistic effects of all elements in the composition are crucial for achieving high catalytic performance, highlighting the importance of their collaborative interactions. In general, our study presents a new approach for discovering novel catalysts and materials that show extraordinary performance through machine learning methods. We anticipate that our findings will not only advance the development of innovative catalysts but also provide insights for interdisciplinary research in the future, emphasizing the importance of a comprehensive approach in catalyst design and optimization.

3.5 References

(1) Sheng, Y.; Polynski, M. V.; Eswaran, M. K.; Zhang, B.; Lim, A. M. H.; Zhang, L.; Jiang, J.; Liu, W.; Kozlov, S. M. A Review of Mechanistic Insights into CO_2 Reduction to Higher Alcohols for Rational Catalyst Design. *Appl. Catal. B,* **2024**, *343*. 123550.

(2) He, Y.; Müller, F. H.; Palkovits, R.; Zeng, F.; Mebrahtu, C. Tandem Catalysis for CO_2 Conversion to Higher Alcohols: A Review. *Appl. Catal. B,* **2024**, *345*, 123663.

(3) Xu, D.; Wang, Y.; Ding, M.; Hong, X.; Liu, G.; Tsang, S. C. E. Advances in Higher Alcohol Synthesis from CO2 Hydrogenation. *Chem* **2021**, *7*, 849–881.

(4) Vo, C. H.; Pérez-Ramírez, J.; Farooq, S.; Karimi, I. A. Prospects of Producing Higher Alcohols from Carbon Dioxide: A Process System Engineering Perspective. *ACS Sustain. Chem. Eng.* **2022**, *10*, 11875–11884.

(5) Ye, R. P.; Ding, J.; Gong, W.; Argyle, M. D.; Zhong, Q.; Wang, Y.; Russell, C. K.; Xu, Z.; Russell, A. G.; Li, Q.; Fan, M.; Yao, Y. G. CO2 Hydrogenation to High-Value Products via Heterogeneous Catalysis. *Nat. Commun*., **2019**, *10*,5698.

(6) Gao, P.; Li, S.; Bu, X.; Dang, S.; Liu, Z.; Wang, H.; Zhong, L.; Qiu, M.; Yang, C.; Cai, J.; Wei, W.; Sun, Y. Direct Conversion of CO_2 into Liquid Fuels with High Selectivity over a Bifunctional Catalyst. *Nat. Chem.* **2017**, *9*, 1019–1024.

(7) Irshad, M.; Chun, H. J.; Khan, M. K.; Jo, H.; Kim, S. K.; Kim, J. Synthesis of N-Butanol-Rich C_{3+} Alcohols by Direct CO_2 Hydrogenation over a Stable Cu–Co Tandem Catalyst. *Appl. Catal., B* **2024**, *340*, 123201.

(8) Ye, X.; Ma, J.; Yu, W.; Pan, X.; Yang, C.; Wang, C.; Liu, Q.; Huang, Y. Construction of Bifunctional Single-Atom Catalysts on the Optimized β-Mo_2C Surface for Highly Selective Hydrogenation of CO_2 into Ethanol. *J. Energy Chem.* **2022**, *67*, 184–192.

(9) Du, P.; Qi, R.; Zhang, Y.; Gu, Q.; Xu, X.; Tan, Y.; Liu, X.; Wang, A.; Zhu, B.; Yang, B.; Zhang, T. Single-Atom-Driven Dynamic Carburization over Pd_1–FeO_x Catalyst Boosting CO_2 Conversion. *Chem* **2022**, *8*, 3252–3262.

(10) Gao, P.; Dang, S.; Li, S.; Bu, X.; Liu, Z.; Qiu, M.; Yang, C.; Wang, H.; Zhong, L.; Han, Y.; Liu, Q.; Wei, W.; Sun, Y. Direct Production of Lower Olefins from CO_2 Conversion via Bifunctional Catalysis. *ACS Catal.* **2018**, *8* (1), 571–578.

(11) Xu, D.; Yang, H.; Hong, X.; Liu, G.; Edman Tsang, S. C. Tandem Catalysis of Direct CO_2 Hydrogenation to Higher Alcohols. *ACS Catal.* **2021**, *11*, 8978–8984.

(12) Li, F.; Li, Y. C.; Wang, Z.; Li, J.; Nam, D.-H.; Lum, Y.; Luo, M.; Wang, X.; Ozden, A.; Hung, S.-F.; Chen, B.; Wang, Y.; Wicks, J.; Xu, Y.; Li, Y.; Gabardo, C. M.; Dinh, C.-T.; Wang, Y.; Zhuang, T.-T.; Sinton, D.; Sargent, E. H. Cooperative CO_2-to-Ethanol Conversion via Enriched Intermediates at Molecule–Metal Catalyst Interfaces. *Nat Catal.* **2019**, *3* (1), 75–82.

(13) An, B.; Li, Z.; Song, Y.; Zhang, J.; Zeng, L.; Wang, C.; Lin, W. Cooperative Copper Centres in a Metal–Organic Framework for Selective Conversion of CO_2 to Ethanol. *Nat. Catal.* **2019**, *2*, 709–717.

(14) Wang, Y.; Kattel, S.; Gao, W.; Li, K.; Liu, P.; Chen, J. G.; Wang, H. Exploring the Ternary Interactions in Cu–ZnO–ZrO_2 Catalysts for Efficient CO_2 Hydrogenation to Methanol. *Nat. Commun.* **2019**, *10*, 1166.

(15) Hu, J.; Wei, Z.; Zhang, Y.; Huang, R.; Zhang, M.; Cheng, K.; Zhang, Q.; Qi, Y.; Li, Y.; Mao, J.; Zhu, J.; Wu, L.; Wen, W.; Yu, S.; Pan, Y.; Yang, J.; Wei, X.; Jiang, L.; Si, R.; Yu, L.; Wang, Y.; Deng, D. Edge-Rich Molybdenum Disulfide Tailors Carbon-Chain Growth for Selective Hydrogenation of Carbon Monoxide to Higher Alcohols. *Nat. Commun.* **2023**, *14*, 6808.

(16) Guo, H.; Shi, T. T.; Chen, J. T.; Chen, Z. X. Theoretical Investigation of the Properties of Pd_2Cu Intermetallics and CO_2 Hydrogenation to Ethanol Catalyzed on Pd_2Cu (110). *J. Phys. Chem. C* **2023**, *127*, 10097–10106.

(17) Liu, P.; Yang, Y.; White, M. G. Theoretical Perspective of Alcohol Decomposition and Synthesis from CO_2 Hydrogenation. *Surf. Sci. Rep.*, **2013**,1, 233–272.

(18) Suvarna, M.; Araújo, T. P.; Pérez-Ramírez, J. A Generalized Machine Learning Framework to Predict the Space-Time Yield of Methanol from Thermocatalytic CO_2 Hydrogenation. *Appl Catal B,* **2022**, *315*, 121530.

(19) Miyazaki, R.; Belthle, K. S.; Tüysüz, H.; Foppa, L.; Scheffler, M. Materials Genes of CO_2 Hydrogenation on Supported Cobalt Catalysts: An Artificial Intelligence Approach Integrating Theoretical and Experimental Data. *J. Am. Chem. Soc.* **2024**, *146*, 5433–5444.

(20) Toyao, T.; Maeno, Z.; Takakusagi, S.; Kamachi, T.; Takigawa, I.; Shimizu, K. I. Machine Learning for Catalysis Informatics: Recent Applications and Prospects. *ACS Catal*., 2020,10, 2260–2297.

(21) McCullough, K.; Williams, T.; Mingle, K.; Jamshidi, P.; Lauterbach, J. High-Throughput Experimentation Meets Artificial Intelligence: A New Pathway to Catalyst Discovery. *Phys. Chem. Chem. Phys.*, **2020**, *20*, 11174–11196.

(22) Ulissi, Z. W.; Medford, A. J.; Bligaard, T.; Nørskov, J. K. To Address Surface Reaction Network Complexity Using Scaling Relations Machine Learning and DFT Calculations. *Nat Commun.* **2017**, *8* , 14621.

(23) Choudhary, K.; DeCost, B.; Chen, C.; Jain, A.; Tavazza, F.; Cohn, R.; Park, C. W.; Choudhary, A.; Agrawal, A.; Billinge, S. J. L.; Holm, E.; Ong, S. P.; Wolverton, C. Recent Advances and Applications of Deep Learning Methods in Materials Science. *npj Comput. Mater*., 2022, 8, 59.

(24) Shields, B. J.; Stevens, J.; Li, J.; Parasram, M.; Damani, F.; Alvarado, J. I. M.; Janey, J. M.; Adams, R. P.; Doyle, A. G. Bayesian Reaction Optimization as a Tool for Chemical Synthesis. *Nature* **2021**, *590*, 89–96.

(25) Butler, K. T.; Davies, D. W.; Cartwright, H.; Isayev, O.; Walsh, A. Machine Learning for Molecular and Materials Science. *Nature*. **2018**, *559*, 547–555.

(26) Suvarna, M.; Pérez-Ramírez, J. Embracing Data Science in Catalysis Research. *Nat. Catal*., **2024**, *7*, 624–635.

(27) Wang, G.; Mine, S.; Chen, D.; Jing, Y.; Ting, K. W.; Yamaguchi, T.; Takao, M.; Maeno, Z.; Takigawa, I.; Matsushita, K.; Shimizu, K. ichi; Toyao, T. Accelerated Discovery of Multi-Elemental Reverse Water-Gas Shift Catalysts Using Extrapolative Machine Learning Approach. *Nat. Commun.* **2023**, *14*, 5861.

(28) Suvarna, M.; Zou, T.; Chong, S. H.; Ge, Y.; Martín, A. J.; Pérez-Ramírez, J. Active Learning Streamlines Development of High-Performance Catalysts for Higher Alcohol Synthesis. *Nat. Commun.* **2024**, *15*, 5844.

(29) Murdock, R. J.; Kauwe, S. K.; Wang, A. Y. T.; Sparks, T. D. Is Domain Knowledge Necessary for Machine Learning Materials Properties? *Integr. Mater. Manuf. Innov.* **2020**, *9*, 221–227.

(30) Kiyohara, S.; Hinuma, Y.; Oba, F. Band Alignment of Oxides by Learnable Structural-Descriptor-Aided Neural Network and Transfer Learning. *J. Am. Chem. Soc.* **2024**, *146*, 9697–9708.

(31) Mine, S.; Takao, M.; Yamaguchi, T.; Toyao, T.; Maeno, Z.; Hakim Siddiki, S. M. A.; Takakusagi, S.; Shimizu, K. ichi; Takigawa, I. Analysis of Updated Literature Data up to 2019 on the Oxidative Coupling of Methane Using an Extrapolative Machine-Learning Method to Identify Novel Catalysts. *ChemCatChem* **2021**, *13*, 3636–3655.

(32) Suzuki, K.; Toyao, T.; Maeno, Z.; Takakusagi, S.; Shimizu, K. ichi; Takigawa, I. Statistical Analysis and Discovery of Heterogeneous Catalysts Based on Machine Learning from Diverse Published Data. *ChemCatChem* **2019**, *11*, 4537–4547.

(33) Guo, C.; Hu, X.; Han, X.; Gao, Y.; Zheng, T.; Chen, D.; Qiu, X.; Wang, P.; Xu, K.; Chen, Y.; Zhou, R.; Zong, M.; Wang, J.; Xia, Z.; Hao, J.; Xie, K. Laser Precise Synthesis of Oxidation-Free High-Entropy Alloy Nanoparticle Libraries. *J. Am. Chem. Soc.* **2024**, *146*, 18407–18417.

(34) Li, H.; Li, X.; Wang, P.; Zhang, Z.; Davey, K.; Shi, J. Q.; Qiao, S. Z. Machine Learning Big Data Set Analysis Reveals C-C Electro-Coupling Mechanism. *J. Am. Chem. Soc.* **2024**., 146, 22850-22858.

(35) Ravel, B.; Newville, M. ATHENA, ARTEMIS, HEPHAESTUS: Data Analysis for X-Ray Absorption Spectroscopy Using IFEFFIT. *J. Synchrotron Radiat.* **2005**, *12*, 537–541.

(36) Geurts, P.; Ernst, D.; Wehenkel, L. Extremely Randomized Trees. *Mach. Learn.* **2006**, *63*, 3–42.

(37) Pedregosa FABIANPEDREGOSA, F.; Michel, V.; Grisel OLIVIERGRISEL, O.; Blondel, M.; Prettenhofer, P.; Weiss, R.; Vanderplas, J.; Cournapeau, D.; Pedregosa, F.; Varoquaux, G.; Gramfort, A.; Thirion, B.; Grisel, O.; Dubourg, V.; Passos, A.; Brucher, M.; Perrot andÉdouardand, M.; Duchesnay, andÉdouard; Duchesnay EDOUARDDUCHESNAY, Fré. *Scikit-Learn: Machine Learning in Python Gaël Varoquaux Bertrand Thirion Vincent Dubourg Alexandre Passos*. *J. Mach. Learn. Res.,* **2011**, 12, 2825-2830.

(38) Varoquaux, G.; Raamana, P. R.; Engemann, D. A.; Hoyos-Idrobo, A.; Schwartz, Y.; Thirion, B. Assessing and Tuning Brain Decoders: Cross-Validation, Caveats, and Guidelines. *Neuroimage* **2017**, *145*, 166–179.

(39) Roberts, D. R.; Bahn, V.; Ciuti, S.; Boyce, M. S.; Elith, J.; Guillera-Arroita, G.; Hauenstein, S.; Lahoz-Monfort, J. J.; Schröder, B.; Thuiller, W.; Warton, D. I.; Wintle, B. A.; Hartig, F.; Dormann, C. F. Cross-Validation Strategies for Data with Temporal, Spatial, Hierarchical, or Phylogenetic Structure. *Ecography*. **2017**, *40*, 913–929.

(40) Djeradi, S.; Dahame, T.; Fadla, M. A.; Bentria, B.; Kanoun, M. B.; Goumri-Said, S. High-Throughput Ensemble-Learning-Driven Band Gap Prediction of Double Perovskites Solar Cells Absorber. *Mach. Learn. Knowl. Extr.* **2024**, *6*, 435–447.

(41) Wang, A. Y. T.; Kauwe, S. K.; Murdock, R. J.; Sparks, T. D. Compositionally Restricted Attention-Based Network for Materials Property Predictions. *NPJ Comput. Mater.* **2021**, *7*, 77.

(42) Jones, D. R.; Schonlau, M.; Welch, W. J. *Efficient Global Optimization of Expensive Black-Box Functions*; *J. Glob. Optim*., **1998**, *13*, 455-492.

(43) Zhan, D.; Xing, H. Expected Improvement for Expensive Optimization: A Review. *J. Glob. Optim*., **2020**, *78*, 507–544.

(44) Du, P.; Ait El Fakir, A.; Zhao, S.; Dostagir, N. H. M.; Pan, H.; Ting, K. W.; Mine, S.; Qian, Y.; Shimizu, K.; Toyao, T. Ethanol Synthesis via Catalytic CO_2 Hydrogenation over Multi-Elemental KFeCuZn/ZrO_2 Catalyst. *Chem. Sci.* **2024**, 15, 15925-15934.

(45) Suvarna, M.; Preikschas, P.; Perez-Ramirez, J. Identifying Descriptors for Promoted Rhodium-Based Catalysts for Higher Alcohol Synthesis via Machine Learning. *ACS Catal.* **2022**, *12*, 15373–15385.

(46) Shanmugavalli, M.; Ignatia, K. M. J. Comparative Study among MAPE, RMSE and R Square Over the Treatment Techniques Undergone for PCOS Influenced Women. *Recent Pat. Eng.* **2023**, *19*, 8.

(47) Bartlett, P. L.; Long, P. M.; Lugosi, G.; Tsigler, A. Benign Overfitting in Linear Regression. *PNAS*, **2019**, *117*, 30663-30070.

(48) Belkin, M.; Hsu, D.; Mitra, P. Overfitting or Perfect Fitting? Risk Bounds for Classification and Regression Rules That Interpolate. **2018**. 1806.05161.

(49) Wang, C.; Fang, W.; Liu, Z.; Wang, L.; Liao, Z.; Yang, Y.; Li, H.; Liu, L.; Zhou, H.; Qin, X.; Xu, S.; Chu, X.; Wang, Y.; Zheng, A.; Xiao, F. S. Fischer–Tropsch Synthesis to Olefins Boosted by MFI Zeolite Nanosheets. *Nat. Nanotechnol.* **2022**, *17*, 714–720.

(50) Lohitharn, N.; Goodwin, J. G.; Lotero, E. Fe-Based Fischer-Tropsch Synthesis Catalysts Containing Carbide-Forming Transition Metal Promoters. *J. Catal.* **2008**, *255*, 104–113.

(51) Xu, D.; Ding, M.; Hong, X.; Liu, G. Mechanistic Aspects of the Role of K Promotion on Cu−Fe-Based Catalysts for Higher Alcohol Synthesis from CO_2 Hydrogenation. *ACS Catal.* **2020**, *10*, 14516–14526.

(52) Xi, X.; Zeng, F.; Zhang, H.; Wu, X.; Ren, J.; Bisswanger, T.; Stampfer, C.; Hofmann, J. P.; Palkovits, R.; Heeres, H. J. CO_2 Hydrogenation to Higher Alcohols over K-Promoted Bimetallic Fe−In Catalysts on a Ce−ZrO_2 Support. *ACS Sustain. Chem. Eng.* **2021**, *9*, 6235–6249.

(53) Zhang, S.; Wu, Z.; Liu, X.; Shao, Z.; Xia, L.; Zhong, L.; Wang, H.; Sun, Y. Tuning the Interaction between Na and Co_2C to Promote Selective CO_2 Hydrogenation to Ethanol. *Appl. Catal., B* **2021**, *293*, 120207.

(54) Xu, D.; Ding, M.; Hong, X.; Liu, G.; Tsang, S. C. E. Selective C_{2+} Alcohol Synthesis from Direct CO_2 Hydrogenation over a Cs-Promoted Cu-Fe-Zn Catalyst. *ACS Catal.* **2020**, *10*, 5250–5260.

(55) Wang, Y.; Wang, W.; He, R.; Li, M.; Zhang, J.; Cao, F.; Liu, J.; Lin, S.; Gao, X.; Yang, G.; Wang, M.; Xing, T.; Liu, T.; Liu, Q.; Hu, H.; Tsubaki, N.; Wu, M. Carbon-Based Electron Buffer Layer on ZnO_x-Fe_5C_2-Fe3O_4 Boosts Ethanol Synthesis from CO_2 Hydrogenation. *Angew. Chem., Int. Ed.* **2023**, *62*, e20231178.

(56) Takagawa, M.; Okamoto, A.; Fujimura, H.; Izawa, Y.; Arakawa, H. Ethanol Synthesis from Carbon Dioxide and Hydrogen. *Stud. Surf. Sci. Catal.* **1998**, *114*, 525–528.

(57) Goryachev, A.; Pustovarenko, A.; Shterk, G.; Alhajri, N. S.; Jamal, A.; Albuali, M.; van Koppen, L.; Khan, I. S.; Russkikh, A.; Ramirez, A.; Shoinkhorova, T.; Hensen, E. J. M.; Gascon, J. A Multi-Parametric Catalyst Screening for CO_2 Hydrogenation to Ethanol. *ChemCatChem* **2021**, *13*, 3324–3332.

(58) Yang, C.; Mu, R.; Wang, G.; Song, J.; Tian, H.; Zhao, Z. J.; Gong, J. Hydroxyl-Mediated Ethanol Selectivity of CO_2 Hydrogenation. *Chem. Sci.,* **2019**, *10*, 3161–3167.

(59) An, K.; Zhang, S.; Wang, J.; Liu, Q.; Zhang, Z.; Liu, Y. A Highly Selective Catalyst of Co/$La_4Ga_2O_9$ for CO_2 Hydrogenation to Ethanol. *J. Energy Chem.* **2021**, *56*, 486–495.

(60) Caparrós, F. J.; Soler, L.; Rossell, M. D.; Angurell, I.; Piccolo, L.; Rossell, O.; Llorca, J. Remarkable Carbon Dioxide Hydrogenation to Ethanol on a Palladium/Iron Oxide Single-Atom Catalyst. *ChemCatChem* **2018**, *10*, 2365–2369.

(61) Lou, Y.; jiang, F.; Zhu, W.; Wang, L.; Yao, T.; Wang, S.; Yang, B.; Yang, B.; Zhu, Y.; Liu, X. CeO_2 Supported Pd Dimers Boosting CO_2 Hydrogenation to Ethanol. *Appl. Catal., B* **2021**, *291*, 120122.

(62) Zhang, F.; Zhou, W.; Xiong, X.; Wang, Y.; Cheng, K.; Kang, J.; Zhang, Q.; Wang, Y. Selective Hydrogenation of CO_2 to Ethanol over Sodium-Modified Rhodium Nanoparticles Embedded in Zeolite Silicalite-1. *J. Phys. Chem. C* **2021**, *125*, 24429–24439.

(63) Wang, Y.; Wang, K.; Zhang, B.; Peng, X.; Gao, X.; Yang, G.; Hu, H.; Wu, M.; Tsubaki, N. Direct Conversion of CO_2 to Ethanol Boosted by Intimacy-Sensitive Multifunctional Catalysts. *ACS Catal.* **2021**, *11*, 11742–11753.

(64) Kusama, H.; Okabe, K.; Sayama, K.; Arakawa, H. CO_2 Hydrogenation to Ethanol over Promoted Rh/SiO_2 Catalysts. *Catal. Today* **1996**, *28*, 261–266.

(65) Liu, S.; Zhou, H.; Zhang, L.; Ma, Z.; Wang, Y. Activated Carbon-Supported Mo-Co-K Sulfide Catalysts for Synthesizing Higher Alcohols from CO_2. *Chem. Eng. Technol.* **2019**, *42*, 962–970.

(66) Yao, R.; Wei, J.; Ge, Q.; Xu, J.; Han, Y.; Ma, Q.; Xu, H.; Sun, J. Monometallic Iron Catalysts with Synergistic Na and S for Higher Alcohols Synthesis via CO_2 Hydrogenation. *Appl. Catal., B* **2021**, *298*, 120556.

(67) da Silva, A. H. M.; Vieira, L. H.; Santanta, C. S.; Koper, M. T. M.; Assaf, E. M.; Assaf, J. M.; Gomes, J. F. Ethanol Formation from CO_2 Hydrogenation at Atmospheric Pressure Using Cu Catalysts: Water as a Key Component. *Appl. Catal., B* **2023**, *324*, 122221.

(68) Chen, J.; Zha, Y.; Liu, B.; Li, Y.; Xu, Y.; Liu, X. Rationally Designed Water Enriched Nano Reactor for Stable CO_2 Hydrogenation with Near 100% Ethanol Selectivity over Diatomic Palladium Active Sites. *ACS Catal.* **2023**, *13*, 7110–7121.

(69) Zhang, S.; Huang, C.; Shao, Z.; Zhou, H.; Chen, J.; Li, L.; Lu, J.; Liu, X.; Luo, H.; Xia, L.; Wang, H.; Sun, Y. Revealing and Regulating the Complex Reaction Mechanism of CO_2 Hydrogenation to Higher Alcohols on Multifunctional Tandem Catalysts. *ACS Catal.* **2023**, *13*, 3055–3065.

(70) Wang, Y.; Zhou, Y.; Zhang, X.; Wang, M.; Liu, T.; Wei, J.; Zhang, G.; Hong, X.; Liu, G. PdFe Alloy-Fe_5C_2 Interfaces for Efficient CO_2 Hydrogenation to Higher Alcohols. *Appl. Catal., B* **2024**, *345*, 123691.

(71) Li, S.; Guo, H.; Luo, C.; Zhang, H.; Xiong, L.; Chen, X.; Ma, L. Effect of Iron Promoter on Structure and Performance of K/Cu-Zn Catalyst for Higher Alcohols Synthesis from CO_2 Hydrogenation. *Catal. Lett.* **2013**, *143*, 345–355.

(72) Yang, C.; Liu, S.; Wang, Y.; Song, J.; Wang, G.; Wang, S.; Zhao, Z.; Mu, R.; Gong, J. The Interplay between Structure and Product Selectivity of CO_2 Hydrogenation . *Angew. Chem., Int. Ed.* **2019**, *131*, 11364–11369.

(73) Wang, G.; Luo, R.; Yang, C.; Song, J.; Xiong, C.; Tian, H.; Zhao, Z. J.; Mu, R.; Gong, J. Active Sites in CO_2 Hydrogenation over Confined VO_x-Rh Catalysts. *Sci. China: Chem.* **2019**, *62*, 1710–1719.

(74) Ding, L.; Shi, T.; Gu, J.; Cui, Y.; Zhang, Z.; Yang, C.; Chen, T.; Lin, M.; Wang, P.; Xue, N.; Peng, L.; Guo, X.; Zhu, Y.; Chen, Z.; Ding, W. CO_2 Hydrogenation to Ethanol over Cu@Na-Beta. *Chem* **2020**, *6*, 2673–2689.

(75) Gnanamani, M. K.; Hamdeh, H. H.; Jacobs, G.; Shafer, W. D.; Hopps, S. D.; Thomas, G. A.; Davis, B. H. Hydrogenation of Carbon Dioxide over K-Promoted FeCo Bimetallic Catalysts Prepared from Mixed Metal Oxalates. *ChemCatChem* **2017**, *9*, 1303–1312.

(76) Guo, H.; Li, S.; Peng, F.; Zhang, H.; Xiong, L.; Huang, C.; Wang, C.; Chen, X. Roles Investigation of Promoters in K/Cu-Zn Catalyst and Higher Alcohols Synthesis from CO_2 Hydrogenation over a Novel Two-Stage Bed Catalyst Combination System. *Chem. Lett.* **2015**, *145*, 620–630.

(77) Nieskens, D. L. S.; Ferrari, D.; Liu, Y.; Kolonko, R. The Conversion of Carbon Dioxide and Hydrogen into Methanol and Higher Alcohols. *Catal. Commun.* **2011**, *14*, 111–113.

(78) Zhang, Q.; Wang, S.; Shi, X.; Dong, M.; Chen, J.; Zhang, J.; Wang, J.; Fan, W. Conversion of CO_2 to Higher Alcohols on K-CuZnAl/Zr-CuFe Composite. *Appl. Catal., B* **2024**, *346*, 123748.

(79) Gogate, M. R.; Davis, R. J. Comparative Study of CO and CO_2 Hydrogenation over Supported Rh-Fe Catalysts. *Catal. Commun.* **2010**, *11*, 901–906.

(80) Kusama, H.; Okabe, K.; Sayama, K.; Arakawa, H. Ethanol synthesis by catalytic hydrogenation of CO_2 over Rh-Fe/SiO_2 catalysts. *energy* **1997**, *22*, 343–348.

(81) Kishida, M.; Yamada, K.; Nagata, H.; Wakabayashi, K. CO_2 Hydrogenation for C_{2+} Alcohols Synthesis over Silica-Supported Ir-Mo Catalysts. *Chem. Lett.* **1994**, 555–556.

(82) Kusama, H.; Okabe, K.; Sayama, K.; Arakawa, H. Rhodium Catalysts Promoted by Cerium Oxide in the CO_2 Hydrogenation to Ethanol. *J. Jpn. Pet. Inst.* **1999**, *42*, 178–179.

(83) Kitamura Bando, K.; Soga, K.; Kunimori, K.; Arakawa, H. Effect of Li Additive on CO_2 Hydrogenation Reactivity of Zeolite Supported Rh Catalysts. *Appl. Catal., A* **1998**, *175*, 67–81.

(84) Calafat, A.; Âtima Vivas, F.; Ân, J.; Brito, L.; San, C.; Âbal, E. T.; Âchira, V. Effects of Phase Composition and of Potassium Promotion on Cobalt Molybdate Catalysts for the Synthesis of Alcohols from CO_2 and H_2. *Appl. Catal., A* **1998**, *172*, 217–224.

(85) Xu, W.; Ramirez, P. J.; Stacchiola, D.; Rodriguez, J. A. Synthesis of α-MoC_{1-x} and β-MoC_y Catalysts for CO_2 Hydrogenation by Thermal Carburization of Mo-Oxide in Hydrocarbon and Hydrogen Mixtures. *Chem. Lett.* **2014**, *144*, 1418–1424.

(86) Ouyang, B.; Xiong, S.; Zhang, Y.; Liu, B.; Li, J. The Study of Morphology Effect of Pt/Co_3O_4 Catalysts for Higher Alcohol Synthesis from CO_2 Hydrogenation. *Appl. Catal., A* **2017**, *543*, 189–195.

(87) Goud, D.; Churipard, S. R.; Bagchi, D.; Singh, A. K.; Riyaz, M.; Vinod, C. P.; Peter, S. C. Strain-Enhanced Phase Transformation of Iron Oxide for Higher Alcohol Production from CO_2. *ACS Catal.* **2022**, *12*, 11118–11128.

(88) Wang, Y.; Xu, D.; Zhang, X.; Hong, X.; Liu, G. Selective C_{2+} Alcohol Synthesis by CO_2 Hydrogenation via a Reaction-Coupling Strategy. *Catal. Sci. Technol.* **2022**, *12*, 1539–1550.

(89) Esterhuizen, J. A.; Goldsmith, B. R.; Linic, S. Interpretable Machine Learning for Knowledge Generation in Heterogeneous Catalysis. *Nat. Catal.*, **2022**, *5*, 175–184.

(90) Mangalathu, S.; Hwang, S. H.; Jeon, J. S. Failure Mode and Effects Analysis of RC Members Based on Machine-Learning-Based SHapley Additive ExPlanations (SHAP) Approach. *Eng. Struct.* **2020**, *219*, 110927.

(91) Nohara, Y.; Matsumoto, K.; Soejima, H.; Nakashima, N. Explanation of Machine Learning Models Using Shapley Additive Explanation and Application for Real Data in Hospital. *Comput. Methods Programs Biomed* **2022**, *214*, 106584.

(92) Reddy, C. V.; Babu, B.; Reddy, I. N.; Shim, J. Synthesis and Characterization of Pure Tetragonal ZrO_2 Nanoparticles with Enhanced Photocatalytic Activity. *Ceram. Int.* **2018**, *44*, 6940–6948.

(93) Liu, T.; Xu, D.; Song, M.; Hong, X.; Liu, G. K-ZrO_2 Interfaces Boost CO_2 Hydrogenation to Higher Alcohols. *ACS Catal.* **2023**, *13*, 4667–4674.

(94) Kvashnina, K. Electronic Structure Interpretation: How Much Do We Understand the Ce L3 XANES? *Chem. Eur. J.* **2024**., 30, e202400755.

(95) Wilson, D.; Langell, M. A. XPS Analysis of Oleylamine/Oleic Acid Capped Fe_3O_4 Nanoparticles as a Function of Temperature. *Appl. Surf. Sci.* **2014**, *303*, 6–13.

(96) Phongprueksathat, N.; Ting, K. W.; Mine, S.; Jing, Y.; Toyoshima, R.; Kondoh, H.; Shimizu, K. I.; Toyao, T.; Urakawa, A. Bifunctionality of Re Supported on TiO_2 in Driving Methanol Formation in Low-Temperature CO_2 Hydrogenation. *ACS Catal.* **2023**, *13*, 10734–10750.

(97) Greiner, M. T.; Rocha, T. C. R.; Johnson, B.; Klyushin, A.; Knop-Gericke, A.; Schlögl, R. The Oxidation of Rhenium and Identification of Rhenium Oxides during Catalytic Partial Oxidation of Ethylene: An in-Situ Xps Study. *Z. Phys. Chem.* **2014**, *228*, 521–541.

(98) Luo, J.; Liang, C. Rhenium in Heterogeneous Catalysis: A Rising Star for Hydrogenation Reactions. *ACS Catal.,* **2024**, *14*, 7032–7049.

(99) Galmiz, O.; Stupavska, M.; Wulff, H.; Kersten, H.; Brablec, A.; Cernak, M. Deposition of Zn-Containing Films Using Atmospheric Pressure Plasma Jet. *Open Chem.* **2015**, *13*, 198–203.

(100) Tzompantzi, F.; Castillo-Rodríguez, J. C.; Tzompantzi-Flores, C.; Pérez-Hernández, R.; Gómez, R.; Santolalla-Vargas, C. E.; Che-Galicia, G.; Ramos-Ramírez, E. Addition of SnO_2 over an Oxygen Deficient Zirconium Oxide (Zr_xO_y) and Its Catalytic Evaluation for the Photodegradation of Phenol in Water. *Catal. Today* **2022**, *394–396*, 376–389.

(101) Sun, P.; Bai, J.; He, J.; Yang, M.; Su, J.; Ji, Y.; Liu, H. Properties of the YbF_3 Films Prepared by Ion-Assisted Deposition. *Coatings* **2022**, *12*, 1693.

(102) Ohno, Y. XPS Studies of the Intermediate Valence State of Yb in $(YbS)_{1.25}CrS_2$. *J. Electron Spectros. Relat. Phenomena.* **2008**, *165*, 1–4.

(103) Mohtar, M.; Omar, R. The effect of K_2CO_3 treatment on self-adhesive carbon grain prepared from oil palm empty fruit bunch. *Solid State Sci. Technol.* **2005**, *13*, 24–31.

(104) Dostagir, N. H. M.; Rattanawan, R.; Gao, M.; Ota, J.; Hasegawa, J. Y.; Asakura, K.; Fukouka, A.; Shrotri, A. Co Single Atoms in ZrO_2 with Inherent Oxygen Vacancies for Selective Hydrogenation of CO_2 to CO. *ACS Catal.* **2021**, *11*, 9450–9461.

(105) Chang, X.; Han, X.; Pan, Y.; Hao, Z.; Chen, J.; Li, M.; Lv, J.; Ma, X. Insight into the Role of Cu-ZrO_2 Interaction in Methanol Synthesis from CO_2 Hydrogenation. *Ind. Eng. Chem. Res.* **2022**, *61*, 6872–6883.

(106) Ishida, T.; Yanagihara, T.; Liu, X.; Ohashi, H.; Hamasaki, A.; Honma, T.; Oji, H.; Yokoyama, T.; Tokunaga, M. Synthesis of Higher Alcohols by Fischer-Tropsch Synthesis over Alkali Metal-Modified Cobalt Catalysts. *Appl. Catal., A* **2013**, *458*, 145–154.

(107) Nlemantsverdrlet, J. W.; Van Der Kraan, A. M.; Van Dljk, W. Il; Van Der Baan, H. S. *Behavior of Metallic Iron Catalysts during Fischer-Tropsch Synthesis Studied with Mtissbauer Spectroscopy, X-Ray Diffraction, Carbon Content Determination, and Reaction Kinetic Measurements. Phys. Chem.* **1980,** *84, 3363–3370*

(108) De Smit, E.; Weckhuysen, B. M. The Renaissance of Iron-Based Fischer-Tropsch Synthesis: On the Multifaceted Catalyst Deactivation Behaviour. *Chem. Soc. Rev.* **2008**, *37* (12), 2758–2781.

(109) Ro, I.; Liu, Y.; Ball, M. R.; Jackson, D. H. K.; Chada, J. P.; Sener, C.; Kuech, T. F.; Madon, R. J.; Huber, G. W.; Dumesic, J. A. Role of the Cu-ZrO_2 Interfacial Sites for Conversion of Ethanol to Ethyl Acetate and Synthesis of Methanol from CO_2 and H_2. *ACS Catal.* **2016**, *6*, 7040–7050.

Chapter 4

Direct Syngas-to-Ethanol Conversion over Lithium-Promoted Rh/MgO Catalysts

4.1 Introduction

The ever-increasing demand for crude oil has caused a notable reduction in oil reserves worldwide. Recently, to reduce the dependency on oil, considerable attention has been directed towards the efficient use of coal, natural gas, shale gas, and biomass. Syngas ($CO+H_2$), derived from diverse sources such as natural gas, carbon dioxide, biomass, coal, and carbon-rich waste materials, is a viable precursor for high-value products.[1–11] Consequently, the direct synthesis of higher oxygenates (C_{2+} oxy) from syngas has significant potential for converting methane, biomass, organic waste, and coal into clean, high-value chemicals and liquid transportation fuels.[6–9] Supported catalysts play an important role in this field, particularly in higher alcohol (HA) synthesis.[12–21] The pronounced interaction between nanomaterials and support materials has been extensively investigated to elucidate the structure–activity relationship in oxide-supported metal catalysts.[5,6,19,22–25] Notably, noble metals exhibit a remarkable synergy with metal oxide supports, modulating CO and H_2 adsorption and activation at elevated reaction temperatures. The supported Rh catalysts exhibit notable activity and selectivity for ethanol and HA production than alternative syngas conversion catalysts.[26–36]

The choice of catalyst support and the introduction of various promoters to Rh catalysts are critically important for achieving high ethanol and hydrocarbon (HC) yields. Among the various promoter elements explored, alkali metals were found to be effective in enhancing both the conversion of CO and the ethanol selectivity of Rh catalysts.[26–28] Alkali metals stabilise partially oxidised Rh clusters and modulate the dispersion and electronic structure of Rh nanoparticles, thereby serving as electronic and structural promoters to fine-tune the catalytic performance.[37,38] Alkali metals can prevent the hydrogenation of CH_x* and alkylation reactions, thereby reducing CH_4 and CH_3OH formation, and increasing the formation of C_{2+} oxygenates.[39,40] The ability of Rh catalysts to catalyse CO dissociation, insertion, and hydrogenation is affected not only by the presence of an alkali promoter but also by the support materials.[41] The variation in the support materials indicates that the selectivity of the products in CO hydrogenation can be significantly altered,[22,41] with surface hydroxyl groups also playing a crucial role in the synthesis of C_{2+} oxygenates over Rh-based catalysts.[42,43] Many studies have focused on SiO_2 and TiO_2 supports and concluded that their high surface area, pronounced porosity, and excellent stability collectively contribute to enhanced selectivity towards C_{2+} oxygenates.[36,44–46] Additionally, γ-Al_2O_3 has been recognized as an effective support for transition metal catalysts for the conversion of both CO and CO_2 to C_{2+}

oxygenates, owing to its high porosity and specific surface area that facilitate optimal dispersion of metal particles.[25,47] Furthermore, supports such as ZrO_2[48,49] and CeO_2[50] have been reported for their catalytic properties in similar applications.

This study focused on the use of MgO as an unconventional support for Rh nanoparticles in the hydrogenation of CO to EtOH. We demonstrate that the introduction of the Li promoter has an impact on the surface structure and enhances the catalytic activity and ethanol production over MgO-supported Rh catalysts. Through comparative analyses with established catalysts, this study aims to explain the mechanistic disparities underlying the superior performance of the $Rh/Li_2O/MgO$ catalysts. Notably, $Rh/LiO_x/MgO$ catalysts exhibit exceptional space time yield (STY) for ethanol in direct syngas conversion (STY_{EtOH}: 12.2 mmol g_{cat}^{-1} h^{-1}). The comprehensive experimental investigations, including *in situ/operando* spectroscopic techniques complemented by density functional theory (DFT) calculations, provided insights into the active sites and reaction mechanisms of our catalyst.

4.2 Experimental details

4.2.1 Chemicals and catalyst preparation

All chemicals and materials were obtained from commercial suppliers and used as received without additional purification. MgO was supplied by Ube Materials Industries, Ltd. TiO_2 (P25) was obtained from Evonik (Denmark). SiO_2 (CARiACT Q-10) was purchased from Fuji Silysia Chemical Company Ltd. γ-Al_2O_3 (Puralox) was obtained from Sasol. Rh and Li were loaded using a sequential impregnation method. An aqueous solution (30 mL) of $LiNO_3$ (>99.5%, Wako Pure Chemical Industries) and 0.97 g of support were added to a 100 mL glass vessel. The slurry was then stirred before evaporating to dryness at 50 °C. After drying at 90 °C for 12 h, the material was calcined at 500 °C for 3 h to obtain Li/support (Li_2O/MgO, Li_2O/TiO_2, Li_2O/AL_2O_3, Li_2O/SiO_2). A 0.98 g portion of Li_2O/support and 0.4 mL of aqueous solution of $Rh(NO_3)_3$ (50 g/L, Furuya Metal Co., Ltd.) was added to a glass vessel (100 mL) containing 30 mL of deionized water, and the slurry was then stirred before being evaporated to dryness at 50 °C. Afterward, it was dried at 110 °C for 12 h to obtain the supported Rh/Li catalysts denoted as $Rh_2O_3/Li_2O/MgO$, $Rh_2O_3/Li_2O/TiO_2$, $Rh_2O_3/Li_2O/Al_2O_3$, $Rh_2O_3/Li_2O/SiO_2$, respectively. The Rh loading was 2 wt%.

4.2.2 Characterization

X-ray diffraction (XRD) analysis was conducted on a Miniflex (Rigaku) diffractometer using Cu Kα radiation. High-angle annular dark-field scanning transmission electron microscopy (HAADF-STEM) and energy-dispersive X-ray spectroscopy (EDX) were performed using a FEI Titan G2 microscope. The samples were prepared by dropping an ethanol solution containing the catalyst onto carbon-supported Cu grids.

Temperature-programmed reduction with H_2 (H_2-TPR) was performed using a BELCAT II instrument equipped with a Thermal Conductivity detector (TCD). Briefly, ~100 mg of the catalyst was placed into a quartz tube and purged with Ar at 200 °C (2 h) to remove physically adsorbed water and surface carbonates. Then, the sample was cooled to 50 °C, subsequently heated to 800 °C under 10 vol% H_2 balanced with Ar (10 °C/min).

Rhodium K-edge X-ray Absorption Spectroscopy (XAS) experiments were conducted in transmission mode at the BL01B1 beamline of SPring-8 housed within the Japan Synchrotron Radiation Research Institute (JASRI) under Proposal No. 2023A1931/2023B2096. A Si (311) double-crystal monochromator was used for the experiments. The spectra of reference compounds were acquired at room temperature under atmospheric conditions. The obtained XAS spectra were analysed using Athena and Artemis software, version 0.9.26, both integrated within the Demeter package.[51]

For Rh *K*-edge *in situ* X-ray absorption near-edge structure (XANES) investigations, the catalyst samples in pellet form (diameter: 7 mm) were inserted into a cell equipped with Kapton film windows and gas lines connected to a micro-gas chromatograph (GC). These measurements were performed in transmission mode. The Rh foil spectra were collected simultaneously for energy calibration. In a typical experiment, initial X-ray absorption fine structure (XAFS) scans were conducted using the catalyst at room temperature under He flow. Following H_2 reduction (100 mL/min) at 360 °C for a duration of 30 minutes, XANES spectra were acquired. The gas feed was then transitioned to He (300 mL/min), CO (100 mL/min), and CO (33.3 mL/min) + H_2 (66.7 mL/min), in succession, while maintaining a temperature of 360 °C.

Operando diffuse reflectance infrared Fourier transform (DRIFT) spectra were recorded on a JASCO FT/IR-4600 instrument equipped with a mercury cadmium telluride (MCT) detector. The sample was pressed into a DRIFT cell (DR-650 Ci) using a CaF_2 window. Spectra were measured by accumulating 20 scans at a resolution of 8 cm^{-1}, 5 bar and

temperature range of 200-320 °C. The reference spectrum in He flow (20 scans) taken at the measurement temperature was subtracted from each spectrum. A high-sampling-rate TCD GC (490 Micro GC; Agilent Technologies Inc.) was installed at the outlet for the analysis of methanol and ethanol.

The Fourier-transform infrared spectroscopy (FTIR) spectra of the adsorbed CO were obtained using a JASCO FTIR-4600 spectrometer with an MCT detector in transmission mode (resolution 4 cm^{-1}). The catalyst (70 mg) was pressed into a pellet (φ: 20 mm) set in a quartz cell equipped with CaF_2 windows and a Dewar vessel. The catalyst was purged with He for a few minutes, and then the feed gas was switched to H_2 (20 mL/min) for reduction at 360 °C for 30 min. Next, the gas was switched back to He, and the sample was cooled to −20 °C via the mixture of liquid nitrogen and ethanol. The background spectrum was taken at −20 °C. The samples were exposed to 10% CO/He (15 mL/min) at 1 bar. Thereafter, He (50 mL/min) was introduced to purge CO in the gas phase, which was physisorbed onto the catalyst.

4.2.3 Catalytic reaction

CO hydrogenation reactions were performed in a fixed-bed continuous-flow reactor operating at a total pressure of 3 MPa. The reactor received a gas mixture comprising H_2/CO/Ar at a ratio of 66.1/33.1/0.8, with argon (Ar) serving as an internal standard gas. Prior to initiating the catalytic measurements, 70 mg of the catalyst was positioned between quartz wool within a 1/4 inch fixed-bed reactor (inner diameter: 2.79 mm). The catalyst underwent pretreatment under ambient pressure conditions with a flow of 99% H_2/Ar at a rate of 20 mL/min and a temperature of 360 °C for 0.5 h. After pretreatment, a gas flow (total flow rate: 30 mL/min) comprising H_2/CO/Ar (66.1/33.1/0.8) was passed through the catalyst bed at a pressure of 30 bar and a space velocity (SV) of 25 L/g_{cat}/h. It is noteworthy that an aging treatment was conducted for 12 h at 360 °C under the reaction atmosphere, serving as an accelerated aging test, preceding the recording of catalytic reaction results (as illustrated in **Figure 4. 1**). Product analysis was performed utilising an online gas chromatograph (Shimadzu GC-2014) equipped with Thermal Conductivity (TCD) and Flame Ionisation (FID) detectors, within a reaction temperature range of 240-360 °C.

The CO conversion (X_{CO}) was calculated as equation:

$$X_{CO} = \frac{\frac{c_{CO}^{in}}{c_{Ar}^{in}} - \frac{c_{CO}^{out}}{c_{Ar}^{out}}}{\frac{c_{CO}^{in}}{c_{Ar}^{in}}} \times 100\%$$

The selectivity (S_i) for individual products was calculated by the following equation:

$$S_i = \frac{c_i \times n_i}{\sum(c_i \times n_i)} \times 100\%$$

Here, c_i is the molar fraction of product *i* (CO_2, hydrocarbons, or oxygenates), and n_i is the carbon number of product *i* in the reaction.

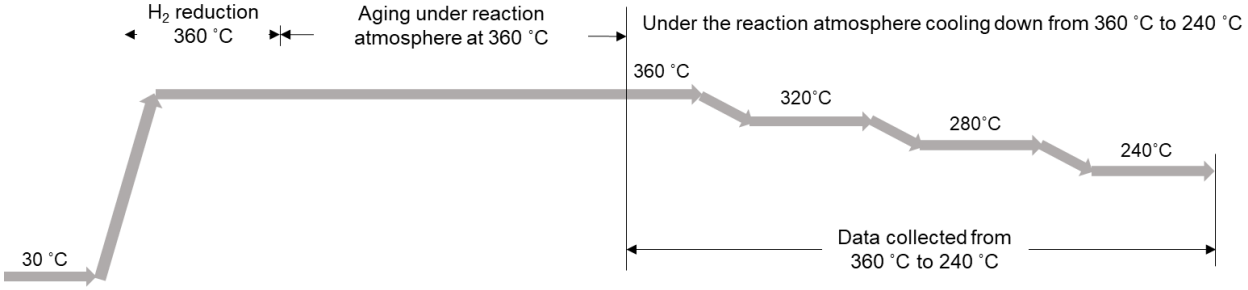

Figure 4. 1. Typical experimental procedure for catalytic tests. After conducting H_2 reduction pre-treatment at 360 °C for 30 min, the accelerated aging treatment was performed at 360 °C in the reaction gas atmosphere after introducing CO (CO:H_2 = 1:2, 3 MPa, 12 h). The catalytic performance at temperatures ranging from 360 °C to 240 °C was then recorded (CO:H_2 = 1:2 at 3 MPa).

4.2.4 DFT Calculations

The Vienna Ab Initio Simulation Package (VASP, version 5.4.4) was used to perform the periodic DFT calculations.[52,53] The Perdew–Burke–Ernzerhof functional revised for solids (PBEsol) was employed in combination with the projector-augmented wave method.[54,55] A kinetic energy cutoff of 400 eV was used for plane-wave basis sets. Gaussian smearing (width: 0.2 eV was applied to occupy the electronic level. The k-point mesh included only the gamma point of the Brillouin zone (1 × 1 × 1). The van der Waals interactions are described using a dispersion-corrected DFT-D3 (BJ) function.[56] The convergence of the force on each atom was set to 0.03 eV $Å^{-1}$.

The MgO (100) surface was simulated using supercell slab models (**Figure 4. 2a**).[57] The repeated slabs along the surface-normal direction were separated by a minimum vacuum region thickness of 15 ° (lattice parameters for the surface: a = 16.78 Å, b = 16.78 Å). The two bottom layers are fixed at their original bulk positions. One layer of Li_2O(111) was

attached to the MgO(100) surface to model the Li_2O(111)/MgO(100) surface (**Figure 4. 2b**). Given that the Brunauer-Emmett-Teller (BET) specific surface area of the MgO support used in this study was 50 m^2/g and the Li loading was 3 wt%, if Li_2O uniformly covered the surface of the MgO support, it formed a monolayer. Based on this, we modelled the Li_2O(111)/MgO (100) surface. To simulate Rh nanoparticles on the supports, a Rh_{13} cluster was employed. This Rh_{13} cluster was placed on a pristine MgO (100) surface (Rh_{13}/MgO(100)) as well as on Li_2O(111)/MgO(100) (Rh_{13}/ Li_2O(111)/MgO(100)), as shown in **Figure 4. 3**.

The adsorption energy (E_{ads}) of a CO molecule on a surface is defined as

$$E_{ads} = E_{A/S} - E_A - E_S$$

where $E_{A/S}$, E_A, and E_S are the electronic energies of the adsorption complex, free-state adsorbate, and the bare metal oxide surface, respectively.

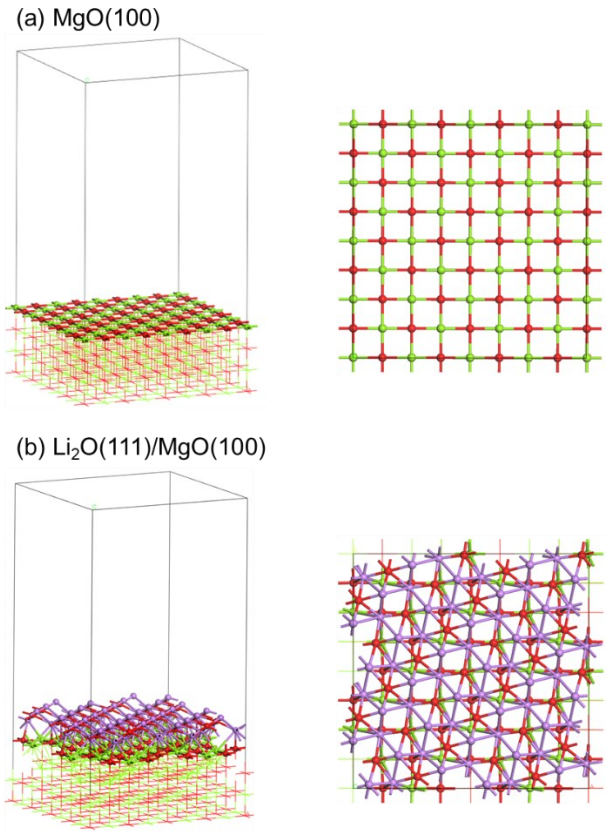

Figure 4. 2. Slab models are used for DFT calculations of the MgO (100) (a) and Li_2O (111)/MgO (100) (b) surfaces. Li, Mg, and O atoms are shown as dark green, purple, light green, and red, respectively.

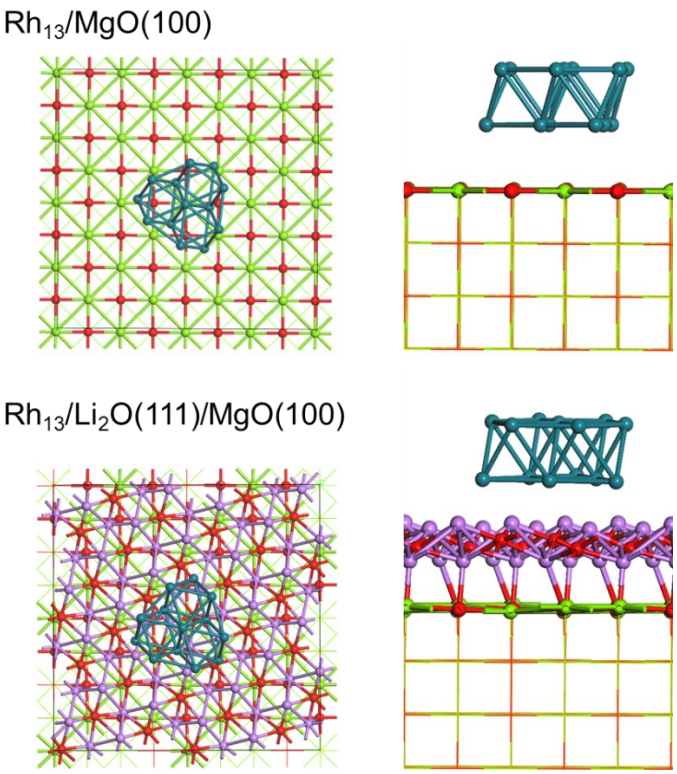

Figure 4. 3. Slab models are used for DFT calculations of the Rh_{13}/MgO(100) and Rh_{13}/Li_2O(111)/MgO(100) surfaces. Rh, Li, Mg, and O atoms are shown as dark green, purple, light green, and red.

4.3 Results and discussion

4.3.1 Catalytic CO hydrogenation to EtOH

The catalytic activities of different Rh-based catalysts were assessed within a fixed-bed reactor under conditions of 320 °C, 3 MPa, and a space velocity of 25700 mL g^{-1} h^{-1}. As evident from the accompanying **Figure 4. 4** and **Table 4. 1**, the unpromoted RhO_x/MgO showed methanol selectivity of 17.7% at 320 °C, whereas selectivity for other products such as methane, ethanol, and higher alcohols were 28.9, 5.3%, and 8.2%, respectively. Methanol formation involves a nondissociative mechanism at sites capable of hydrogenating the adsorbed CO.[41,58] Therefore, the increased total selectivity of the C1 species (methanol) for RhO_x/MgO suggests both a low CO insertion activity and sufficient hydrogenation activity for conversion to C1 products. The addition of alkali metals (K, Li, Cs, and Na) increased the ethanol selectivity (**Figure 4. 4a**) from 5.3% for RhO_x/MgO to 9.2%, 10.4%, 10.9%, and 20% for RhO_x/Na_2O/MgO, RhO_x/K_2O/MgO, RhO_x/Cs_2O/MgO, and RhO_x/Li_2O/MgO, respectively. Notably, the catalyst promoted by Li exhibited the highest ethanol yield, increasing from the 4.8 mmol g_{cat}^{-1} h^{-1} for RhO_x/MgO to 12.2 mmol g_{cat}^{-1} h^{-1}, with a corresponding increase in CO conversion from 20.5% to 36.4%. The production of $C_{2+}OH$ species was observed at the expense of the C_1 products (CO_2, methanol, and methane), which was attributed to the moderating effect of Li on the CO dissociation ability of RhO_x/MgO.[38] Analysis of the effect of the Li loading on the performance, as shown in **Figure 4. 4b**, revealed that 3 wt.% Li yielded optimal rates and selectivity, reaching 12.2 mmol g_{cat}^{-1} h^{-1} and 20%, respectively. **Figure 4. 4c** shows the effect of Rh loading on the performance. An increase in the Rh loading from 2 wt.% to 5 wt.% increases the formation rate and selectivity to 13.8 mmol g_{cat}^{-1} h^{-1} and 25%, respectively. However, we chose to use 2 wt.% due to the high cost of Rh.

We further investigated the effects of the reaction conditions, including the reaction temperature, pressure, and WHSV, on the EtOH synthesis (**Figure 4. 5a** and **b**). On varying the reaction temperature within the range of 240–360 °C, the STY_{EtOH} and C_{2+} alcohol distribution exhibited a characteristic volcano-shaped curve with a maximum at approximately 320 °C. The reaction pressure was varied from 3 to 5 MPa, and the highest STY_{EtOH} (12.2 mmol g_{cat}^{-1} h^{-1}) was achieved at 3 MPa. Furthermore, we explored the influence of the WHSV, by varying it between 25700 and 51000 mL g_{cat}^{-1} h^{-1} and observed that the higher the WHSV, the higher the ethanol yield.

The activity of the Rh catalysts for CO dissociation, insertion, and hydrogenation was affected by the presence of an alkali promoter and support. MgO is a promising electronic or structural promoter for facilitating the high-yield synthesis of methanol via direct CO hydrogenation, achieved through combined reverse water-gas shift (RWGS) and Fischer–Tropsch synthesis (FTS) processes.[59–62] Despite this potential, investigations on MgO-promoted Rh catalysts remain relatively limited. In addition, comprehensive studies exploring the relationship between the distinct catalyst support structures and their activities are lacking. **Figure 4. 4d** shows the support effects of syngas on ethanol, such as MgO, TiO_2, Al_2O_3, and SiO_2. The RhOx/Li_2O/MgO catalyst exhibited the best performance, highlighting the effectiveness of MgO in ethanol production.

The catalytic stability of RhO_x/Li_2O/MgO was evaluated over a 90-hour reaction period under the optimised conditions (**Figure 4. 4e**), revealing no significant changes in CO conversion, product selectivity, and STY_{EtOH}, indicating excellent stability over the RhO_x/Li_2O/MgO catalyst. For comparison, we also summarised the literature data on syngas conversion to ethanol over various catalysts in **Table 4. 2**. Notably, the selectivity and formation rate of C_{2+}OH and EtOH achieved in this study rank among the highest compared to those of representative catalysts reported in the existing literature.

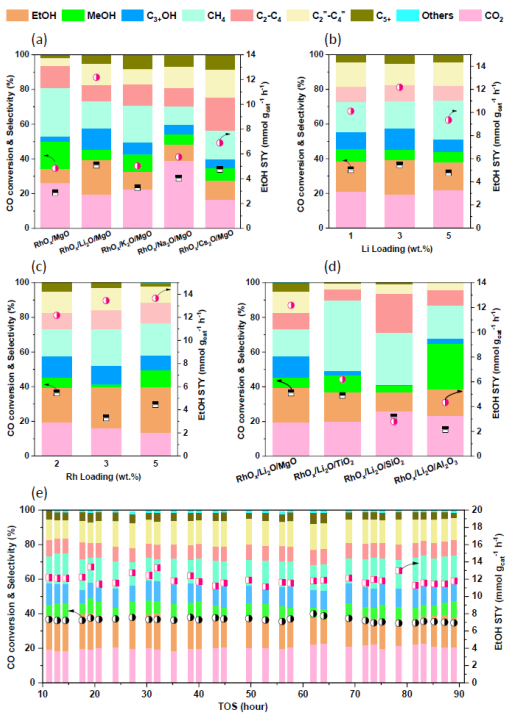

Figure 4. 4. Catalytic performance. (a) product selectivity and STY_{EtOH} on different alkali metals-RhO_x/MgO; product selectivity and STY_{EtOH} on different (b) Li loading (c) and Rh loading. (d) product selectivity and STY_{EtOH} on RhO_x/Li_2O/supports. (e) stability of RhO_x/Li_2O/MgO at 320 °C, 25700 mL g_{cat}^{-1} h^{-1}, 3.0 MPa, Conditions: 70 mg catalyst, H_2/CO as 2 by volume, and Ar as internal standard (0.8 vol %).

Table 4. 1. Catalytic performance of syngas conversion on the RhO_x/MgO catalysts at 320 °C and 3.0 MPa.

Catalysts[a]	CO conversion (%)	selectivity (%)						STY_{EtOH} (mmol g_{cat}^{-1} h^{-1})
		MeOH	EtOH	$C_{2+}OH$	CH_4	$C_{2+}HC$	CO_2	
RhO_x/MgO	20.5	17.7	5.3	8.2	28.9	19.0	26.1	4.8
$RhO_x/Cs_2O/MgO$	33.9	7.0	10.9	16.3	15.5	43.3	16.8	6.9
$RhO_x/K_2O/MgO$	23.4	9.8	10.4	17.3	20.4	29.1	22.5	5.0
$RhO_x/Na_2O/MgO$	28.8	6.1	9.2	14.6	9.8	29.5	39.1	5.7
$RhO_x/Li_2O/MgO$	36.4	6.0	19.9	32.2	15.5	26.7	17.6	12.4
$RhO_x/Li_2O/TiO_2$	35	9.7	16.9	19.3	40.8	10.1	20.2	6.2
$RhO_x/Li_2O/SiO_2$	22.4	3.6	11.1	11.8	30.1	28.5	26	2.8
$RhO_x/Li_2O/Al_2O_3$	15.3	25.9	15.3	18.2	19.1	13	23.5	4.3

[a] Accelerated aging treatment at 360 °C for 12 hours was performed before the reaction in order to ensure the catalyst stability.

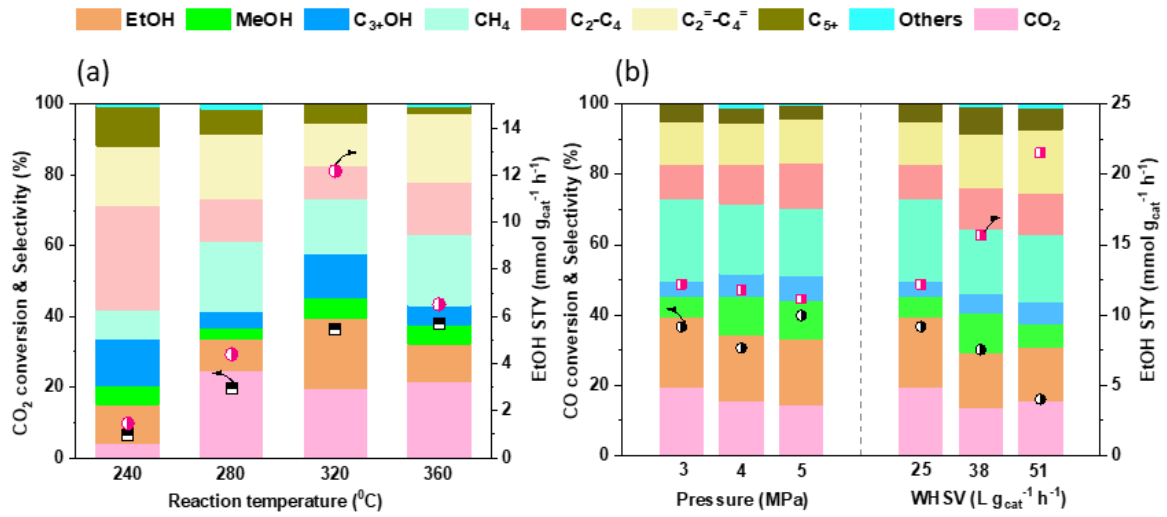

Figure 4. 5. Catalytic performance. (a) Reaction temperature effect on product selectivity and EtOH STY on alkali metals-RhO_x/MgO; (b) Pressure and WHSV effect on product selectivity and EtOH STY, conditions: 70 mg catalyst, H_2/CO as 2 by volume, and Ar as internal standard (0.8 vol %).

Table 4. 2. Catalytic performance over different catalysts for CO hydrogenation in this work and literature.

Catalyst	T (°C)	P (MPa)	WHSV (mL g_{cat}^{-1} h^{-1})	CO conversion (%)	C_{2+}OH selectivity (%)	EtOH selectivity (%)	STY (mmol $gcat^{-1}$ h^{-} ^{1})	Ref.
$RhO_x/Li_2O/MgO$[a]	320	3	25700	36.4	32.2	19.9	12.2	This work
$RhO_x/Li_2O/MgO$[a]	280	3	25700	19.7	12	8.9	4.9	This work
Co_1Mn_2	240	3	30456	30	28	~13	6.9	[63]
CuCoMn	270	2.5	20000	29.7	32.6	19	7	[64]
CoMn/CuZnAlZr	230	6	2000	17.8	~18	~10.0	0.3	[65]
CuCoMg	270	2.5	12000	30.7	28.2	~18	-	[66]
CuCoAl	220	2.5	7500	36.2	22.9	~12	5	[67]
Co/MnO_x MOF-74	230	3	4500	21.4	35.9	~9	1.3	[68]
$Cu1Co4@ZrO_2$	270	5	24000	8.7	31.8	~9.1	1.2	[69]
$Co1 /CeO_2$	260	5	9000	1	14.2	~5	-	[70]
$CoMnZn/r– TiO_2$	260	4	2000	44.7	19	~5	0.23	[71]
Fe1Co1	250	6	3000	>80%	30	4.2	0.55	[72]
K/CuFe/CNF	270	5	32000	11	18	-	-	[73]
$2\%Rh-1\%Fe/TiO_2$	270	2	8000	7.47	-	13.4	1.5	[74]
Cu_1Co_2La	250	3	36000	0.86	17.6	10.8	0.23	[75]
CoFe-350	260	3	10800	24.0	50	25	2.1	[76]
$CS/Cu/ZnO/Al_2O_3$	290	5.4	1875	41.6	28	6.1	0.29	[77]
RM@UiO-67	300	2	50 000	21.9	54.0 (C_{2+} Oxy)	35.1	4.52	[78]
$Rh–Mn/SiO_2$	260	3	5833	9.4	27.2	21	1.83	[79]
Rh–Mn/WxC	300	5	8000	8.1	15.4	7.2	1.41	[80]
$Rh–Mn/TiO_2$	280	3	10,000	6.8	39.0	20.0	0.73	[46]
$Rh–Mn/ZrO_2$	300	3	10,000	16.8	43.2 (C_{2+} Oxy)	25.2	2.5	[81]
$K/Co/β-Mo_2C$	300	8	2000	23.41	33.8	21	0.72	[82]
$K-Rh-MoS_2/Al_2O_3$	350	10	4800	11	48	19	-	[83]
$K-Fe-β-Mo_2C$	320	7	4000	50.3	13.4	6.5	-	[84]
$YRh_{0.5}Fe0._5O_3/ZrO_2$	290	4	3000	34.1	35	25.5	1.09	[85]
$Rh-Mn/SiO_2$	270	3	15000	1.6	38.2(C_{2+} Oxy)	19.9	5.45	[86]
$Fe-Rh-Mn-Li/SiO_2$	300	3	10000	18.9	54.3 (C_{2+} Oxy)	27.1	3.63	[87]
$Sm-V-Rh/ SiO_2$	280	3	13000	5.4	50.5(C_{2+} Oxy)	28.9	4.72	[88]
$Cr-Fe-Rh/SiO_2$	280	5	5000	10.2	27.9	26	1.82	[89]
$Rh/Ce_{0.8}Zr_{0.2}O_2$	275	2.4	10000	27.3	39.2	35.2	3.63	[90]
$K-Co-MoS_2/$ AC	330	5	4800	14.3	26.7	17.3	1.74	[91]
$Rh−Mn−Li−Fe/SiO_2$	320	5	12000	17	42	22	4.36	[92]
Rh/TiO_2	250	2	10000	55.7	-	34.9	14.04	[93]

[a] Accelerated aging treatment at 360 °C for 12 hours was performed before the reaction in order to ensure the catalyst stability.

4.3.2 Structural characterization

HAADF-STEM was used to characterise the supported Rh nanoparticles. **Figure 4. 6** displays the HAADF-STEM images of RhO_x/MgO and $RhO_x/Li_2O/MgO$ (reduced samples) coupled with X-ray energy-dispersive spectroscopy (EDS) for elemental analysis. The Rh species exhibited a uniform distribution on both catalysts (**Figure 4. 6a** and **e**), with the introduction of a promoter resulting in a subtle increment in particle size from 1.8 to 2.8 nm. Elemental mapping demonstrated the homogeneous distribution of Rh across the catalyst surface, confirming the co-localisation of Rh and Mg (**Figures 4. 6b-d**). We also characterised the spent $RhO_x/Li_2O/MgO$, and the results are presented in **Figure 4. 6i**. HAADF-STEM resolved larger particles ranging from 6 to 12 nm and were discernible in the spent catalyst, which was absent in the reduced catalyst (before the reaction), suggesting their formation through sintering during the catalytic reaction. The STEM-EDS elemental mappings (**Figures 4. 6j-l)** reveal a consistent distribution of Rh throughout the MgO support.

Similarly, HAADF-STEM characterisation was performed on $RhO_x/Li_2O/SiO_2$, $RhO_x/Li_2O/TiO_2$ and $RhO_x/Li_2O/Al_2O_3$ after H_2 reduction. As can be seen in **Figure 4. 7**, the particle sizes of all supported Rh catalysts exhibit slight differences, with average sizes of 1.85 nm, 1.99 nm, and 1.57 nm for $RhO_x/Li_2O/SiO_2$, $RhO_x/Li_2O/TiO_2$, and $RhO_x/Li_2O/Al_2O_3$ catalysts, respectively. STEM-EDS elemental mapping indicated that the Rh atoms were homogeneously distributed across the catalyst surfaces.

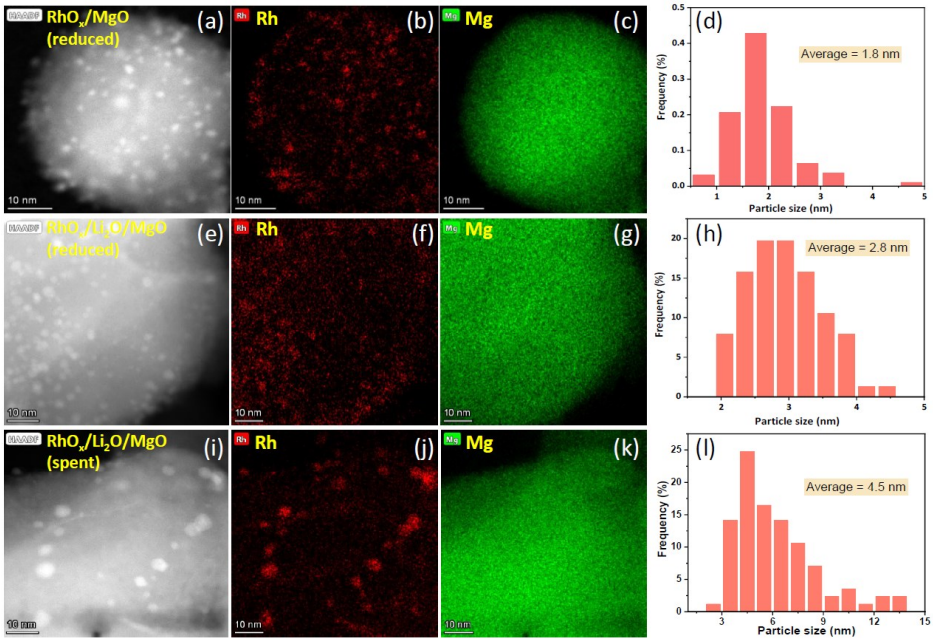

Figure 4. 6. HAADF-STEM images (a, e, i), corresponding EDX mapping images (b, c, f, g, j and k), and particle size distribution (d, h, l) of the RhO_x/MgO, $RhO_x/Li_2O/MgO$ (reduced samples) and $RhO_x/Li_2O/MgO$ (spent sample).

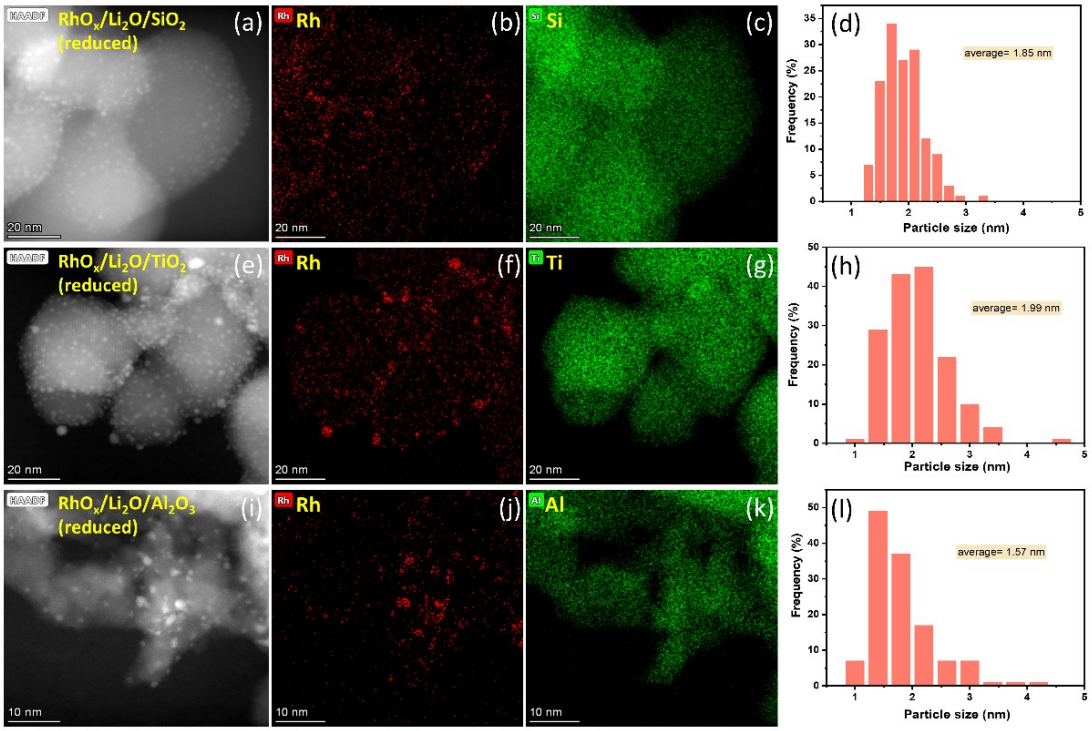

Figure 4. 7. HAADF-STEM image and corresponding EDX mapping images of the $RhO_x/Li_2O/SiO_2$ (a-d), $RhO_x/Li_2O/TiO_2$ (e-h) and $RhO_x/Li_2O/Al_2O_3$ (i-l) (reduced samples).

The presence of crystalline phases within the catalyst was examined after calcination, H_2 reduction, and the reaction using XRD, as shown in **Figure 4. 8a**. The XRD pattern contains peaks associated with MgO.[94] Analysis of the peaks formed after loading the Li species showed that the Li species introduced in the Rh catalyst existed as Li_2O. In addition, The Rh_2O_3/MgO and Rh_2O_3/Li_2O/MgO (unreduced sample) catalysts are indicative of the absence of crystalline structures corresponding to Rh_2O_3 or metallic Rh. This is due to the high dispersion of the Rh species, rendering the crystalline domains below the detection limit of the instrument. After H_2 reduction, changes in the crystal structure were observed, with patterns indicating the presence of the Rh crystal phase but not oxidised Rh_2O_3 as shown in the XAS analysis (this will be discussed in a later section). Similar observations were made for the spent catalyst, where Rh metal diffraction peaks were present, albeit larger particles were observed in the STEM analysis. The XRD pattern of the alternative support exhibits similar results, indicating the absence of crystalline structures corresponding to Rh (**Figure 4. 9**). This is attributed to the high dispersion of the Rh species within the material.

Temperature-programmed reduction with H_2 (H_2-TPR) was employed to study the reducibility of the catalysts, and the results are summarised in (**Figure 4. 8b**). The

$Rh_2O_3/Li_2O/MgO$ catalyst exhibited the highest reduction temperature, centred at 370 °C, which is higher than that of the Rh_2O_3/MgO catalyst. This suggests that the reducibility of Rh on the MgO support was further hindered by the introduction of Li (**Figure 4. 8b**). $Rh_2O_3/Li_2O/SiO_2$ shows medium reducibility, resulting in the reduction peak shifting to approximately 270 °C. For $Rh_2O_3/Li_2O/TiO_2$ and $Rh_2O_3/Li_2O/Al_2O_3$, the first reduction temperature is much lower at approximately 100 °C. Therefore, the reduction capability follows the order: $RhO_x/Li_2O/MgO < RhO_x/Li_2O/SiO_2 < RhO_x/Li_2O/TiO_2 \approx RhO_x/Li_2O/Al_2O_3$.

XAS was further employed to investigate the effects of the Li promoter on the reducibility, environment, and oxidation state of Rh. *Ex situ* XANES spectra of the Rh *K*-edge of the Rh catalysts are shown in **Figure 4. 10a**. $Rh_2O_3/LiO_2/MgO$ (unreduced sample) clearly indicated the presence of cationic Rh (Rh_2O_3). Extended X-ray absorption fine structure (EXAFS) spectra revealed Rh–O scattering paths, with Rh–O contributions at 2.05 Å (**Table 4. 3**).[47–49] The formation of metallic Rh is observed after the treatment with H_2 at 360 °C for 30 minutes as evidenced by the shift of the absorption edge to lower energies for both $RhO_x/Li_2O/MgO$ and RhO_x/MgO catalysts (reduced samples). The XANES and EXAFS spectra of these materials are different from those of the Rh foil, which we attribute to the presence of some remaining unreduced cationic Rh or to charge transfer between the metal and the support.[26,38,47] **Figure 4. 10b** and **Table 4. 3** summarise the curve-fitting results for the EXAFS data for all the measured catalysts. The CN values obtained for the Rh–Rh shells of the unpromoted and promoted RhO_x/MgO catalysts after reduction were smaller than the bulk value, indicating the presence of small Rh particles. The high dispersion of Rh is also in line with the observed decrease in the coordination distance relative to the bulk value (R = 2.69 Å). The presence of the promoter resulted in a slight increase in the particle size, as evidenced by the larger CN values in the EXAFS fits and STEM results.

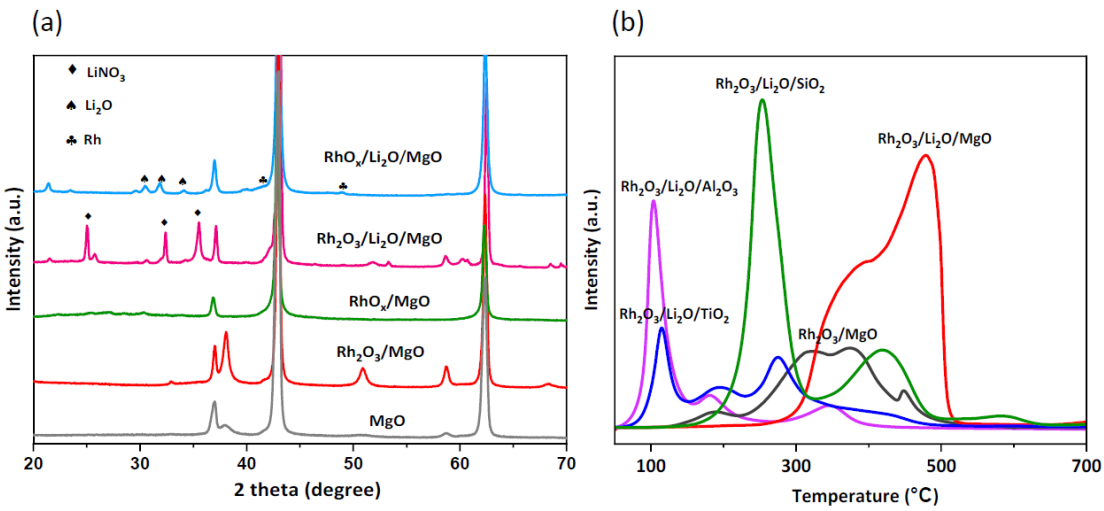

Figure 4. 8. (a) XRD patterns of various MgO based catalysts; (b) H_2-TPR results over different control catalysts. Condition: Ar pretreatment at 200 °C for 1hr, heating in 10%H_2/Ar from 50 to 700 °C.

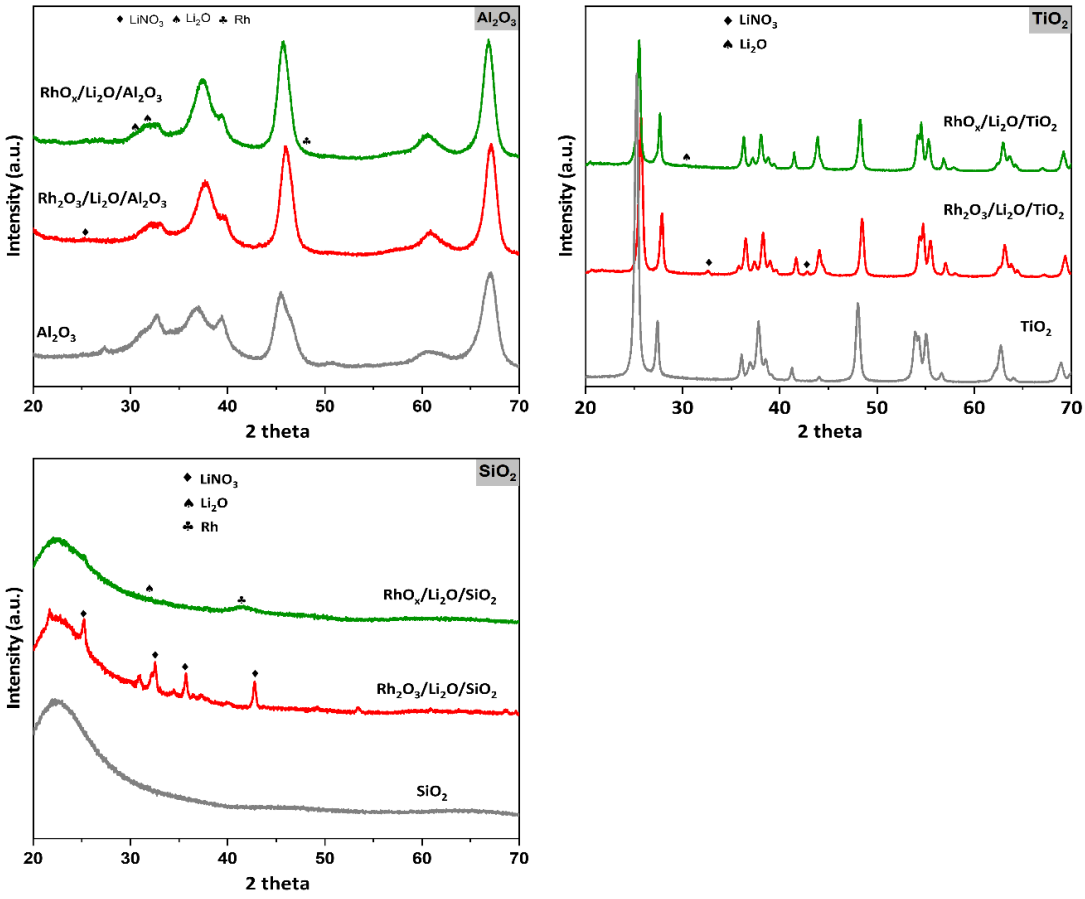

Figure 4. 9. XRD patterns over $RhO_x/Li_2O/Al_2O_3$; $RhO_x/Li_2O/TiO_2$ and $RhO_x/Li_2O/SiO_2$ catalysts.

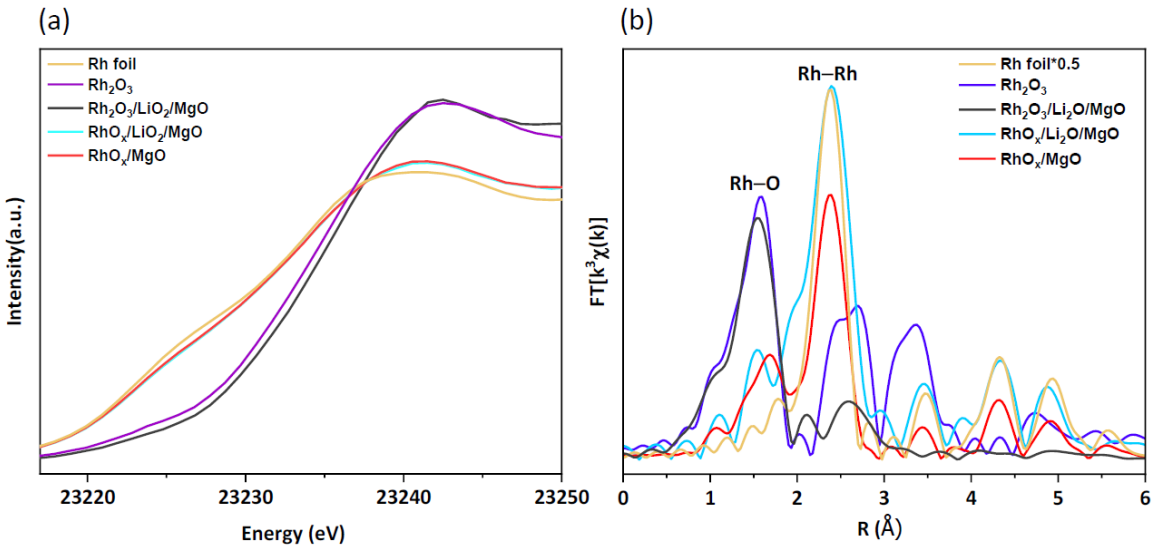

Figure 4. 10. XAS results. (a) Rh *K*-edge XANES measurements; (b) comparison of the Fourier transform (FT)-EXAFS of Rh *K*-edge for the $Rh_2O_3/Li_2O/MgO$ (unreduced sample), $RhO_x/Li_2O/MgO$ and RhO_x/MgO (reduced samples).

Table 4. 3. Curve-fitting results of the *ex situ* Rh *K*-edge FT-EXAFS spectra of the studied samples.

Sample	shell	CN	R (Å)	σ^2 (Å^2)	ΔE	R factor
Rh_2O_3	Rh–O	6.3± 0.5	2.05± 0.03	0.003	3.7	0.02
Rh	Rh–Rh	12.0 (fixed)	2.68± 0.01	0.003	5.9	0.01
$Rh_2O_3/Li_2O/MgO$-before H_2 reduction	Rh–O	6.2 ± 0.5	2.05 ± 0.01	0.003	1.6	0.02
$RhO_x/Li_2O/MgO$ After H_2 reduction	Rh–O	2.0 ± 1.1	2.05 ± 0.02	0.003	4.7	0.01
	Rh–Rh	6.5 ± 0.4	2.68 ± 0.01	0.003		
RhO_x/MgO After H_2 reduction	Rh–O	2.3 ± 0.7	2.05 ± 0.02	0.004	3.1	0.02
	Rh–Rh	5.3 ± 0.7	2.68 ± 0.01	0.004		

CN: coordination numbers; R: bond distance; σ^2: Debye-Waller factors; R factor: goodness of fit. S_0^2 was set to 0.82, according to the EXAFS fit of Rh foil.

4.3.3 Mechanistic studies

The *operando* Diffuse Reflectance Infrared Fourier Transform Spectroscopy (DRIFTS) coupled with Mass Spectrometry was employed to elucidate the mechanism governing the hydrogenation of CO to EtOH under reaction conditions at 320 °C, 0.5 MPa, and a H_2/CO ratio of 2 on $RhO_x/Li_2O/MgO$ and RhO_x/MgO catalysts and other reference catalysts. The results (**Figure 4. 11a**) for the Li promoted catalyst ($RhO_x/Li_2O/MgO$) reveals, the band at 3016 cm^{-1} corresponding to the C–H stretching vibration in CH_4,[40,95,96] and the gradual buildup of the bands due to C–H bond asymmetric stretching (ν_{as} C–H) and asymmetric

bending (δ_{as} C–H) vibration in CH_x* at approximately 2850 cm^{-1} and 1450 cm^{-1}. After 5 minutes, bands characteristic of CH_3CHO* (1435 cm^{-1} and 2790 cm^{-1}) and the C–H asymmetric (ν_{as} C–H) and symmetric (ν_s C–H) stretching bands in CH_3CH_2O* (2924 cm^{-1}, 2963 cm^{-1}, and 1161 cm^{-1}) [40,95,97,98] emerged and intensified. The generated CH_3CHO* species can be further hydrogenated to an ethoxy species (CH_3CH_2O*). Furthermore, bands corresponding to CH_3COO* (1515 and 1541 cm^{-1}) existed throughout the reaction, commonly observed on the surfaces of Rh-based catalysts with superior ethanol selectivity.[99] Additional bands at 2770, 2723, 1606, and 1342 cm^{-1} corresponded to HCOO*.[100] DRIFT spectra also revealed a minor peak at 2798 cm^{-1} assigned to CH_3O*,[101] alongside a decrease in the intensity of the peak at 2723 cm^{-1} attributable to formate,[102] which are important intermediates of methanol production. Online gas chromatography was used to track and quantify the formation of EtOH and MeOH in the gas phase (**Figure 4. 11b**). After 10 min, the EtOH formation rate increased compared to that of MeOH, indicating facile CO hydrogenation to CH_3CH_2OH under the specified conditions.

As depicted in **Figure 4. 11c**, the DRIFTS analysis of the RhO_x/MgO catalysts shows a notable increase in the relative band intensity of unsaturated CH_x* at 2850 cm^{-1}, in comparison to RhO_x/Li_2O/MgO. The observed peaks at 2723 and 1384 cm^{-1} correspond to the characteristic features of adsorbed formate (HCOO*), [40,98] whereas the band centred at 1600 cm^{-1} is associated with the O–C–O vibration (referred to as C=O) [100] of formate species. Furthermore, intense IR bands, at 2798 cm^{-1} and 1102 cm^{-1}, representing methoxy groups (CH_3O*),[100] were detected. The results also revealed that the relative band intensity of CH_3O* to HCOO* increased in the unpromoted RhO_x/MgO catalyst, indicating that these intermediates were directly hydrogenated to CH_3OH rather than forming C_{2+} oxygenate intermediates. The results showed a higher absolute number of adsorbed species on the RhO_x/MgO catalyst. However, these species did not effectively contribute to the formation of the C_2 products. We speculate that the presence of the Li promoter effectively mitigated the formation of methoxy intermediates. A comparison of the data in **Figure 4. 11b** and **d** reveals a higher formation rate of ethanol over Rh/Li/MgO than over the Rh/MgO catalysts. The latter showed a significant increase in MeOH production after 15 min compared to EtOH. The enhanced coverage of C_{2+} oxygenate intermediates and reduced concentration of CH_3O* over the RhO_x/Li_2O/MgO catalyst contributed to the improved EtOH selectivity.

The investigation delved into the impact of varying the support material for RhO_x/Li_2O catalysts, transitioning from MgO to TiO_2, SiO_2, and Al_2O_3, all within identical reaction conditions set at 320 °C and 0.5 MPa. The spectral data, depicted in **Figure 4. 12** and **13a**,

were acquired after the syngas conversion process was conducted on the diverse support matrices. This study aimed to discern the alterations in the catalytic performance and reaction pathways induced by different support materials employed in conjunction with RhO_x/Li_2O catalyst systems. In the depicted **Figure 4. 13a**, it is evident that the relative band intensity ratio of CH_4 at 3016 cm^{-1} to the unsaturated CH_x* species at 2927 cm^{-1},[95] exhibits a notable augmentation in the $RhO_x/Li_2O/TiO_2$ catalyst compared to other support materials. This observation underscores the efficacy of TiO_2 as a support in markedly improving the hydrogenation of CH_x* to CH_4, thereby reducing the coverage of CH_x* species. Conversely, the relative band intensities corresponding to HCOO* (2723, 1650, 1606, and 1342 cm^{-1}),[100] along with the CH_3O* group (2894 cm^{-1}, 2830 cm^{-1}, 1059 cm^{-1}),[101] exhibit a pronounced elevation in the $RhO_x/Li_2O/Al_2O_3$ catalysts, indicative of significant intermediates crucial for methanol production. Furthermore, analysis reveals that the $RhO_x/Li_2O/MgO$ catalyst displayed the highest intensity of CH_3CH_2O* after 60 min of the reaction, accompanied by the detection of CH_3CHO species, signifying the importance of intermediates for ethanol formation. Among the evaluated catalyst systems, the formation rate of ethanol identified $RhO_x/Li_2O/MgO$ as the catalyst with the highest efficacy for facilitating ethanol synthesis (**Figure 4. 13b**).

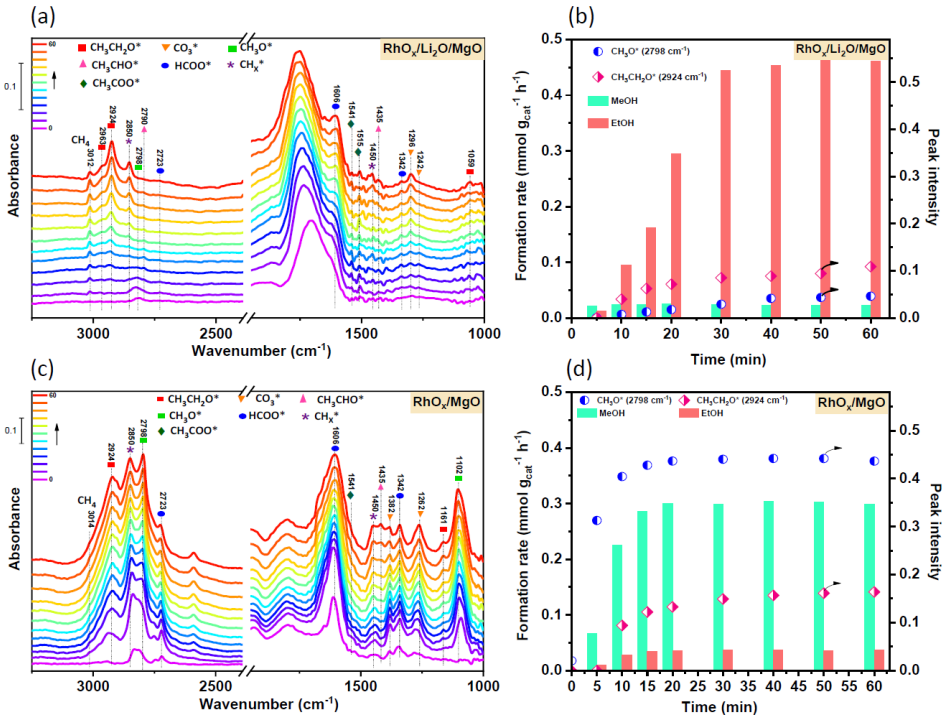

Figure 4. 11. *Operando* DRIFT spectra of CO hydrogenation over the $RhO_x/Li_2O/MgO$ (a) and RhO_x/MgO (c) catalysts. Dynamic IR peak intensities of CH_3CH_2O* and CH_3O* and formation rate resulted from Micro GC over the $RhO_x/Li_2O/MgO$ (b) and RhO_x/MgO (d) catalysts. Reaction conditions: 0.5 MPa, CO/H_2 = 1/2, 30 mL min^{-1}, and 320 °C.

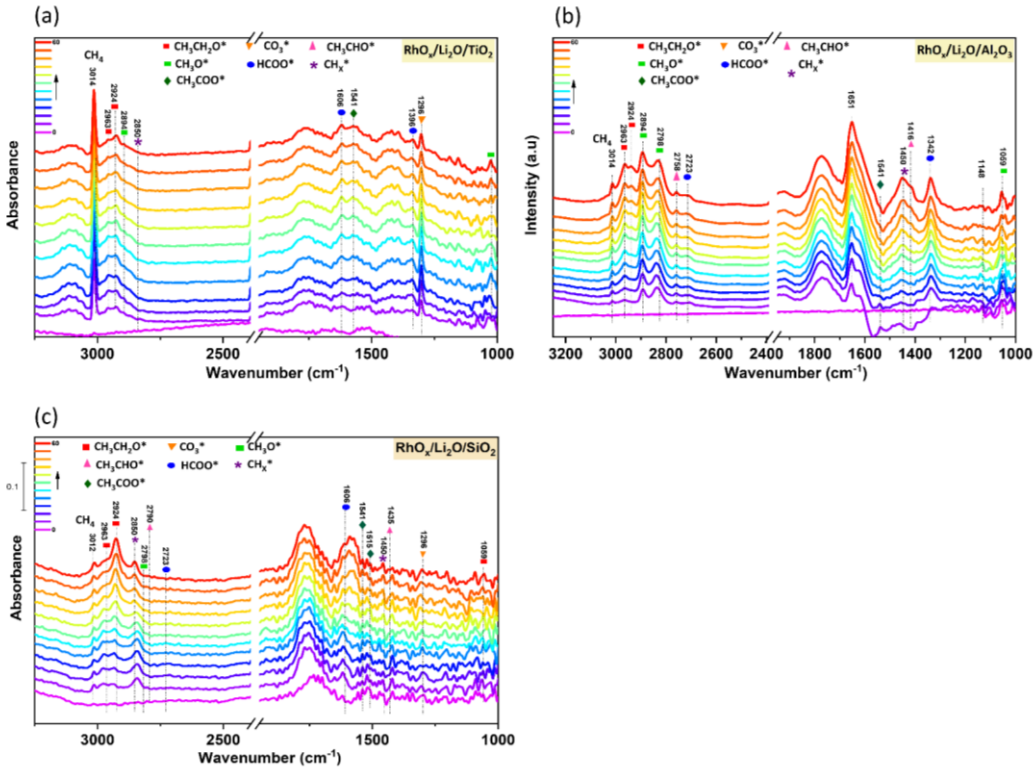

Figure 4. 12. *Operando* DRIFTS spectra of CO hydrogenation over the $RhO_x/Li_2O/TiO_2$ (a), $RhO_x/Li_2O/Al_2O_3$ (b), and $RhO_x/Li_2O/SiO_2$ (c) catalysts. Reaction conditions: 0.5 MPa, CO/H_2 = 1/2, 30 mL min^{-1}, and 320 °C.

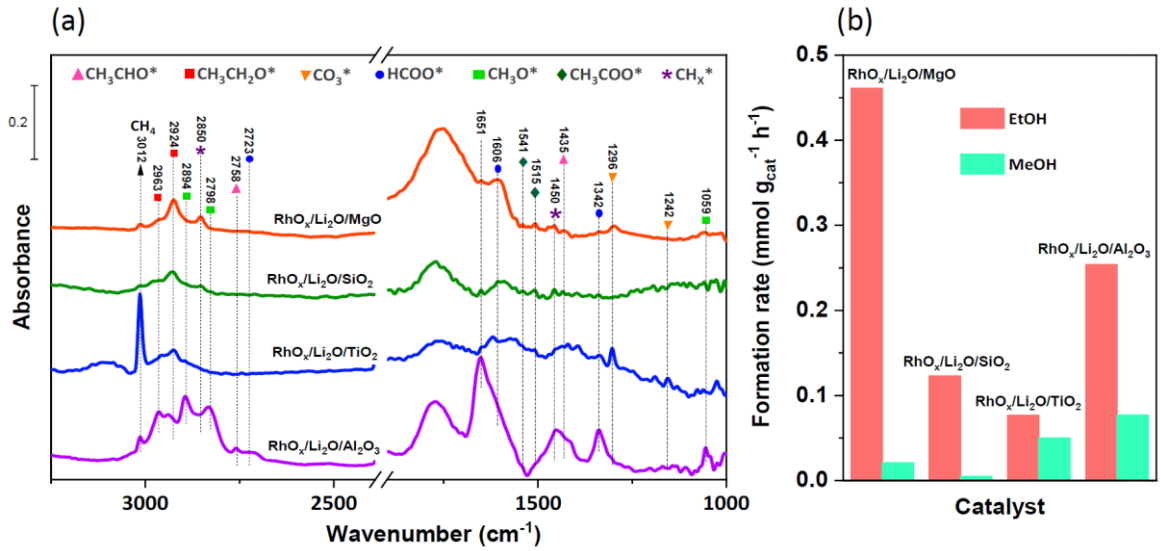

Figure 4. 13. (a) *Operando* DRIFT spectra of CO hydrogenation over the $RhO_x/Li_2O/MgO$, $RhO_x/Li_2O/TiO_2$, $RhO_x/Li_2O/SiO_2$ and $RhO_x/Li_2O/Al_2O_3$ catalysts. Reaction conditions: 0.5 MPa, CO/H_2 = 1/2, 30 mL min^{-1}, and 320 °C. (b) formation rate resulted from Micro GC over different catalytic systems.

In situ X-ray absorption (XAS) experiments were conducted to investigate the structural and chemical characteristics of the $RhO_x/Li_2O/MgO$ catalyst under the reaction conditions at the Rh *K*-edges, given its significantly enhanced activity and ethanol selectivity compared to

unpromoted RhO_x/MgO. The structural evolution of the catalyst after H_2 reduction under the reaction conditions was probed via EXAFS analysis, whereas alterations in the chemical state were investigated by analysing the XANES region. The *in situ* XANES and FT-EXAFS spectra under He flow immediately after the H_2 reduction at 360 °C are shown in **Figure 4. 14**. No significant changes were observed upon exposure to CO and CO+H_2 gasses at ambient pressure, the curve fitting results also confirmed this (**Table 4. 4**), indicating that the chemical state of the Rh species was similar to that of the reduced catalyst.

To further elucidate the role of Li, Fourier-transform infrared spectroscopy (FTIR) spectra were obtained in transmission mode for CO adsorption on the two MgO-based catalysts at low temperature (**Figure 4. 15**). When CO was introduced into RhO_x/MgO, three strong adsorption peaks were observed in the region of 1800–2100 cm^{-1} region. The peaks centred at 1856, 1987, and 2055 cm^{-1} can be assigned to CO adsorbed on the hollow site (CO bound to three Rh atoms), bridge site (CO bound to two Rh atoms), and on-top site (CO bound to one Rh atom), respectively. The addition of Li species to RhO_x/MgO (RhO_x/Li_2O/MgO) significantly reduced the absorption intensities of all CO species. In addition, all the peaks shifted toward higher wavenumbers. It is well known that back-donation from the metal surface to the adsorbed CO strongly contributes to the adsorption strength and C–O bond vibrations.[103,104] The π back-donation contribution is weakened when Rh is positively charged, thus leading to a weaker adsorption of CO and a shift in the C–O bond vibrational frequency for RhO_x/Li_2O/MgO. The adsorption energy of CO was also examined using DFT calculations (**Figure 4. 16**). E_{ads} of a CO molecule on the Rh_{13}/MgO (100) and Rh_{13}/Li_2O (111)/MgO (100) surfaces were calculated to be -2.34 and -2.02 eV, respectively. It should also be noted that only the on-top sites were considered as adsorption sites, and the most stable structures were employed in this investigation for each model. This result also suggests that the addition of Li species leads to weaker adsorption of CO. When the supported metal nanoparticles become electron-rich, the formation of CH_4 is favored.[105] In the present study, because CH_4 is an undesired by-product, it is thought that suppressing CH_4 production by making the supported Rh nanoparticles electron-deficient through Li addition would be advantageous for ethanol synthesis. Thus, over RhO_x/Li_2O/MgO catalysts, hydrogenation to CH_4 may be suppressed, and CO species can be more readily inserted into the CH_x-Rh bond, producing C_2 oxygenates more efficiently than on RhO_x/MgO catalysts.

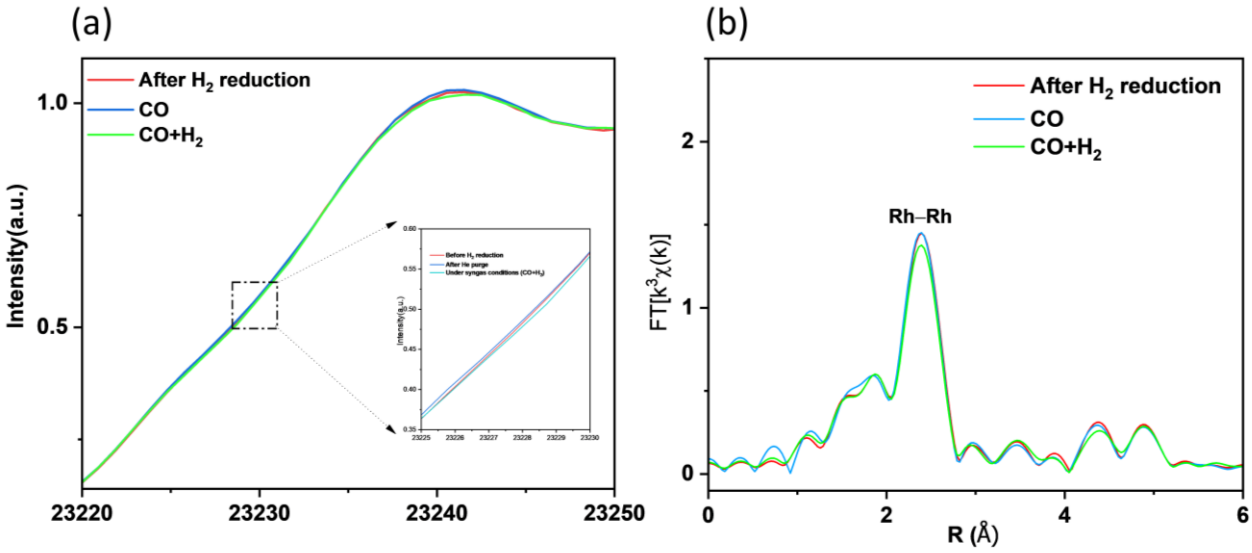

Figure 4. 14. *In situ* Rh *K*-edge (a) XANES and FT-EXAFS spectra of $RhO_x/Li_2O/MgO$. (b)After H_2 reduction pretreatment with 100% H_2 at 360 °C and 1bar, CO (100%) was introduced the *in situ* cell. Total flow rate = 100 mL/min.

Table 4. 4. Curve-fitting results of the *in situ* Rh *K*-edge FT-EXAFS spectra of the $RhO_x/Li_2O/MgO$ catalyst.

Sample	shell	CN	R (Å)	σ^2 (Å^2)	ΔE	R factor
$RhO_x/Li_2O/MgO$ After H_2 reduction	Rh–O	1.5±1.3	2.04±0.03	0.007	5.7	0.01
	Rh–Rh	7.8 ± 0.6	2.68 ± 0.01	0.008		
Under syngas conditions ($CO+H_2$)	Rh–O	1.4 ± 0.4	2.01 ± 0.01	0.008	6.32	0.02
	Rh–Rh	7.6 ± 0.5	2.68 ± 0.01	0.008		

CN: coordination numbers; R: bond distance; σ^2: Debye-Waller factors; R factor: goodness of fit. S_0^2 was set to 0.82, according to the EXAFS fit of Rh foil.

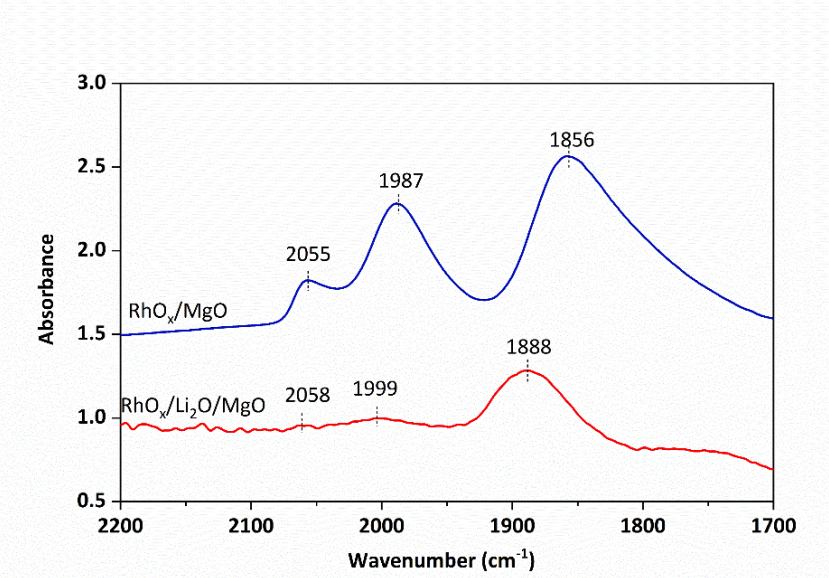

Figure 4. 15. FTIR spectra of CO adsorption for the $RhO_x/Li_2O/MgO$, RhO_x/MgO. Prior to CO adsorption, the catalyst was treated with H_2, and CO was introduced at −20 °C.

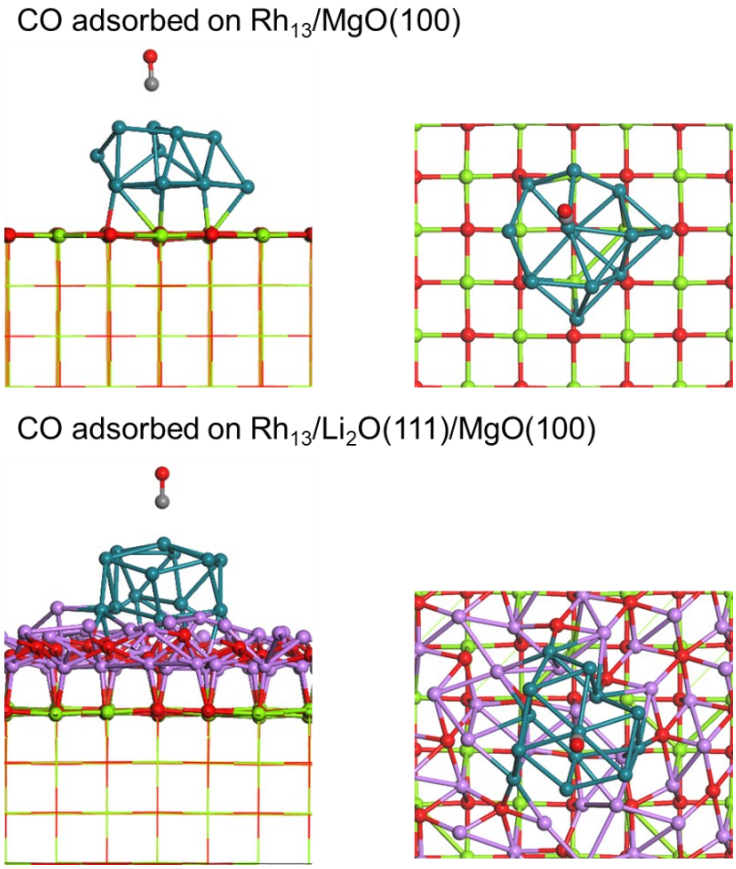

Figure 4. 16. Optimized structures for DFT calculations of CO adsorbed on the Rh_{13}/MgO (100) and Rh_{13}/Li_2O (111)/MgO (100) surfaces.

4.4 Conclusion

In this study, we achieved high ethanol production by utilising MgO as an effective support for Rh catalysts in a syngas-to-ethanol conversion reaction. Among the alkali metals tested, Li was the most favourable promoter for ethanol formation. Through optimisation of the reaction conditions, we attained the highest ethanol space-time yield (STY_{EtOH}) of 12.2 mmol g_{cat}^{-1} h^{-1} with a selectivity of 20 %. The addition of Li as an effective promoter, which likely interacts closely with Rh to form new active sites, enhanced ethanol yield and selectivity. The introduction of Li promoted Rh electron deficiency, suppressed the formation of undesired CH_4 and promoted the formation of ethanol. In addition, we examined the roles of various catalyst supports (SiO_2, Al_2O_3, and TiO_2) in ethanol synthesis to elucidate their effects. Our findings highlight the significance and implications of MgO as a support for Rh catalysts, offering insights into the design of next-generation catalysts that can upgrade small molecules to chemicals and synthetic fuels.

4.5 References

(1) Jiao, F.; Bai, B.; Li, G.; Pan, X.; Ye, Y.; Qu, S.; Xu, C.; Xiao, J.; Jia, Z.; Liu, W.; Peng, T.; Ding, Y.; Liu, C.; Li, J.; Bao, X. Disentangling the Activity-Selectivity Trade-off in Catalytic Conversion of Syngas to Light Olefins. *Science* **2023**, *380*, 727–730.

(2) Jiao, F.; Li, J.; Pan, X.; Xiao, J.; Li, H.; Ma, H.; Wei, M.; Pan, Y.; Zhou, Z.; Li, M.; Miao, S.; Li, J.; Zhu, Y.; Xiao, D.; He, T.; Yang, J.; Qi, F.; Fu, Q.; Bao, X. Selective Conversion of Syngas to Light Olefins. *Science* **2016**, *351*, 1065–1068.

(3) Zhong, L.; Yu, F.; An, Y.; Zhao, Y.; Sun, Y.; Li, Z.; Lin, T.; Lin, Y.; Qi, X.; Dai, Y.; Gu, L.; Hu, J.; Jin, S.; Shen, Q.; Wang, H. Cobalt Carbide Nanoprisms for Direct Production of Lower Olefins from Syngas. *Nature* **2016**, *538*, 84–87.

(4) Xu, Y.; Li, X.; Gao, J.; Wang, J.; Ma, G.; Wen, X.; Yang, Y.; Li, Y.; Ding, M. A Hydrophobic FeMn@Si Catalyst Increases Olefins from Syngas by Suppressing C1 By-Products. *Science* **2021**, *371*, 610–613.

(5) van Deelen, T. W.; Hernández Mejía, C.; de Jong, K. P. Control of Metal-Support Interactions in Heterogeneous Catalysts to Enhance Activity and Selectivity. *Nat. Catal.* **2019**, *2*, 955–970.

(6) Ma, S.; Huang, S.-D.; Liu, Z.-P. Dynamic Coordination of Cations and Catalytic Selectivity on Zinc–Chromium Oxide Alloys during Syngas Conversion. *Nat. Catal.* **2019**, *2*, 671–677.

(7) Ji, Y.; Gao, P.; Zhao, Z.; Xiao, D.; Han, Q.; Chen, H.; Gong, K.; Chen, K.; Han, X.; Bao, X.; Hou, G. Oxygenate-Based Routes Regulate Syngas Conversion over Oxide–Zeolite Bifunctional Catalysts. *Nat. Catal.* **2022**, *5*, 594–604.

(8) Luk, H. T.; Mondelli, C.; Ferré, D. C.; Stewart, J. A.; Pérez-Ramírez, J. Status and Prospects in Higher Alcohols Synthesis from Syngas. *Chem. Soc. Rev.* **2017**, *46*, 1358–1426.

(9) Liu, G.; Yang, G.; Peng, X.; Wu, J.; Tsubaki, N. Recent Advances in the Routes and Catalysts for Ethanol Synthesis from Syngas. *Chem. Soc. Rev.* **2022**, *51*, 5606–5659.

(10) Chen, Z.; Wang, H.; Liu, Z.; Xu, X. Dynamic and Intermediate-Specific Local Coverage Controls the Syngas Conversion on Rh (111) Surfaces: An *Operando* Theoretical Analysis. *ACS Catal.* **2021**, *11*, 3830–3841.

(11) Wang, J.; Liu, Z.; Zhang, R.; Wang, B. Ethanol Synthesis from Syngas on the Stepped Rh (211) Surface: Effect of Surface Structure and Composition. *J. Phys. Chem. C* **2014**, *118*, 22691–22701.

(12) Subramani, V.; Gangwal, S. K. A Review of Recent Literature to Search for an Efficient Catalytic Process for the Conversion of Syngas to Ethanol. *Energy & Fuels* **2008**, *22*, 814–839.

(13) Kang, J.; He, S.; Zhou, W.; Shen, Z.; Li, Y.; Chen, M.; Zhang, Q.; Wang, Y. Single-Pass Transformation of Syngas into Ethanol with High Selectivity by Triple Tandem Catalysis. *Nat. Commun.* **2020**, *11*, 827.

(14) Spivey, J. J.; Egbebi, A. Heterogeneous Catalytic Synthesis of Ethanol from Biomass-Derived Syngas. *Chem. Soc. Rev.* **2007**, *36*, 1514.

(15) Subramani, V.; Gangwal, S. K. A Review of Recent Literature to Search for an Efficient Catalytic Process for the Conversion of Syngas to Ethanol. *Energy & Fuels* **2008**, *22*, 814–839.

(16) Gupta, M.; Smith, M. L.; Spivey, J. J. Heterogeneous Catalytic Conversion of Dry Syngas to Ethanol and Higher Alcohols on Cu-Based Catalysts. *ACS Catal.* **2011**, *1*, 641–656.

(17) Ao, M.; Pham, G. H.; Sunarso, J.; Tade, M. O.; Liu, S. Active Centers of Catalysts for Higher Alcohol Synthesis from Syngas: A Review. *ACS Catal.* **2018**, *8*, 7025–7050.

(18) Mäki-Arvela, P.; Aho, A.; Simakova, I.; Yu. Murzin, D. Sustainable Aviation Fuel from Syngas through Higher Alcohols. *ChemCatChem* **2022**, *14*, e202201005.

(19) Xiang, Y.; Barbosa, R.; Kruse, N. Higher Alcohols through CO Hydrogenation over CoCu Catalysts: Influence of Precursor Activation. *ACS Catal.* **2014**, *4*, 2792–2800.

(20) Li, X.; San, X.; Zhang, Y.; Ichii, T.; Meng, M.; Tan, Y.; Tsubaki, N. Direct Synthesis of Ethanol from Dimethyl Ether and Syngas over Combined H-Mordenite and Cu/ZnO Catalysts. *ChemSusChem* **2010**, *3*, 1192–1199.

(21) Cao, A.; Liu, G.; Wang, L.; Liu, J.; Yue, Y.; Zhang, L.; Liu, Y. Growing Layered Double Hydroxides on CNTs and Their Catalytic Performance for Higher Alcohol Synthesis from Syngas. *J. Mater. Sci.* **2016**, *51* (11), 5216–5231.

(22) Feng, Y.; Zhang, Y.; Wang, J.; Ling, L.; Zhang, R.; Fan, M.; Hou, B.; Li, D.; Wang, B. Promotion of Anatase/Rutile Junction to Direct Conversion of Syngas to Ethanol on the Rh/TiO_2 Catalysts. *ACS Catal.* **2024**, *14*, 1874–1881.

(23) Wu, D.; Liu, S.; Zhong, M.; Zhao, J.; Du, C.; Yang, Y.; Sun, Y.; Lin, J.; Wan, S.; Wang, S.; Huang, J.; Yao, Y.; Li, Z.; Xiong, H. Nature and Dynamic Evolution of Rh Single Atoms Trapped by CeO_2 in CO Hydrogenation. *ACS Catal.* **2022**, *12*, 12253–12267.

(24) Bordoloi, A.; Anton, J.; Ruland, H.; Muhler, M.; Kaluza, S. Metal–Support Interactions in Surface-Modified Cu–Co Catalysts Applied in Higher Alcohol Synthesis. *Catal. Sci. Technol.* **2015**, *5*, 3603–3612.

(25) Sun, J.; Cai, Q.; Wan, Y.; Wan, S.; Wang, L.; Lin, J.; Mei, D.; Wang, Y. Promotional Effects of Cesium Promoter on Higher Alcohol Synthesis from Syngas over Cesium-Promoted $Cu/ZnO/Al_2O_3$ Catalysts. *ACS Catal.* **2016**, *6*, 5771–5785.

(26) Asundi, A. S.; Hoffman, A. S.; Bothra, P.; Boubnov, A.; Vila, F. D.; Yang, N.; Singh, J. A.; Zeng, L.; Raiford, J. A.; Abild-Pedersen, F.; Bare, S. R.; Bent, S. F. Understanding Structure–Property Relationships of MoO_3 -Promoted Rh Catalysts for Syngas Conversion to Alcohols. *J. Am. Chem. Soc.* **2019**, *141*, 19655–19668.

(27) Yang, N.; Yoo, J. S.; Schumann, J.; Bothra, P.; Singh, J. A.; Valle, E.; Abild-Pedersen, F.; Nørskov, J. K.; Bent, S. F. Rh-MnO Interface Sites Formed by Atomic Layer Deposition Promote Syngas Conversion to Higher Oxygenates. *ACS Catal.* **2017**, *7*, 5746–5757.

(28) Huang, X.; Teschner, D.; Dimitrakopoulou, M.; Fedorov, A.; Frank, B.; Kraehnert, R.; Rosowski, F.; Kaiser, H.; Schunk, S.; Kuretschka, C.; Schlögl, R.; Willinger, M.; Trunschke, A. Atomic-Scale Observation of the Metal–Promoter Interaction in Rh-Based Syngas-Upgrading Catalysts. *Angew. Chem., Int. Ed.* **2019**, *58*, 8709–8713.

(29) Yang, N.; Medford, A. J.; Liu, X.; Studt, F.; Bligaard, T.; Bent, S. F.; Nørskov, J. K. Intrinsic Selectivity and Structure Sensitivity of Rhodium Catalysts for C_{2+} Oxygenate Production. *J. Am. Chem. Soc.* **2016**, *138*, 3705–3714.

(30) Granlund, M. Z.; Jansson, K.; Nilsson, M.; Dawody, J.; Pettersson, L. J. Evaluation of Co, La, and Mn Promoted Rh Catalysts for Autothermal Reforming of Commercial Diesel: Aging and Characterization. *Appl. Catal. B* **2015**, *172–173*, 145–153.

(31) Nathan, S. S.; Asundi, A. S.; Hoffman, A. S.; Hong, J.; Zhou, C.; Vila, F. D.; Cargnello, M.; Bare, S. R.; Bent, S. F. Surface Fe Clusters Promote Syngas Reaction to Oxygenates on Rh Catalysts Modified by Atomic Layer Deposition. *J. Catal.* **2022**, *414*, 125–136.

(32) Liu, Y.; Göeltl, F.; Ro, I.; Ball, M. R.; Sener, C.; Aragão, I. B.; Zanchet, D.; Huber, G. W.; Mavrikakis, M.; Dumesic, J. A. Synthesis Gas Conversion over Rh-Based Catalysts Promoted by Fe and Mn. *ACS Catal.* **2017**, *7*, 4550–4563.

(33) Zhong, H.; Wang, J.; Guo, S.; Fang, K.; Liu, Y. Mutual Tailored Bimetallic Rh–Co Supported on La Modified SiO_2 for Direct Ethanol Synthesis from Syngas. *Ind. Eng. Chem. Res.* **2019**, *58*, 2631–2643.

(34) Mu, Y.; Zheng, J.; Yang, Q.; Liu, G.; Liu, X.; Wang, X.; Wang, G.; Liang, X.; Yuan, Y. Active Site Synergy of Rh and Co Derived from ZrO_2-Supported $LaRh_x Co_{1-x} O_3$ Perovskite Nanostructures for the Direct Synthesis of Ethanol from Syngas. *ACS Appl. Nano. Mater.* **2023**, *6* (7), 5692–5702.

(35) Zhao, W.; Guan, Z.; Li, D.; Wang, B.; Fan, M.; Zhang, R. Syngas Conversion to C_2 Species over WC and M/WC (M = Cu or Rh) Catalysts: Identifying the Function of Surface Termination and Supported Metal Type. *ACS Appl. Mater. Interfaces* **2022**, *14* (17), 19491–19504.

(36) Subramanian, N. D.; Gao, J.; Mo, X.; Goodwin Jr., J. G.; Torres, W.; Spivey, J. J. La and/or V Oxide Promoted Rh/SiO_2 Catalysts: Effect of Temperature, H_2/CO Ratio, Space Velocity, and Pressure on Ethanol Selectivity from Syngas. *J. Catal.* **2010**, *272*, 204–209.

(37) Egbebi, A.; Schwartz, V.; Overbury, S. H.; Spivey, J. J. Effect of Li Promoter on Titania-Supported Rh Catalyst for Ethanol Formation from CO Hydrogenation. *Catal. Today* **2010**, *149*, 91–97.

(38) Schwartz, V.; Campos, A.; Egbebi, A.; Spivey, J. J.; Overbury, S. H. EXAFS and FT-IR Characterization of Mn and Li Promoted Titania-Supported Rh Catalysts for CO Hydrogenation. *ACS Catal.* **2011**, *1*, 1298–1306.

(39) Xu, D.; Ding, M.; Hong, X.; Liu, G. Mechanistic Aspects of the Role of K Promotion on Cu–Fe-Based Catalysts for Higher Alcohol Synthesis from CO_2 Hydrogenation. *ACS Catal.* **2020**, *10*, 14516–14526.

(40) Zeng, Z.; Li, Z.; Guan, T.; Guo, S.; Hu, Z.; Wang, J.; Rykov, A.; Lv, J.; Huang, S.; Wang, Y.; Ma, X. CoFe Alloy Carbide Catalysts for Higher Alcohols Synthesis from Syngas: Evolution of Active Sites and Na Promoting Effect. *J. Catal.* **2022**, *405*, 430–444.

(41) Katzer, J. R.; Sleight, A. W.; Gajardo, P.; Michel, J. B.; Gleason, E. F.; McMillan, S. The Role of the Support in CO Hydrogenation Selectivity of Supported Rhodium. *Faraday Discuss Chem. Soc.* **1981**, *72*, 121.

(42) SOLYMOSI, F. Hydrogenation of CO on Supported Rh Catalysts. *J. Catal.* **1982**, *75* (1), 78–93.

(43) Yu, J.; Mao, D.; Han, L.; Guo, Q.; Lu, G. Catalytic Conversion of Syngas into C_{2+} Oxygenates over Rh/SiO_2-Based Catalysts: The Remarkable Effect of Hydroxyls on the SiO_2. *J. Mol. Catal. A Chem.* **2013**, *367*, 38–45.

(44) Kusama, H.; Okabe, K.; Sayama, K.; Arakawa, H. CO_2 Hydrogenation to Ethanol over Promoted Rh/SiO_2 Catalysts. *Catal. Today* **1996**, *28*, 261–266.

(45) Camposeco, R.; Castillo, S.; Hinojosa-Reyes, M.; Zanella, R.; López-Curiel, J. C.; Fuentes, G. A.; Mejía-Centeno, I. Active TiO_2-Nanostructured Surfaces for CO Oxidation on Rh Model Catalysts at Low-Temperature. *Catal. Letters* **2019**, *149*, 1565–1578.

(46) Yu, J.; Yu, J.; Shi, Z.; Guo, Q.; Xiao, X.; Mao, H.; Mao, D. The Effects of the Nature of TiO_2 Supports on the Catalytic Performance of Rh–Mn/TiO_2 Catalysts in the Synthesis of C_2 Oxygenates from Syngas. *Catal. Sci. Technol.* **2019**, *9*, 3675–3685.

(47) Jing, Y.; He, C.; Zhang, N.; Murano, Y.; Toyoshima, R.; Kondoh, H.; Kageyama, Y.; Inomata, H.; Toyao, T.; Shimizu, K. Promotional Effect of Ag on the Catalytic Decomposition of N_2O in the Presence of O_2 over the Al_2O_3 -Supported Rh Catalyst. *ACS Catal.* **2023**, *13*, 12983–12993.

(48) Jing, Y.; Taketoshi, K.; Zhang, N.; He, C.; Toyao, T.; Maeno, Z.; Ohori, T.; Ishikawa, N.; Shimizu, K. Catalytic Decomposition of N_2O in the Presence of O_2 through Redox of Rh Oxide in a RhO_x/ZrO_2 Catalyst. *ACS Catal.* **2022**, *12*, 6325–6333.

(49) Zhang, N.; He, C.; Jing, Y.; Qian, Y.; Toyao, T.; Shimizu, K. Enhanced N_2O Decomposition on Rh/ZrO_2 Catalysts through the Promotional Effect of Palladium. *Surf. Interfac.* **2024**, *46*, 104120.

(50) Wu, D.; Liu, S.; Zhong, M.; Zhao, J.; Du, C.; Yang, Y.; Sun, Y.; Lin, J.; Wan, S.; Wang, S.; Huang, J.; Yao, Y.; Li, Z.; Xiong, H. Nature and Dynamic Evolution of Rh Single Atoms Trapped by CeO_2 in CO Hydrogenation. *ACS Catal.* **2022**, *12* (19), 12253–12267.

(51) Ravel, B.; Newville, M. *ATHENA* , *ARTEMIS* , *HEPHAESTUS* : Data Analysis for X-Ray Absorption Spectroscopy Using *IFEFFIT*. *J Synchrotron Radiat* **2005**, *12*, 537–541.

(52) Kresse, G.; Furthmüller, J. Efficient Iterative Schemes for *Ab Initio* Total-Energy Calculations Using a Plane-Wave Basis Set. *Phys. Rev. B* **1996**, *54*, 11169–11186.

(53) Kresse, G.; Furthmüller, J. Efficiency of Ab-Initio Total Energy Calculations for Metals and Semiconductors Using a Plane-Wave Basis Set. *Comput. Mater. Sci.* **1996**, *6*, 15–50.

(54) Perdew, J. P.; Ruzsinszky, A.; Csonka, G. I.; Vydrov, O. A.; Scuseria, G. E.; Constantin, L. A.; Zhou, X.; Burke, K. Restoring the Density-Gradient Expansion for Exchange in Solids and Surfaces. *Phys. Rev. Lett.* **2008**, *100*, 136406.

(55) Blöchl, P. E. Projector Augmented-Wave Method. *Phys. Rev. B.* **1994**, *50*, 17953–17979.

(56) Grimme, S.; Ehrlich, S.; Goerigk, L. Effect of the Damping Function in Dispersion Corrected Density Functional Theory. *J Comput. Chem.* **2011**, *32*, 1456–1465.

(57) Hinuma, Y.; Toyao, T.; Kamachi, T.; Maeno, Z.; Takakusagi, S.; Furukawa, S.; Takigawa, I.; Shimizu, K. Density Functional Theory Calculations of Oxygen Vacancy Formation and Subsequent Molecular Adsorption on Oxide Surfaces. *J. Phys. Chem. C* **2018**, *122*, 29435–29444.

(58) CHUANG, S. The Effect of Alkali Promotion on CO Hydrogenation over Rh/TiO_2. *J. Catal.* **1985**, *95*, 435–446.

(59) Behrendt, G.; Mockenhaupt, B.; Prinz, N.; Zobel, M.; Ras, E.; Behrens, M. CO Hydrogenation to Methanol over Cu/MgO Catalysts and Their Synthesis from Amorphous Magnesian Georgeite Precursors. *ChemCatChem* **2022**, *14*, e202200299.

(60) Cao, A.; Wang, Z.; Li, H.; Elnabawy, A. O.; Nørskov, J. K. New Insights on CO and CO_2 Hydrogenation for Methanol Synthesis: The Key Role of Adsorbate-Adsorbate Interactions on Cu and the Highly Active MgO-Cu Interface. *J. Catal.* **2021**, *400*, 325–331.

(61) He, C.; Ruan, T.; Ouyang, X.; Ma, Y.; Qian, Y.; Qiu, X. Selective Hydrodeoxygenation of Monophenolics from Lignin Bio-Oil for Preparing Cyclohexanol and Its Derivatives over Ni-Co/Al_2O_3-MgO Catalyst. *Ind. Crops. Prod.* **2023**, *202*, 117045.

(62) Ahmed, S.; Irshad, M.; Yoon, W.; Karanwal, N.; Sugiarto, J. R.; Khan, M. K.; Kim, S. K.; Kim, J. Evaluation of MgO as a Promoter for the Hydrogenation of CO_2 to Long-Chain Hydrocarbons over Fe-Based Catalysts. *Appl. Catal. B* **2023**, *338*, 123052.

(63) Guo, S.; Li, Z.; Yin, R.; Li, J.; Zeng, Z.; Hu, Z.; Luo, G.; Lv, J.; Huang, S.; Wang, Y.; Ma, X. Oxygen Vacancy over $CoMnO_x$ Catalysts Boosts Selective Ethanol Production in the Higher Alcohol Synthesis from Syngas. *ACS Catal.* **2023**, *13*, 14404–14414.

(64) Sun, K.; Tan, M.; Bai, Y.; Gao, X.; Wang, P.; Gong, N.; Zhang, T.; Yang, G.; Tan, Y. Design and Synthesis of Spherical-Platelike Ternary Copper-Cobalt-Manganese Catalysts for Direct Conversion of Syngas to Ethanol and Higher Alcohols. *J. Catal.* **2019**, *378*, 1–16.

(65) Lin, T.; Qi, X.; Wang, X.; Xia, L.; Wang, C.; Yu, F.; Wang, H.; Li, S.; Zhong, L.; Sun, Y. Direct Production of Higher Oxygenates by Syngas Conversion over a Multifunctional Catalyst. *Angew. Chem., Int. Ed.* **2019**, *58*, 4627–4631.

(66) Sun, K.; Liu, Z.; Song, S.; Liu, W.; Wang, P.; Zhang, T.; Xue, Y.; Wang, Y.; Tan, Y. Effect of Hydroxyl Groups on CuCoMg Nanosheets for Ethanol and Higher Alcohol Synthesis from Syngas. *Ind. Eng. Chem. Res.* **2021**, *60*, 2388–2399.

(67) Sun, K.; Wu, Y.; Tan, M.; Wang, L.; Yang, G.; Zhang, M.; Zhang, W.; Tan, Y. Ethanol and Higher Alcohols Synthesis from Syngas over CuCoM (M=Fe, Cr, Ga and Al) Nanoplates Derived From Hydrotalcite-Like Precursors. *ChemCatChem* **2019**, *11*, 2695–2706.

(68) Cui, W.-G.; Li, Y.-T.; Zhang, H.; Wei, Z.-C.; Gao, B.-H.; Dai, J.-J.; Hu, T.-L. In Situ Encapsulated Co/MnOx Nanoparticles inside Quasi-MOF-74 for the Higher Alcohols Synthesis from Syngas. *Appl. Catal. B* **2020**, *278*, 119262.

(69) Ge, Y.; Zou, T.; Martín, A. J.; Pérez-Ramírez, J. ZrO_2 -Promoted Cu-Co, Cu-Fe and Co-Fe Catalysts for Higher Alcohol Synthesis. *ACS Catal.* **2023**, *13*, 9946–9959.

(70) Chen, T.; Su, J.; Zhang, Z.; Cao, C.; Wang, X.; Si, R.; Liu, X.; Shi, B.; Xu, J.; Han, Y.-F. Structure Evolution of Co–CoO_x Interface for Higher Alcohol Synthesis from Syngas over Co/CeO_2 Catalysts. *ACS Catal.* **2018**, *8*, 8606–8617.

(71) Qi, X.; Lin, T.; An, Y.; Wang, X.; Lv, D.; Tang, Z.; Zhong, L. Regulating Oxygen Vacancies for Enhanced Higher Oxygenate Synthesis via Syngas. *ACS Catal.* **2023**, *13*, 11566–11579.

(72) Gong, K.; Wei, Y.; Lin, T.; Qi, X.; Sun, F.; Jiang, Z.; Zhong, L. Maximizing the Interface of Dual Active Sites to Enhance Higher Oxygenate Synthesis from Syngas with High Activity. *ACS Catal.* **2023**, *13*, 4533–4543.

(73) Luk, H. T.; Mondelli, C.; Mitchell, S.; Siol, S.; Stewart, J. A.; Curulla Ferré, D.; Pérez-Ramírez, J. Role of Carbonaceous Supports and Potassium Promoter on Higher Alcohols Synthesis over Copper–Iron Catalysts. *ACS Catal.* **2018**, *8*, 9604–9618.

(74) HAIDER, M.; GOGATE, M.; DAVIS, R. Fe-Promotion of Supported Rh Catalysts for Direct Conversion of Syngas to Ethanol. *J. Catal.* **2009**, *261*, 9–16.

(75) Wang, Z.; Kumar, N.; Spivey, J. J. Preparation and Characterization of Lanthanum-Promoted Cobalt–Copper Catalysts for the Conversion of Syngas to Higher Oxygenates: Formation of Cobalt Carbide. *J. Catal.* **2016**, *339*, 1–8.

(76) Zeng, Z.; Li, Z.; Guan, T.; Guo, S.; Hu, Z.; Wang, J.; Rykov, A.; Lv, J.; Huang, S.; Wang, Y.; Ma, X. CoFe Alloy Carbide Catalysts for Higher Alcohols Synthesis from Syngas: Evolution of Active Sites and Na Promoting Effect. *J. Catal.* **2022**, *405*, 430–444.

(77) Sun, J.; Wan, S.; Wang, F.; Lin, J.; Wang, Y. Selective Synthesis of Methanol and Higher Alcohols over Cs/Cu/ZnO/Al_2O_3 Catalysts. *Ind. Eng. Chem. Res.* **2015**, *54*, 7841–7851.

(78) Yu, J.; Li, G.; Han, Y.; Zheng, X.; Mao, H.; Mao, D. Comparative Study on Ethanol-Based Oxygenate Synthesis via Syngas over Rh–Mn Bimetallic Catalysts Supported on Different UiO MOFs. *Energy & Fuels* **2022**, *36*, 11940–11949.

(79) Huang, X.; Teschner, D.; Dimitrakopoulou, M.; Fedorov, A.; Frank, B.; Kraehnert, R.; Rosowski, F.; Kaiser, H.; Schunk, S.; Kuretschka, C.; Schlögl, R.; Willinger, M.; Trunschke, A. Atomic-Scale Observation of the Metal–Promoter Interaction in Rh-Based Syngas-Upgrading Catalysts. *Angew. Chem., Int. Ed.* **2019**, *58*, 8709–8713.

(80) Da Won, B.; Ham, H.; Cho, J. M.; Lee, J.-B.; Kim, C.-U.; Roh, H.-S.; Moon, D. J.; Bae, J. W. Effect of Mn Promoter on Rh/Tungsten Carbide on Product Distributions of Alcohols and Hydrocarbons by CO Hydrogenation. *RSC Adv.* **2016**, *6*, 101535–101543.

(81) Xue, X.; Yu, J.; Han, Y.; Xiao, X.; Shi, Z.; Mao, H.; Mao, D. Zr-Based Metal–Organic Frameworks Drived Rh–Mn Catalysts for Highly Selective CO Hydrogenation to C_2 Oxygenates. *J. Ind. Eng. Chem.* **2020**, *86*, 220–231.

(82) Xiang, M.; Li, D.; Li, W.; Zhong, B.; Sun, Y. Synthesis of Higher Alcohols from Syngas over K/Co/β-Mo_2C Catalysts. *Catal. Commun.* **2007**, *8*, 503–507.

(83) Li, Z.; Fu, Y.; Jiang, M. Structures and Performance of Rh–Mo–K/Al_2O_3 Catalysts Used for Mixed Alcohol Synthesis from Synthesis Gas. *Appl. Catal. A Gen.* **1999**, *187*, 187–198.

(84) Wang, N.; Fang, K.; Lin, M.; Jiang, D.; Li, D.; Sun, Y. Synthesis of Higher Alcohols from Syngas over Fe/K/β-Mo_2C Catalyst. *Catal. Letters* **2010**, *136*, 9–13.

(85) Han, T.; Zhao, L.; Liu, G.; Ning, H.; Yue, Y.; Liu, Y. Rh-Fe Alloy Derived from $YRh_{0.5}Fe_{0.5}O_3/ZrO_2$ for Higher Alcohols Synthesis from Syngas. *Catal. Today* **2017**, *298*, 69–76.

(86) Mao, W.; Su, J.; Zhang, Z.; Xu, X.-C.; Fu, D.; Dai, W.; Xu, J.; Zhou, X.; Han, Y.-F. A Mechanistic Basis for the Effects of Mn Loading on C_{2+} Oxygenates Synthesis Directly from Syngas over Rh–MnO/SiO_2 Catalysts. *Chem. Eng. Sci.* **2015**, *135*, 301–311.

(87) Yu, J.; Mao, D.; Han, L.; Guo, Q.; Lu, G. Conversion of Syngas to C_{2+} Oxygenates over Rh-Based/SiO_2 Catalyst: The Promoting Effect of Fe. *J. Ind. Engin.Chem.* **2013**, *19* (3), 806–812.

(88) Luo, H. Y.; Zhang, W.; Zhou, H. W.; Huang, S. Y.; Lin, P. Z.; Ding, Y. J.; Lin, L. W. A Study of Rh-Sm-V/SiO_2 Catalysts for the Preparation of C_2-Oxygenates from Syngas. *Appl. Catal. A Gen.* **2001**, *214*, 161–166.

(89) Xue, F.; Chen, W.; Song, X.; Cheng, X.; Ding, Y. Promotional Effects of Cr and Fe on Rh/SiO_2 Catalyst for the Preparation of Ethanol from CO Hydrogenation. *RSC Adv.* **2016**, *6*, 35348–35353.

(90) Liu, Y.; Murata, K.; Inaba, M.; Takahara, I.; Okabe, K. Synthesis of Ethanol from Syngas over Rh/$Ce_{1-x}Zr_xO_2$ Catalysts. *Catal Today* **2011**, *164*, 308–314.

(91) Li, Z.; Fu, Y.; Bao, J.; Jiang, M.; Hu, T.; Liu, T.; Xie, Y. Effect of Cobalt Promoter on Co–Mo–K/C Catalysts Used for Mixed Alcohol Synthesis. *Appl. Catal. A Gen.* **2001**, *220*, 21–30.

(92) Yin, H.; Ding, Y.; Luo, H.; Yan, L.; Wang, T.; Lin, L. The Performance of C_2 Oxygenates Synthesis from Syngas over Rh−Mn−Li−Fe/SiO_2 Catalysts with Various Rh Loadings. *Energy & Fuels* **2003**, *17* (6), 1401–1406.

(93) Feng, Y.; Zhang, Y.; Wang, J.; Ling, L.; Zhang, R.; Fan, M.; Hou, B.; Li, D.; Wang, B. Promotion of Anatase/Rutile Junction to Direct Conversion of Syngas to Ethanol on the Rh/TiO_2 Catalysts. *ACS Catal.* **2024**, *14*, 1874–1881.

(94) Fang, H.; Wu, S.; Ayvali, T.; Zheng, J.; Fellowes, J.; Ho, P.-L.; Leung, K. C.; Large, A.; Held, G.; Kato, R.; Suenaga, K.; Reyes, Y. I. A.; Thang, H. V.; Chen, H.-Y. T.; Tsang, S. C. E. Dispersed Surface Ru Ensembles on MgO (111) for Catalytic Ammonia Decomposition. *Nat. Commun.* **2023**, *14*, 647.

(95) Egbebi, A.; Schwartz, V.; Overbury, S. H.; Spivey, J. J. Effect of Li Promoter on Titania-Supported Rh Catalyst for Ethanol Formation from CO Hydrogenation. *Catal. Today* **2010**, *149*, 91–97.

(96) Li, Z.; Hu, Z.; Zeng, Z.; Guo, S.; Lv, J.; Huang, S.; Wang, Y.; Ma, X. Lamellar-Structured Silicate Derived Highly Dispersed CoCu Catalyst for Higher Alcohol Synthesis from Syngas. *Ind. Eng. Chem. Res.* **2022**, *61*, 6859–6871.

(97) Huynh, H. L.; Zhu, J.; Zhang, G.; Shen, Y.; Tucho, W. M.; Ding, Y.; Yu, Z. Promoting Effect of Fe on Supported Ni Catalysts in CO_2 Methanation by in Situ DRIFTS and DFT Study. *J. Catal.* **2020**, *392*, 266–277.

(98) Zeng, Z.; Li, Z.; Guo, S.; Lv, J.; Huang, S.; Wang, Y.; Ma, X. Janus Au–$Fe_{2.2}C$ Catalyst for Direct Conversion of Syngas to Higher Alcohols. *ACS Sustain. Chem. Eng.* **2021**, *9*, 11258–11268.

(99) Bwoker, M. On the Mechanism of Ethanol Synthesis on Rhodium. *Catal. Today* **1992**, *15*, 77–100.

(100) Zeng, Z.; Li, Z.; Kang, L.; Han, X.; Qi, Z.; Guo, S.; Wang, J.; Rykov, A.; Lv, J.; Wang, Y.; Ma, X. A Monodisperse E′-$(Co_xFe_{1-x})_{2.2}$ C Bimetallic Carbide Catalyst for Direct Conversion of Syngas to Higher Alcohols. *ACS Catal.* **2022**, *12*, 6016–6028.

(101) Wang, Y.; Kattel, S.; Gao, W.; Li, K.; Liu, P.; Chen, J. G.; Wang, H. Exploring the Ternary Interactions in Cu–ZnO–ZrO_2 Catalysts for Efficient CO_2 Hydrogenation to Methanol. *Nat. Commun.* **2019**, *10*, 1166.

(102) Wu, C.; Lin, L.; Liu, J.; Zhang, J.; Zhang, F.; Zhou, T.; Rui, N.; Yao, S.; Deng, Y.; Yang, F.; Xu, W.; Luo, J.; Zhao, Y.; Yan, B.; Wen, X.-D.; Rodriguez, J. A.; Ma, D. Inverse ZrO_2/Cu as a Highly Efficient Methanol Synthesis Catalyst from CO_2 Hydrogenation. *Nat. Commun.* **2020**, *11*, 5767.

(103) Zeinalipour-Yazdi, C. D.; Cooksy, A. L.; Efstathiou, A. M. CO Adsorption on Transition Metal Clusters: Trends from Density Functional Theory. *Surf. Sci.* **2008**, *602*, 1858–1862.

(104) Gajdo, M.; Eichler, A.; Hafner, J. CO Adsorption on Close-Packed Transition and Noble Metal Surfaces: Trends from *Ab Initio* Calculations. *J. Phys. Condens. Matter.* **2004**, *16*, 1141–1164.

(105) Tian, X.; Wang, T.; Yang, Y.; Li, Y.-W.; Wang, J.; Jiao, H. About Copper Promotion in CH_4 Formation from CO Hydrogenation on Fe(100): A Density Functional Theory Study. *Appl. Catal. A Gen.* **2017**, *530*, 83–92.

Chapter 5

General conclusion

In this work, I focused on developing supported catalysts for ethanol synthesis via CO_2 hydrogenation and syngas conversion. By combing the comprehensive characterizations and advanced data science, we not only discovered the high-performance catalysts for CO_2 hydrogenation to ethanol, but also highlighted the role of each element in contributing to superior activity. Considering the CO is one of the important intermediates for CO_2 hydrogenation to ethanol, we further developed an unexpected support (MgO) that showed high efficiency in ethanol synthesis via syngas conversion. *In situ/operando* spectroscopic techniques and theoretical calculations identified that interactions between Li_2O and Rh species on the MgO surface are playing a crucial role in promoting the ethanol synthesis process. The main conclusions are summarized as follows:

Chapter 2 introduces a highly efficient catalyst, K–Fe–Cu–Zn/ZrO_2 (KFeCuZn/ZrO_2), which significantly boosts the ethanol space time yield (STY_{EtOH}) to 5.4 mmol g_{cat}^{-1} h^{-1} under optimized conditions (360 °C, 4 MPa, and 12 L g_{cat}^{-1} h^{-1}). Through *in situ/operando* spectroscopic techniques, the crucial roles of K and Fe in higher alcohols synthesis and C–C coupling were uncovered, respectively. The incorporation of Cu promoted the formation of the key intermediate (CH_3CH_2O*), while Zn addition suppressed ethanol decomposition, thus enhancing the overall efficiency of the ethanol synthesis process.

Chapter 3 displays an alternative approach, a machine learning (ML) approach, which goes beyond the traditional element pool to include previously studied elements in the development of efficient catalysts for ethanol synthesis via CO_2 hydrogenation. We took the above catalyst and some similar catalysts from previous work (58 catalysts and 274 data points in total) as an initial dataset and performed 24 iterations (ML prediction + experimental validation), testing a total of 555 catalysts (2477 data points). More than 70 catalysts with superior performance were discovered by a data science approach, among these, The multi-element Pd(0.8)–Au(0.3)/K(2.5)–Sr(1)–Fe(20)–Zn(4)–Cd(2)–Yb(1)–Re(1)/CeO_2(25%)-ZrO_2 catalyst was clarified as the most effective catalyst in ethanol synthesis (STY_{EtOH}: 8.2 mmol g_{cat}^{-1} h^{-1}). Comprehensive characterizations and control reactions were employed to validate the reliability of ML model and critical roles of each element in ethanol synthesis.

Chapter 4 describes the direct conversion of syngas to ethanol using Li-promoted RhO_x/MgO catalysts (RhO_x/Li_2O/MgO). The ethanol selectivity and space time yield (STY_{EtOH}) reached 20% and 12.2 mmol g_{cat}^{-1} h^{-1}, respectively, at a CO conversion of 35% over the RhO_x/Li_2O/MgO catalyst. *In situ/operando* spectroscopic techniques, along with other characterizations and theoretical calculations, underscored the importance of interactions

between Li_2O and Rh on the MgO surface in moderating CO adsorption on the Rh surface, thereby enhancing ethanol production.

Acknowledgement

I would like to extend my deepest gratitude to my supervisor, Prof. Ken-ichi Shimizu, for providing me with the opportunity to be a part of his laboratory and for generously sharing his knowledge and expertise. My sincere appreciation goes to Prof. Takashi Toyao for his daily support and excellent supervision throughout my research. Under the guidance of Prof. Shimizu and Prof. Toyao, I have grown significantly in scientific critical thinking, experimental skills, and achievement presentation.

I am also extremely grateful to Prof. Ichigaku Takigawa from Hokkaido University, Prof. Evgeny Pidko from Delft University of Technology, Lecturer. Ryo Toyoshima from the University of Tokyo, as well as Dr. Shinya Mine and Dr. Abdellah Ait El Fakir, postdoctoral fellows from the Shimizu Lab, for their technical expertise, which made this work possible.

I would also like to acknowledge the Advanced Graduate School and EXEX Doctoral Fellowship of Hokkaido University for providing me with the valuable opportunity and financial support to obtain my PhD degree.

I am thankful to all other members of Prof. Shimizu's laboratory for their assistance and camaraderie.

Lastly, I would like to express my heartfelt thanks to my family and friends, particularly my wife, Xu Xiaoyan, for their unwavering support, understanding, and encouragement.

Du Pengfei